VAAL UNIVERSITY OF TECHNOLOGY

PREPARATION AND APPLICATION OF PINE-MAGNETITE COMPOSITE GRAFTED WITH FUNCTIONAL VINYL MONOMERS FOR REMOVAL OF DYES FROM SINGLE AND BINARY SOLUTIONS

KGOMOTSO NTOMBIZODWA GINA MTSHATSHENI

STUDENT NUMBER: 215272617

BSc Hons, MSc (CHEMISTRY)

Thesis submitted in fulfillment of the requirement for the degree of

DOCTOR OF PHILOSOPHY: CHEMISTRY

FACULTY OF APPLIED AND COMPUTER SCIENCES

DEPARTMENT OF CHEMISTRY

PROMOTER: Prof A.E. OFOMAJA (BSc Hons, M.Sc, D.Tech)

CO-PROMOTER: Prof E.B. NAIDOO (B.Sc Hons, M.Sc, Ph.D)

MAY 2021

DECLARATION OF CANDIDATE

I declare this thesis is my own work, unilateral. It has not been submitted for any degree or examination in any other university. It is being submitted for the degree Doctor of philosophy to the Department of Chemistry, Vaal University of Technology, Vanderbijlpark, South Africa

_____on this _____day of _____2021

CANDIDATE

_____on this _____day of _____2021

PROMOTER

_____on this _____day of _____2021

CO-PROMOTER

DEDICATION

I dedicate this work to my late father, Fikile Solomon Mtshatsheni. I know how much you wanted to see me being a doctor. I know you are smiling down on me.

ACKNOWLEDGEMENTS

I would like to express my sincere appreciation and gratitude to the following people who assisted me in their own special ways:

- My promoter late Prof AE Ofomaja and co-promoter Prof EB Naidoo for their supervision, assistance, support, and trust in my ability throughout my studies.
- Prof EN Nxumalo for his assistance, countless suggestions, sacrifices and motivation. I thank God our paths crossed. I pray God's blessings upon your life.
- Mr SA Zikalala for countless assistance and sacrifices he has made. May God bless you.
- Dr O Ayanda for endless efforts and profound contributions towards my studies.
- Vaal University of Technology (VUT), Department of Chemistry at VUT, Research Directorate at VUT and the National Research Foundation of South Africa for financial assistance.
- Prof MJ Moloto for every contribution and financial sacrifices towards my studies.
- Colleagues in the Department of Chemistry at VUT: Dr M Klink, Dr T Xaba, Dr W Maboya, Mr M Ngoy for every assistance towards my studies.
- Dr S Takaidza for his countless assistance with dry freezer.
- Anthony for your assistance with XRF analysis
- Biosorption & Wastewater Treatment Research group, Dr Okoli, Dr A Pholosi, Dr A Kupeta, Dr L Ouma, Dr O Saheed, Mrs N Mabaso and everyone who is part of the group for the assistance I received.
- Dr J Maloma, Dr OB Omole and mama Christina Bungane for continuous motivation and prayers.
- Tshifhiwa Matamela and Puleng Molete for provision of glassware and chemicals.
- Ntombi Ditlopo and Siya Bacela for encouragement and an ear to listen. I am forever grateful.
- Carol Motale, Zakea Shivambu, Malesole Bucibo, Ronette Kemp, Cindy Baburam and Unisa Terblanche for the talks and motivation during the hard days.
- My mom, Cynthia Mtshatsheni, and sister, Dineo Wesi, for their constant encouragement, support and love. This one is for you!
- Boingotlo Wesi my dearest niece, thank you for all the encouragement and your sweet words.

- Uncle Bakang Oliphant for all the encouragement, thank you.
- Ntando Mtshatsheni, my boy, thank you for perseverance during mummy's absence during some of your school activities and late nights in the lab with mummy. Much love for you.

I am eternally grateful to my Heavenly Father for His grace, mercy, and the strength He gave me to persevere until the end of this work.

PRESENTATIONS AND PUBLICATIONS

The work presented in this thesis has been presented at both national and international conferences and published in peer-reviewed journals and in a book as a book chapter.

A. CONFERENCE PRESENTATIONS

1. Kgomotso N.G. Mtshatsheni, Eliazer B. Naidoo, Augustine E Ofomaja Preparation and optimization of pine-magnetite composite for removal of methylene blue International conference on Pure and Applied Chemistry (ICPAC) 18 – 22 July 2016, Flic en Flac, Mauritius, Oral presentation
2. Kgomotso N.G. Mtshatsheni, Eliazer B. Naidoo, Augustine E Ofomaja, Preparation and optimization of pine-magnetite composite for removal of methylene blue, Center for Renewable Energy and Water (CREW) International conference on Environment, Materials and Green Technology, 24 – 25 November 2016, Vanderbijlpark, South Africa
3. Kgomotso N.G. Mtshatsheni, Eliazer B. Naidoo, Augustine E Ofomaja, Synthesis and optimization of pine-magnetite composite for removal of methylene blue, 9th International conference of the African Materials Research Society, 11 – 14 December 2017, Gaborone International Convention Center, Gaborone, Botswana, Oral presentation
4. Kgomotso N.G. Mtshatsheni, Eliazer B. Naidoo, Augustine E Ofomaja, Synthesis and optimization of pine-magnetite composite for removal of methylene blue, South African Chemical Institute 43rd SACI National Convention 2018, Council for Scientific and Industrial Research-International Convention Center, Pretoria, Poster presentation
5. Kgomotso N.G. Mtshatsheni, Eliazer B. Naidoo, Augustine E Ofomaja, Grafting of pine-magnetite composite with acrylic acid for removal of methylene, 10th International conference of the African Materials Research Society, Nelson Mandela African Institution Science Technology Arusha, Tanzania (10 – 13 December 2019), Poster presentation

B. PUBLICATIONS

PEER-REVIEWED PUBLICATIONS

1. Kgomotso N.G. Mtshatsheni, Augustine. Ofomaja, Eliazer.B. Naidoo, (2019): Synthesis and optimization of reaction variables in the preparation of pine-magnetite composite for removal of methylene blue dye, South African Journal of Chemical Engineering 29, 33–41, https://doi.org/10.1016/j.sajce.2019.05.002

2. Kgomotso N.G. Mtshatsheni, Sithembela A. Zikalala, Eliazer B. Naidoo, Edward N. Nxumalo, AE Ofomaja, (2021). Surface structure-property relationship of acrylic acid-grafted pine-magnetite bionanocomposites and its effect on the adsorption of MB from water. (*Under review at the Journal of Journal of Nanoscience and Nanotechnolgy*)

3. Kgomotso N.G. Mtshatsheni, Sithembela A. Zikalala, Eliazer B. Naidoo, Edward N. Nxumalo, AE Ofomaja, (2021). Pinecone-based adsorptive bionanocomposites as modifiers for monodoped and co-doped amorphous TiO_2: Towards greener photocatalyst synthesis and degradation processes. (*Under review at the Journal of Environmental and Chemical Engineering*)

BOOK CHAPTER

Kgomotso N.G. Mtshatsheni, Augustine. Ofomaja, Eliazer.B. Naidoo (2020): Characterization of grafted acrylamide onto pine-magnetite composite for the removal of methylene blue from wastewater, Waste in textile and leather sectors, INTECHOPEN, ISBN: 987-1-78985-244-1

ABSTRACT

Water is a basic resource to mankind. The environment is deteriorating daily due to industrial pollution of water resources. Industrial effluents containing organic pollutants such as dyes are undesirable even at low concentrations in the environment. Natural biomaterials have been applied as adsorbents for dye removal from water systems, however, their application has been limited by their low adsorption capacity. Much attention has been focused on the chemical modification of natural biomass via grafting processes. The modification of natural polymers by graft copolymerization is a promising technique since it functionalizes a biopolymer thus imparting desirable properties. The purpose of the study was to prepare and optimize the working conditions for the pine-magnetite bionanocomposites (PMC) as adsorbents and as photocatalysts modifiers. First, this work focuses on the synthesis and optimization of reaction variables in the preparation of PMC for the removal of methylene blue (MB). The thesis also explores the synthesis of acrylamide and acrylic acid-grafted PMC, resulting in the formation of acrylamide-grafted PMC (GACA) and acrylic acid-grafted pine-magnetite bionanocomposites (GAA), respectively. The grafting of functional groups such as –CO, $–NH_2$ onto cellulose from acrylamides is also explored in detail. The adsorption conditions optimized were used to investigate the adsorption efficiency of GAA and GACA on MB. Finally, the application of PMC and GAA as modifiers for amorphous TiO_2 and N-doped $TiO_2$was carried out. The photocatalytic bionanocomposites from PMC (namely PMC–a-C,TiO_2 and PMC–a-C,$NTiO_2$) and those from GAA (labeled GAA–a-C,TiO_2 and GAA–a-C,$NTiO_2$) are compared by their photocatalytic efficiency on the degradative removal of an alkaline dye mixture formed from Reactive red 120 (RR 120) and Rhodamine B (Rh B).

The synthesis procedure for PMC involved treating pinecone biomass with 0.15 M NaOH solution to remove unwanted plant extracts and the subsequent coating of the treated pinecone with iron oxide magnetic particles through a co-precipitation method. The variables used for the experiments were volume of NH_4OH (5 to 40 cm^3), reaction temperature (40 to 100 °C), effect of time (15 to 60 min) and mass (1.0 to 3.5 g).

The PMC and acrylic acid grafted pine-magnetite composite (GAA) were probed for structural morphology and surface properties using various surface characterization instrumental techniques. Strong chemical interactions between pinecone magnetite and acrylic acid were

demonstrated by thermogravimetric (TGA), differential thermal analysis (DTA) and X-ray photoelectron spectroscopy (XPS) for these unique bionanocomposites as such suggesting high chemical stability. Grafting acrylic acid was shown by XPS to form polyacrylic acid on the surface of the bionanocomposites and thus capping the surface groups. Significant differences in size were shown by transmission electron spectroscopy (TEM) and scanning electron microscopy (SEM); i.e., smaller particle sizes (Ave = 13.0 nm) for GAA and slightly larger for PMC (Ave = 14.0 nm). Brunauer Emmett Teller (BET) surface analysis demonstrated a larger surface area, pore volume and pore diameter (59.9 $m^2.g^{-1}$, 0.2254 $cm^3.g^{-1}$ and 28.14) for GAA compared to PMC. These characteristics coupled with the point of zero charge for GAA (pH_{pzc} = 6.8) were critical in enhancing the efficiency of GAA adsorption of MB at pH 12 and further enable GAA to have a higher desorption efficiency of up to 99.7% after four cycles of washing with 0.10 M HCl. The adsorption kinetics and isotherm studies indicated that the adsorption process follows the pseudo second order kinetics and Langmuir isotherm respectively. The adsorbent also showed improvement in the adsorption capacity and reusability promising to be used for the removal of dyes in a prototype scale. GAA and MB adsorption mechanism was confirmed to be through intra particle diffusion. The overall performance of the GAA bionanocomposites is hinged on the formation of polyacrylic acid on the surface, its structural morphology, and the enhanced surface properties. Most importantly, the plant-based materials (lignin and cellulose) provide an environment that is rich with surface (–COOH and –OH) groups for the attachment of the magnetite nanoparticles while the polyacrylic acid stabilizes the magnetite onto the pinecone nanoparticles while reducing the point of zero charge for increased adsorption of cationic species.

The photocatalytic bionanocomposites were fabricated from the adsorptive bionanocomposites using a simple solgel process in which ~10 wt.% of PMC and GAA, respectively, were used as a starting agent. Titanium butoxide was used as a precursor, acetylacetone as a dispersant and ethylene diamine as a nitrogen source. Using this procedure, amorphous carbon-doped titania (a-C,TiO_2) and amorphous carbon and nitrogen co-doped titania (a-C,$NTiO_2$) were fabricated except that the biopolymer was not added. Two sets of amorphous titania bionanocomposites were fabricated. One set was the nitrogen doped forms that had been modified with PMC and GAA (PMC–a-C,TiO_2 and GAA–a-C,$NTiO_2$). The other set of photocatalytic bionanocomposites produced in this work were without nitrogen (PMC–a-C,TiO_2 and GAA–a-C,TiO_2).

TEM and SEM micrographs showed that all the photocatalysts consisted of globular, smooth aggregates of nanosized a-CTiO_2 and a-C,NTiO_2 which decreased in size with N-doping and the incorporation of GAA and PMC to as low as <30 nm. Surface chemical analysis through FTIR, XPS and EDS confirmed the presence of C, O, Ti and N (for the N-doped photocatalysts). In addition, it was demonstrated that N-doping into TiO_2 had taken place, albeit with most of the N incorporated as organic nitrogen. It was further demonstrated that because of the absence of high temperature calcination, the process chemicals played a significant role in doping the photocatalysts with carbon resulting in the promotion of photocatalytic activity for a-C,TiO_2 to the point of surpassing that of, a-C,NTiO_2 and all the PMC-modified photocatalytic bionanocomposites. a-C,TiO_2 had an overall 94% removal of the dyes, Rhodamine B (RhB) and Reactive red 120(RR 120), under UV illumination. The benefit of co-doping a-TiO_2 with C, N and the biopolymers was realized with the incorporation of GAA as a modifier. The result was 97% removal of the dyes by GAA–a-CTiO_2 and 99% for GAA–a-C,NTiO_2. It was further observed that the degradation of the binary mixture of the dyes (RhB and RR 120) proceeded through the zero order kinetics for the a-C,TiO_2 based photocatalysts and first order kinetics for the N-doped photocatalysts.

The work, has, therefore demonstrated the applicability of plant-based biopolymers in the fabrication of nanoadsorbents and nanophotocatalysts. While the photocatalytic degradations were carried out under UV-light, there still remains a number of possible avenues that researchers can build on to improve the visible light-driven photocatalytic bionanocomposites. The research work has proven the effectiveness of novel pinecone magnetic nanoparticle materials and TiO_2-based photocatalyst for the degradation of undesirable dyes from wastewater.

TABLE OF CONTENTS

LIST OF FIGURES

LIST OF TABLES

LIST OF ABBREVIATIONS AND SYMBOLS

AAS	atomic absorption spectroscopy
a-C,TiO_2	amorphous carbon-doped titania
a-C,NTiO_2	amorphous carbon and nitrogen co-doped titania
BET	Brunauer-Emmett-Teller
CCD	central composite design
EDS	electron dispersive X-ray spectroscopy
FTIR	Fourier-transform infrared
GAA	grafted acrylic acid
GACA	grafted acrylamide
pH_{pzc}	pH at point of zero charge
PFO	pseudo-first order
PMC	pine-magnetite composite
PSO	pseudo-second order
rpm	revolutions per minute
RSM	response surface methodology
SEM	scanning electron microscopy
TEM	transmission electron microscopy
TGA	thermal gravimetric analysis
UV-vis	UV-visible
VSM	Vibrating sample magnetometer
XRD	X-ray diffraction
XRF	X-ray fluorescence
XPS	X-ray photoelectron spectroscopy

Symbols

C_e	equilibrium concentration
C_0	initial concentration
h	the initial adsorption rate
k_1	pseudo-first order rate constant
k_2	pseudo-second order rate constant
K_f	Feundlich constant
m	mass of the adsorbent

q_e	equilibrium capacity
$q_{e,m}$	equilibrium capacity obtained by calculating from model
q_t	equilibrium capacity at time t
R^2	coefficient of determination
$t^{0.5}$	the time in minutes raised to the power of 0.5
V	solution volume
$\% R$	percentage removal
$F(R)$	reflectance coeficient
E_g	energy band gap
α	optical absorption coeficient of a material
hv	photon energy

CHAPTER 1

INTRODUCTION

1.1. Background

The rapid growth of the world's population, industrialization, poorly planned urbanization, agricultural activities as well as the excessive use of chemicals have significantly contributed to environmental pollution [1]. Environmental pollutants that are of primary concern include among others heavy metals, dyes, biodegradable wastes, phosphates and nitrates, fluorides, hazardous and toxic chemicals, radioactive pollutants, pharmaceuticals and personal care products [2]–[4]. Consequently, trace amounts of these undesirable compounds lead to an enormous pollution of water sources.

Many industries involved in the manufacture of textile, paper, rubber, plastics, leather, cosmetics, pharmaceutical and food industries use dyes to tincture their products. However, dyes are common water contaminants and are regularly found in the industrial wastewaters [5]. Most dyes are complex organic molecules that are mostly resistant to detergents and therefore easily make their way into our water systems.

A vast amount of research investigating the removal of either dyes or heavy metals from industrial effluents has been carried out over the years [6], [7]. Due to their toxic effects, dyes have generated much concern and several processes such as adsorption, precipitation, chemical degradation, photodegradation, biodegradation, chemical coagulation and electrocoagulation have been applied in the removal of dyes from colored effluents [8]. Due to the typical high concentrations of dyes in effluent from dyehouses, the amount of adsorbent required to remove the dyes is typically high and hence making it expensive to use the synthetic adsorbents. As such, adsorbents derived from naturally produced polymers offer a cheaper alternative. Such adsorbents are commonly plant materials.

Several research articles showed that pinecone shell (PCS) can selectively adsorb heavy metals. For example, Deniz *et al.* (2011) studied the biosorption of Ni (II) and Cr (VI) from aqueous solution by cone biomass [9]. Argun *et al.* (2008), described activation of pinecone with Fenton reagent and determined the removal of Cd (II) and Pb (II) ions from aqueous solution obtaining excellent results [10]. Ofojama and Naidoo (2010), examined the effect of surface modification

on the biosorption kinetics of lead (II) ions onto raw and NaOH modified pinecone powder [11]. The authors also treated pinecone powder with KOH and their studies revealed that KOH treated pinecone powder had a higher capacity for Cu (II) than untreated pinecone shell [11]. In another investigation, the variation caused by the NaOH modification of pinecone powder on the kinetics and diffusion of Pb (II) and Cu (II) ions onto the pinecone powder surface was investigated [12]. These authors also studied the kinetic behavior of the Cu (II)–pinecone powder system with the variation of several process variables including solution pH, initial concentration and temperature [13]. All these studies show the great ability which pinecone has towards its application in the removal of pollutants from water.

The current study investigates the preparation of novel, efficient and eco-friendly pine-iron oxide magnetite bionanocomposites. The biomaterials were grafted using vinyl monomers. Grafting of these bionanocomposite materials increased reactivity and improved surface area. The pinecone-iron oxide magnetite bionanocomposites were thus modified with acrylic acid and acrylamide. It was envisaged that this modification will enhance surface properties of the bionanocomposites, and in turn increase its adsorption capacity. The adsorption capacity of the targeted pollutants was therefore improved by the introduction of monomers onto the biomaterials. One of the limitations on pinecone is that it contains lignin which further affects the adsorption capacity of pinecone and the grafting of acrylic modifiers onto its surface. As an extension of this study, iron oxide nanoparticles were used as initiators to introduce active Fe-OH radicals to the –OH groups of the cellulose. Then acrylic acid and acrylamide were grafted on the active Fe-OH radical to obtain a high percentage and efficient grafting such that the –OH groups of the cellulose are retained. This modification will increase $–COO^-$ and $–NH_2$ functionalities on pinecone. Acrylic acid has strong $–COO^-$ functional groups that easily ionizes the pinecone charge and acts as the adsorption site to hold cations. Acrylamide has $–NH_2$ groups which bear lone pairs of electrons that donates them to cations. Therefore, these groups were expected to increase the functional groups on the surface of the pinecone. The chemical grafting was carried out using a conventional heating process. The method was explored to understand the percentage of acrylic acid and acrylamide grafted onto the pine-iron oxide magnetite bionanocomposites which was then used to adsorb cationic dyes from aqueous solutions.

Photocatalysis promotes the degradation of contaminants in water, transforming them into by-products with lower or no toxicity. The photocatalysts can be applied in suspension or

immobilized onto a support. The aim of using the immobilized form against the suspension form is that the costly extra final filtration process can be avoided, which is particularly important in water decontamination. Photocatalysis has attracted a great deal of attention due to the limitation of other techniques in the wastewater treatment. The photodegradation is one of the most effective route for degradation of organic pollutions to harmless materials such as CO_2 and H_2O or other species in wastewater [14], [15]. One of the main obstacles for industrial applications of photocatalysis is the worry of the release and destiny of the photocatalyst in the environment. Therefore, it is favorable to recover and retain the catalysts. Using magnetic core is a good candidate to overcome this problem [16]. Other treatment techniques such as adsorption by activated carbon and air stripping merely concentrates the chemical available by carrying them over to the adsorbent or air, which does not convert them to non-toxic wastes [17], [18]. Dyes used in textile industries, are known to be resistant to biodegradation [19]. They can undesirably color water, resulting in a reduced penetration of the sunlight [20], thus increasing the biochemical oxygen and chemical oxygen demand levels. Also, the release of these colored dyes into our environment is a source of aesthetic pollution and is detrimental to the environmental ecosystems. In addition, large concentrations of dyes in the aquatic environment may be toxic to aquatic species and desulphonated dyes have been reported to be a major source of problem in drinking water plants globally [21].

The novel bio-nanocomposite-magnetic nanoparticle materials were explored in overcoming the limitations of using bionanocomposites alone and to selectively remove dyes from environmental effluents. This research will benefit South Africa as it envisages providing simple techniques that are cost effective, efficient, and non-toxic for the removal of dyes in wastewater. In such as process, the dyes will be adsorbed before being discharged into water streams, thus, making our water easier to recycle and reuse.

1.2. Problem statement

Based on the literature reviewed, it is evident that there has been an increase in the production and utilization of dyes, resulting in an increase in environmental pollution. Effluents discharged from many of industries contain residues and derivatives of dyes. Consequently, the presence of very low concentrations in effluent is highly visible [22], [23]. Discharge of colored wastewater without proper treatment can result in numerous problems such as chemical oxygen demand (COD) by the water body, and an increase in toxicity. Currently, there are about 10,000

different commercial dyes and pigments and over 7 X 10^5 tons of synthetic dyes are produced annually world-wide [24]. It is estimated that 10 – 15% of the dyes are lost in the effluent during the dyeing processes.

It is a serious challenge to treat dye effluents because of their synthetic origins and mainly aromatic structures, which are biologically non-degradable. Among several chemical and physical methods, the adsorption process is one of the most effective techniques that have been successfully employed for color removal from wastewater [25]. There are currently numerous treatment processes for effluent discharged from industrial processes containing dyes; amongst which are biodegradation electrolysis [26], [27], foam flotation [28], chemical oxidation [6], [29], adsorption [30], electro-coagulation [31] and photocatalysis [32].

Various techniques have been utilized in the removal of dyes; however, a successful methodology for removal of all types of dyes at a low cost has not been established [33]. Different processes involving adsorption yields rewarding results but has not been exhausted. Despite their efficiency and applicability, they are restricted because a substantial amount of adsorbent is lost during the regeneration processes, and they are also non-selective (i.e., they cannot isolate each pollutant and removed it independently of one another).

This work primarily focuses on the development of a novel, cost-effective bio-nanocomposite which can be more economical and efficient at commercial level. The major objective was to synthesize pine-magnetite composite from pinecone powder. Thereafter, graft the PMC with acrylic acid and acrylamide to increase its reactivity and improve its surface area. It was envisaged that the grafting will enhance the surface properties of this bio-nanocomposite, and in turn increase its adsorption capacity bionanocomposites. The focus of this research work is therefore a combination of photocatalysis and adsorption through the fabrication of photocatalytic adsorbent nanomaterials. To further reduce the environmental footprint and the capital costs, the adsorbent used in this study mainly consists of pinecone powder.

1.3. Research questions

The current study seeks to answers the following research questions:

i. What effect does functional grafting with acrylic acid and acrylamide have on the surface and adsorptive properties of pine-magnetite bionanocomposites?

ii. What effect does TiO_2 and nitrogen doped TiO_2 ($NTiO_2$) have on the optical and structural properties of pinecone bionanocomposites?

iii. How does the modification of TiO_2 and $NTiO_2$ on pinecone affect its performance on the degradation of synthetic dyes?

iv. Can pinecone bionanocomposites be regenerated for reuse?

v. What effect does the *in-situ* modification of amorphous TiO_2 and amorphous $NTiO_2$ using the adsorptive bionanocomposites have on the photocatalytic removal efficiency of dyes in a binary solution.

1.4. Aim and objectives

1.4.1. Aim of the study

The aim of this study is to prepare effective and cheap bio-nanocomposite adsorbents from a locally available material (pinecone) collected in Vanderbijpark, Gauteng Province in South Africa for the removal of dyes from aqueous solutions. The bionanocomposites are further employed as modifiers for TiO_2 and $NTiO_2$ in the *in-situ* synthesis of amorphous TiO_2 for use in the degradation of a binary mixture of Reactive red 120 (RR 120) and Rhodamine B (RhB) dyes.

1.4.2. Objectives of the study

The objectives of this study are:

(i) To modify the surface of pinecone powder using NaOH to improve the cation exchange capacity.

(ii) To prepare pine-magnetite bionanocomposites using the co-precipitation method.

(iii) To optimize the adsorption variables such as solution pH, adsorbent dose, temperature and contact time for adsorptive removal of methylene blue from wastewater.

(iv) To graft acrylic acid or acrylamide monomers to the prepared bionanocomposite via a free radical initiated grafting.

(v) To determine the best fitting kinetic model, isotherms and thermodynamic parameters for the adsorption process and propose adsorption mechanism

(vi) To carry out the desorption and regeneration studies.

(vii) To synthesize grafted PMC/GAA TiO_2 and grafted PMC/GAA $NTiO_2$ photocatalytic bionanocomposites.

(viii) To carry out the photocatalytic degradation of binary dye mixtures from wastewater using photocatalytic bionanocomposites.

1.5. Hypothesis of the study

Functionally grafted pinecone-magnetite bionanocomposites are effective as adsorbents and photocatalysts in the removal of dyes from single and binary mixtures from wastewater.

1.6. Value of the research study

Water pollution has received great attention and remains a serious perennial problem worldwide. South Africa has become highly industrialized, and this has resulted in water shortage and several environmental challenges. Therefore, there is a need to develop cost-effective adsorbents which are more economical and efficient at the commercial level. Adsorption technique, by itself is an economically viable technique in that it is more suited for removal of waste material from real textile wastewater that advanced oxidation processes (AOPs) such as photocatalysis, electrocatalysis and Fenton processes, to name a few. Adsorption has the advantage of enabling removal of highly concentrated dyes through several cycles whereas AOPs are limited to effluent with low concentrations.

1.7. Novelty

A novel, effective and cheap bio-nanocomposite adsorbents from a locally available material (pinecone) in South Africa was successfully synthesized and employed in the removal of basic dyes from aqueous solutions. The bio-nanocomposite was further applied in the modification of TiO_2 and $NTiO_2$ and the effect of the different bio-nanocomposites on the TiO_2 is evaluated through the degradation of an alkaline mixture of dyes. The application of such bionanocomposites in the synthesis of photocatalysts is reported for the first time in this study.

1.8. Thesis outline

This thesis is divided into eight (8) chapters. A brief explanation of the aims of each chapter is summarized below.

Chapter 1

This chapter gives a general insight of the work presented in the thesis. It briefly presents the background of the work, the problem statement, justification, hypothesis, novelty statement, aims and objectives as well as the thesis outline.

Chapter 2

This chapter covers the general review of relevant literature that served as a guide into the research. The review on dyes and its pollution and toxicity, techniques and method for removal of dyes, kinetics and equilibrium modelling of experimental adsorption data is presented in this chapter. The calculation of thermodynamic adsorption parameters and the use of statistical error functions are described.

Chapter 3

Chapter 3 summarizes all the methods and analytical techniques used in the synthesis procedures and characterization for all the bionanocomposites used in the study, even though specific details pertaining experimental strategies are given in each chapter.

Chapter 4

Chapter 4 discusses the synthesis of pine-magnetite composite prepared from the pinecone powder using a co-precipitation method. The work demonstrates the preparation and optimization process of variables needed for the bio-nanocomposite working conditions. It presents an introduction into factors affecting adsorption and the optimization process following one factor at a time. Kinetic and equilibrium modelling of experimental adsorption calculations are explained. Characterization using FTIR, VMS, BET, XRD, TGA, TEM, SEM were studied and discussed. Regeneration and desorption cycles are discussed.

K.N.G. Mtshatsheni, A.E. Ofomaja, E.B. Naidoo, (2019): Synthesis and optimization of reaction variables in the preparation of pine-magnetite composite for removal of methylene blue dye, South African Journal of Chemical Engineering 29 (2019) 33–41, https://doi.org/10.1016/j.sajce.2019.05.002

Chapter 5

In this chapter, the effect of grafting of acrylamide onto pine-magnetite composite is investigated. Adsorption data is fitted into kinetic and isotherm models and the adsorption processes are calculated and presented. Characterization using FTIR, XRD, TGA, TEM, SEM were studied and discussed. The work also discusses regeneration and desorption cycles.

KNG Mtshatsheni, EB Naidoo and AE Ofomaja (2020): Characterization of grafted acrylamide onto pine-magnetite composite for the removal of methylene blue from wastewater: Waste in the textile and leather sectors, INTECHOPEN, ISBN: 987-1-78985-244-1

Chapter 6

This chapter systematically probes the surface structure-property relationship of acrylic acid-grafted pine-magnetite bionanocomposites and its effect on the adsorption of MB from water. It further investigates the effect of coupling pinecone dust with magnetite nanoparticles and further grafting of pine-magnetite composite (PMC) with acrylic acid using ceric ammonium nitrate (CAN) as an initiator on the adsorptive mechanism of the resultant bionanocomposites and its stability under reuse. The pine-magnetite (PMC) and acrylic acid grafted pine-magnetite composite (GAA) were probed for structural morphology and surface properties using various surface characterization instrumental techniques.

Kgomotso N.G. Mtshatsheni[a,*], Sithembela A. Zikalala, Eliazer B. Naidoo[a], Edward N. Nxumalo[b], AE Ofomaja[a], (2021). Surface structure-property relationship of acrylic acid-grafted pine-magnetite bionanocomposites and its effect on the adsorption of MB from water, Journal of Nanoscience and Nanotechnology. (*Under Review*)

Chapter 7

Chapter 7 investigates differences in which the adsorptive bionanocomposites PMC and GAA influence the morphology and chemical composition of TiO_2. In doing so, two paths are pursued: the in-situ deposition of TiO_2 onto GAA and PMC bionanocomposites and the in-situ deposition of TiO_2 onto the bionanocomposites in the presence of a nitrogen source. The process results in the formation of amorphous carbon doped (a-C,TiO_2) photocatalyst and its counterpart amorphous carbon and nitrogen co-doped TiO_2 (a-C,NTiO_2). Photocatalytic

bionanocomposites PMC–a-C,TiO_2, GAA–a-C,TiO_2 and their nitrogen-doped counterparts PMC–a-C,$NTiO_2$ and GAA–a-C,$NTiO_2$ were fabricated in the process. The photocatalysts are characterized form morphological. Chemical and optical properties. These properties are correlated to the performance of the photocatalysts in the removal of a mixture of Rh B and RR120 dyes under UV light.

Kgomotso N.G. Mtshatsheni, Sithembela A. Zikalala, Eliazer B. Naidoo, Edward N. Nxumalo, AE Ofomaja, (2021). Surface structure-property relationship of acrylic acid-grafted pine-magnetite bionanocomposites and its effect on the adsorption of MB from water, Journal of Environmental and Chemical Engineering. (*Under Review*)

Chapter 8

Chapter 8 summarizes the findings of this thesis in the form of conclusions.
Recommendations for future work are also made in this Chapter

1.9. References

[1] V.K. Gupta, Suhas, Application of low-cost adsorbents for dye removal - A review, J. Environ. Manage. 90 (2009) 2313–2342. https://doi.org/10.1016/j.jenvman.2008.11.017.

[2] H.P. Srivastava, G. Arthanareeswaran, N. Anantharaman, V.M. Starov, Performance of modified poly(vinylidene fluoride) membrane for textile wastewater ultrafiltration, Desalination. 282 (2011) 87–94. https://doi.org/10.1016/j.desal.2011.05.054.

[3] A. Bhatnagar, E. Kumar, M. Sillanpää, Fluoride removal from water by adsorption-A review, Chem. Eng. J. 171 (2011) 811–840. https://doi.org/10.1016/j.cej.2011.05.028.

[4] R. Srivastava, D.C. Rupainwar, Eucalyptus bark powder as an effective adsorbent: Evaluation of adsorptive characteristics for various dyes, Desalin. Water Treat. 11 (2009) 302–313. https://doi.org/10.5004/dwt.2009.864.

[5] L.B. de Lima, L.O. Pereira, S.G. de Moura, F. Magalhães, Degradation of organic contaminants in effluents—synthetic and from the textile industry—by Fenton, photocatalysis, and H_2O_2 photolysis, Environ. Sci. Pollut. Res. 24 (2017) 6299–6306. https://doi.org/10.1007/s11356-016-6973-x.

[6] S. Dawood, T.K. Sen, Review on Dye Removal from Its Aqueous Solution into Alternative Cost Ef-fective and Non-Conventional Adsorbents Citation: Tushar K Sen, et al. (2014) Review on Dye Removal from Its Aqueous Solution into Alternative Cost Effective and Non-Conventional Ads, J Chem Proc Eng. 1 (2014) 104.

[7] M.B. Chabalala, B.C. Seshabela, S.W.H. Van Hulle, B.B. Mamba, S.D. Mhlanga, E.N. Nxumalo, Cyclodextrin-Based Nanofibers and Membranes: Fabrication, Properties and Applications, in: P. Arora, N. Dhingra (Eds.), Cyclodext. - A Versatile Ingred., InTechOpen, 2018: pp. 135–169. https://doi.org/10.5772/intechopen.74737.

[8] A.Y. Zahrim, C. Tizaoui, N. Hilal, Coagulation with polymers for nanofiltration pre-treatment of highly concentrated dyes: A review, Desalination. 266 (2011) 1–16. https://doi.org/10.1016/j.desal.2010.08.012.

[9] F. Deniz, S. Karaman, S.D. Saygideger, Biosorption of a model basic dye onto Pinus brutia Ten.: Evaluating of equilibrium, kinetic and thermodynamic data, Desalination. 270 (2011) 199–205. https://doi.org/10.1016/j.desal.2010.11.046.

[10] M.E. Argun, S. Dursun, M. Karatas, M. Gürü, Activation of pine cone using Fenton oxidation for Cd(II) and Pb(II) removal, Bioresour. Technol. 99 (2008) 8691–8698. https://doi.org/10.1016/j.biortech.2008.04.014.

[11] A.E. Ofomaja, E.B. Naidoo, Biosorption of copper from aqueous solution by chemically activated pine cone: A kinetic study, Chem. Eng. J. 175 (2011) 260–270. https://doi.org/10.1016/j.cej.2011.09.103.

[12] A.E. Ofomaja, Intraparticle diffusion process for lead(II) biosorption onto mansonia wood sawdust, Bioresour. Technol. 101 (2010) 5868–5876. https://doi.org/10.1016/j.biortech.2010.03.033.

[13] A.J.K. Kupeta, E.B. Naidoo, A.E. Ofomaja, Kinetics and equilibrium study of 2-nitrophenol adsorption onto polyurethane cross-linked pine cone biomass, J. Clean. Prod. 179 (2018) 191–209. https://doi.org/10.1016/j.jclepro.2018.01.034.

[14] S.A. Zikalala, A.T. Kuvarega, H. Madhav, B.B. Mamba, S.D. Mhlanga, E.N. Nxumalo, Applied Catalysis A , General A comparison of the influence of synthesis methods on the photocatalytic activity of nitrogen doped titania-carbon nanotube nanohybrids, Appl. Catal. A, Gen. 604 (2020) 117776. https://doi.org/10.1016/j.apcata.2020.117776.

[15] A.R.R. Khataee, M.B.B. Kasiri, Photocatalytic degradation of organic dyes in the presence of nanostructured titanium dioxide: Influence of the chemical structure of dyes, J. Mol. Catal. A Chem. 328 (2010) 8–26. https://doi.org/10.1016/j.molcata.2010.05.023.

[16] N. Masunga, O.K. Mmelesi, K.K. Kefeni, B.B. Mamba, Recent advances in copper ferrite nanoparticles and nanocomposites synthesis, magnetic properties and application in water treatment: Review, J. Environ. Chem. Eng. 7 (2019) 103179. https://doi.org/10.1016/j.jece.2019.103179.

[17] J.R. De Andrade, M.F. Oliveira, M.G.C. Da Silva, M.G.A. Vieira, Adsorption of Pharmaceuticals from Water and Wastewater Using Nonconventional Low-Cost Materials: A Review, Ind. Eng. Chem. Res. 57 (2018) 3103–3127. https://doi.org/10.1021/acs.iecr.7b05137.

[18] H.A. Hegazi, Removal of heavy metals from wastewater using agricultural and industrial wastes as adsorbents, HBRC J. 9 (2013) 276–282. https://doi.org/10.1016/j.hbrcj.2013.08.004.

[19] Y. Çalışkan, H.C. Yatmaz, N. Bektaş, Photocatalytic oxidation of high concentrated dye solutions enhanced by hydrodynamic cavitation in a pilot reactor, Process Saf. Environ. Prot. 111 (2017) 428–438. https://doi.org/10.1016/j.psep.2017.08.003.

[20] ZDHC Foundation, The Zero Discharge of Hazardous Chemicals Programme Chemical Management for the Textile Industry, (2017) 1–20. http://www.roadmaptozero.com (accessed December 21, 2017).

[21] D.A. Yaseen, M. Scholz, Textile dye wastewater characteristics and constituents of synthetic effluents: a critical review, Springer Berlin Heidelberg, 2019. https://doi.org/10.1007/s13762-018-2130-z.

[22] S. Ahirrao, Zero Liquid Discharge Solutions, in: Ind. Wastewater Treat. Recycl. Reuse, Elsevier Ltd., 2014: pp. 489–520. https://doi.org/10.1016/B978-0-08-099968-5.00013-1.

[23] G. Boczkaj, A. Fernandes, Wastewater treatment by means of advanced oxidation processes at basic pH conditions: A review, Chem. Eng. J. 320 (2017) 608–633. https://doi.org/10.1016/j.cej.2017.03.084.

[24] B.S. Choudri, Y. Charabi, M. Baawain, M. Ahmed, Textiles, Water Environ. Res. 89 (2017) 1424–1440. https://doi.org/10.2175/106143017X15023776270502.

[25] K. Yokwana, A.T. Kuvarega, S.D. Mhlanga, E.N. Nxumalo, Mechanistic aspects for the removal of Congo red dye from aqueous media through adsorption over N-doped graphene oxide nanoadsorbents prepared from graphite flakes and powders, Phys. Chem. Earth. 107 (2018) 58–70. https://doi.org/10.1016/j.pce.2018.08.001.

[26] T.L.S. Silva, S. Morales-Torres, C.M.P. Esteves, A.R. Ribeiro, O.C. Nunes, J.L. Figueiredo, A.M.T. Silva, Desalination and removal of organic micropollutants and microorganisms by membrane distillation, Desalination. 437 (2018) 121–132. https://doi.org/10.1016/j.desal.2018.02.027.

[27] R. Saravanane, V. V. Ranade, V.M. Bhandari, A. Seshagiri Rao, Urban wastewater treatment for recycling and reuse in industrial applications: Indian scenario, in: V.M.B. Renadi, ViVek V. (Ed.), Ind. Wastewater Treat. Recycl. Reuse, 1st ed., Elsevier Ltd., Oxford, 2014: pp. 283–322. https://doi.org/10.1016/B978-0-08-099968-5.00007-6.

[28] L. Chang, Y. Cao, G. Fan, C. Li, W. Peng, A review of the applications of ion floatation: Wastewater treatment, mineral beneficiation and hydrometallurgy, RSC Adv. 9 (2019) 20226–20239. https://doi.org/10.1039/c9ra02905b.

[29] D.J. Chang, I.P. Chen, M. Ten Chen, S.S. Lin, Wet air oxidation of a reactive dye solution using CoAlPO4-5 and CeO2 catalysts, Chemosphere. 52 (2003) 943–949. https://doi.org/10.1016/S0045-6535(03)00302-3.

[30] M. Saifuddin, P. Kumaran, Removal of heavy metal from industrial wastewater using chitosan coated oil palm shell charcoal, Electron. J. Biotechnol. 8 (2005). http://www.scielo.cl/scielo.php?pid=S0717-34582005000100008&script=sci_arttext&tlng=pt.

[31] A.K. Golder, N. Hridaya, A.N. Samanta, S. Ray, Electrocoagulation of methylene blue and eosin yellowish using mild steel electrodes, J. Hazard. Mater. 127 (2005) 134–140. https://doi.org/10.1016/j.jhazmat.2005.06.032.

[32] K.E. Tettey, M.Q. Yee, D. Lee, Photocatalytic and conductive MWCNT/TiO_2 nanocomposite thin films, ACS Appl. Mater. Interfaces. 2 (2010) 2646–2652. https://doi.org/10.1021/am1004656.

[33] M.T. Yagub, T.K. Sen, S. Afroze, H.M. Ang, Dye and its removal from aqueous solution by adsorption: A review, Adv. Colloid Interface Sci. 209 (2014) 172–184. https://doi.org/10.1016/j.cis.2014.04.002.

[34] A. Islam, A.K. Guha, Removal of pH , TDS and Color from textile effluent by using coagulants and aquatic/non aquatic plants as adsorbents, 3 (2013) 101–114. https://doi.org/10.5923/j.re.20130305.01.

[35] Z. Liu, Y. Miao, Z. Wang, G. Yin, Synthesis and characterization of a novel super-absorbent based on chemically modified pulverized wheat straw and acrylic acid, Carbohydr. Polym. 77 (2009) 131–135. https://doi.org/10.1016/j.carbpol.2008.12.019.

[36] L. Wang, J. Li, Adsorption of C.I. Reactive Red 228 dye from aqueous solution by modified cellulose from flax shive: Kinetics, equilibrium, and thermodynamics, Ind. Crops Prod. 42 (2013) 153–158. https://doi.org/10.1016/j.indcrop.2012.05.031.

CHAPTER 2

LITERATURE REVIEW

2.1. Introduction

Water is an essential component to human life, agricultural and industrial activities. More areas suffer from water scarcity because of the increasing world-wide population, industrialization and the decreasing of available freshwater resources due to pollution [1]. Water pollution has caused an enormous concern worldwide [2,3]. Due to the fast growth of industry, the quality of water has been significantly reduced due to the industrial and agricultural wastewater discharges which contain heavy metals [4]**.** Once they are emitted, they can remain in the environment for years, and due to their toxic effects and their tendency to accumulate, they pose a risk to humans and the environment. Inorganic and organic wastes produced by human activities have resulted in high volumes of contaminated water which threatens human health and other living organisms [5]. Dye-bearing effluents are known to be significant source of water pollution. Dyes are known to be complex chemical organic compounds that can connect themselves to surfaces or fabrics to impart color. These dyes are purged from various industrial sources such as textile, cosmetic, paper, leather, rubber, and printing industries. The discharge of coloured substances into the water bodies causes aesthetic damage to the ecology and is harmful to biological organisms [6].

Given the scourge of dye pollution, there is a necessity for the development of novel, efficient and cost-effective methods for wastewater remediation. This is particularly so because most of the present day municipal methods of both wastewater and drinking water treatment methods are ineffective in the removal for synthetic dyes [7]. This inefficiency can be due to i) the technologies employed being unable to remove the dyes or, ii) where the technology is suited to remove dyes, the capacity of the treatment plants were designed for smaller volumes of water [8,9]. In either, case, the water treatment plants are overloaded with the barrage of dye pollution due to increase in the density of textile industries. Typical municipal wastewater treatment plants use techniques such as flocculation, adsorption, chlorination, to name a few [10].

Advanced treatment plants do employ techniques such as membrane technology and adsorbents, however, at a small scale [11,12]. Presently, systems that use photocatalysis and adsorption, either in a series or as a hybrid system, are among the leading potential technologies towards the removal of dye from wastewater [13,14]. This is because the adsorptive techniques

can be able to remove the high concentration of dyes while photocatalysis is able to deal with trace concentration of toxic pollutants that form in the wastewater. These two techniques are mainly viewed as an add-on to the currently existing municipal technologies so that the carbon footprint due to dye pollution is reduced [15]. This chapter will explore the properties of dyes, the fundamental principles of adsorption, the fundamental principles of photocatalysis and the advances made in fine tuning of these technologies.

2.2. Dye species found in wastewater

2.2.1. Introduction to dyes

A dye is a colored substance that has an affinity to the substrate to which it is being applied. The dye is generally applied in an aqueous solution, and requires a mordant to improve the fastness of the dye. The majority of natural dyes are derived from plant sources: roots, berries, bark, leaves, wood, fungi and lichens [16]. Most dyes are synthetic, i.e., are man-made from petrochemicals. Other than pigmentation, they have a range of applications including organic dye lasers**,** food colorants, pharmaceuticals, tracers in geological studies and human anatomy, cell markers to name a few [17]**,** [18]. Dyes being natural or synthetic organic compounds have been used for coloring many different types of materials for thousands of years. Synthetic dyes are widely used in many fields of advanced technology, such as the textile industry, paper, leather tanning, food processing, plastics, cosmetics, rubber, and in the printing as well as dye manufacturing industries [18]. Synthetic dyes are also employed in ground water tracing for the determination of specific surface area of activated sludge, sewage and wastewater treatment [18].

The textile industry and its dye-containing wastewater is one of the main sources of severe pollution worldwide [19,20]. About 10-25% of textile dyes are lost during the dyeing process, and 2-20% are directly discharged as aqueous effluents in different water bodies. Synthetic dyes have been used extensively due to their low cost, bright colors, resistance to fading, and ease of use. The residual dyes from different sources (e.g., textile industries, paper and pulp industries, dye and dye intermediates industries, pharmaceutical industries, tannery, and kraft bleaching industries, etc.) introduces a wide variety of organic pollutants into the natural water resources or wastewater treatment systems.

Dyes are one of the most easily recognizable pollutants in the environment. The discharge of dye-bearing wastewater into natural streams and rivers is toxic to aquatic life and damages the aesthetic nature of the environment [21]. In addition, the discharge of dyes into watercourses threatens the water supply and quality due to their non-degradability, toxicity, and accumulation throughout the food chain.

A wide range of physical and chemical processes such as flocculation, electro-flotation, precipitation, electro-kinetic coagulation, ion exchange, membrane filtration, oxidation, irradiation and ozonation have been investigated extensively for removing dyes from aquatic bodies [22,23]. However, these processes are costly and cannot effectively be used to treat the vast volume of wastewater containing dyes [24]**.**

The rapid advance of nanoscience and nanotechnology has brought new opportunities for wastewater treatment. Due to its unique physical and chemical properties such as large specific surface area, higher adsorption capacity and faster adsorption rate, nanomaterials have tremendous potential for capture of inorganic or organic pollutants in water [25]. Several treatment processes and methods have been used for removing heavy metal ions from contaminated water, including adsorption, chemical precipitation, chemical oxidation or reduction, ion exchange, filtration, reverse osmosis and electro-dialysis [26]**.**

Among these approaches, adsorption has been found to be superior to other techniques for removal of colors, odor, oils, and organic pollutants from processed or waste effluents in terms of its high efficiency, initial cost, simplicity of design and easy handling in terms of operation [24]**.**

2.2.2. Classification of dyes

There are several ways for classification of dyes. Dyes can be classified according to the chemical structure (acid, basic, direct, mordant, reactive, disperse, azo, and sulfur) [27], color and application method [18,28]. However, due to the complexities of the color nomenclature from the chemical structure system, the classification based on application is often favorable [1]. Dye molecules consists of chromophores (OH, NH_2, NHR, NR_2Cl and COOH) which are responsible for the production of color and auxochromes (NO_2, NO, N=N) enhance the affinity of the dye towards the fibers [29]. Chemical structure classification dyes are identified by groups with characteristic properties [30], e.g. azo dyes (-N=N-). They are strong, with good

all-round properties and are cost effective. On the other hand, anthraquinone dyes are weak and expensive.

Application-based classification is based on usage or method of application [31]. Dyes can also be classified based on their particle charge upon dissolution in an aqueous medium [28] such as cationic (all basic dyes), anionic (direct, acid, and reactive dyes) and non-ionic (dispersed dyes). Dyes are classified according to their solubility and chemical properties [16]**.**

2.2.3. Types of dyes

2.2.3.1. *Acid dyes*

Acid dyes are renowned for being soluble in water and they are anionic as such they are applied to fibers such as silk, wool, nylon and modified acrylic fibers. Their mode of attachment to the fiber is due through an electrostatic attraction between the cationic dye and the positively charged surface moieties of the fibers. As such, they are best suited for fibers with negatively charged surface groups. The most common category of dyes in this group are the synthetic food colorants.

2.2.3.2. *Basic dyes*

Basic dyes are also renowned for being highly soluble in water owing to them being cationic. As such basic dyes attach onto negatively charged fibers or fibers with negatively charged surface groups. As such they are mainly applied to acrylic fibers, wool and silk and paper.

2.2.3.3. *Methylene blue dye*

Methylene blue (***Figure 2.1***) is a common basic dye which has a wide variety of economic relevance. It has also been used as adsorption model for some adsorbents. It is used in many industries such as batik, textile, and tanning industry and in some universities' laboratories for practicing and researching. Discharge of methylene blue without treatment prior could contribute to water pollution. Due to this reason, it is evident that removal of methylene blue is of significantly important for the environmental and commerce. Some techniques have been used for the removal of methylene blue in the wastewater. Several physiochemical technologies like chemical oxidation [32], coagulation and flocculation [33], biological oxidation [34], electrochemical [35], ultrafiltration [36], and adsorption have been extensively studied for the

removal of dyes in the wastewater [37,38]**.** The adsorption process is found to be quite suitable, low investment, flexible, ease of operation, insensitive to pollutants and effective for the removal of dyes from aqueous solution. A considerable amount of work has also been published in the literatures regarding the adsorption of MB dye on various adsorbent surfaces such as alumina [39], clay [40,41], zeolite [42], peat [43], activated carbon [44] , silica [45], organic polymers [46], algae [47], plants wastes, wood sawdust [48], agricultural waste materials [49,50], nanocomposites [21], organic–inorganic hydrogel composites [51] and nanotubes [52]**.**

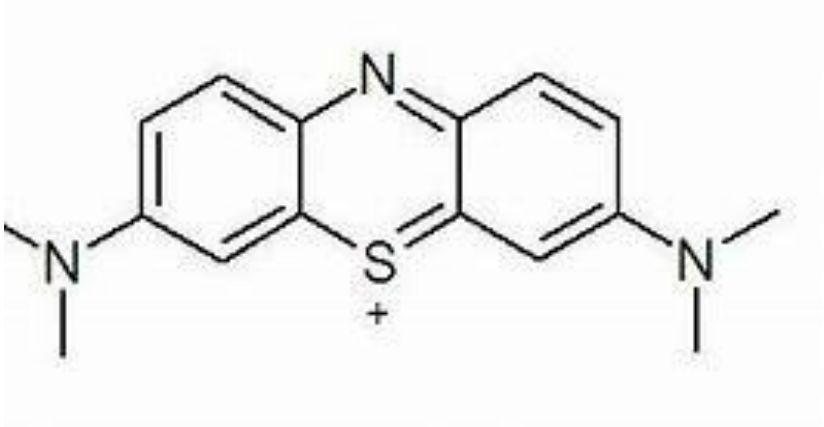

Figure 2.1 Chemical structure of methylene blue

2.2.3.4. *Direct dye*

Direct dyeing is normally carried out in a neutral or slightly alkaline dye bath, at or near boiling point, with the addition of either sodium chloride (NaCl) or sodium sulfate (Na_2SO_4) or sodium carbonate (Na_2CO_3) [53]. Direct dyes are used on cotton, paper, leather, wool, silk and nylon. Direct dyes are also used as pH indicators and as biological stains.

2.2.3.5. *Mordant dyes*

Mordant dyes require a dye fixative, which improves the fastness of the dye against water, light and perspiration [54]. The choice of mordant is very important as different mordants can change the final color significantly. Most natural dyes are mordant dyes and there is therefore a large literature base describing dyeing techniques. The most important mordant dyes are the synthetic mordant dyes, or chrome dyes, which comprise 30% of dyes used for wool, and are especially useful for black and navy shades [55]. The mordant potassium dichromate is applied as an after-treatment. It is important to note that many mordants,

particularly those in the heavy metal category, can be hazardous to health and extreme care must be taken in using them.

2.2.3.6. *Vat dyes*

Vat dyes are essentially insoluble in water and incapable of dyeing fibers directly [54]. However, reduction in alkaline liquor produces the water-soluble alkali metal salt of the dye. This form is often colorless, in which case it is referred to as a leuco dye, and has an affinity for the textile fiber. Subsequent oxidation reforms the original insoluble dye. The color of denim is due to indigo, the original vat dye.

2.2.3.7. *Reactive dyes*

Reactive dyes utilize a chromophore attached to a substituent that is capable of directly reacting with the fiber substrate [55]. The covalent bonds that attach reactive dye to natural fibers make them among the most permanent of dyes. "Cold" reactive dyes, such as Procion MX, Cibacron F, and Drimarene K, are very easy to use because the dye can be applied at room temperature. Reactive dyes are by far the best choice for dyeing cotton and other cellulose fibers at home or in the art studio.

2.2.3.8. *Disperse dyes*

Disperse dyes were originally developed for the dyeing of cellulose acetate, and are water-insoluble [54]. The dyes are finely ground in the presence of a dispersing agent and sold as a paste, or spray-dried and sold as a powder. Their main use is to dye polyester, but they can also be used to dye nylon, cellulose triacetate, and acrylic fibers. In some cases, a dyeing temperature of 130 °C (266 °F) is required, and a pressurized dyebath is used. The very fine particle size gives a large surface area that aids dissolution to allow uptake by the fiber. The dyeing rate can be significantly influenced by the choice of dispersing agent used during the grinding.

2.2.3.9. *Azo dye*

Azo dye is produced directly onto or within the fiber. This is achieved by treating a fiber with both diazoic and coupling components. With suitable adjustment of dyebath conditions, the two components react to produce the required insoluble azo dye [56]. This technique of dyeing

is unique, in that the final color is controlled by the choice of the diazoic and coupling components. This method of dyeing cotton is declining in importance due to the toxic nature of the chemicals used.

2.2.3.10. *Sulfur dyes*

Sulfur dyes are inexpensive dyes used to dye cotton with dark colors. Dyeing is effected by heating the fabric in a solution of an organic compound, typically a nitrophenol derivative, and sulfide or polysulfide [57]. The organic compound reacts with the sulfide source to form dark colors that adhere to the fabric. Sulfur Black 1, the largest selling dye by volume, does not have a well-defined chemical structure.

2.3. Toxicity effects on dyes

Dyes are known to have high intensity in color and greatly visible in very little concentration. Dyes may affect the photosynthetic activity in aquatic life due to decreased light penetration [18]. They may also be toxic to some aquatic life due to the presence of metals, aromatics, dyes etc. They are dangerous to humans and affects the kidneys, reproductive system, liver and central nervous system [58]. Dyes are reported to cause mutagenesis, chromosomal fractures, carcinogenesis, and respiratory toxicity. Due to their toxic effects, dyes have generated much concern regarding their use. Therefore, there is a need to focus on specific methods and technologies to remove dyes from wastewater streams.

2.4. Methods for Dye removal

Dyes are highly visible materials and a minor release into the environment may produce a color. Therefore, there is a need to develop new and improved methods to remove dyes from wastewater before it is discharged to receiving waters. Techniques to remove dye contaminants from wastewater such as photocatalytic degradation, adsorption/precipitation processes coagulation, chemical oxidation, membrane separation process, electro-chemical, aerobic and anaerobic microbial degradation have inherent limitations [59]. These technologies can be divided into three categories: biological, chemical and physical [34].

Current treatment technologies for color removal involving physical and chemical and biological processes have been extensively studied. The conventional methods for the treatment of colored wastewater are physical, chemical and biological treatments. However, these technologies have advantage and disadvantages. At large scale, most of these conventional methods are not applicable because of the high cost and disposal problems as large amount of sludge is been generated at the end of the process [34].

2.4.1. Physical methods

Physical treatments like electro-kinetic coagulation, ion-exchange, membrane filtration, electrochemical oxidation and photocatalytic degradation process have found to be successful in treating these wastewaters [60–62] however they have certain drawbacks. Treatment processes like coagulation produce huge amount of sludge leading to high disposal expenditure, while the ion-exchange process is expensive. Membrane separation process is effective, but due to membrane fouling problems and high investment its application is restricted. The major drawback in this technology, is analysis of their economic viability. Among all the physical treatments, adsorption process has been reported to be the most effective method for water decontamination [63]. Adsorption is known to be a promising technique, which has great importance due to the ease of operation and comparable low cost of application in the declaration process. Commercially activated carbon is a remarkable highly adsorbent material with many applications in the remediation of contaminated groundwater and industrial wastes such as colored effluents. However, activated carbon is an expensive adsorbent due to its high costs of manufacturing and regeneration. For the purpose of removing unwanted hazardous compounds from contaminated water at a low cost, much attention has been focused on various naturally occurring adsorbents such as chitosan, zeolites, fly ash, coal, paper mill sludge, and various clay minerals [64,65]. An attempt to develop cheaper and effective adsorbents and many non-conventional low-cost adsorbents such as clay materials, zeolites, siliceous material, agricultural wastes and industrial waste products have also been suggested [66,67].

2.4.2. Chemical treatment

The major agents of chemical treatment of dye wastewater are coagulants/flocculants [68]. It involves the addition of substances such as calcium, aluminum, or ferric ions to the effluent, as such flocculation is induced [69]. Furthermore, Mishara and Yue have report the use of other

agents for chemical processes such as, ferric sulphate [21,70], and some synthetic organic polymers. While Shi et al. (2014) suggests the combination of coagulation and flocculation may also be added to enhance the process. Generally, chemical treatment has economic feasibility and efficiency, but a major drawback is that the cost of chemicals is high and the price fluctuates in the market due to high demand and the rate at which chemicals are being produced. Moreover, even though it is efficient, the overall disadvantage of chemical treatment is the production of sludge and other unknown by products formed between the chemicals and the wide range of chemicals in the water. The chemistry of the sludge at the final stage treatment is pH dependent and brings about disposal problems [33].

2.4.3. Biological methods

Biological treatment of wastewater is an alternative and most economical method compared to physical and chemical methods. Biodegradation methods such as adsorption by (living or dead) microbial biomass, fungal decolorization, bioremediation systems and microbial degradation are commonly used in the treatment of industrial effluents. Microorganisms such as yeasts, bacteria, fungi and algae are able to accumulate and degrade different pollutants, but due to some technical constraints their applications is often restricted [71,72]. Biological treatment may be aerobic and anaerobic [73]. But the major drawback is that, it requires substantial land area and is constrained by sensitivity toward diurnal variation as well as toxicity of chemicals [66]. Moreover, contradictory findings were reported in a review of current technologies [19] which states that, with current conventional technology, biological treatment is incapable of obtaining satisfactory color elimination. Furthermore, dyes such as (azo dyes) are not easily degradable due to their complex chemical structure, synthetic organic origin and xenobiotic nature [74]. The strengths and limitations of these methods are summarized in ***Table 2.1***.

Table 2.1 Summary of advantages and disadvantages of methods for removal of dyes [75]

Method	Strengths	Limitations
Chemical treatments		
Oxidative process	Simplicity of application	Water is needed for the activation of the dyes
H_2O_2 + Fe(II) salts(Fenton's reagent)	Fenton's reagent is a suitable chemical means	Sludge generation
Ozonation	Ozone can be applied in its gaseous state and does not increase the volume of wastewater and sludge	Short half-life
Photochemical	No sludge is produced and foul odors are greatly reduced	Formation of by-products
Sodium hypochlorite (NaOCl)	Initiates and accelerate azo-bond cleavage	Release aromatic amines
Electrochemical destruction	No consumption of chemicals and no sludge build up	Relatively high flow rates cause a direct decrease in dye removal
Biological treatments		
Decolorization by white-rot fungi Other microbial cultures (mixed bacterial)	White rot fungi are able to degrade dyes using enzymes	Enzyme production has also been shown to be unreliable
Adsorption by living/dead microbial biomass	Decolorized in 24-30h	Under aerobic conditions azo dyes are not readily metabolized
Anaerobic textile dye bioremediation systems	Certain dyes have particular affinity for binding with microbial species Allows azo and other water-soluble dyes to be decolorized	Not effective for all dyes Anaerobic breakdown yields methane and hydrogen sulfide
Physical treatments		
Adsorption	Good removal of variety of dyes	Very expensive
Membrane filtration	Removes all dye types	Concentrated sludge production

Ion exchange	Regeneration: no adsorbent loss	Not effective for all dyes
Irradiation	Effective oxidation at lab scale	Requires a lot of dissolved O_2
electrokinetic coagulation	Economically feasible	High sludge production

2.5. Adsorption technologies

Adsorption is the accumulation of a substance at the interface between two phases which can either be liquid-solid or gas-solid interface. The substance that accumulates at the interface is called the adsorbate and the solid on which adsorption occurs is the adsorbent [63]. Adsorption can be classified into two types, chemical and physical. Chemical adsorption or chemisorption is characterized by the formation of strong chemical association of ions or molecules of the adsorbate to adsorbent surface. This is due to the exchange of electrons and thus it is known to be irreversible [76]. Physical adsorption or physisorption is characterized by weak Van der Waals intraparticle bonds between the adsorbate and the adsorbent and is thus reversible in most cases [76]. The main physical forces controlling adsorption are Van der Waals forces, hydrogen bonds, polarity, dipole-dipole π-π interaction, etc .[30]. This process provides an attractive alternative for the treatment of polluted waters, especially if the adsorbent is inexpensive and does not require an additional pre-treatment step before its application [63]**.** As for environmental remediation purpose, adsorption techniques have been widely studied and used to remove certain classes of chemical contaminants from water, mostly those that are practically unaffected by conventional biological wastewater treatments [63,76].

Factors that influence the adsorption efficiency include adsorbate, adsorbent interaction, adsorbent surface area, adsorbent to adsorbate ratio, adsorbent particle size, temperature, pH and contact time [66,76].

In recent years, the search for low-cost adsorbents with pollutant-binding capacities has intensified. Locally available natural materials such as agricultural and industrial wastes can be utilized as low-cost adsorbents. When a solution containing adsorptive solute meets a solid with a highly porous or a gel-like structure, intermolecular forces of attraction (physical or chemical nature) cause some of the solute molecules from the solution to be concentrated or deposited at the structure. The creation of an adsorbed phase having a composition different from that of the bulk fluid phase forms the basis of separation by adsorption technology [66,76]**.**

In removing dyes from aqueous solutions, adsorbents can bind and capture heavy metal ions from the aqueous solutions. The key part of an adsorption process are the adsorbents. Thus, good adsorbents should be abundant and easy to process, and have high selectivity, large surface area and long service time [77]. So far, many natural materials and synthetic compounds have been used as adsorbents, including bark, lignin, dead biomass, zeolite, peat, xanthate, clay, modified wool and cotton, fly ash, chitosan [78], as well as homopolymer, copolymer and composites of water soluble monomers (e.g., acrylic acid and acrylamide).

2.5.1. Factors affecting adsorption of dye

Factors that need to be taken into consideration and optimized are solution pH, temperature, and initial dye concentration and biosorbent dosage.

2.5.1.1. *Effect of solution pH*

The pH of a solution affects the capacity of the adsorbent in wastewater treatment. The efficiency of adsorption is dependent on the solution pH, because variation in pH leads to the variation in the degree of ionization of the adsorptive molecule and the surface properties of the adsorbent [79]. The adsorption ability of the surface and the type of the surface active centers are indicated by the point zero charge pHp_{zc} [51]. The pH at which the surface charge is zero is called the point of zero charge (pzc) and is used to quantify or define the electro-kinetic properties of a surface. The pH is used to describe point of zero charge only for systems in which H^+/ OH^- are the potentially determined ions. Most researchers have studied the point of zero charge of various adsorbents which were prepared from agricultural solid wastes to understand the adsorption mechanism. Due to the presence of the OH^- group, cationic dye adsorption is favored at $pH > pH_{pzc}$ and anionic dye adsorption is favored at $pH < pH_{pzc}$ where the surface becomes positively charged [51].

2.5.1.2. *Effect of temperature*

Temperature is another significant physico-chemical process parameter because it will change the adsorption capacity of the adsorbent [80]. If the amount of adsorption increases with increase in temperature, then the adsorption is an endothermic process. This might be due to the increasing mobility of the dye molecules and an increase in the number of active sites for the adsorption with increasing temperature. The decrease of the adsorption capacity with

increase in temperature indicates that the adsorption is an exothermic process. When temperature increases, there is a decrease in the adsorptive forces between the dye species and the active sites on the adsorbent surface leading to a decrease in adsorption [75].

2.5.1.3. *Effect of initial dye concentration*

The effect of initial dye concentration depends on the immediate relation between the concentration of the dye and the available sites on an adsorbent surface. The amount of adsorption for dye removal is highly dependent on the initial dye concentration. The percentage of dye removal decreases with an increase in the initial dye concentration. This may be due to the saturation of adsorption sites on the adsorbent surface, whereas the increase in initial dye concentration will cause an increase in the capacity of the adsorbent. This may be due to the high driving force for mass transfer at a high initial concentration [81].

2.5.1.4. *Effect of adsorbent dosage*

Biosorbent dosage on the dye removal efficiency is an important process parameter to determine the capacity of an adsorbent. The percentage of dye removal increases with increase in adsorbent dosage. The quantity of adsorption sites at the surface of adsorbent will increase by increasing the amount of the adsorbent. The effect of the adsorbent dosage gives an idea for the ability of a dye adsorption efficiency [75].

2.5.1.5. *Effect of contact time*

The rate of reaction is examined at different time intervals. Adsorption rate initially is meant to increase rapidly, and the optimal removal efficiency be reached within about 60 min. Further increase in contact time mostly does not show significant changes in equilibrium concentration; that is, the adsorption phase reached equilibrium. That is how the effect of contact time on adsorption efficiency is obtained

2.6. Biosorbents

2.6.1. Introduction to biosorbents

Biosorbents, either by themselves or in conjunction with a substrate can extract and/or concentrate a desired molecule by means of its selective retention. Biosorbents are considered

to be eco-friendly and effective with a low cost [82]. They also have high selectivity, requires little processing and are easy to regenerate. Natural materials and certain waste from agricultural operations that are available in large quantities may have the potential to be used as low cost adsorbents, as they represent unused resources that are widely available and are environmentally friendly [83]. Various biosorbents like commercial activated carbon [84], clay [85] and agricultural solid wastes [86,87] have been used for the removal of dyes. Activated carbon is still widely used [88,89]. It has been found to disclose a very high adsorption capacity and a high volume of micro porosity because it increases the speed of absorption. However, it is limited because of high cost involved and their regeneration by chemical and thermal procedures usually result in adsorbent deactivation [90,91]. Biosorbents of biological origin have been found to be efficient in the removal of pollutants at very low concentrations but the disadvantage is that they are limited by their low extraction capacities, poor mechanical strength and selectivity for targeted pollutants.

Crini and Badot indicated that an ideal adsorbent for dye removal should have the following characteristics: 1) large surface area, 2) high adsorption capacity, 3) suitable pore size and volume, 4) easy accessibility, 5) cost effectiveness, 6) mechanical stability, 7) compatibility, 8) ease of regeneration, 9) environmentally friendly, and 10) high selectivity to remove a wide range of dyes and does not require high processing procedures. Hence, researchers have recently focused on developing materials based on natural polymers such as chitosan to serve as alternative adsorbents with improved adsorption capacity and not compromising the low cost [92].

2.6.2. Pinecone as a biosorbent

Pinecone as a biosorbent has been widely studied because of its potential to treat industrial wastewater. One major advantage of pinecone powder as a biosorbent is the removal of large amount of dyes and metal ions from aqueous solution at a shorter contact period [93]. Other advantages include natural availability, cost effectiveness, pollutant removal at low concentrations and easy modification. The disadvantages of using pinecone as a biosorbent are low binding capabilities, low filtration properties, low surface area and the leaching of colored plant pigments into treated water. These limitations can be reduced by modifying the adsorbent.

Several research articles showed that pinecone shell (PCS) is able to selectively adsorb heavy metals [94]. Argun *et al.* (2008) in their paper described the activation of pinecone with Fenton reagent and determined the removal of Cd(II) and Pb(II) ions from an aqueous solution examined the effect of surface modification on the biosorption kinetics of Pb (II) ions onto raw and NaOH modified pinecone powder [94]. They also treated pinecone powder with KOH and their studies revealed that KOH treated pinecone powder had a higher capacity for Cu (II) than untreated pinecone shell [94]. In another investigation, the variation caused by the NaOH modification of pinecone powder on the kinetics and diffusion of Pb (II) and Cu (II) ions onto the pinecone powder surface was investigated [94]. These two authors also studied the kinetic behavior of the Cu (II)–pinecone powder system by varying several process variables including solution pH, initial concentration and temperature [93]. It appears that pinecone powder needs to be modified to increase its adsorption capacity. Biosorbent modification is a process of chemically or physically manipulating the surface properties of biological materials such as type and functional groups, surface area and porosity by extraction of plant chemical components to improve its adsorptive ability.

2.7. Magnetic Properties

2.7.1. Iron Magnetic nanoparticle

Magnetic nanoparticles have attracted increased attention due to their excellent physical and chemical properties such as super-paramagnetism, good dispersity, low toxicity and good biocompatibility [95].

Nano-sized magnetic iron oxide particles have been assessed for removal of dyes because of its high surface area, good mechanical strength, high reactivity and the fact that nanoparticles can be easily functionalized [96,97]**.** However, the production cost, agglomeration and small sizes limited its widespread use [98]**.**

Coating magnetic nanoparticles onto biomaterials shows a combination of relatively large numbers of active sites, high specific surface area and the convenience of separation offered by the magnetic species, and with the improved adsorption properties of the biomaterial due to the presence of the functional groups it contains. Coating of nano-sized magnetic composite onto the pinecone may be applied in addressing the problems highlighted and activation of surface area and will increase the reactivity and mechanical strength.

Development and modification of pinecone magnetite as a biosorbent will create a space for valorization of waste materials, possible elimination of filtration, introduction of magnetic separation and improvement in surface area due to the particles being in the nanoparticle range.

Compared to traditional micro-sized supports used in separation process, nano-sized adsorbents possess better performance that can be attributed to their high specific surface area, small size, absence of internal diffusion resistance and quantum size effect. Magnetic nanoparticles are coated on solid matrix such as polymers, carbon, zeolites and biomaterials to make separation from the effluent easier [99]. Coating biomaterials with magnetic nanoparticles combines the relatively large numbers of active sites, the high specific surface area and the convenience of separation offered by the magnetic species. Magnetic nanoparticles are also known to have good mechanical strength, high reactivity, and functionality.

Recently, magnetic separation has been applied in many areas to remove, isolate, or concentrate the desired components from a sample solution. Research has proven that iron oxide magnetic nanoparticles have been coated or functionalized and stabilized by biological materials. Several types of iron magnetic particles such as Fe_2O_3 [100], maghemite [101], Fe_3O_4 [102] and $CuFe_2O_4$ [103] have been explored for their ability to perform as adsorbents for metallic and organic pollutants from water. Some examples are chitosan [77], gum arabic [104], humic acid [105], polyacrylic acid , tea waste [106], cross-linked pectin [107], shellac [108] and orange peel powder [109]. The prepared magnetic nanomaterial used as adsorbents have been applied for the removal of heavy metals and organic pollutants from aqueous solutions.

2.8. Grafting as modification

Grafting is the modification process whereby a polymer containing a known functional group is added onto the surface of the biosorbent particles to increase its binding capacity. Grafting plays a crucial role as it improves the physiochemical properties of the material. Grafted surface material demonstrates much better adsorption, improved surface coverage at low pH and smoother surfaces at high pH. Importance of a grafted surface gives biopolymers desirable properties like increase of hydrophilicity when grafting with a monomer containing hydrophilic groups to the cellulose. Considerable amount of work has been done on techniques of graft co-polymerization of different monomers on polymeric backbones. These techniques include chemical, radiation, photochemical, plasma-induced techniques and enzymatic grafting [110]. Grafting reactions to improve and enhance the dye adsorption characteristics has received an

intense interest [111].Grafting has the advantage of improving the removal of color that is present in the wastewater. This can be done since new functional groups are introduced onto the biosorbent [112] and forms stronger bonds between pollutant and the biosorbent.

2.8.1. Chemical grafting

Grafting initiated by chemical means can proceed along two major paths, that is, free radical and ionic (***Figure 2.2***). In this process, the role of the initiator is very important as it determines the path of the grafting process. A typical example of grafting is as follows:

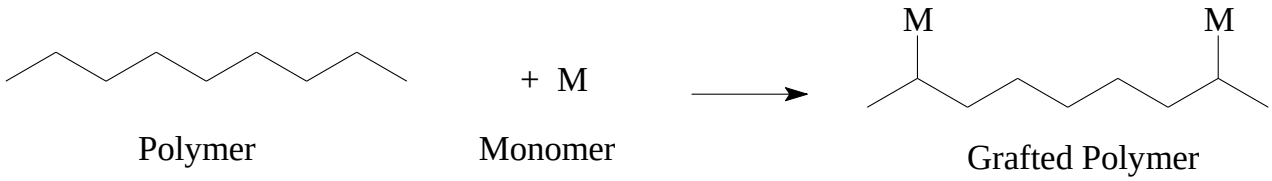

Figure 2.2 An example of polymer grafting

2.8.2. Free-radical grafting

This process involves free radicals that are produced from initiators and transferred to the substrate to react with monomers to form the graft polymers. The generation of free radicals can be considered to be direct or indirect methods [113]**.**

2.8.3. Ionic grafting

The process involves ions formed through high energy irradiation. Ionic grafting is defined by two types which are cationic and anionic. The polymer is irradiated to form the polymeric ion and then reacts with the monomer to form the grafted polymer. The primary advantage of the ionic grafting is the high reaction rate [113]**.**

2.8.4. Radiation grafting

Radiation is a process that is performed in solution or emulsion a whereby the reaction medium is water with a small amount of surfactant. For example, if radiation is carried out in air,

peroxides may be formed on the polymer. The life time of the free radical depends on the nature of the backbone polymer [114].

2.8.5. Photochemical grafting

This process involves grafting initiated when a macromolecule containing a chromophore absorbs light and dissociates into reactive free radicals. If the absorption of light does not lead to the formation of free radical sites through bond rupture, the process can be promoted by the addition of photosensitizers, benzoin ethyl ether, dyes like sodium 2,7 anthraquinone sulphonate or acrylated azo dye, aromatic ketones or metal ions like UO_2^{2+} [115]**.**

2.8.6. Plasma induced grafting

This process involves electrons that are used to initiate grafting. The electron induced is excited resulting in ionization and dissociation. Thus, the accelerated electrons from the plasma have sufficient energy to induce cleavage of the chemical bonds in the polymeric structure to form macromolecule radicals, which initiate grafting of copolymers [110].

2.8.7. Acrylic acid and Acrylamide monomers for grafting

Acrylic acid and acrylamide are known to be water soluble monomers with significant solubility. Acrylic acid is an organic unsaturated acid. Acrylic acid with its polymers, poly (acrylic acid) can be easily polarized, and pH can be adjusted by an inorganic base such as sodium hydroxide. If it is cross-linked by a cross linking agent or grafted onto non-water-soluble material, it is known to adsorb water molecules and swell, but it will not dissolve in water.

Many methods for polymerization of acrylic acid are available. For example, acrylic acid is initiated and polarized in aqueous solutions using water-soluble initiators like oil-soluble initiators such as 2,2-azoisobutyronitrile (AIBN) [116] or $K_2S_2O_8$ [117] (***Figure 2.2***)**.**

Acrylamide is a non-ionic compound, appearing at pH of neutralization in aqueous solutions. To expand the applicability of polyelectrolyte materials, acrylic acid (sodium acrylate) and its derivatives are usually used to produce copolymers with other water-soluble monomers like

acrylamide and its derivatives. Acrylamide monomers can be inserted into the chain segment of poly (acrylic acid), decreasing the sequence length and tacticity of the acrylic acid chain segment (***Figure 2.3***). This is expected to enhance the efficiency of carboxyl groups in acrylic acid to associate with the metal ions or dyes. It is important that the co-monomer improves macromolecular chain structure of acrylic acid and obtain a desired morphology of the condense state. With respect to copolymers of acrylic acid and acrylamide it is important to consider H-bond formation between carboxyl groups and amides because carboxyl groups on acrylic acid are known not only to bind metal ions but also to act with the amides on the acrylamide [118]**.**

The grafting copolymers of acrylic acid and acrylamide are usually used as hydrogel materials to capture metal ions from aqueous solution [119–121]

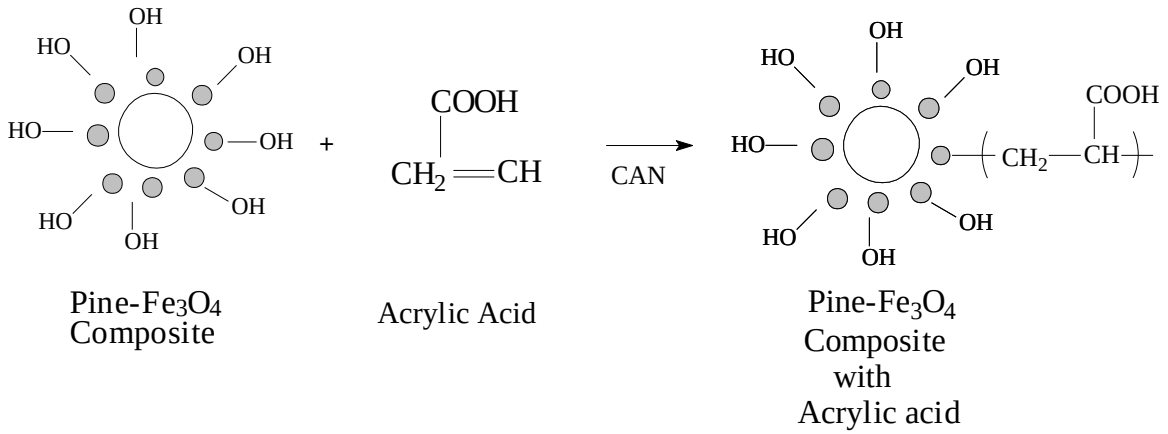

Figure 2.3 Grafting of Pine-Fe_3O_4 composite with acrylic acid

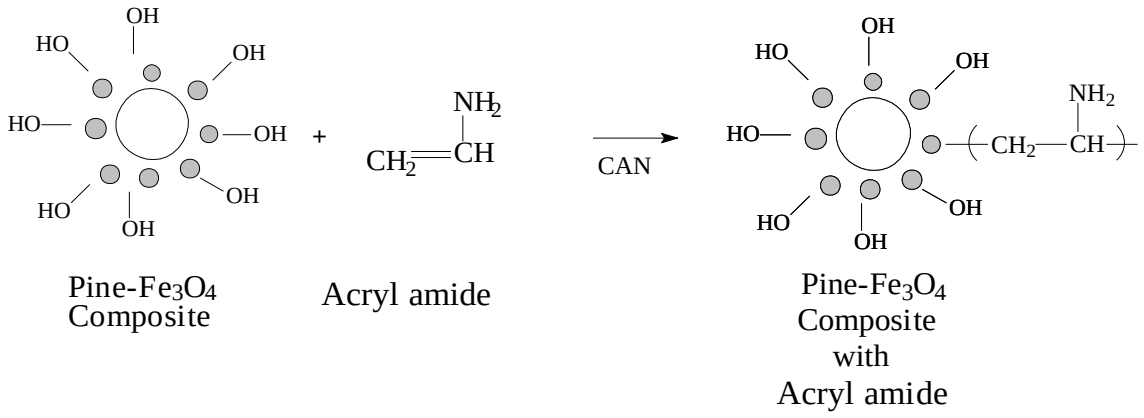

Figure 2.4 Grafting of Pine-Fe_3O_4 composite with Acrylamide

2.9. Desorption

Desorption is a phenomenon whereby a substance is released from or through a surface. The process is the opposite of sorption (that is, either adsorption or absorption). Desorption can occur when an equilibrium situation is altered. The main aim for desorption is the reusability of adsorbents in the multiple adsorption or desorption cycles and beneficial for their practical and economical applications [122,123]. Regeneration of the spent adsorbent is necessary to restore its original adsorption capacity. Diluted acids like hydrochloric acid, nitric acid and sulfuric acid can be used as the chemical regenerant. Dilute acids are very effective regenerants for cellulosic adsorbents.

2.10. Adsorption Isotherms

Isotherm studies can describe the qualitative information of the adsorbate interaction with adsorbent at constant temperature [124]. For example, the capacity of an adsorbent can be described by the adsorption isotherms, which helps us to understand the proper adsorption mechanism. The isotherm provides the relationship between the concentration of dye in solution and the amount of dye adsorbed on the solid phase when both phases are in equilibrium.

2.10.1. Langmuir isotherm

The Langmuir model [125] is based on the assumption that the process takes a place on a homogeneous surface, assuming monolayer adsorption onto a surface with a finite number of identical sites, so a monolayer of adsorbate is formed at saturation on the adsorbent surface. The linearized isotherm model is given by the expression

$$\frac{C_e}{q_e} = \frac{1}{q_m} K_L + \frac{C_e}{q_m} \qquad \textbf{Equation 2.1}$$

where q_e is the amount of dye adsorbed at the equilibrium time ($mg.g^{-1}$), C_e is the equilibrium dye concentration ($dm^3.mg^{-1}$), q_m is the maximum adsorption capacity ($mg.g^{-1}$) and K_L is the Langmuir adsorption equilibrium constant ($dm^3.mg^{-1}$).

2.10.2. Freundlich isotherm

Freundlich model [126] describes the non-ideal adsorption on heterogeneous surfaces as well as the multiplayer adsorption. The isotherm model is expressed by Equation 2.2

$$Log\ q_e = LogK_f + \frac{1}{n} Log\ C_e$$ **Equation 2.2**

Where C_e represents the equilibrium concentration of dye at the equilibrium time ($mg.L^{-1}$), n is the Feundlich constant related to the adsorption intensity, K_f is the Feundlich constant that represents the relative adsorption capacity ($mg.g^{-1}$).

2.10.3. Temkin isotherm

The Temkin and Pyzhev (1940) isotherm model describes the chemisorption between the adsorbate and adsorbent [127]. The model assumes that the heat of adsorption decreases linearly with the coverage. The equation works better for gas-phase equilibria. The non-linear form of the Temkin isotherm which on linearization gives:

$$q_e = B_l \ln K_T + B_l \ln C_e$$ **Equation 2.3**

where $B_l = RT/b$, b (mol/kJ) is the Temkin isotherm constant, K_T ($dm^3.mg^{-1}$) is equilibrium binding constant, q_e ($mg.g^{-1}$) is the adsorption capacity and C_e ($mg.dm^{-3}$) is the equilibrium adsorbate concentration, T (K) is temperature and R (8.314×10^{-3} $kJ.mol^{-1}K^{-1}$) is the ideal gas constant. The linear plot of q_e versus $\ln C_e$ gives the isotherm parameters, b and K_T are calculated from the slope and intercept.

2.10.4. Adsorption Kinetics

Kinetic studies are of utmost importance to the adsorption process because they depict the uptake rate of adsorbate and control the residual time of the whole adsorption process [27]. For a batch contact time process, the rate of sorption of dye on to the given adsorbent is proportional to the amount of dye absorbed from the solution phase. Several kinetic models have been proposed to clarify the mechanism of a solute adsorption from aqueous solution onto an adsorbent [128]**.**

2.10.5. Pseudo-first order

The rate constant of adsorption was determined from the pseudo-first-order rate expression given by Lagergren. The linear forms of the pseudo-first order is represented by the following equation [129]:

$$Ln(q_e - q_t) = Lnq_e - K_1 t$$ **Equation 2.4**

where q_e and q_t are the amount of MB adsorbed at equilibrium and at time t ($mg.g^{-1}$), respectively, and k_1t (min^1) is rate constant of adsorption. The values of the K_1t and $q_{e\,cal}$ were calculated from the slopes (k_1t) and the intercepts (Ln qe) of the plots of ln (qe–qt) vs. t (min)

2.10.6. Pseudo-second order

In this model, the rate-limiting step is the surface adsorption that involves chemisorption, where the removal from a solution is due to physicochemical interactions between the two phases [130]. The linear forms of the pseudo-second order are represented by the following equation:

$$\frac{t}{q_t} = \frac{1}{K_2} q_e^2 + \frac{t}{q_e}$$ **Equation 2.5**

where K_2 ($g.mg^{-1}.min^{-1}$) is the rate constants of the pseudo-second order. The parameters q_e and q_t ($mg.g^{-1}$) are the amount of MB adsorbed at equilibrium and at time t (min).

2.11. Photocatalysis

2.11.1. TiO_2 in photocatalysis

Photocatalysis is the chemical reaction induced by the absorption of photons by a semiconductor particle (photocatalyst) [8]. The photocatalyst does not undergo any chemical changes during and after the reaction. In thermodynamics, the concept of catalysis and photocatalysis is different whereby energy storing reactions can be driven by light energy even when it is not thermodynamically favorable ($\Delta G > 0$) while normal catalysis is limited to thermodynamically possible reaction ($\Delta G < 0$). The reaction rate whether absolute or relative of the photocatalytic process is usually referred as photocatalytic activity [131]). The five steps that are usually distinguished during catalysis are transfer of pollutants to the photocatalyst surface, adsorption of pollutants on the surface, photonic activation and decomposition of adsorbed molecules, reaction product desorption and removal of reaction products from photocatalyst's surface.

The main principle of photocatalysis can be explained according to the fact that electron-hole pairs are generated when photocatalytic material is exposed to the light with equal or larger energy than that of photocatalyst band gap. Formed electron hole pairs dissociates into electrons (e^-) in conduction band and holes (h^+) valence band. The e^- and h^+ lead to the reduction and oxidation of molecules adsorbed on the surface of photocatalytic material. Extensive studies have been conducted on the photocatalytic treatment of wastewater effluents at the laboratory and pilot scale [132,133]. Photocatalysis is one of the most researched branches of advance oxidation processes (AOPs). Advanced oxidation processes are methods of pollutant removal in which the active species is a radical or a charged nanoparticle that degrades the pollutant through the activity of the radical or the charged species [134].Advanced oxidation processes (AOPs) has been identified as active methods for the treatment of wastewater [135]. They result in the formation of oxidizing species such a OH, which remove organic pollutants by oxidation and inactivate microorganisms present in wastewater upon visible light irradiation [136] Photocatalytic degradation of organic effluents is considered to be the best approach for the abstraction of organic effluents from industrial wastewater. Examples of semiconducting nanocatalysts that have been used in the literature are ZnO, TiO_2, WO_3, ZnS, CdS, Fe_2O_3, etc. [137,138]**.** Among various transition metal oxides, TiO_2 is known to be widely used as a photocatalyst due to its unique characteristics of low cost, good optical activity, high chemical stability and non-toxic nature [139]. Doping with metals and non-metals is an effective method for enhancing the photocatalytic efficiency of TiO_2 as this impedes electron-hole recombination and increases its visible- light harvesting capacity. Doping TiO_2 with metal or non-metal ions can increase its capacity for visible light absorption or its reactivity in the UV spectrum [140,141]**.** Park et al. synthesized $NTiO_2$ nano-structured materials via graft polymerization method [142]. The resultant materials exhibited enhanced catalytic activity for the degradation of methylene orange (MO) dyes after irradiation with visible light. These were due to the incorporation of N into TiO_2 structure, which reformed the electronic band level of TiO_2. The doped material absorbed visible light. As a result, e^-/h^+ pair recombination was suppressed as such influencing the degradation reaction that could be strongly catalyzed. Some examples like activated carbon impregnated magnetite composites (PAC/Fe_3O_4) have been fabricated which not only have high ability of adsorbing pollutants, but also can be easily catalyzed by UV light as well as separated from solution, due to its magnetic features [143]. The sol–gel process has been used to fabricate the coating of nanosized crystalline TiO_2 directly onto magnetic core particles [135]. The enhancement of the photocatalytic activity of Fe_3O_4/TiO_2 core–shell nanoparticles can be interpreted by energy level theory: the energy level of $Fe_3þ/Fe_2þ$ closest to

the energy level of TiO_2 conduction band, and the energy level of $Fe_3þ/Fe_4þ$ closest to the energy level of the TiO_2 valence band; Fe3þ dissolved from Fe_3O_4 nanoparticles can come into not only electron capture position but also hole capture position, which causes the electron–hole pair recombination of TiO_2 to decrease [144,145]. Hang et al. have also synthesized the cryptomelane-type manganese oxide (K-OMS-2) nano wires, and then loaded it with TiO_2 nanoparticles by a hydro-thermal method, and finally coated with the magnetic Fe_3O_4 nanoparticles via a co-precipitation method. The hierarchically magnetic K-OMS-2/TiO_2/Fe_3O_4 heterojunction exhibited good photocatalytic activity for the degradation of humic acid under solar light [146]. More recently, Hu et al. have prepared the magnetic double-shell Fe_3O_4@TiO_2/Au@Pd@TiO_2 microsphere composed of a Fe_3O_4 core and double mesoporous TiO_2 shells with Au and Pd nanoparticles encapsulated via a multi-step building-up method, resulting in a high catalytic activity and stability for reduction of 4-nitrophenol [147].

TiO_2 is mainly applied in photocatalysis in its crystalline form (c-TiO_2). However, despite the advantages offered by its amorphous form (a-TiO_2), studies pertaining to a-TiO_2 have been lagging. The advantages and disadvantages of TiO_2 are summarized in ***Table 2.2***:

Table 2.2 A comparison of the advantages and disadvantages of amorphous TiO_2 in photocatalysis

Advantages of TiO_2	**Disadvantages of TiO_2**
Small particle size and large surface area	High aggregation
Eliminates high temperature calcination hence improved economic feasibility	High charge recombination
a-TiO_2 and c-TiO_2 share similar properties provided they have the same chemical composition, size and preparation conditions	
Ease of preparation	

2.11.2. Amorphous TiO_2, fabrication and applications in photocatalysis

Studies on the viability of a-TiO_2 as a photocatalyst has been under evaluation for some time, though such studies have been surpassed by the interest in the applications of crystalline TiO_2 (c-TiO_2) [148–150]. One or the earliest reported studies by Ohtani et al.(2011) the characteristics of a-TiO_2 and c-TiO_2 were compared by studying the properties of a-TiO_2 calcined in the temperature range 300 – 800 ℃ [148]. The studies indicate that amorphous and crystalline TiO_2 of the same size and composition have the same optical properties such as the energy band gap [148]. The optical properties and the photocatalytic efficiency of a-TiO_2 are affected by the tendency of high charge recombination. A comparison of the photocatalytic

efficiency of a-TiO_2 and c-TiO_2 showed that photocatalytic removal of 2-propanol under UV-irradiation was low for a-TiO_2 and increased with calcination temperature. Subsequent studies demonstrated through computational modelling and experimental work that doping a-TiO_2 with either a p-type or n-type dopant was effective in reducing the energy band gap and the charge recombination [151]. It was further shown that co-doping with such dopants has a greater effect in enhancing the photocatalytic activity through red shifting of the band edge. Subsequent studies on a-TiO_2 have demonstrated that with carefully controlled synthesis parameters, a-TiO_2 can outperform P25 in the removal of organic pollutants as demonstrated in the table above [152]. In addition, doping with C has also been shown to enhance the photocatalytic performance of TiO_2 to surpass that of P25 [153]. Furthermore, a-TiO_2 has also been applied as a co-catalyst for other catalytic semiconductors and shown to be effective in enhancing the photocatalytic activity. For example a-TiO_2 encapsulated $CsPbBr_3$ (a-TiO_2@ $CsPbBr_3$) had a six-fold increase in photodecomposition of CO_2 under UV-light [154]. The a-TiO_2 was found to particularly increase the affinity between a-TiO_2@ $CsPbBr_3$ and CO_2. Selected studies pertaining to the synthesis and application of a-TiO_2 have been summarized in the ***Table 2.3*** below.

Table 2.3 Fabrication, applications, and general results for amorphous TiO_2

Material	Synthesis parameters	Physicochemical and optical properties	Application and results	Refs
a-TiO_2	Commercial a-TiO_2 calcined in temperature ranges 300 - 800℃	Band edge – 380 nm for a-TiO_2 and red-shifted by calcination	- 2-propanol under UV-light - 2-propanol conversion lowest for a-TiO_2	[148]
c-doped a-TiO_2	Microwave assisted sol-gel in situ doping of TiO_2 with calcination in temperature range 300 – 600 ℃	Energy band gap – 1.94 eV for a-TiO_2 calcined at 300℃ and highest charge recombination	- Rhodamine B and 4-chlorophenol with $k_{1app} = 4.6 \times 10^{-2}$for 4-Chlorophenol removal	[155]
Microwave prepared C-doped a-TiO_2	Microwave assisted solgel with varied microwave treatment	Band gap in the range 3.37 – 3.4 eV Spherical aggregates with diameter at ~300 nm	Highest removal of Rhodamine B (~98% removal of RhB) in 80 min	[153]
Alcothermal preparation of a-TiO_2	Tetraisopropyl titanate+ethylene glycol+acetic acid aged for 8 h and thermally	Band-edge at 395 nm BET surface area of 50 $m^2.g^{-1}$	RhB decolorization under simulated solar light. $k_{1app} = 5.1 \times 10^{-2}$ for a-TiO_2 and 3.7 for P25	[152]

	treated for 3 h in Teflon lined autoclave	compared to 15 $m^2.g^{-1}$

2.11.3. TiO_2 based photocatalytic bionanocomposites: Value proposition, synthesis and applications.

The development of advanced oxidation processes past lab scale research has been mainly hindered by the high process costs as projected from the processes employed in the fabrication of the semiconductor catalysts at the lab scale. One of the main issues of concern in the fabrication of semiconductors for photocatalysis is the calcination to transform an amorphous matrix into a crystalline nanomaterial. As such there has been research into the use of the amorphous forms of the semiconductor nanomaterials as an alternative to the crystalline forms [150]. The costs of producing semiconductors has been the drive towards making semiconductor nanoparticles absorb visible light in order to make them applicable as photocatalysts that can use the regular light from the sun [156]. Such modifications typically involve the use of additional chemicals to achieve such things as chemical doping, particle size control and morphology control [152].

In addressing these issues, research has taken the direction of using plant materials and plant derived biopolymers as modifiers for semiconductors such as TiO_2. This has led to the fabrication of TiO_2– plant biopolymer composites with improved mechanical strength, visible light absorption, uniform particle size, decreased particle aggregation to name a few of these characteristics [157]. Given that lignin, cellulose and hemicellulose are the major constituents of plant materials they are therefore viable biopolymers for the modification of photocatalytic semiconductors [158]. For example, the use of lignin as a template in the synthesis of titania nanoparticles, a process involving post-synthesis calcination at 300 ℃, resulted in nanoparticles with a smaller particle size (8.5 nm), increased surface area and hence high photocatalytic degradation TiO_2 [159]. In a separate work, cellulose nanofiber mats were coated with CdS and applied for the H_2 generation under visible light [160]. Titania has also been deposited onto wood with results demonstrating improved mechanical and thermal properties of wood [161]. The process involved in-situ, ultrasonication-assisted solgel deposition of the titania and subsequent curing of the wood-titania composite in air at 103 ℃ for 20h. The results demonstrated the value in the use of biopolymers for the modification of nanoparticulate photocatalysts.

The processes for forming plant biopolymer-semiconductor composites are also favored for their simplicity as opposed to the use of synthetic chemical modifiers. These processes typically involve i) precipitation of the semiconductor in a suspension of the plant material powder, ii) aging the mixture, drying, washing and iii) calcination of the composite [158,162]. Where calcination is desired, different types of nanocomposites can be achieved by choosing a suitable environment. When the calcination of the bionanocomposite is carried out in an oxidizing atmosphere the plant/biopolymer material typically burns leaving the semiconductor nanoparticles with small amounts of nano carbon doped into the nanoparticles. In this way, the plant material acts as a template. Calcination of the amorphous bio-nanocomposite in an inert atmosphere, however, results in formation of carbon nanosheets with the semiconductor nanoparticles anchored onto the surfaces of these nanosheets. In all the scenarios, the plant material has demonstrated a profound effect in reducing the particle size of the semiconductor nanoparticles [163,164].

These techniques for the fabrication of plant biopolymer-based photocatalysts have been applied fabricated in several ways including supporting ZnO on plant-material derived-carbon [163,164]. The resultant bionanocomposites had a lower energy band gap, low charge recombination and high BET surface area; characteristics that are suffice to improve photocatalytic degradation of organic dyes by the composites [165]. A similar procedure was adopted for anchoring CeO_2 nanoparticles onto lignin-derived carbon resulting in a composite with improved optical properties and photocatalytic activity for desulfurization of water [166]. Most importantly, these results demonstrated that the mechanism by which lignin keeps the particle size of the semiconductors low is hinged on the surface properties of lignin. The crystallinity of TiO_2 is influenced by several factors such as, i) drying and calcination temperature, ii) presence of impurities. Typically, the presence of impurities reduces the crystallinity. Selected literature references of photocatalytic bionanocomposites have been summarized in ***Table 2.4*** below.

Table 2.4 Fabrication, applications, and general results for amorphous TiO_2 bionanocomposites

Material	Synthesis parameters	Physicochemical and optical properties	Application and results	Refs
TiO_2–microfibrilated cellulose (MFC)–polyamide amine epichlorohydrin (PAE)	Polyamide-amine-epichlorohydrin and TiO_2 suspensions sequentially added into a microfibrilated cellulose suspension under co-ultrasonication	Strong bond between TiO_2 and MFC. Binding mediated by PAE. Bonding results in high reusability	TiO_2 loaded MFC dipped in 5 ppm MO with 95% decolorization of MO in 150 min	[167]
TiO_2 – carbon fiber–cellulose fibers (Na_2SiO_3, $Al_2(SO_4)_3$ and PAE as binders	TiO_2–carbon fibers using aluminum silicate and sodium silicate as binders	TiO_2 bound as clusters onto the carbon fiber	99% MO removal after 7 h and recyclability of the composite due to strengthening effect of PAE	[168]
TiO_2/Ag–cellulose fibers	Hydrothermal method for TiO_2 nanobelts Ag–TiO_2 nanobelts prepared through UV reduction Ag-TiO_2–paper composites by immersion	Even dispersion of Ag-TiO_2 nanobelts onto the cellulose paper fibers	Degradation of 20 ppm MO under UV. ~ 95% removal of MO in 4 h	[169]

It is worth noting that while co-doping of a-TiO_2 has been hailed as a promising route towards circumventing the low photocatalytic efficiency in TiO_2, there is little literature to date that couples co-doping of a-TiO_2 using photocatalytic bionanocomposites. The main aim of this work is to further apply the magnetite-based adsorptive bionanocomposites as modifiers for a-TiO_2. With the elimination of high temperature calcination, it is expected that the carbon from the synthesis process chemicals will remain in the a-TiO_2 products and thus play a significant role in altering the properties of TiO_2. This work will investigate the value in using plant-based

bionanocomposites as a carbon source versus using the process chemicals. In addition, the effect of co-doping a-TiO_2 with C and N through synthetic chemicals and plant-based bionanocomposites will be investigated.

2.12. Summary

Water pollution and water shortages are becoming a more serious problem worldwide. The results of most human activities ultimately end up in water bodies. The quality of water in a stream or river is often a good indication of healthy living. Based on the literature reviewed thus far, it is evident that there has been an increase in the production and utilization of dyes, resulting in an increase in environmental pollution. Effluents discharged from a lot of industries contain residues of dyes. Most researchers have always been focused on single component dye solutions while in real effluent you have a combination of dyes. Therefore, the purpose of this study was to design adsorbents which can be more economical and efficient at commercial level and the focus is the removal of multiple species of dyes in a solution.

In this study, a novel, efficient and eco-friendly pine-iron oxide magnetite biosorbent was synthesized. The biomaterial was be grafted using vinyl monomers. Grafting increased reactivity and improved surface area. The pine-iron oxide magnetite biosorbent was then modified with acrylic acid and acrylamide. It was envisaged that this modification will increase surface properties of this biosorbent, and in turn increase its adsorption capacity. Low capacity was overcome by introduction of monomers onto the biomaterial to give high capacity and selectivity in the removal of the targeted pollutants. The presence of lignin affects the adsorption capacity of the pinecone and may also affect the grafting of acrylic modifiers onto its surface. As an extension of this study, iron oxide nanoparticles were used as an initiator to introduce active Fe-OH radical to the –OH group of the cellulose, then acrylic acid and acrylamide were grafted on the active Fe-OH radical to obtain high percentage and efficient grafting that will not destroy the –OH of the cellulose. This modification increased $–COO^-$ and $–NH_2$ functionalities on the pinecone. Acrylic acid has strong $–COO^-$ as a functional group that easily ionizes the pinecone charge and acts as the adsorption site to hold cationic material. Acrylamide has $–NH_2$ with lone pairs that donates them to cations materials. The novel biosorbent-magnetic nanoparticle materials was therefore explored in overcoming the limitations of the biosorbent alone and selectively removes multiple dyes effluents. Further to

this research study, a photocatalytic TiO_2-based biosorbent was produced and used in the degradation of undesirable dyes from wastewater.

2.13. References

[1] V.K. Gupta, Suhas, Application of low-cost adsorbents for dye removal - A review, J. Environ. Manage. 90 (2009) 2313–2342. https://doi.org/10.1016/j.jenvman.2008.11.017.

[2] FAO, Coping with water scarcity An action framework for agriculture and food security, 2012. https://doi.org/http://www.fao. org/docrep/016/i3015e/i3015e.pdf.

[3] E. Curry, Water Scarcity and the Recognition of the Human Right to Safe Freshwater Water Scarcity and the Recognition of the Human, 9 (2010).

[4] G.N. Hlongwane, P.T. Sekoai, M. Meyyappan, K. Moothi, Simultaneous removal of pollutants from water using nanoparticles: A shift from single pollutant control to multiple pollutant control, Sci. Total Environ. 656 (2019) 808–833. https://doi.org/10.1016/j.scitotenv.2018.11.257.

[5] Ö. Ceyhan, D. Baybaş, Adsorption of some textile dyes by hexadecyltrimethylammonium bentonite, Turkish J. Chem. 25 (2001) 193–200.

[6] A.L. Prasad, T. Santhi, Adsorption of hazardous cationic dyes from aqueous solution onto Acacia nilotica leaves as an eco friendly adsorbent The isotherm studies were performed by varying, Sustain. Environ. Res. 22 (2012) 113–122.

[7] I.W.K. Suryawan, Q. Helmy, S. Notodarmojo, Laboratory scale ozone-based post-treatment from textile wastewater treatment plant effluent for water reuse, J. Phys. Conf. Ser. 1456 (2020). https://doi.org/10.1088/1742-6596/1456/1/012002.

[8] J.J. Rueda-Marquez, I. Levchuk, P. Fernández Ibañez, M. Sillanpää, A critical review on application of photocatalysis for toxicity reduction of real wastewaters, J. Clean. Prod. 258 (2020). https://doi.org/10.1016/j.jclepro.2020.120694.

[9] A.C. Mecha, M.S. Onyango, A. Ochieng, M.N.B. Momba, UV and solar photocatalytic disinfection of municipal wastewater: inactivation, reactivation and regrowth of bacterial pathogens, Int. J. Environ. Sci. Technol. 16 (2019) 3687–3696. https://doi.org/10.1007/s13762-018-1950-1.

[10] L.N. Nthunya, L. Gutierrez, S. Derese, E.N. Nxumalo, A.R. Verliefde, B.B. Mamba, S.D. Mhlanga, A review of nanoparticle-enhanced membrane distillation membranes: membrane synthesis and applications in water treatment, J. Chem. Technol. Biotechnol. 94 (2019) 2757–2771. https://doi.org/10.1002/jctb.5977.

[11] M.R.D. Khaki, M.S. Shafeeyan, A.A.A. Raman, W.M.A.W. Daud, Application of doped photocatalysts for organic pollutant degradation: A review, J. Environ. Manage. 198 (2017) 78–94. https://doi.org/10.1016/j.jenvman.2017.04.099.

[12] L. Yang, X. Liang, Y. Han, Y. Cai, H. Zhao, M. Sheng, G. Cao, The coupling use of advanced oxidation processes and sequencing batch reactor to reduce nitrification inhibition of industry wastewater: Characterization and optimization, Chem. Eng. J. (2018) 1–10. https://doi.org/10.1016/j.cej.2018.10.232.

[13] B. Bethi, S.H. Sonawane, B.A. Bhanvase, S.P. Gumfekar, Nanomaterials-based advanced oxidation processes for wastewater treatment: A review, Chem. Eng. Process. Process Intensif. 109 (2016) 178–189. https://doi.org/10.1016/j.cep.2016.08.016.

[14] B. Szczepanik, Photocatalytic degradation of organic contaminants over clay-TiO2 nanocomposites: A review, Appl. Clay Sci. 141 (2017) 227–239. https://doi.org/10.1016/j.clay.2017.02.029.

[15] T. Fazal, A. Razzaq, F. Javed, A. Hafeez, N. Rashid, U.S. Amjad, M.S. Ur Rehman, A. Faisal, F. Rehman, Integrating adsorption and photocatalysis: A cost effective strategy for textile wastewater treatment using hybrid biochar-TiO_2 composite, J. Hazard. Mater. 390 (2020) 121623. https://doi.org/10.1016/j.jhazmat.2019.121623.

[16] H.E.M. Ustroph, Dyes, General Survey, Ullman's Encycl. Ind. Chem. (2014) 1–38. https://doi.org/10.1002/14356007.a09_073.pub2.

[17] W.T. Silvfast, Laser Fundamentals, 2nd Editio, Cambridge University Press, Cambridge, 2004.

[18] M.T. Yagub, T.K. Sen, S. Afroze, H.M. Ang, Dye and its removal from aqueous solution by adsorption: A review, Adv. Colloid Interface Sci. 209 (2014) 172–184. https://doi.org/10.1016/j.cis.2014.04.002.

[19] T. Robinson, G. McMullan, R. Marchant, P. Nigam, Remediation of dyes in textile effluent: A critical review on current treatment technologies with a proposed alternative, Bioresour. Technol. 77 (2001) 247–255. https://doi.org/10.1016/S0960-8524(00)00080-8.

[20] A. Baban, A. Yediler, N.K. Ciliz, Integrated water management and CP implementation for wool and textile blend processes, Clean - Soil, Air, Water. 38 (2010) 84–90. https://doi.org/10.1002/clen.200900102.

[21] Q.Y. Yue, B.Y. Gao, Y. Wang, H. Zhang, X. Sun, S.G. Wang, R.R. Gu, Synthesis of polyamine flocculants and their potential use in treating dye wastewater, J. Hazard. Mater. 152 (2008) 221–227. https://doi.org/10.1016/j.jhazmat.2007.06.089.

[22] N.K. Lazaridis, T.D. Karapantsios, D. Georgantas, Kinetic analysis for the removal of a reactive dye from aqueous solution onto hydrotalcite by adsorption, Water Res. 37 (2003) 3023–3033. https://doi.org/10.1016/S0043-1354(03)00121-0.

[23] A.K. Golder, N. Hridaya, A.N. Samanta, S. Ray, Electrocoagulation of methylene blue and eosin yellowish using mild steel electrodes, J. Hazard. Mater. 127 (2005) 134–140. https://doi.org/10.1016/j.jhazmat.2005.06.032.

[24] C.R.T. Tarley, M.A.Z. Arruda, Biosorption of heavy metals using rice milling by-products. Characterisation and application for removal of metals from aqueous effluents, Chemosphere. 54 (2004) 987–995. https://doi.org/10.1016/j.chemosphere.2003.09.001.

[25] T.G. Chuah, A. Jumasiah, I. Azni, S. Katayon, S.Y. Thomas Choong, Rice husk as a potentially low-cost biosorbent for heavy metal and dye removal: An overview, Desalination. 175 (2005) 305–316. https://doi.org/10.1016/j.desal.2004.10.014.

[26] C. J.C., T. R.R., H.G. Hand DW, T. G., MWH's Water Treatment Principles and Design, 2nd Editio, John Wiley & Sons, New Jersey, 2012.

[27] A. Demirbas, Agricultural based activated carbons for the removal of dyes from aqueous solutions: A review, J. Hazard. Mater. 167 (2009) 1–9. https://doi.org/10.1016/j.jhazmat.2008.12.114.

[28] E.A. Clarke, R. Anliker, Organic Dyes and Pigments, in: 0. Hutzinger (Ed.), Handb. Environ. Chem., 3rd Ed., Springer-Verlag Berlin Heidelberg, Berlin, 1980: pp. 181–215. https://doi.org/10.1007/978-3-540-38522-6-7.

[29] T.A. Saleh, V.K. Gupta, Functionalization of tungsten oxide into MWCNT and its application for sunlight-induced degradation of Rhodamine B, J. Colloid Interface Sci. 362 (2011) 337–344. https://doi.org/10.1016/j.jcis.2011.06.081.

[30] H. Ali, Biodegradation of synthetic dyes - A review, Water. Air. Soil Pollut. 213 (2010) 251–273. https://doi.org/10.1007/s11270-010-0382-4.

[31] Klaus Hunger, ed., Industrial Dyes: Chemistry, Properties, Applications, 2nd ed., WILEY-VCH Verlag GmbH & Co. KGaA, Weinheim, 2003. http://www.fbsa.org.za/who-we-serve.

[32] D.J. Chang, I.P. Chen, M. Ten Chen, S.S. Lin, Wet air oxidation of a reactive dye solution using $CoAlPO_{4-5}$ and CeO_2 catalysts, Chemosphere. 52 (2003) 943–949. https://doi.org/10.1016/S0045-6535(03)00302-3.

[33] S. Sadri Moghaddam, M.R. Alavi Moghaddam, M. Arami, Coagulation/flocculation process for dye removal using sludge from water treatment plant: Optimization through response surface methodology, J. Hazard. Mater. 175 (2010) 651–657. https://doi.org/10.1016/j.jhazmat.2009.10.058.

[34] S.M. Ghoreishi, R. Haghighi, Chemical catalytic reaction and biological oxidation for treatment of non-biodegradable textile effluent, Chem. Eng. J. 95 (2003) 163–169. https://doi.org/10.1016/S1385-8947(03)00100-1.

[35] S. Raghu, C.W. Lee, S. Chellammal, S. Palanichamy, C.A. Basha, Evaluation of electrochemical oxidation techniques for degradation of dye effluents-A comparative approach, J. Hazard. Mater. 171 (2009) 748–754. https://doi.org/10.1016/j.jhazmat.2009.06.063.

[36] L. Zheng, Y. Su, L. Wang, Z. Jiang, Adsorption and recovery of methylene blue from aqueous solution through ultrafiltration technique, Sep. Purif. Technol. 68 (2009) 244–249. https://doi.org/10.1016/j.seppur.2009.05.010.

[37] B.S. Choudri, Y. Charabi, M. Baawain, M. Ahmed, Textiles, Water Environ. Res. 89 (2017) 1424–1440. https://doi.org/10.2175/106143017X15023776270502.

[38] H. Bhuta, Advanced treatment technology and strategy for water and wastewater management, in: Ind. Wastewater Treat. Recycl. Reuse, Elsevier Ltd., 2014: pp. 193–213. https://doi.org/10.1016/B978-0-08-099968-5.00004-0.

[39] I.A. Salem, M.S. El-Maazawi, Kinetics and mechanism of color removal of methylene blue with hydrogen peroxide catalyzed by some supported alumina surfaces, Chemosphere. 41 (2000) 1173–1180. https://doi.org/10.1016/S0045-6535(00)00009-6.

[40] C.H. Weng, Y.F. Pan, Adsorption of a cationic dye (methylene blue) onto spent activated clay, J. Hazard. Mater. 144 (2007) 355–362. https://doi.org/10.1016/j.jhazmat.2006.09.097.

[41] A.C. Suwandi, N. Indraswati, S. Ismadji, Adsorption of N-methylated diaminotriphenilmethane dye (malachite green) on natural rarasaponin modified kaolin, Desalin. Water Treat. 41 (2012) 342–355. https://doi.org/10.1080/19443994.2012.664738.

[42] C. Yan, C. Wang, J. Yao, L. Zhang, X. Liu, Adsorption of methylene blue on mesoporous carbons prepared using acid- and alkaline-treated zeolite X as the template, Colloids Surfaces A Physicochem. Eng. Asp. 333 (2009) 115–119. https://doi.org/10.1016/j.colsurfa.2008.09.028.

[43] A.N. Fernandes, C.A.P. Almeida, C.T.B. Menezes, N.A. Debacher, M.M.D. Sierra, Removal of methylene blue from aqueous solution by peat, J. Hazard. Mater. 144 (2007) 412–419. https://doi.org/10.1016/j.jhazmat.2006.10.053.

[44] S. Altenor, B. Carene, E. Emmanuel, J. Lambert, J.J. Ehrhardt, S. Gaspard, Adsorption studies of methylene blue and phenol onto vetiver roots activated carbon prepared by chemical activation, J. Hazard. Mater. 165 (2009) 1029–1039. https://doi.org/10.1016/j.jhazmat.2008.10.133.

[45] M. Zhao, Z. Tang, P. Liu, Removal of methylene blue from aqueous solution with silica nano-sheets derived from vermiculite, J. Hazard. Mater. 158 (2008) 43–51. https://doi.org/10.1016/j.jhazmat.2008.01.031.

[46] D. Zhao, L. Zhao, C.S. Zhu, X. Shen, X. Zhang, B. Sha, Comparative study of polymer containing β-cyclodextrin and -COOH for adsorption toward aniline, 1-naphthylamine and methylene blue, J. Hazard. Mater. 171 (2009) 241–246. https://doi.org/10.1016/j.jhazmat.2009.05.134.

[47] M.C. Ncibi, A.M.B. Hamissa, A. Fathallah, M.H. Kortas, T. Baklouti, B. Mahjoub, M. Seffen, Biosorptive uptake of methylene blue using Mediterranean green alga Enteromorpha spp., J. Hazard. Mater. 170 (2009) 1050–1055. https://doi.org/10.1016/j.jhazmat.2009.05.075.

[48] A.E. Ofomaja, E.B. Naidoo, S.J. Modise, Removal of copper(II) from aqueous solution by pine and base modified pine cone powder as biosorbent, J. Hazard. Mater. 168 (2009) 909–917. https://doi.org/10.1016/j.jhazmat.2009.02.106.

[49] B.H. Hameed, A.A. Ahmad, Batch adsorption of methylene blue from aqueous solution by garlic peel, an agricultural waste biomass, J. Hazard. Mater. 164 (2009) 870–875. https://doi.org/10.1016/j.jhazmat.2008.08.084.

[50] R. Han, L. Zhang, C. Song, M. Zhang, H. Zhu, L.J. Zhang, Characterization of modified wheat straw, kinetic and equilibrium study about copper ion and methylene blue adsorption in batch mode, Carbohydr. Polym. 79 (2010) 1140–1149. https://doi.org/10.1016/j.carbpol.2009.10.054.

[51] T. Liu, Y. Li, Q. Du, J. Sun, Y. Jiao, G. Yang, Z. Wang, Y. Xia, W. Zhang, K. Wang, H. Zhu, D. Wu, Adsorption of methylene blue from aqueous solution by graphene, Colloids Surfaces B Biointerfaces. 90 (2012) 197–203. https://doi.org/10.1016/j.colsurfb.2011.10.019.

[52] L. Xiong, Y. Yang, J. Mai, W. Sun, C. Zhang, D. Wei, Q. Chen, J. Ni, Adsorption behavior of methylene blue onto titanate nanotubes, Chem. Eng. J. 156 (2010) 313–320. https://doi.org/10.1016/j.cej.2009.10.023.

[53] Z. Carmen, S. Danelia, Textile organic dyes– characteristics , polluting effects and separation/elimination procedures from industrial effluents – A critical overview, in: T. Puzyn (Ed.), Org. Pollut. Ten Years After Stock. Conv. - Environ. Anal. Updat., 1st ed., InTechOpen, Stockholm, 2012: pp. 55–84. https://doi.org/10.5772/32373.

[54] P. Gregory, Classification of Dyes by Chemical Structure, in: D.R. Waring, G. Hallas (Eds.), Chem. Appl. Dye., Plenum Press, New York, 1990: pp. 17–47. https://doi.org/10.1007/978-0-387-30160-0_7570.

[55] M. Séquin-Prey, The chemistry of plant and animal dyes, J. Chem. Educ. 58 (1981) 301–305. https://doi.org/10.1021/ed058p301.

[56] K. Singh, S. Arora, Removal of synthetic textile dyes from wastewaters: A critical review on present treatment technologies, Crit. Rev. Environ. Sci. Technol. 41 (2011) 807–878. https://doi.org/10.1080/10643380903218376.

[57] N. Tüfekci, N. Sivri, İ. Toroz, Pollutants of Textile Industry Wastewater and Assessment of its Discharge Limits by Water Quality Standards, Turkish J. Fish. Aquat. Sci. 103 (2007) 97–103.

[58] K. Kadirvelu, M. Kavipriya, C. Karthika, M. Radhika, N. Vennilamani, S. Pattabhi, Utilization of various agricultural wastes for activated carbon preparation and application for the removal of dyes and metal ions from aqueous solutions, Bioresour. Technol. 87 (2003) 129–132. https://doi.org/10.1016/S0960-8524(02)00201-8.

[59] S.S. Idris, N.A. Rahman, K. Ismail, A.B. Alias, Z.A. Rashid, M.J. Aris, Investigation on thermochemical behaviour of low rank Malaysian coal, oil palm biomass and their blends during pyrolysis via thermogravimetric analysis (TGA), Bioresour. Technol. 101 (2010) 4584–4592. https://doi.org/10.1016/j.biortech.2010.01.059.

[60] J.A. Laszlo, Preparing an ion exchange resin from sugarcane bagasse to remove reactive dye from wastewater, Text. Chem. Color. 28 (1996) 13–17.

[61] A.H. Gemeay, I.A. Mansour, R.G. El-Sharkawy, A.B. Zaki, Kinetics and mechanism of the heterogeneous catalyzed oxidative degradation of indigo carmine, J. Mol. Catal. A Chem. 193 (2003) 109–120. https://doi.org/10.1016/S1381-1169(02)00477-6.

[62] V. López-Grimau, M.C. Gutiérrez, Decolourisation of simulated reactive dyebath effluents by electrochemical oxidation assisted by UV light, Chemosphere. 62 (2006) 106–112. https://doi.org/10.1016/j.chemosphere.2005.03.076.

[63] A. Dąbrowski, Adsorption - From theory to practice, Adv. Colloid Interface Sci. 93 (2001) 135–224. https://doi.org/10.1016/S0001-8686(00)00082-8.

[64] M. Rafatullah, O. Sulaiman, R. Hashim, A. Ahmad, Adsorption of methylene blue on low-cost adsorbents: A review, J. Hazard. Mater. 177 (2010) 70–80. https://doi.org/10.1016/j.jhazmat.2009.12.047.

[65] E.I. Unuabonah, G.U. Adie, L.O. Onah, O.G. Adeyemi, Multistage optimization of the adsorption of methylene blue dye onto defatted Carica papaya seeds, Chem. Eng. J. 155 (2009) 567–579. https://doi.org/10.1016/j.cej.2009.07.012.

[66] G. Crini, Non-conventional low-cost adsorbents for dye removal: A review, Bioresour. Technol. 97 (2006) 1061–1085. https://doi.org/10.1016/j.biortech.2005.05.001.

[67] M.A. Rauf, I. Shehadeh, A. Ahmed, A. Al-zamly, Removal of Methylene Blue Dye from Aqueous Solution by Using Cestrum nocturnum Leaves, as a Low Cost Adsorbent, J. Chem. Biol. Phys. Sci. 7 (2017) 608–613. https://doi.org/10.24214/jcbps.d.7.3.51225.

[68] B. Shi, G. Li, D. Wang, C. Feng, H. Tang, Removal of direct dyes by coagulation: The performance of preformed polymeric aluminum species, J. Hazard. Mater. 143 (2007) 567–574. https://doi.org/10.1016/j.jhazmat.2006.09.076.

[69] A.K. Verma, R.R. Dash, P. Bhunia, A review on chemical coagulation/flocculation technologies for removal of colour from textile wastewaters, J. Environ. Manage. 93 (2012) 154–168. https://doi.org/10.1016/j.jenvman.2011.09.012.

[70] A. Mishra, M. Bajpai, The flocculation performance of Tamarindus mucilage in relation to removal of vat and direct dyes, Bioresour. Technol. 97 (2006) 1055–1059. https://doi.org/10.1016/j.biortech.2005.04.049.

[71] Y. Fu, T. Viraraghavan, Fungal decolorization of dye wastewaters: A review, Bioresour. Technol. 79 (2001) 251–262. https://doi.org/10.1016/S0960-8524(01)00028-1.

[72] F. Banat, S. Al-Asheh, L. Al-Makhadmeh, Evaluation of the use of raw and activated date pits as potential adsorbents for dye containing waters, Process Biochem. 39 (2003) 193–202. https://doi.org/10.1016/S0032-9592(03)00065-7.

[73] K.G. Bhattacharyya, A. Sharma, Adsorption of Pb(II) from aqueous solution by Azadirachta indica (Neem) leaf powder, J. Hazard. Mater. 113 (2004) 97–109. https://doi.org/10.1016/j.jhazmat.2004.05.034.

[74] M. Rauf, M. Meetani, S. Hisaindee, An overview on the photocatalytic degradation of azo dyes in the presence of TiO2 doped with selective transition metals, Desalination. 276 (2011) 13–27. https://doi.org/10.1016/j.desal.2011.03.071.

[75] M.A.M. Salleh, D.K. Mahmoud, W.A.W.A. Karim, A. Idris, Cationic and anionic dye adsorption by agricultural solid wastes: A comprehensive review, Desalination. 280 (2011) 1–13. https://doi.org/10.1016/j.desal.2011.07.019.

[76] B. Koumanova, S.J. Allen, Decolourisation of Water/Wastewater Using Adsorption(Review), J. Univ. Chem. Technol. Metall. 40 (2005) 175–192.

[77] C. Srisa-ard, Removal of heavy metals from wastewater by adsorption on coir pith activated carbon, Suranaree University of Technology, 2002. https://doi.org/10.1081/SS-200036561.

[78] S.E. Bailey, T.J. Olin, R. Mark Bricka, D. Dean Adrian, A review of potentially low-cost sorbents for heavy metals, 33 (1999). https://ac.els-cdn.com/S0043135498004758/1-s2.0-S0043135498004758-main.pdf?_tid=9ffae7a9-0359-410e-a030-ec8bcf5539f8&acdnat=1536143568_1518847685656e6223b2234982236a65.

[79] B.K. Nandi, A. Goswami, M.K. Purkait, Applied Clay Science Removal of cationic dyes from aqueous solutions by kaolin : Kinetic and equilibrium studies, Appl. Clay Sci. 42 (2009) 583–590. https://doi.org/10.1016/j.clay.2008.03.015.

[80] M.E. Argun, S. Dursun, M. Karatas, M. Gürü, Activation of pine cone using Fenton oxidation for Cd(II) and Pb(II) removal, Bioresour. Technol. 99 (2008) 8691–8698. https://doi.org/10.1016/j.biortech.2008.04.014.

[81] Y. Bulut, H. Aydin, A kinetics and thermodynamics study of methylene blue adsorption on wheat shells, Desalination. 194 (2006) 259–267. https://doi.org/10.1016/j.desal.2005.10.032.

[82] N. Das, R. Vimala, P. Karthika, Biosorption of heavy metals - An overview, Indian J. Biotechnol. 7 (2008) 159–169.

[83] N.T. Abdel-Ghani, M. Hefny, G.A.F. El-Chaghaby, Removal of lead from aqueous solution using low cost abundantly available adsorbents, Int. J. Environ. Sci. Technol. 4 (2007) 67–73. https://doi.org/10.1007/BF03325963.

[84] M. Abbas, A. Zaini, Y. Amano, M. Machida, Adsorption of heavy metals onto activated carbons derived from polyacrylonitrile fiber, J. Hazard. Mater. 180 (2010) 552–560. https://doi.org/10.1016/j.jhazmat.2010.04.069.

[85] E. Errais, J. Duplay, M. Elhabiri, M. Khodja, R. Ocampo, R. Baltenweck-Guyot, F. Darragi, Anionic RR120 dye adsorption onto raw clay: Surface properties and adsorption mechanism, Colloids Surfaces A Physicochem. Eng. Asp. 403 (2012) 69–78. https://doi.org/10.1016/j.colsurfa.2012.03.057.

[86] F. Deniz, S. Karaman, S.D. Saygideger, Biosorption of a model basic dye onto Pinus brutia Ten.: Evaluating of equilibrium, kinetic and thermodynamic data, Desalination. 270 (2011) 199–205. https://doi.org/10.1016/j.desal.2010.11.046.

[87] D.H.K. Reddy, K. Seshaiah, A.V.R. Reddy, S.M. Lee, Optimization of Cd (II), Cu (II) and Ni (II) biosorption by chemically modified Moringa oleifera leaves powder, Carbohydr. Polym. 88 (2012) 1077–1086. https://doi.org/10.1016/j.carbpol.2012.01.073.

[88] Y. Zhou, X. Liu, Y. Xiang, P. Wang, J. Zhang, F. Zhang, J. Wei, L. Luo, M. Lei, L. Tang, Modification of biochar derived from sawdust and its application in removal of tetracycline and copper from aqueous solution: Adsorption mechanism and modelling, Bioresour. Technol. 245 (2017) 266–273. https://doi.org/10.1016/j.biortech.2017.08.178.

[89] Y. Xiang, Z. Xu, Y. Wei, Y. Zhou, X. Yang, Y. Yang, J. Yang, J. Zhang, L. Luo, Z. Zhou, Carbon-based materials as adsorbent for antibiotics removal: Mechanisms and influencing factors, J. Environ. Manage. 237 (2019) 128–138. https://doi.org/10.1016/j.jenvman.2019.02.068.

[90] J.L. Sotelo, G. Ovejero, A. Rodríguez, S. Álvarez, J. García, Study of natural clay adsorbent sepiolite for the removal of caffeine from aqueous solutions: Batch and fixed-bed column operation, Water. Air. Soil Pollut. 224 (2013). https://doi.org/10.1007/s11270-013-1466-8.

[91] J.R. De Andrade, M.F. Oliveira, M.G.C. Da Silva, M.G.A. Vieira, Adsorption of Pharmaceuticals from Water and Wastewater Using Nonconventional Low-Cost Materials: A Review, Ind. Eng. Chem. Res. 57 (2018) 3103–3127. https://doi.org/10.1021/acs.iecr.7b05137.

[92] W.S. Wan Ngah, L.C. Teong, M.A.K.M. Hanafiah, Adsorption of dyes and heavy metal ions by chitosan composites: A review, Carbohydr. Polym. 83 (2011) 1446–1456. https://doi.org/10.1016/j.carbpol.2010.11.004.

[93] A.E. Ofomaja, E.B. Naidoo, Biosorption of copper from aqueous solution by chemically activated pine cone: A kinetic study, Chem. Eng. J. 175 (2011) 260–270. https://doi.org/10.1016/j.cej.2011.09.103.

[94] A.E. Ofomaja, Intraparticle diffusion process for lead(II) biosorption onto mansonia wood sawdust, Bioresour. Technol. 101 (2010) 5868–5876. https://doi.org/10.1016/j.biortech.2010.03.033.

[95] K. Yokwana, A.T. Kuvarega, S.D. Mhlanga, E.N. Nxumalo, Mechanistic aspects for the removal of Congo red dye from aqueous media through adsorption over N-doped graphene oxide nanoadsorbents prepared from graphite flakes and powders, Phys. Chem. Earth. 107 (2018) 58–70. https://doi.org/10.1016/j.pce.2018.08.001.

[96] Y.C. Chang, D.H. Chen, Preparation and adsorption properties of monodisperse chitosan-bound Fe_3O_4 magnetic nanoparticles for removal of Cu(II) ions, J. Colloid Interface Sci. 283 (2005) 446–451. https://doi.org/10.1016/j.jcis.2004.09.010.

[97] L. Madhura, S. Singh, S. Kanchi, M. Sabela, K. Bisetty, Inamuddin, Nanotechnology-based water quality management for wastewater treatment, Springer International Publishing, 2019. https://doi.org/10.1007/s10311-018-0778-8.

[98] Y. Zhang, B. Wu, H. Xu, H. Liu, M. Wang, Y. He, B. Pan, Nanomaterials-enabled water and wastewater treatment, NanoImpact. 3–4 (2016) 22–39. https://doi.org/10.1016/j.impact.2016.09.004.

[99] G. Daneshvar Tarigh, F. Shemirani, N.S. Maz'hari, Fabrication of a reusable magnetic multi-walled carbon nanotube–TiO_2 nanocomposite by electrostatic adsorption: enhanced photodegradation of malachite green, RSC Adv. 5 (2015) 35070–35079. https://doi.org/10.1039/C4RA15593A.

[100] F. Šulek, Ž. Knez, M. Habulin, Immobilization of cholesterol oxidase to finely dispersed silica-coated maghemite nanoparticles based magnetic fluid, Appl. Surf. Sci. 256 (2010) 4596–4600. https://doi.org/10.1016/j.apsusc.2010.02.055.

[101] J. Hu, G. Chen, I.M.C. Lo, Removal and recovery of Cr(VI) from wastewater by maghemite nanoparticles, Water Res. 39 (2005) 4528–4536. https://doi.org/10.1016/j.watres.2005.05.051.

[102] Y. Hu, S. Mignani, J.P. Majoral, M. Shen, X. Shi, Construction of iron oxide nanoparticle-based hybrid platforms for tumor imaging and therapy, Chem. Soc. Rev. 47 (2018) 1874–1900. https://doi.org/10.1039/c7cs00657h.

[103] N. Masunga, O.K. Mmelesi, K.K. Kefeni, B.B. Mamba, Recent advances in copper ferrite nanoparticles and nanocomposites synthesis, magnetic properties and application in water treatment: Review, J. Environ. Chem. Eng. 7 (2019) 103179. https://doi.org/10.1016/j.jece.2019.103179.

[104] S.S. Banerjee, D.H. Chen, Fast removal of copper ions by gum arabic modified magnetic nano-adsorbent, J. Hazard. Mater. 147 (2007) 792–799. https://doi.org/10.1016/j.jhazmat.2007.01.079.

[105] G. Moussavi, S. Talebi, M. Farrokhi, R.M. Sabouti, The investigation of mechanism, kinetic and isotherm of ammonia and humic acid co-adsorption onto natural zeolite, Chem. Eng. J. 171 (2011) 1159–1169. https://doi.org/10.1016/j.cej.2011.05.016.

[106] S.H. Huang, D.H. Chen, Rapid removal of heavy metal cations and anions from aqueous solutions by an amino-functionalized magnetic nano-adsorbent, J. Hazard. Mater. 163 (2009) 174–179. https://doi.org/10.1016/j.jhazmat.2008.06.075.

[107] F.T. Li, H. Yang, Y. Zhao, R. Xu, Novel modified pectin for heavy metal adsorption, Chinese Chem. Lett. 18 (2007) 325–328. https://doi.org/10.1016/j.cclet.2007.01.034.

[108] J. Gong, L. Chen, G. Zeng, F. Long, J. Deng, Q. Niu, X. He, Shellac-coated iron oxide nanoparticles for removal of cadmium(II) ions from aqueous solution, J. Environ. Sci. (China). 24 (2012) 1165–1173. https://doi.org/10.1016/S1001-0742(11)60934-0.

[109] V.K. Gupta, R. Kumar, A. Nayak, T.A. Saleh, M.A. Barakat, Adsorptive removal of dyes from aqueous solution onto carbon nanotubes: A review, Adv. Colloid Interface Sci. 193–194 (2013) 24–34. https://doi.org/10.1016/j.cis.2013.03.003.

[110] A. Bhattacharya, B.N. Misra, Grafting: A versatile means to modify polymers: Techniques, factors and applications, Prog. Polym. Sci. 29 (2004) 767–814. https://doi.org/10.1016/j.progpolymsci.2004.05.002.

[111] G. Crini, P.M. Badot, Application of chitosan, a natural aminopolysaccharide, for dye removal from aqueous solutions by adsorption processes using batch studies: A review of recent literature, Prog. Polym. Sci. 33 (2008) 399–447. https://doi.org/10.1016/j.progpolymsci.2007.11.001.

[112] L. Wojnárovits, C.M. Földváry, E. Takács, Radiation-induced grafting of cellulose for adsorption of hazardous water pollutants: A review, Radiat. Phys. Chem. 79 (2010) 848–862. https://doi.org/10.1016/j.radphyschem.2010.02.006.

[113] K. Littunen, U. Hippi, L.S. Johansson, M. Österberg, T. Tammelin, J. Laine, J. Seppälä, Free radical graft copolymerization of nanofibrillated cellulose with acrylic monomers, Carbohydr. Polym. 84 (2011) 1039–1047. https://doi.org/10.1016/j.carbpol.2010.12.064.

[114] I.M. Abdelmonem, E. Metwally, T.E. Siyam, F. Abou El-Nour, A.R.M. Mousa, Gamma radiation-induced preparation of chitosan-acrylic acid-1-vinyl-2-vinylpyrrolidone/multiwalled

carbon nanotubes composite for removal of 152+154Eu, 60Co and 134Cs radionuclides, Int. J. Biol. Macromol. 164 (2020) 2258–2266. https://doi.org/10.1016/j.ijbiomac.2020.08.120.

[115] H. Wang, A. Zhou, F. Peng, H. Yu, J. Yang, Mechanism study on adsorption of acidified multiwalled carbon nanotubes to Pb(II), J. Colloid Interface Sci. 316 (2007) 277–283. https://doi.org/10.1016/j.jcis.2007.07.075.

[116] B.L. Rivas, B. Quilodrán, E. Quiroz, Metal ion retention properties of poly(acrylic acid) and poly[N-3-(dimethylamino)propyl acrylamide-co-acrylic acid], J. Appl. Polym. Sci. 97 (2005) 1385–1394. https://doi.org/10.1002/app.21836.

[117] G.S. Misra, C. V Gupta, Aqueous polymerization of methacrylamide initiated by the redox system K2S2O8/ascorbic acid, Die Makromol. Chemie. 165 (1973) 205–216. http://dx.doi.org/10.1002/macp.1973.021650119.

[118] B.L. Rivas, S.A. Pooley, H.A. Maturana, S. Villegas, Ion uptake properties of acrylamide derivative resins, Macromol. Chem. Phys. 202 (2001) 443–447. https://doi.org/10.1002/1521-3935(20010201)202:3<443::AID-MACP443>3.0.CO;2-F.

[119] B.L. Rivas, I.M.- Villoslada, Chelation properties of polymer complexes of poly(acrylic acid) with poly(acrylamide), and poly(acrylic acid) with poly(N,N- dimethylacrylamide), Macromol. Chem. Phys. 1160 (1998) 1153–1160.

[120] S. Çavuş, G. Gürdag, K. Sözgen, M.A. Gürkaynak, The preparation and characterization of poly(acrylic acid-co-methacrylamide) gel and its use in the non-competitive heavy metal removal, Polym. Adv. Technol. 20 (2009) 165–172. https://doi.org/10.1002/pat.1248.

[121] Z. Yang, H. Peng, W. Wang, T. Liu, Fast Responsive Poly(acrylic acid-co-N-isopropylacrylamide) Hydrogels Based on New Crosslinker, J. Appl. Polym. Sci. 116 (2010) 2658–2667. https://doi.org/10.1002/app.

[122] B. Volesky, Biosorption and me, Water Res. 41 (2007) 4017–4029. https://doi.org/10.1016/j.watres.2007.05.062.

[123] K. Vijayaraghavan, Y.S. Yun, Bacterial biosorbents and biosorption, Biotechnol. Adv. 26 (2008) 266–291. https://doi.org/10.1016/j.biotechadv.2008.02.002.

[124] Q.S. Liu, T. Zheng, P. Wang, J.P. Jiang, N. Li, Adsorption isotherm, kinetic and mechanism studies of some substituted phenols on activated carbon fibers, Chem. Eng. J. 157 (2010) 348–356. https://doi.org/10.1016/j.cej.2009.11.013.

[125] I. Langmuir, The evaporation, condensation and reflection of molecules and the mechanism of adsorption, Phys. Rev. 8 (1916) 149–176. https://doi.org/10.1103/PhysRev.8.149.

[126] D. L.Sparks, Sorption Phenomena on Soils, in: Environ. Soil Chem., 2nd ed., Elsevier B.V, Academic Press, 2003: pp. 133–186. https://doi.org/10.1016/B978-012656446-4/50005-0.

[127] D. A.O, Langmuir, Freundlich, Temkin and Dubinin–Radushkevich Isotherms Studies of Equilibrium Sorption of Zn 2+ Unto Phosphoric Acid Modified Rice Husk, IOSR J. Appl. Chem. 3 (2012) 38–45. https://doi.org/10.9790/5736-0313845.

[128] Y.H. Li, Z. Di, J. Ding, D. Wu, Z. Luan, Y. Zhu, Adsorption thermodynamic, kinetic and desorption studies of Pb2+ on carbon nanotubes, Water Res. 39 (2005) 605–609. https://doi.org/10.1016/j.watres.2004.11.004.

[129] S.M. Miraboutalebi, S.K. Nikouzad, M. Peydayesh, N. Allahgholi, L. Vafajoo, G. McKay, Methylene blue adsorption via maize silk powder: Kinetic, equilibrium, thermodynamic studies and residual error analysis, Process Saf. Environ. Prot. 106 (2017) 191–202. https://doi.org/10.1016/j.psep.2017.01.010.

[130] P. Kazemi, M. Peydayesh, A. Bandegi, T. Mohammadi, O. Bakhtiari, Pertraction of methylene blue using a mixture of D2EHPA/M2EHPA and sesame oil as a liquid membrane, Chem. Pap. 67 (2013) 722–729. https://doi.org/10.2478/s11696-013-0374-0.

[131] B. Ohtani, Photocatalysis by inorganic solid materials: Revisiting its definition, concepts, and experimental procedures, in: Adv. Inorg. Chem., 1st ed., Elsevier Inc., 2011: pp. 395–430. https://doi.org/10.1016/B978-0-12-385904-4.00001-9.

[132] P. Karaolia, I. Michael-Kordatou, E. Hapeshi, C. Drosou, Y. Bertakis, D. Christofilos, G.S. Armatas, L. Sygellou, T. Schwartz, N.P. Xekoukoulotakis, D. Fatta-Kassinos, Removal of antibiotics, antibiotic-resistant bacteria and their associated genes by graphene-based TiO2 composite photocatalysts under solar radiation in urban wastewaters, Appl. Catal. B Environ. 224 (2018) 810–824. https://doi.org/10.1016/j.apcatb.2017.11.020.

[133] C. Berberidou, V. Kitsiou, D.A. Lambropoulou, A. Antoniadis, E. Ntonou, G.C. Zalidis, I. Poulios, Evaluation of an alternative method for wastewater treatment containing pesticides using solar photocatalytic oxidation and constructed wetlands, J. Environ. Manage. 195 (2017) 133–139. https://doi.org/10.1016/j.jenvman.2016.06.010.

[134] A.G. R Ananthashankar, Production, Characterization and Treatment of Textile Effluents: A Critical Review, J. Chem. Eng. Process Technol. 05 (2013). https://doi.org/10.4172/2157-7048.1000182.

[135] J. Jing, J. Li, J. Feng, W. Li, W.W. Yu, Photodegradation of quinoline in water over magnetically separable Fe_3O_4/TiO_2 composite photocatalysts, Chem. Eng. J. 219 (2013) 355–360. https://doi.org/10.1016/j.cej.2012.12.058.

[136] Y. Ju, J. Qiao, X. Peng, Z. Xu, J. Fang, S. Yang, C. Sun, Photodegradation of malachite green using UV-vis light from two microwave-powered electrodeless discharge lamps (MPEDL-2): Further investigation on products, Dominant routes and mechanism, Chem. Eng. J. 221 (2013) 353–362. https://doi.org/10.1016/j.cej.2012.06.055.

[137] M. Shekofteh-Gohari, A. Habibi-Yangjeh, M. Abitorabi, A. Rouhi, Magnetically separable nanocomposites based on ZnO and their applications in photocatalytic processes: A review, Crit. Rev. Environ. Sci. Technol. 48 (2018) 806–857. https://doi.org/10.1080/10643389.2018.1487227.

[138] M. Pirhashemi, A. Habibi-Yangjeh, S. Rahim Pouran, Review on the criteria anticipated for the fabrication of highly efficient ZnO-based visible-light-driven photocatalysts, J. Ind. Eng. Chem. 62 (2018) 1–25. https://doi.org/10.1016/j.jiec.2018.01.012.

[139] S. Feizpoor, A. Habibi-Yangjeh, K. Yubuta, Integration of carbon dots and polyaniline with TiO2 nanoparticles: Substantially enhanced photocatalytic activity to removal various pollutants under visible light, J. Photochem. Photobiol. A Chem. 367 (2018) 94–104. https://doi.org/10.1016/j.jphotochem.2018.08.017.

[140] A. Zada, Y. Qu, S. Ali, N. Sun, H. Lu, R. Yan, X. Zhang, L. Jing, Improved visible-light activities for degrading pollutants on TiO2/g-C3N4 nanocomposites by decorating SPR Au nanoparticles and 2,4-dichlorophenol decomposition path, J. Hazard. Mater. 342 (2018) 715–723. https://doi.org/10.1016/j.jhazmat.2017.09.005.

[141] J. Zhou, G. Tian, Y. Chen, J.Q. Wang, X. Cao, Y. Shi, K. Pan, H. Fu, Synthesis of hierarchical TiO2 nanoflower with anatase-rutile heterojunction as Ag support for efficient visible-light photocatalytic activity, Dalt. Trans. 42 (2013) 11242–11251. https://doi.org/10.1039/c3dt51293b.

[142] J.T. Park, D.J. Kim, D.H. Kim, J.H. Kim, A facile graft polymerization approach to N-doped TiO2 heterostructures with enhanced visible-light photocatalytic activity, Mater. Lett. 202 (2017) 66–69. https://doi.org/10.1016/j.matlet.2017.05.070.

[143] A. Buthiyappan, A.R. Abdul Aziz, W.M.A. Wan Daud, Recent advances and prospects of catalytic advanced oxidation process in treating textile effluents, Rev. Chem. Eng. 32 (2016) 1–47. https://doi.org/10.1515/revce-2015-0034.

[144] Y. Lu, P.R. Chang, P. Zheng, X. Ma, Rectorite-TiO_2-Fe_3O_4 composites: Assembly, characterization, adsorption and photodegradation, Chem. Eng. J. 255 (2014) 49–54. https://doi.org/10.1016/j.cej.2014.06.062.

[145] C. Di Valentin, G. Pacchioni, Trends in non-metal doping of anatase TiO_2: B, C, N and F, Catal. Today. 206 (2013) 12–18. https://doi.org/10.1016/j.cattod.2011.11.030.

[146] M.E. Hassan, J. Chen, G. Liu, D. Zhu, J. Cai, Enhanced photocatalytic degradation of methyl orange dye under the daylight irradiation over CN-TiO_2 modified with OMS-2, Materials (Basel). 7 (2014) 8024–8036. https://doi.org/10.3390/ma7128024.

[147] S. Lian, E. Wang, Z. Kang, Y. Bai, L. Gao, M. Jiang, C. Hu, L. Xu, Synthesis of magnetite nanorods and porous hematite nanorods, Solid State Commun. 129 (2004) 485–490. https://doi.org/10.1016/j.ssc.2003.11.043.

[148] B. Ohtani, Y. Ogawa, S.I. Nishimoto, Photocatalytic activity of amorphous-anatase mixture of titanium(IV) oxide particles suspended in aqueous solutions, J. Phys. Chem. B. 101 (1997) 3746–3752. https://doi.org/10.1021/jp962702+.

[149] B. Prasai, B. Cai, M.K. Underwood, J.P. Lewis, D.A. Drabold, Properties of amorphous and crystalline titanium dioxide from first principles, J. Mater. Sci. 47 (2012) 7515–7521. https://doi.org/10.1007/s10853-012-6439-6.

[150] S. Sun, P. Song, J. Cui, S. Liang, Amorphous TiO_2 nanostructures: Synthesis, fundamental properties and photocatalytic applications, Catal. Sci. Technol. 9 (2019) 4198–4215. https://doi.org/10.1039/c9cy01020c.

[151] K.K. Ghuman, C.V. Singh, Effect of doping on electronic structure and photocatalytic behavior of amorphous TiO_2, J. Phys. Condens. Matter. 25 (2013). https://doi.org/10.1088/0953-8984/25/47/475501.

[152] Y. Wang, H. Yang, W. Zou, Preparation of amorphous sphere-like TiO_2 with excellent photocatalytic performance, Mater. Lett. 254 (2019) 54–57. https://doi.org/10.1016/j.matlet.2019.06.108.

[153] A. Luna-Flores, J.L. Sosa-Sánchez, M.A. Morales-Sánchez, R. Agustín-Serrano, J.A. Luna-López, An easy-made, economical and efficient carbon-doped amorphous TiO_2 photocatalyst obtained bymicrowave assisted synthesis for the degradation of Rhodamine B, Materials (Basel). 10 (2017). https://doi.org/10.3390/ma10121447.

[154] Y.F. Xu, X.D. Wang, J.F. Liao, B.X. Chen, H.Y. Chen, D. Bin Kuang, Amorphous-TiO_2-Encapsulated $CsPbBr_3$ Nanocrystal Composite Photocatalyst with Enhanced Charge Separation and CO_2 Fixation, Adv. Mater. Interfaces. 5 (2018) 1–8. https://doi.org/10.1002/admi.201801015.

[155] P. Shao, J. Tian, Z. Zhao, W. Shi, S. Gao, F. Cui, Amorphous TiO_2 doped with carbon for visible light photodegradation of rhodamine B and 4-chlorophenol, Appl. Surf. Sci. 324 (2015) 35–43. https://doi.org/10.1016/j.apsusc.2014.10.108.

[156] S. Mohan, O.S. Oluwafemi, N. Kalarikkal, S. Thomas, S.P. Songca, Biopolymers – Application in Nanoscience and Nanotechnology, in: Recent Adv. Biopolym., 2016: pp. 47–72. https://doi.org/http://dx.doi.org/10.5772/62225.

[157] J.C. Colmenares, R.S. Varma, P. Lisowski, Sustainable hybrid photocatalysts: Titania immobilized on carbon materials derived from renewable and biodegradable resources, Green Chem. 18 (2016) 5736–5750. https://doi.org/10.1039/c6gc02477g.

[158] B. Joseph, S. Krishnan, V.K. Sagarika, A. Tharayil, N. Kalarikkal, S. Thomas, Bionanocomposites as industrial materials, current and future perspectives: a review, Emergent Mater. 3 (2020) 711–725. https://doi.org/10.1007/s42247-020-00133-x.

[159] X. Chen, D.H. Kuo, D. Lu, Y. Hou, Y.R. Kuo, Synthesis and photocatalytic activity of mesoporous TiO_2 nanoparticle using biological renewable resource of un-modified lignin as a template, Microporous Mesoporous Mater. 223 (2016) 145–151. https://doi.org/10.1016/j.micromeso.2015.11.005.

[160] D. Ke, S. Liu, K. Dai, J. Zhou, L. Zhang, T. Peng, CdS/regenerated cellulose nanocomposite films for highly efficient photocatalytic H2 production under visible light irradiation, J. Phys. Chem. C. 113 (2009) 16021–16026. https://doi.org/10.1021/jp903378q.

[161] B. Wang, M. Feng, H. Zhan, Improvement of wood properties by impregnation with TiO_2 via ultrasonic-assisted sol-gel process, RSC Adv. 4 (2014) 56355–56360. https://doi.org/10.1039/c4ra04852k.

[162] P. Lisowski, J.C. Colmenares, O. Mašek, W. Lisowski, D. Lisovytskiy, A. Kamińska, D. Łomot, Dual Functionality of TiO_2/Biochar Hybrid Materials: Photocatalytic Phenol Degradation in the Liquid Phase and Selective Oxidation of Methanol in the Gas Phase, ACS Sustain. Chem. Eng. 5 (2017) 6274–6287. https://doi.org/10.1021/acssuschemeng.7b01251.

[163] H. Wang, X. Qiu, W. Liu, D. Yang, Facile preparation of well-combined lignin-based carbon/ZnO hybrid composite with excellent photocatalytic activity, Appl. Surf. Sci. 426 (2017) 206–216. https://doi.org/10.1016/j.apsusc.2017.07.112.

[164] A. Khan, V. Nair, J.C. Colmenares, R. Gl, Lignin-Based Composite Materials for Photocatalysis, in: M. Olivucci, W.-Y. Wong (Eds.), Top. Curr. Chem. Collect. Chem., 1st ed., 2018: pp. 1–31. https://doi.org/10.1007/978-3-030-00590-0.

[165] H. Wang, X. Qiu, R. Zhong, F. Fu, Y. Qian, D. Yang, One-pot in-situ preparation of a lignin-based carbon/ZnO nanocomposite with excellent photocatalytic performance, Mater. Chem. Phys. 199 (2017) 193–202. https://doi.org/10.1016/j.matchemphys.2017.07.009.

[166] N. Wang, H. Fan, S. Ai, Lignin templated synthesis of porous carbon-CeO_2 composites and their application for the photocatalytic desulphuration, Chem. Eng. J. 260 (2015) 785–790. https://doi.org/10.1016/j.cej.2014.09.051.

[167] U.M. Garusinghe, V.S. Raghuwanshi, W. Batchelor, G. Garnier, Water Resistant Cellulose-Titanium Dioxide Composites for Photocatalysis, Sci. Rep. 8 (2018) 1–13. https://doi.org/10.1038/s41598-018-20569-w.

[168] J. Zhang, W. Liu, P. Wang, K. Qian, Photocatalytic behavior of cellulose-based paper with TiO_2 loaded on carbon fibers, J. Environ. Chem. Eng. 1 (2013) 175–182. https://doi.org/10.1016/j.jece.2013.04.022.

[169] J. Wang, W. Liu, H. Li, H. Wang, Z. Wang, W. Zhou, H. Liu, Preparation of cellulose fiber-TiO_2 nanobelt-silver nanoparticle hierarchically structured hybrid paper and its photocatalytic and antibacterial properties, Chem. Eng. J. 228 (2013) 272–280. https://doi.org/10.1016/j.cej.2013.04.098.

CHAPTER 3

METHODS, CHEMICALS AND EQUIPMENT

3.1. Introduction

This chapter summarizes all the laboratory work that was carried out in this study. This includes preparation of treated pinecone with sodium hydroxide, pine-magnetite composite (PMC), modification by grafting with acrylic acid (GAA), acrylamide (GACA) obtained from pinecone and synthesis of grafted PMC/GAA doped TiO_2 samples. It also covers the description of instrumental techniques employed in the characterization of the synthesized bionanocomposites. In addition, optimization methods and experimental procedures of adsorption variables such as initial solution pH, biosorbent dose and contact time are described. Kinetic models and equilibrium experiments for PMC, GAA and GACA studied are also described. The response surface methodology (RSM) for the optimization of grafting acrylic acid to PMC is also discussed from preparation to results obtained.

3.2. Materials and methods

3.2.1. Chemicals and reagents

Pinecones are naturally occurring agricultural wastes obtained from a plantation in Vanderbijlpark, Gauteng, South Africa. The following chemicals used $Fe_2(SO_4)_3.4H_2O$, $FeSO_4 \cdot 7H_2O$, NH_4OH, NaOH, titanium butoxide, ethanol, methanol, Acrylic Acid, Acrylamide, Ceric Ammonium nitrate (CAN) and methylene blue were supplied by Merck, South Africa. All reagents were of analytical grade and were used without any further treatment. Nitrogen gas was supplied by Afrox.

3.2.2. Apparatus

All glass apparatus were thoroughly washed and thereafter dried in an oven at 80℃ before use. The reactions were conducted in a three-neck round bottom flask under a dry nitrogen atmosphere to ensure uniformity. A heating block was used to regulate the temperature for all

reactions. The following equipment or apparatus were used to carry out the experimental procedure: Magnetic stirrer, pH meter, weighing balance, incubator shaker, reflux apparatus grinder and vacuum oven.

3.2.3. Preparation of treated pinecone powder

The pinecones were collected and washed to remove impurities without destroying the cone matrix. The pinecone scales were peeled and crushed to a powder using a pulverizer and then sieved. The washed cones were dried at 90°C for 48 h in an oven. The pinecone powder (PCP) was then sieved and particles at size of 45 and 90 μm were characterized and used for further experiments. A weighed amount (50 g) of PCP was mixed with 500 cm^3 of 0.15 $mol.dm^{-3}$ sodium hydroxide solutions and the slurry stirred for 18 h at room temperature. The solution mixture was rinsed with 500 cm^3 of distilled water. This procedure was repeated four times to ensure the removal of sodium hydroxide from the suspension. The residue was dried overnight at 90°C.

3.2.4. Synthesis of pine-Fe_3O_4 magnetite

A magnetite was prepared using two iron salts. A mixture of $FeSO_4.7H_2O$ (2.1 g) and of $Fe(SO_4)_3.XH_2O$ (3.1 g) were dissolved under inert atmosphere in 100 cm^3 of double distilled water with vigorous stirring. Thereafter, 20 cm^3 of 28% ammonium hydroxide and the appropriate amount of pine powder were added. The reaction was left to run for 45 min at 80 °C under constant stirring. The resulting nanoparticles consisting of magnetite attached to the cellulose was washed several times with deionized water and ethanol and dried in a vacuum oven at 60 °C overnight. Parameters which were varied in this experimental work included volume of NH_4OH from 5, 10, 20, 30, and 40 cm^3; weight of pine powder from 1.0, 1.5, 2.0, 2.5, 3.0 and 3.5 g; temperature from 40, 60, 80 and 100 °C and reaction time from 15, 30, 45 and 60 min.

3.2.5. Grafting with acrylic acid and acrylamide

PMC (1 g), 20 cm^3 of 1.5 $mol.dm^{-3}$ acrylic acid or acrylamide and 135 cm^3 of deionized water were transferred into a three-neck round bottom flask at 42 °C. The reaction was bubbled under nitrogen gas for 30 min to remove the dissolved oxygen under stirring. About 10 cm^3 of 0.5 M CAN, dissolved in 0.3 M HNO_3 was slowly added to the reaction to initiate graft co-polymerization and stirring was continued for 2 h. Reaction mass was neutralized by 50%

NaOH and precipitated in methanol and thereafter washed with methanol/ water (90:10) several times, so that the unreacted PMC and ceric salt were removed. The final residue was dried in a vacuum oven over night at 40 ^{o}C.

3.2.6. Synthesis of grafted PMC/GAA doped TiO_2 samples

Approximately 5.0 mg of the bionanocomposite powders (PMC/GAA) (calculated to be equivalent to 9 wt.% of the mass of Ti in the amount of titanium precursor) was sonicated in 50 mL ethanol (EtOH) at 40 for 30 min. A TiO_2 precursor was prepared by dissolving 10 mL of titanium butoxide (TiOBut) in a 100 cm^3 butanol: propanol (80:20 v/v) and adding 2 cm^3 acetylacetone. A hydrolysing solution was made by mixing EtOH and deionized water at 1:1 (v/v). The hydrolysing solution and the precursor solution were simultaneously added dropwise into the suspension of the bionanocomposite with continued sonication and stirring using a mechanical stirrer. The preparation of the bionanocompostes with N doped TiO_2 was carried out using a similar procedure except that the hydrolysing solution also functioned as the dopant carrier in that ethylene diamine was added such that the v/v ratio was 1:1:1. At completion of mixing the reagents, the resultant sol was stirred for 5 h on a heater/ stirrer plate. Afterwards the heating mantle was switched on and set at 70 ℃ to evaporate the solvents. After complete evaporation of the solvents (about 24 h), the remaining powder was crushed using a mortar and pestle and stored for further use.

3.3. Characterization techniques

Complete characterization of the pine-magnetite composite, pine-magnetite composite grafted with acrylic acid and acrylamide was studied through different techniques. Incorporation of Fe_3O_4 magnetic nanoparticles in the grafting network on the pine-magnetite composite were confirmed through different techniques such as TEM (Transmission Electron Microscopy), XRD (X-ray diffraction (XRD) spectroscopy), TGA (Thermal Gravimetric Analysis), FTIR (Fourier transform infrared (FTIR) spectroscopy), SEM (Scanning electron microscopy) and Brunauer-Emmett-Teller (BET).

3.3.1. Fourier transform infrared (FTIR) spectroscopy

Qualitative and fundamental identification of the functional chemical groups of treated pinecones with NaOH, pine-magnetite composite (PMC), modification by grafting with acrylic acid (GAA) and acrylamide (GACA) was analyzed with a FTIR (Perkin- Elmer) in the range

450 - 4000 cm^{-1} using diamond attenuated total reflectance (ATR). Different organic functional groups peaks were explained using FTIR spectroscopy.

3.3.2. X-ray diffraction (XRD) spectroscopy

XRD analysis was done to identify the chemical composition and crystallographic structure of the cellulose powder magnetite. An X'Pert PRO X-ray diffractometer (PANalytical, PW3040/60 XRD; CuKα anode; λ = 0.154 nm) was used for XRD patterns. The samples were placed in an aluminum holder and scanned at 45 kV and 40 mA from 10° to 120° 2θ, the exposure time for each sample was 20 min and a step size of 0.02°. The Debye-Scherrer equation was used to determine particle sizes of the prepared bionanocomposites.

3.3.3. Transmission Electron Microscopy (TEM)

The morphology and size of the synthesized particles were observed using transmission electron microscope (TEM, FEI TECNAI G^2 SPIRIT) at an accelerating voltage of 150 kV. Samples were prepared by placing drops of diluted ethanol dispersed of nanocrystalline on the surface of coper grids, which were purchased commercially.

3.3.4. Scanning electron microscopy (SEM)

Scanning electron microscopy (SEM) was used to observe the microstructure and surface morphology of all the bio-nanocomposite. SEM images were generated from a Jeol JSM 7800F field emission microscope equipped with an LED detector. Samples were carbon coated using a Quorum QT 150 sputter coater before HRSEM analysis and Thermofischer UltraDry EDS Detector was used for elemental analysis.

3.3.5. Brunauer-Emmett-Teller (BET) Method

A surface property of an adsorbent describes the effect of modification on the surface area of the adsorbent. The specific surface area of the PMC, GAA, PMC-TiO_2, PMC-$NTiO_2$, GAA-TiO_2 and GAA-$NTiO_2$ bionanocomposites were measured by BET analyzer. The BET surface area and pore size distribution were determined using computer-controlled nitrogen gas adsorption analyzer. Degassing was carried out for 1 hr at 90 °C and increased to 120 °C for 2 h. A mass of 0.2 g of the PMC, GAA, PMC-TiO_2, PMC-$NTiO_2$, GAA-TiO_2 and GAA-$NTiO_2$ adsorbent material was applied for analysis.

3.3.6. X-ray photoelectron spectroscopy

The surface elemental composition of the bionanocomposites was determined through X-ray photoelectron spectroscopic (XPS) analysis on a Thermo ESCAlab 250Xi model. A monochromatic X-ray beam with a spot size of 900 μm, generated from an Al Kα (1486.7eV) shell was blazed onto a pelletized sample that was held in a pressurized chamber at 10^{-8} mBar. X-ray photoelectron spectroscopy (XPS) analysis was carried out on PHI 5000 scanning ESCA microprobe with a 100 µm diameter monochromatic Al Kα x-ray beam (hν = 1486.6 eV) generated by a 25 W, 15 kV electron beam to analyze different binding energy peaks. Multipack version 9 software was utilized to analyze the spectra to identify the chemical compounds and their electronic states using Gaussian–Lorentz fits.

3.3.7. Vibrating sample magnetometer

Magnetic properties of powder samples were characterized with a Quantum Design MPMS-7, by measuring the applied field dependence of magnetization between -15 and 15 kOe.

3.3.8. Thermal Gravimetric Analysis (TGA)

Thermogravimetric analysis (TGA) was used to determine weight loss as a function of temperature. Changes of the pinecone matrix were determined due to the different chemical treatments because each kind of biomass has a characteristic pyrolysis behavior which is explained based on its individual component characteristics. The cone samples were forced to pyrolysis from 30 – 900 °C in a N_2/air atmosphere at a heating rate of 10 °C.min^{-1} using a Perkin-Elmer (USA) Simultaneous Thermal Analyzer 6000 instrument.

3.3.9. X-ray fluorescence (XRF)

Energy Dispersive X-ray Fluorescence (EDXRF) elemental analyzer supplied by NEXQC was used to determine the elemental composition of iron oxide (FeO). X-ray fluorescence is a non-destructive analytical technique. It provides one of the simplest, most accurate and most economic analytical methods. This was done by measuring the fluorescent x-ray emitted from a sample when it is excited by a primary x-ray source.

3.3.10. Adsorption and Kinetic studies

Various Methylene Blue (MB) solutions with different pH range, contact time, initial concentrations and mass dosage were prepared by diluting 1000 M. Equilibrium experiments, to determine the adsorption capacity of pine-magnetite composite and grafted pine-magnetite composite with acrylic acid and acrylamide was conducted using 250 cm^3 bottles. Approximately 0.1 g of PMC/GAA/GACA and 100 cm^3 of the MB solution were added and shaken for 2 h at 26 ℃. Thereafter, absorbance was determined using UV-VIS spectrophotometer at the wavelength corresponding to the maximum absorbance (λ_{max}=665 nm) as determined from the plot. This wavelength was used for measuring the absorbance of residual concentration of MB. pH of the solution was adjusted using 0.1 M HCl and 0.1 M NaOH.

Batch contact kinetic experiments were performed by contacting 0.1 g of the adsorbent material with 100 cm^3 of MB solution of concentrations (100, 150, 200, 250 and 300 M). Agitation was made for 120 min which is more sufficient time to reach equilibrium at a constant stirring speed of 200 rpm and temperature of 26℃. Aliquots (0.1 cm^3) of sample was drawn at suitable time intervals and were analyzed using UV-VIS spectrophotometer (Perkin Elmer Lambda 25).

3.3.11. Desorption and recycling efficiency

The main aim of desorption studies is the reusability of adsorbents in the multiple adsorption or desorption cycles and beneficial for their practical and economical applications. Desorption studies were performed with 0.01, 0.05 and 0.1 M HCl. PMC, GAA and GACA (1 g) of saturated with 100 cm^3 of methylene blue was placed in different desorption solutions and constantly stirred in a water bath at 200 rpm, 26 ℃ for 2 h. The adsorbent solutions were centrifuged and analyzed using UV-VIS spectrophotometer.

3.3.12. pH at point zero charge

To further investigate the effects of modifications on the suitability of the synthesized materials for adsorption, the isoelectric point or point of zero charge (pH_{PZC}) was determined. The solution pH is an important parameter for dye adsorption because it does not only change the surface charge of the adsorbent but also it affects the molecule structure of the dye. As methylene blue is a cationic dye, it can easily form positively charged species over a wide pH

range. The solid addition method was used to determine the pH_{pzc} of the pinecone composite. To a series of 100 cm^3 volumetric flasks, 45 cm^3 of 0.01 $mol.dm^{-3}$ KNO_3 solution were transferred. The pH_i values of the solutions were roughly adjusted between pH 2 to 12 by addition of either 0.1 M HCl or NaOH on a pH meter with constant stirring. Total volume of the solution in each flask was made up to 50 cm^3 by addition of KNO_3 solution of the same strength. The pH_i for the solutions was accurately noted, and 0.1 g of pinecone composite were added to each volumetric flask, which was then immediately closed. The suspensions were allowed to equilibrate for 48 h on a shaker operating at 200 rpm. The pH_f values of the supernatant were accurately noted and the difference between the initial and final pH values ($\Delta pH = pH_f - pH_i$) were plotted against the pH_i. At the isoelectric point, the net surface charge is 0 therefore the material is neither negatively nor positively charged and is effectively neutral. Below the isoelectric point, the surface possesses a positive charge and attracts negatively charged ions through electrostatic attraction. Above the point of zero charge, the surface has a net negative charge hence attracting positively charged ions.

Adsorption measurement was determined by batch experiments of known amount of the adsorbent with 50 cm^3 of aqueous methylene blue solutions of known concentration in a series of 250 cm^3 conical flasks. The mixture was shaken at a constant temperature using Thermoline Scientific Orbital Shaker Incubator at 120 rpm at 30 °C temperature for 180 min. At predetermined time, the bottles were withdrawn from the shaker, and the residual dye concentration in the reaction mixture was analyzed by centrifuging the reaction mixture and then measuring the absorbance of the supernatant at the wavelength that correspond to the maximum absorbance of the sample. Dye concentration in the reaction mixture was calculated from the calibration curve. Adsorption experiments were conducted by varying initial solution pH, contact time, adsorbent dose, initial methylene blue dye concentration, temperature, and salt concentration under the aspect of adsorption kinetics, adsorption isotherm and thermodynamic study.

3.3.13. Experimental design and Response Surface Methodology optimization

Optimization is the term referring to improvement of the performance of a system, a process, or a product to obtain the maximum benefits from it. In analytical chemistry is a term that describes conditions at which to apply a procedure that produces the best possible response [1].

It monitors the influence of one factor at a time on an experimental response. While one parameter is changed, others are kept at a constant level.

Response surface methodology (RSM) is one of the multivariate statistics techniques used in an analytical optimization procedure. It is a collection of mathematical and statistical techniques based on the fit of a polynomial equation to the experimental data, which describes the behavior of a data set with the objective of making statistical provisions. Linear or square polynomial functions are employed to describe the system studied. It is applied when a response or a set of responses of interest are influenced by several variables. Thus, RSM objective is to simultaneously optimize the levels of these variables to attain the best system performance [2]. Basic principles were followed to attain the results. The following steps were followed for application of RSM as an optimization technique and explored in the experimental conditions until its optimization [3] selection of independent variables of major effects on the system through screening studies and the delimitation of the experimental region: (i) choice of the experimental design and carrying out the experiments according to the selected experimental matrix; (ii) mathematics- statistical treatment of the obtained experimental data through the fit of a polynomial functions and evaluation of model's fitness; (iii) verification of the necessity and possibility of performing a displacement in the direction of the optimal region and (iv) obtaining the optimum values for each studied variable

In this study, grafting of PMC onto acrylic acid bio-nanocomposite optimization were synthesized by using RSM to examine the simultaneous interaction between concentration of acrylic acid and other preparation parameters. In this design the concentration, temperature, CAN and time were selected as the synthesis parameters. The RSM design known as central composite design (CCD) was used in this study, to monitor the influence and interaction of the synthetic process variables for the grafting with acrylic acid using CAN as the initiator. The independent variables selected in the synthetic procedure for the grafting with acrylic acid were the temperature, concentration, initiator (CAN) and time. The independent variables used were varied between the lower (-1) and the higher (+1) levels as shown in (***Table 3.1***). The number of experimental runs (N) generated from a partial factorial design for the four independent variables consisted of sixteen factorial points, eight axial points and six replicates at the center points, indicating that altogether 30 experiments were required, (***Table 3.2***) as calculated from ***Equation 3.1***:

$$N = 2^n + 2n + n_c \qquad \textbf{Equation 3.1}$$

where n is the number of variable factor and n_c is a constant which has a value of 6.

The three responses (Y) were particle size (Y_1), % grafting of acrylic acid (Y_2) and rate constant (k_2) (Y_3) of the synthesized grafted PMC with acrylic acid bio-nanocomposite. Each response was utilized to develop an empirical model which correlated the response to the four synthetic process variables using a second-degree polynomial equation as given by Equation 3.2

$$Y = b_0 + \sum_{i=1}^{4} b_i x_i + \sum_{i=1}^{4} b_{ii} x_i^2 + \sum_{i=1}^{4} \sum_{j=i1}^{4} b_{ij} x_i x_j \qquad \textbf{Equation 3.2}$$

where Y is the response variable, b_o is the constant coefficient, *bi* the linear coefficient, b_{ij} the interaction coefficient, b_{ii} the quadratic coefficient, while x_i and x_{ij} are the coded variables which determine the response Y. The response data in this study were analyzed using the design-expert software (version 10), and the fitting of the models was evaluated based on the statistical significance of the equation. Parameters such as F-value, probability >F and adequate precision, which is a measure of error or the signal-to-noise ratio, were used as the indicators of how the suggested models fit the experimental values.

The response surface methodology emanates from a graphical presentation of the independent variables and the response. The response values are viewed as a surface lying above the plane of the independent variables, which shows the graphical relationship between the response (yield %) and the two independent variables (time and temperature). When all points with the same response in the plane of the independent variables are joined, a contour plot results [1].

Table 3.1 Variable levels for RSM experiment

Variables				**Levels**			
Factor	Name	Minimum	Maximum	Values of Code			
A	Acrylic acid	0.5000	1.50	-1↔0.50+1↔1.50	1.0000	0.3939	
B	CAN (mL)	5.00	15.00	-1↔20.00	+1↔70.00	45.00	19.70
C	Temperature (℃)	20.00	70.00	-1↔20.00	+1 ↔ 70.00	45.00	19.70
D	Time (min)	0.5000	4.00	-1↔0.50	+1↔4.00	2.25	1.38

In this experimental design, a total of 30 experiment runs were performed and the observed percentage grafting and grafting efficiency of the grafted bio-nanocomposite were determined based on the adsorption capacity (***Table 3.2***). Central composite design (CCD) was used to

develop a relationship between the GAA bio-nanocomposite preparation variables influence on the grafting % , grafting efficiency and adsorption capacity.

Table 3.2 Experimental design and results for preparation of grafted pine-magnetite bio-nanocomposite with grafting % and efficiency and adsorption capacities for methylene blue

Run	A: Acrylic acid	B: CAN	C: Temp	D: Time	Grafting %	Grafting Efficiency	Adsorption capacity
1	1.00	10.00	45.00	4.00	96.0414	58.3042	5.925
2	1.50	10.00	45.00	2.25	86.8039	79.0203	6.412
3	1.00	10.00	45.00	2.25	98.0583	71.7784	6.412
4	1.00	10.00	45.00	2.25	98.0583	71.7784	6.142
5	0.50	10.00	45.00	2.25	79.6075	83.8223	5.369
6	1.00	10.00	20.00	2.25	99.6209	50.0751	6.118
7	0.50	5.00	70.00	0.50	54.2294	94.2011	6.497
8	0.50	5.00	70.00	4.00	84.0908	57.737	6.412
9	1.00	10.00	45.00	2.25	98.0583	71.7784	6.412
10	0.50	15.00	70.00	4.00	97.2531	47.1655	6.142
11	1.50	5.00	20.00	4.00	82.1115	60.8199	5.923
12	0.50	15.00	20.00	4.00	85.6027	50.4541	6.142
13	1.00	10.00	45.00	2.25	98.0583	71.7784	6.118
14	0.50	5.00	20.00	4.00	73.0363	66.3053	5.923
15	1.00	10.00	70.00	2.25	87.6641	62.7408	5.923
16	1.50	5.00	20.00	0.50	86.6906	57.4581	6.263
17	1.50	5.00	70.00	4.00	94.949	47.7638	5.369
18	0.50	15.00	70.00	0.50	64.799	81.2031	6.142
19	1.00	10.00	45.00	2.25	98.0583	71.7784	6.118
20	1.50	5.00	70.00	0.50	51.6376	92.3948	5.923
21	1.00	10.00	45.00	2.25	98.0583	71.7784	6.118
22	1.50	15.00	70.00	0.50	54.2073	88.7431	6.142
23	1.50	15.00	20.00	4.00	87.6934	54.0687	5.369
24	1.00	5.00	45.00	2.25	96.837	64.5198	5.369
25	0.50	15.00	20.00	0.50	94.4627	49.5175	6.142
26	0.50	5.00	20.00	0.50	80.8424	64.9773	5.807
27	1.00	10.00	45.00	0.50	89.905	76.6232	6.142
28	1.50	15.00	70.00	4.00	98.054	47.7692	6.142
29	1.50	15.00	20.00	0.50	93.057	47.515	6.113
30	1.00	15.00	45.00	2.25	98.973	56.8196	5.875

Table 3.3* (a-c)** present the ANOVA of regression of the predicted response from the quadratic models for the grafting %, grafting efficiency and adsorption capacity. The calculated F values from the ANOVA (Table 3.3***(a-c) for the grafting %, % grafting efficiency and adsorption capacity were found to be 58.16, 70.05 and 1050.60 with lower probability (< 0.0001) indicating that the models were significant. Values presented in ***Table 3.3***(a-c) with "Prob > F" less than 0.05 indicates model terms are significant whilst the insignificant terms are omitted from the tables. The calculated coefficient of determination (R^2) values was 0. 9819, 0.9849, and 0.9990 for the grafting %, % grafting efficiency and adsorption capacity respectively which highlights an acceptable accuracy of the datas with the model. The adequacy of the model equation in describing the experimental data was validated from the plot of predicted versus actual values. The relationship between predicted and actual values of grafting %, % grafting efficiency and adsorption capacity ($mg.g^{-1}$) are indicated in

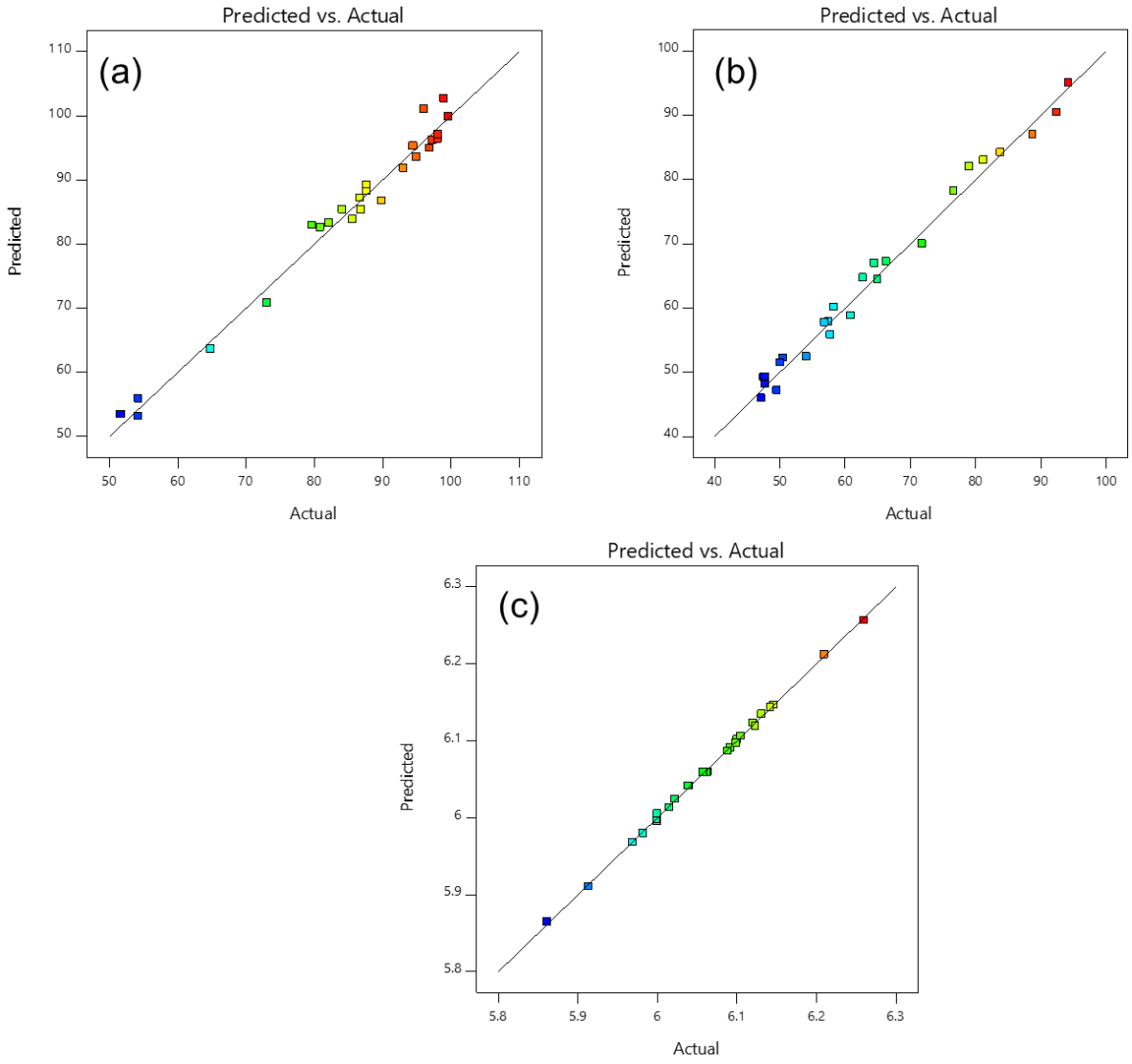

Figure 3.1**.** It is observed that the plots show a high correlation between the predicted and actual results indicating, this model can be used to navigate the design space.

Table 3.3 Analysis of variance for Grafting %

Source	**Sum of Squares**	**df**	**Mean Square**	**F- value**	**p-value**	
Model	5716.06	14	408.29	58.16	< 0.0001	significant
A-Acrylic acid	25.16	1	25.16	3.58	0.0778	
B-CAN	269.72	1	269.72	38.42	< 0.0001	
C-Temperature	514.49	1	514.49	73.28	< 0.0001	
D-Time	924.52	1	924.52	131.68	< 0.0001	
AB	65.19	1	65.19	9.29	0.0082	
AD	62.28	1	62.28	8.87	0.0094	
BC	4.76	1	4.76	0.6782	0.4231	
CD	1937.82	1	1937.82	276.01	< 0.0001	
A^2	437.52	1	437.52	62.32	< 0.0001	
Residual	105.31	15	7.02			
Lack of Fit	105.31	10	10.53			
Pure Error	0.0000	5	0.0000			
Cor Total	5821.37	29				

Std. Dev.	2.65	**R^2**	0.9819
Mean	86.88	**Adjusted R^2**	0.9650
C.V. %	3.05	**Predicted R^2**	0.9080
		Adeq Precision	26.4579

Table 3.4 Analysis of variance for % Grafting efficiency

Source	Sum of Squares	df	Mean Square	F- value	p-value	
Model	5549.16	14	396.37	70.05	< 0.0001	significant
A-Acrylic acid	21.85	1	21.85	3.86	0.0682	
B-CAN	382.00	1	382.00	67.51	< 0.0001	
C-Temperature	780.49	1	780.49	137.94	< 0.0001	
D-Time	1462.42	1	1462.42	258.45	< 0.0001	
AB	74.56	1	74.56	13.18	0.0025	
BC	27.01	1	27.01	4.77	0.0452	
CD	1770.03	1	1770.03	312.82	< 0.0001	
A^2	445.82	1	445.82	78.79	< 0.0001	
B^2	151.00	1	151.00	26.69	0.0001	
C^2	366.64	1	366.64	64.80	< 0.0001	
Residual	84.87	15	5.66			
Lack of Fit	84.87	10	8.49			
Pure Error	0.0000	5	0.0000			
Cor Total	5634.03	29				

Std. Dev.	2.38	**R^2**	0.9849
Mean	65.69	**Adjusted R^2**	0.9709
C.V. %	3.62	**Predicted R^2**	0.9190
		Adeq Precision	29.1698

Table 3.5 Analysis of variance for Adsorption capacity

Source	Sum of Squares	df	Mean Square	F- value	p-value	
Model	0.1907	14	0.0136	1050.60	< 0.0001	significant
A-Acrylic acid	0.0092	1	0.0092	706.60	< 0.0001	
B-CAN	0.0512	1	0.0512	3951.72	< 0.0001	
C-Temperature	0.0713	1	0.0713	5497.08	< 0.0001	
D-Time	0.0587	1	0.0587	4529.45	< 0.0001	
AB	5.641E-08	1	5.641E-08	0.0044	0.9483	
AC	3.452E-07	1	3.452E-07	0.0266	0.8726	
AD	3.106E-06	1	3.106E-06	0.2396	0.6316	
BC	5.814E-07	1	5.814E-07	0.0449	0.8351	
BD	0.0001	1	0.0001	4.80	0.0447	
CD	0.0001	1	0.0001	5.23	0.0371	
A^2	0.0001	1	0.0001	4.71	0.0464	
B^2	0.0001	1	0.0001	8.82	0.0095	
C^2	2.373E-06	1	2.373E-06	0.1831	0.6748	
D^2	0.0000	1	0.0000	1.46	0.2449	
Residual	0.0002	15	0.0000			
Lack of Fit	0.0002	10	0.0000	2.74	0.1391	not significant
Pure Error	0.0000	5	6.010E-06			
Cor Total	0.1909	29				

Std. Dev.	0.0036	**R^2**	0.9990
Mean	6.06	**Adjusted R^2**	0.9980
C.V. %	0.0594	**Predicted R^2**	0.9942
		Adeq Precision	153.9255

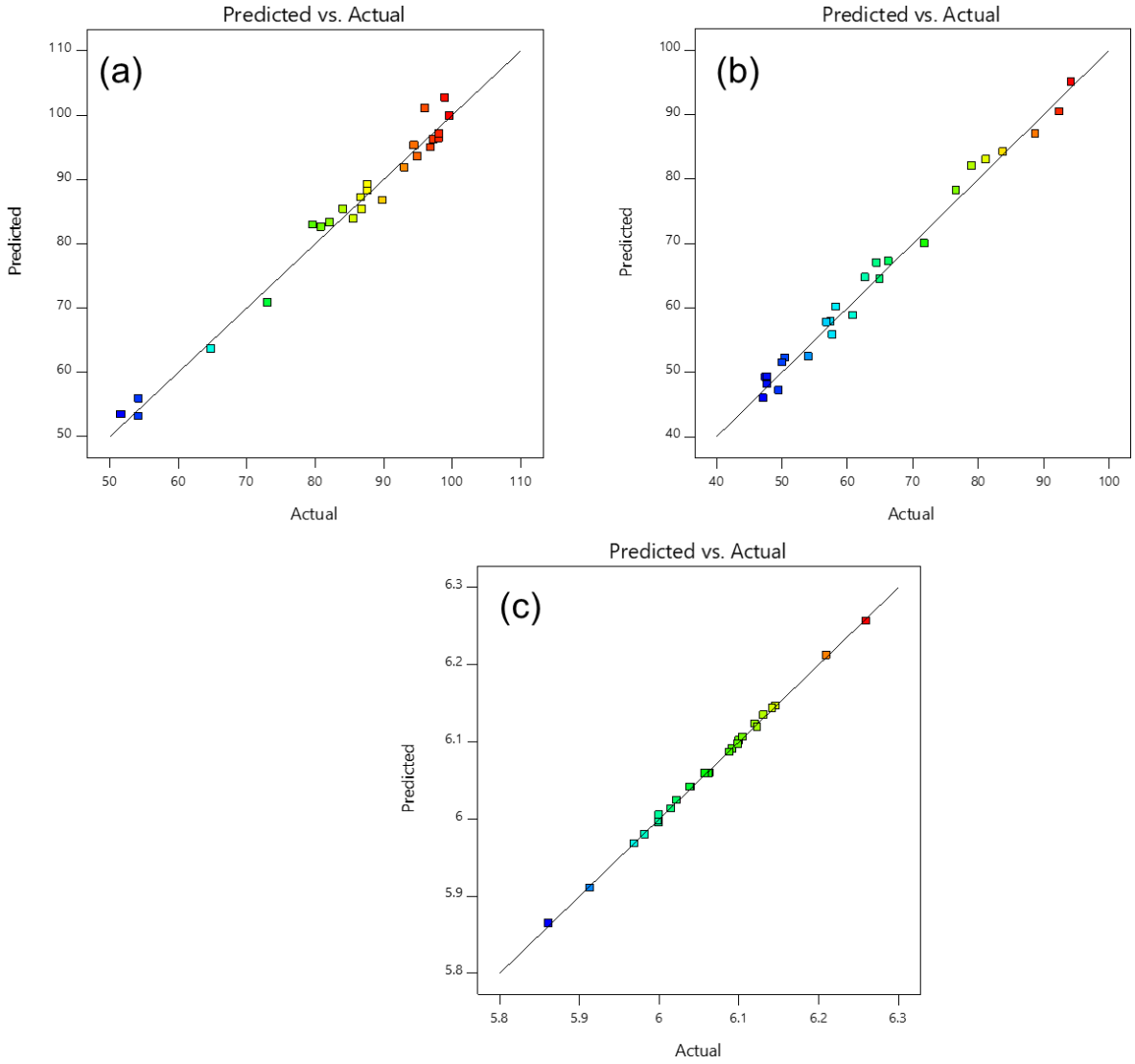

Figure 3.1 Plot of predicted vs. experimental values of GAA on (a) % grafting (b) % grafting efficiency (c) Adsorption capacity ($mg.g^{-1}$)

The three-dimensional (3D) surface response was used to understand the interactive relationships between preparation variables and the responses of the model [4]. In ***Figure 3.2***, a-3D response surface plots depict the significant interaction between the preparation parameters (concentration acrylic acid (AA), temperature, initiator (CAN) and time in accordance with the ANOVA ***Table 3.5***(a-c) are discussed. In ***Figure 3.2*** A, the contour graph shows increase in AA concentration to 1.1 increase the grafting % and when you increase the AA concentation above 1.1 it decreases the grafting %. The highest grafting % is obtained at CAN being 15 and AA concentration of 1.1. ***Figure 3.2*** B contour graph shows maximum time increased at 4 h increases the grafting % and ***Figure 3.2*** C contour graph shows highest grafting % at temperature 20 ℃. ***Figure 3.3*** A-C shows the contour graph whereby highest grafting

efficiency % is obtained at AA concentration of 0.5, CAN at 9, temperature at 70℃ and time at 4 h. Adsortion capacity showed no influence for both AA concentration and CAN. ***Figure 3.4*** A and B showed the adsorption capacity to be at the the maximum when CAN is at 15 and time at 0.5 min. adsorption capacity increased with increase in temperature at maximum of 70 ℃ (***Figure 3.4*** C). Time has more infulence on % grafting and grafting efficiency % (***Table 3.1***) and temperaturehas more influence on the adsorption capacity (***Table 3.5***). These observation proofs a significant impact on the grafting optimization as well as based on the F values presented on (***Table 3.5***) that time and temperature has influence on the adsorption capacity.

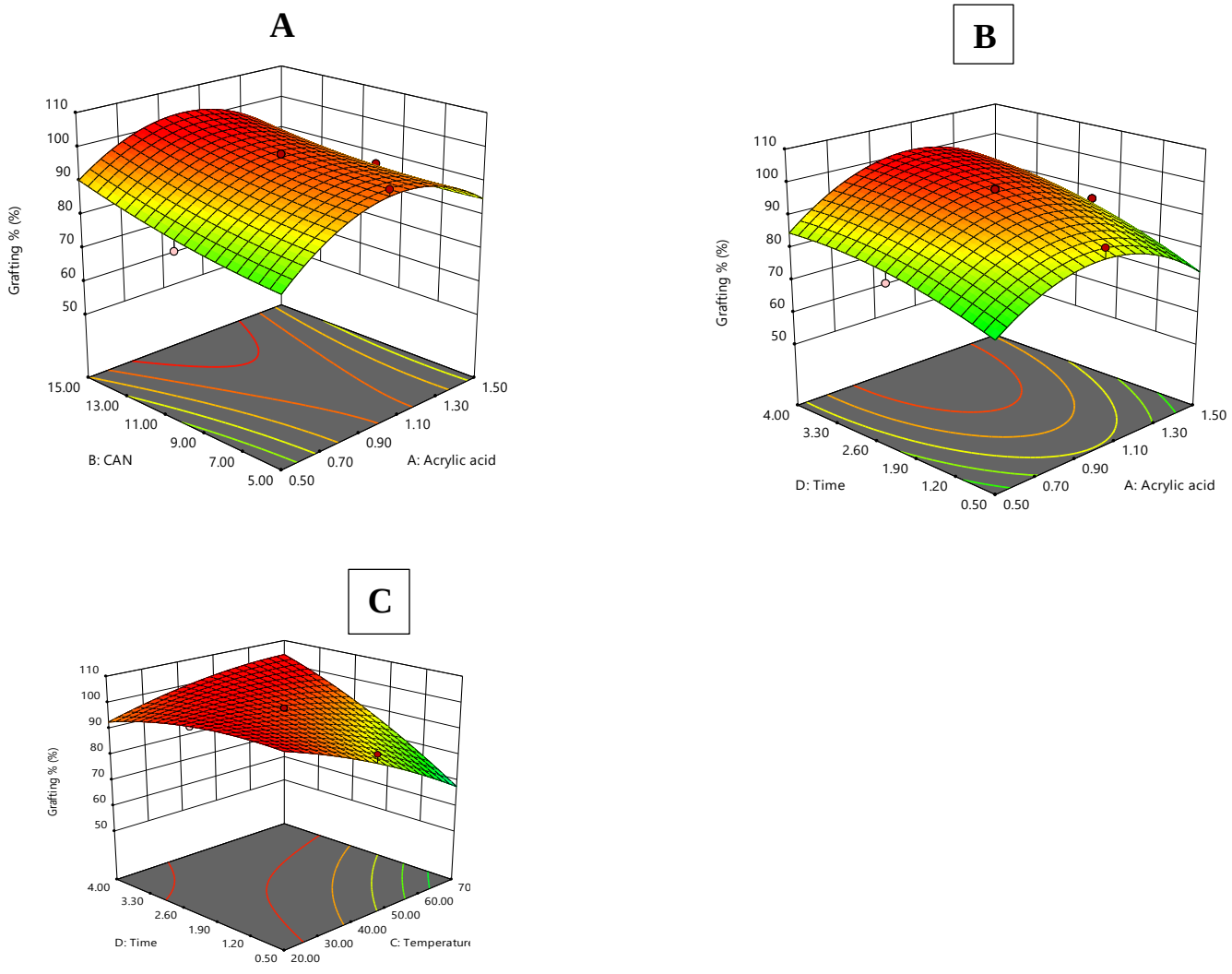

Figure 3.2 3D surface plots of interactions between (a) GAA and the grafting % (b) GAA and the grafting efficiency

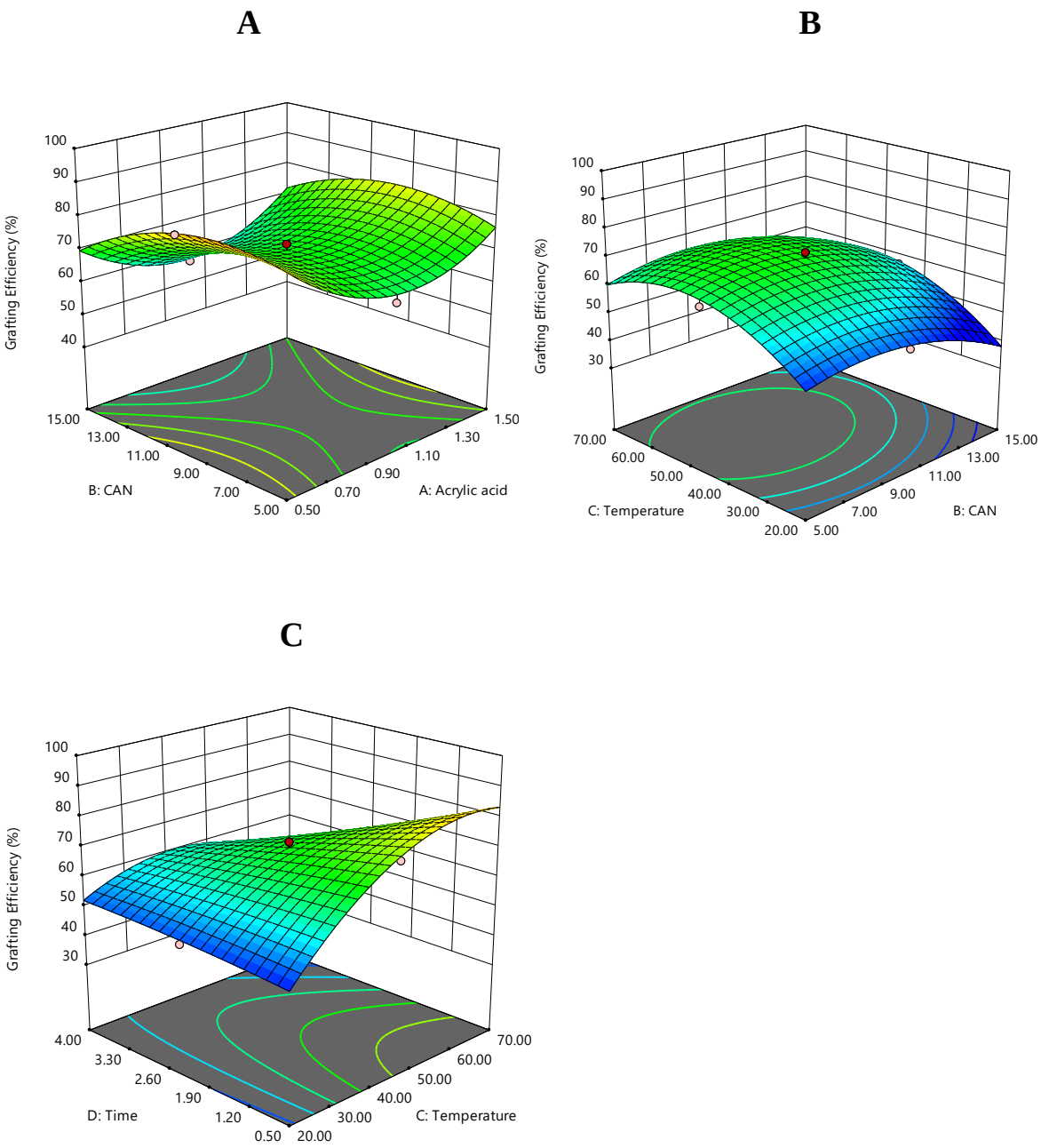

Figure 3.3 3D surface plots of interactions between (b) GAA and the % grafting efficiency

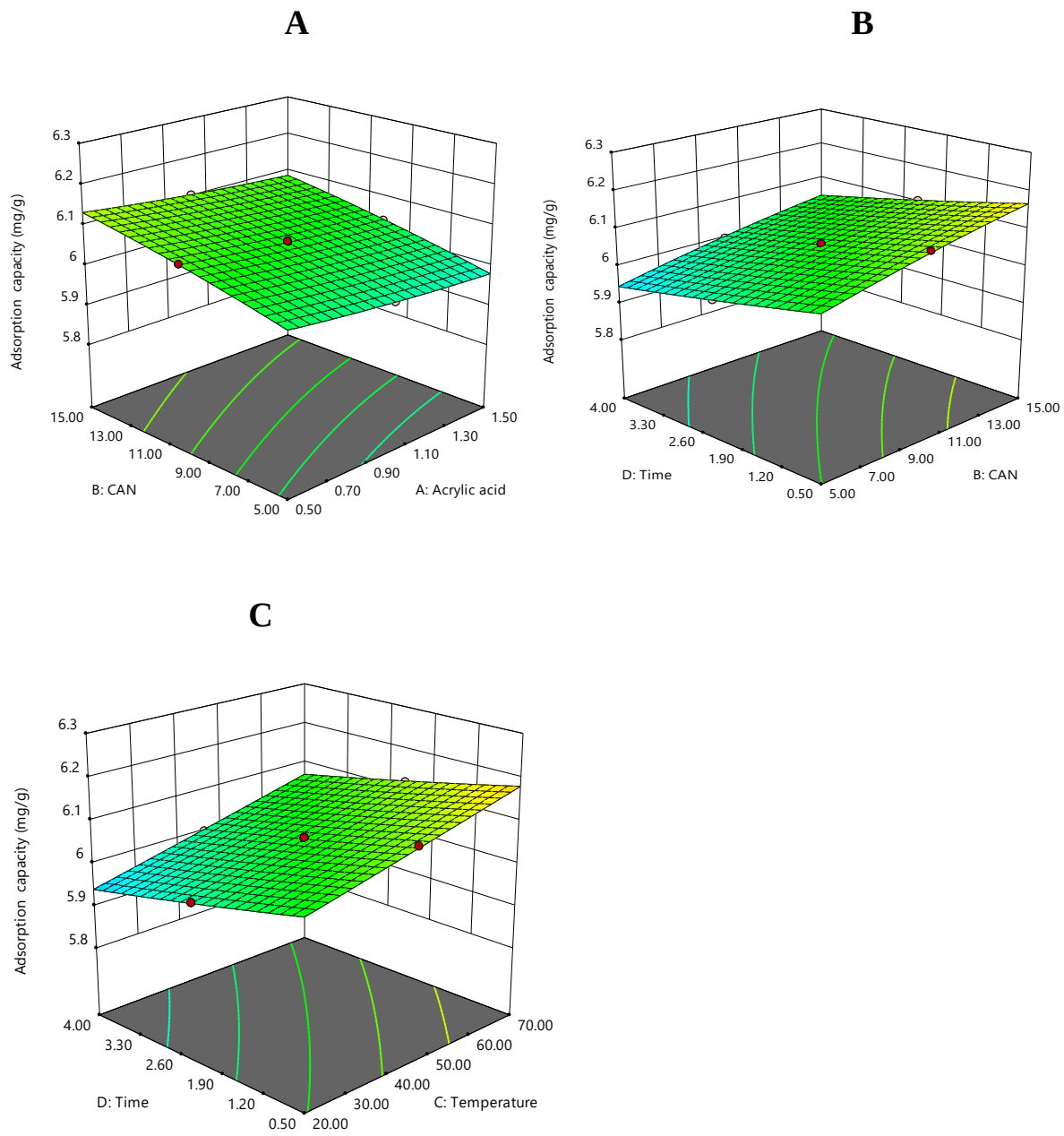

Figure 3.4 3D surface plots of interactions between (b) GAA and the adsorption capacity

3.4. Conclusions

The results show the successful preparation of grafting acrylic acid onto the PMC. The optimization conditions estimated by CCD for the grafting optimization were 1.5 mol.dm^{-3}, 15 mL CAN, 240 min for time and 70 ℃ for temperature. Discussion of results obtained in this chapter is carried out in subsequent chapters.

3.5. References

[1] W. Huang, X. Zhang, Randomized Smoothing Variance Reduction Method for Large - Scale Non - smooth Convex Optimization, SN Oper. Res. Forum. 2 (2021) 1–28. https://doi.org/10.1007/s43069-021-00059-y.

[2] J.E. Usen, S.S. Akpan, T.A. Ugbe, I.N. Ikpang, J.O. Uket, B.O. Obeten, Multivariate-Based Technique for Solving Multi-Response Surface Optimization (MRSO) Problems: The Case of a Maximization Problem, Asian J. Probab. Stat. 11 (2021) 60–85. https://doi.org/10.9734/ajpas/2021/v11i430275.

[3] I. Cahyadi, I.D. Anna, T. Prasetyo, Biomass Characteristics Optimization Design of Corn Cobs-Based Pellet Using Response Surface Methodology, SSRN Electron. J. (2021). https://doi.org/10.2139/ssrn.3793663.

[4] A.A. Savvides, M. Papadrakakis, A computational study on the uncertainty quantification of failure of clays with a modified Cam-Clay yield criterion, SN Appl. Sci. 3 (2021). https://doi.org/10.1007/s42452-021-04631-3.

CHAPTER 4

SYNTHESIS AND OPTIMIZATION OF REACTION VARIABLES IN THE PREPARATION OF PINE-MAGNETITE COMPOSITE FOR REMOVAL OF METHYLENE BLUE DYE[1]

4.1. Introduction

Dyes are known to be chemical compounds that can connect themselves to surfaces or fabrics to impart color. They are mostly used in textile, paper printing, carpet, plastic, food and cosmetic industries. It has been estimated that total dye consumption in the textile industry worldwide is more than 10 000 tons per year. It is known that 10–15% of these dyes are released as effluents during the dyeing process [1,2]. Dye bearing effluent is a significant source of water pollution. Discharge of colored wastewater without proper treatment can result in numerous problems such as chemical oxygen demand (COD) by the water body, and an increase in toxicity. Major problems associated with colored effluent are lowering light penetration, photosynthesis and damaging the aesthetic nature of the water surface [3,4]. Moreover, their degradation products may be mutagenic and carcinogenic [5–7]. For instance, many dyes may cause allergic dermatitis, skin irritation, dysfunction of kidney, liver, brain, reproductive and central nervous system [8]. Industrial effluents is influenced by rapid growth of the world population, industrialization and unplanned urbanization, agricultural activities as well as the excessive use of chemicals which have contributed to environmental pollution [9]. Pollutants that are of primary concern include metals, dyes, biodegradable waste, phosphate and nitrates, heat, sediment, fluoride, hazardous and toxic chemicals, radioactive pollutants, pharmaceuticals and personal care products [10,11]. Trace amounts of any of these compounds have been found leading to major pollution problems and consequently, the treatment of wastewater is of universal importance. Some techniques have been used to decrease methylene blue concentration in wastewater. Chemical oxidation, coagulation, flocculation, ozonation, electrochemical, fungal decolorization, and adsorption are techniques used by scientists [12]. Above it all, adsorption is a process technique which is still used because of its low cost, simplicity, and efficiency. Granulated activated carbon (GAC) or

[1] Chapter published with the South African Journal of Chemical Engineering DOI: https://doi.org/10.1016/j.sajce.2019.05.002

powdered activated carbon (PAC) has been widely used as adsorbent, however it is expensive and difficult to regenerate [14]. Other adsorbents used because of their low cost are waste orange peel, banana bith, cotton waste, bentonite clay, neem leaf powder, powdered activated sludge perlite, bamboo dust, and sewage dust [15]. Although these adsorbents do not imply high cost, they may be used for other purposes.

In the present research, pine-magnetite composite was used as an adsorbent to test its usefulness and learn its adsorption capabilities. It is abundant, cheap, effective and can be regenerated [13]. As there are many factors that affect dye adsorption, the adsorption of dye by using pinecone was conducted employing varying parameters such as temperature, mass time volume NH_4OH and initial concentration.

The study results led to potential application to solve two waste problems: (a) annual generation of large quantities of pinecone in South Africa for which there's no current use, and (b) the treatment of polluted water generated by the textile industry.

4.2. Materials and methods

4.2.1. Preparation of pinecone powder

Pinecones are naturally occurring agricultural waste, a plantation in Vanderbijlpark, Gauteng, South Africa. All the following chemicals used were of analytical grade $Fe_2(SO_4)_3.4H_2O$, $FeSO_4 \cdot 7H_2O$, NH_4OH, NaOH, methylene blue supplied by Merck, South Africa. Nitrogen gas supplied by Afrox.

The pinecones were washed with deionized water to remove impurities and some volatile organics such as resin acids without destroying the cone matrix. The pinecone scales were peeled and crushed to a powder using a pulverizer and then sieved. The washed cones were then dried at 90 °C for 48 h in an oven. The pinecone powder (PCP) was subsequently sieved and particles of size of 45–90 μm were then used in the experiments.

A weighed amount (50 g) of the powder was mixed with 500 cm^3 of 0.15 $mol.dm^{-3}$ sodium hydroxide solution and the slurry stirred for 18 h at room temperature. The solution mixture was rinsed with 500 cm^3 of distilled water, a procedure that was repeated four times to remove sodium hydroxide from the suspension. The filtrate was then dried overnight at 90 °C.

4.2.2. Synthesis of pine-magnetite composite

A mixture of $FeSO_4.7H_2O$ (2.1 g) and of $Fe(SO4)_3.XH_2O$ (3.1 g) were dissolved under inert atmosphere in 100 cm^3 of double-distilled water with vigorous stirring. Thereafter, 20 cm^3 of 28% ammonium hydroxide and the appropriate amount of pine powder was added. The reaction was left to run for 45 min at 80 °C under constant stirring. The resulting particles, consisting of magnetite attached to the cellulose (hereafter referred to as bio-composite) were washed several times with deionized water and ethanol and dried in a vacuum oven at 60 °C overnight. To determine the optimum conditions to achieve the desired production of the bio-composite, we experimented with the following variables: volume of NH_4OH 5, 10, 20, 30, and 40 cm^3; weight of pine powder 1.0, 1.5, 2.0, 2.5, 3.0 and 3.5 g; temperature 40, 60, 80 and 100 °C; reaction time 15, 30, 45 and 60 min.

4.2.3. Characterization of the bionanocomposite

4.2.3.1. *Fourier transform infrared analysis*

Qualitative and fundamental identification of the functional chemical groups of pinecone treated with NaOH and the bio-composite were analyzed with a Perkin- Elmer Fourier transform infrared (FTIR) in the range 450–4000 cm^{-1}. The FTIR spectra of NaOH treated pinecone and the bio-composite were recorded.

4.2.3.2. *X-ray diffraction analysis*

XRD analysis was done to identify the chemical composition and crystallographic structure of the cellulose powder magnetite. An X'Pert PRO X-ray diffractometer (PANalytical, PW3040/60 XRD; CuKα anode; λ = 0.154 nm) was used for XRD patterns. The samples were placed in an aluminum holder and scanned at 45 kV and 40 mA from 10° to 120° 2θ, the exposure time for each sample was 20 min and a step size of 0.02°. The Debye Scherrer equation (Burton et al., 2009) was used to determine particle sizes of the bio-composite.

4.2.3.3. *Transmission electron microscopy analysis*

The morphology and size of the synthesized particles were observed using transmission electron microscope (TEM, FEI TECNAI G^2 SPIRIT) at an accelerating voltage of 150 kV. Samples were prepared by placing drops of diluted ethanol dispersed of nanocrystalline on the surface of copper grids.

4.2.3.4. *Thermal gravimetric analysis*

Thermogravimetric analysis (TGA) was used to determine weight loss as a function of temperature. Changes of the pinecone matrix were determined due to the different chemical treatments because each kind of biomass has a characteristic pyrolysis behavior explained based on its individual component characteristics. Pyrolysis of cone samples were done from 30 to 900 °C in a N_2/air atmosphere at a heating rate of 10 °C.min^{-1} using a PerkinElmer (USA) Simultaneous Thermal Analyzer 6000 instrument.

4.2.3.5. *Adsorption and kinetic studies*

Adsorption studies were performed by batch technique to obtain rate and equilibrium data. Various Methylene Blue (MB) solutions with different pH range, initial concentrations and mass dosage were prepared by diluting 1000 mg.dm^{-3}. Equilibrium experiments, to determine the adsorption capacity of pine-magnetite composite were conducted using 250 cm^3 bottles. 0.1 g of PMC and 100 cm^3 of the MB solution were added and shaken for 2 h at 26 °C. Thereafter, absorbance was determined using UV-VIS spectrophotometer at the wavelength corresponding to the maximum absorbance (λ_{max} = 665 nm) as determined from the plot. This wavelength was used for measuring the absorbance of residual concentration of MB. pH of the solution was adjusted using 0.1 M HCl and 0.1 M NaOH.

Batch contact kinetic experiments were performed by contacting 0.1 g of the adsorbent material with 100 cm^3—of MB solution of concentrations (100, 150, 200, 250 and 300 mg.dm^{-3}). The solution was agitated for 120 min which has been previously shown to be sufficient time to reach equilibrium at a constant stirring speed of 200 rpm and temperature of 26 °C. Aliquots (0.1 cm^3) of sample was drawn at suitable time intervals and were analyzed using UV-VIS spectrophotometer. 5. Results and discussion

4.3. Results and Discussions

4.3.1. Fourier transform infrared analysis

The FTIR spectrum of NaOH treated pinecone is shown in ***Figure 4.1 (a)***. FTIR showed different organic functional groups. A broad intense spectrum at 3313.5 cm^{-1} corresponding to

the stretching vibration of –OH assigned to –OH by Fe_3O_4 nanoparticles is observed [16]**.** The peak observed at 2895.5 cm^{-1} represents the aliphatic C–H group, the one at 1600.3 cm^{-1} corresponds to C=O stretching [17], the peak at 1269.9 cm^{-1} shows aromatic –OH and at 1020.6 cm^{-1} correspond to C–O–C stretching [16]. In ***Figure 4.1(b)*** FTIR spectra represent the pine-Fe_3O_4 magnetite or pine-magnetite composite (PMC). FTIR spectra showed some changes in band intensities, indicating the functional groups on the surface had been modified. A compressed –OH peak with an increase in intensity at 3313.5 cm^{-1} is observed, it is an indication of possible extraction of lignin present in the pinecone, COO- peak is converted to esters, C–H aliphatic peaks are observed at 1415.2 cm^{-1} which represent the increase in the internal surface of the pinecone and there is a new peak at 557.2 cm^{-1} assigned to the vibration of Fe–O band of Fe_3O_4 [18].

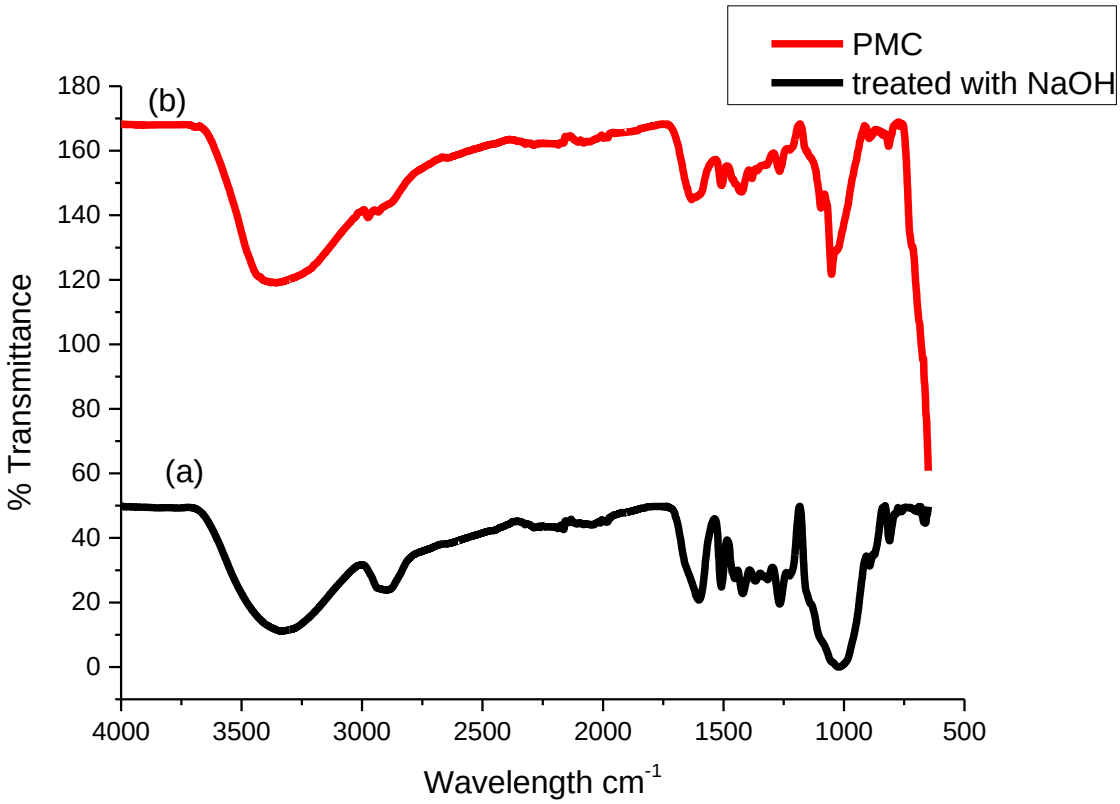

Figure 4.1 FTIR spectra for (a) treated pinecone and (b) Pine-magnetite composite

4.3.2. X-ray diffraction analysis

X-ray diffraction analysis was used for structural determination and estimation of crystallite size of the bio-composite as shown in ***Figure 4.2***. The XRD pattern was contributed by

crystalline and amorphous cellulose in the lignocellulosic material. Prominent peaks were observed at 2θ values of 27.5°, 28.7° and 32.0° corresponding to the cellulose. The XRD spectra of the samples optimized for NH_4OH volume, pinecone mass, temperature and time of reaction showed the diffraction peak at 2θ = 41.0°, 45,4°, 43.20°, 50.49°, 53.9°, 58,5°, 59.8°, 65.3°, 76.6° and 84.7° which correspond to the lattice indices for the Fe_3O_4 magnetite [19]. Crystalline size for PMC is 11.6 nm.

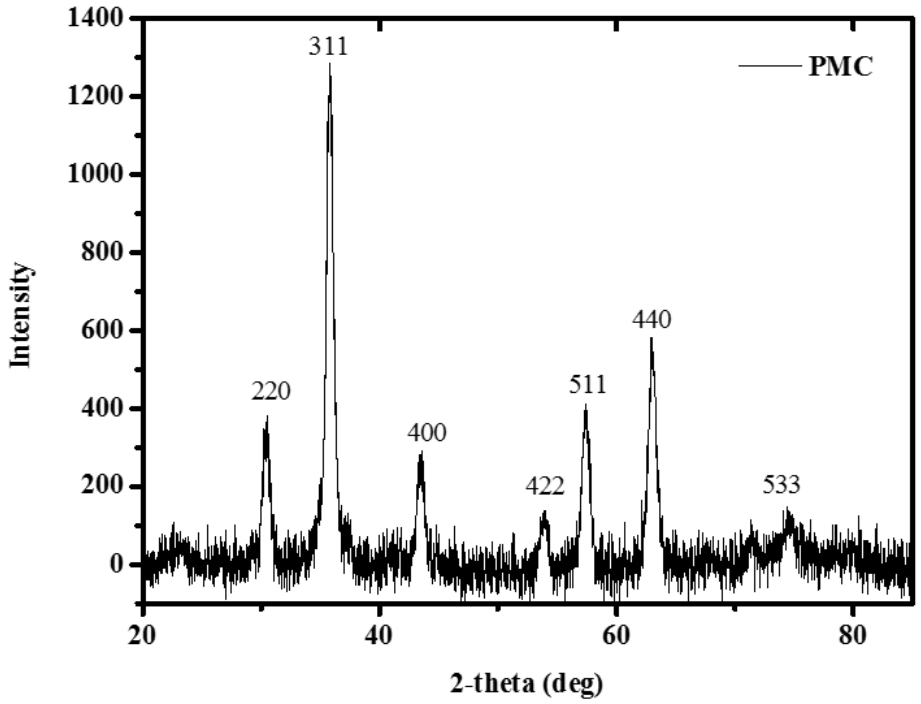

Figure 4.2 XRD spectrum of pine-magnetite composite.

4.3.3. Transmission electron microscopy analysis

The TEM image in ***Figure 4.3***(a) shows the appearance of the synthesized pine magnetic composite, as spherical nanoparticles. ***Figure 4.3*** (b) shows the size distribution of the pine-magnetite particle (PMC) and that the mean particle size is 14.0 ± 3.20 nm. In addition, the particle size range for PMC is 6 – 24 nm. Modal particle size range for PMC is in the range 14 – 16 nm and accounts for 23% of the nanoparticle count.

A B

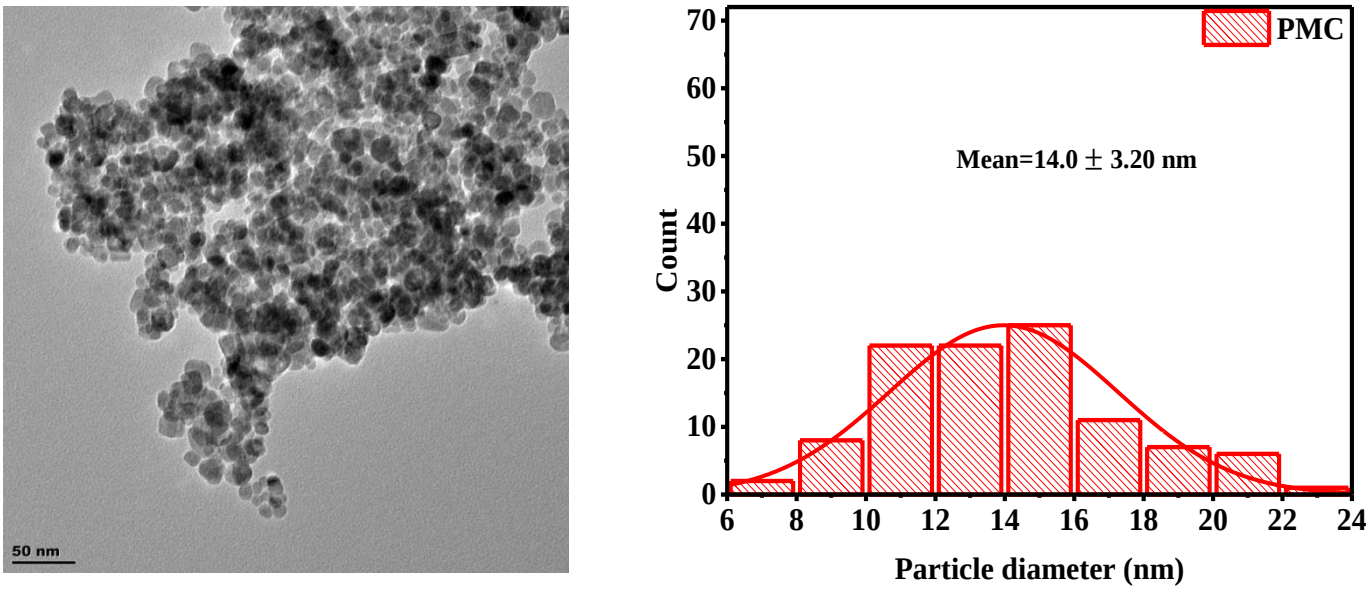

Figure 4.3 (a) TEM image and (b) size distribution of pine-magnetite particles

4.3.4. Thermal gravimetric analysis

The thermal degradation of the pinecone biomass occurred in three stages [20]**:** (a) moisture evolution from 30 to 150 °C, (b) hemicellulose and cellulose decomposition from 200 to 350 °C, and (c) lignin decomposition from 160 to 700 °C. The weight loss focused in the temperature range 200–400 °C. ***Figure 4.4*** (a) shows the comparison in thermogravimetric curves for raw, treated and modified pine composite, Temperature at 30–150 °C corresponds to evaporation of water, showing the hygroscopic nature of the pinecone biomass surface [18]. The thermal degradation in the region 200–350 °C is attributed to hemicellulose and cellulose degradation. Hemicellulose decomposes at relatively low temperatures due to their random and amorphous structure [21–23]. Their decomposition took place from 200 to 310 °C with maximum rate of weight loss rate at 270 °C. Cellulose decomposition took place from 310 to 350 °C, with maximum weight loss rate around 330 °C. Temperature at 160–700 °C corresponds to lignin degradation. Differential thermal analysis (DTA) shows endothermic peaks associated with degradation of various materials (***Figure 4.4 (b)***). Observation at different temperatures confirms the stabilizing effect of the presence of Fe_3O_4 on the composite. The treated pine proved to be less stable than the raw pine due to the surface adsorption of the Fe_3O_4. The content for pine-magnetite composite was calculated as follows:

$$PMC\ wt.\% = \frac{1-L_{total}}{1-L_{water}} \times 100$$ **Equation 4.1**

Where L total and L water are total weight loss and weight loss from water respectively. It was calculated that the real content of PMC synthesized is 58 wt.% also for raw pine 21.3 wt.% and NaOH treated pinecone 26.9 wt.% respectively.

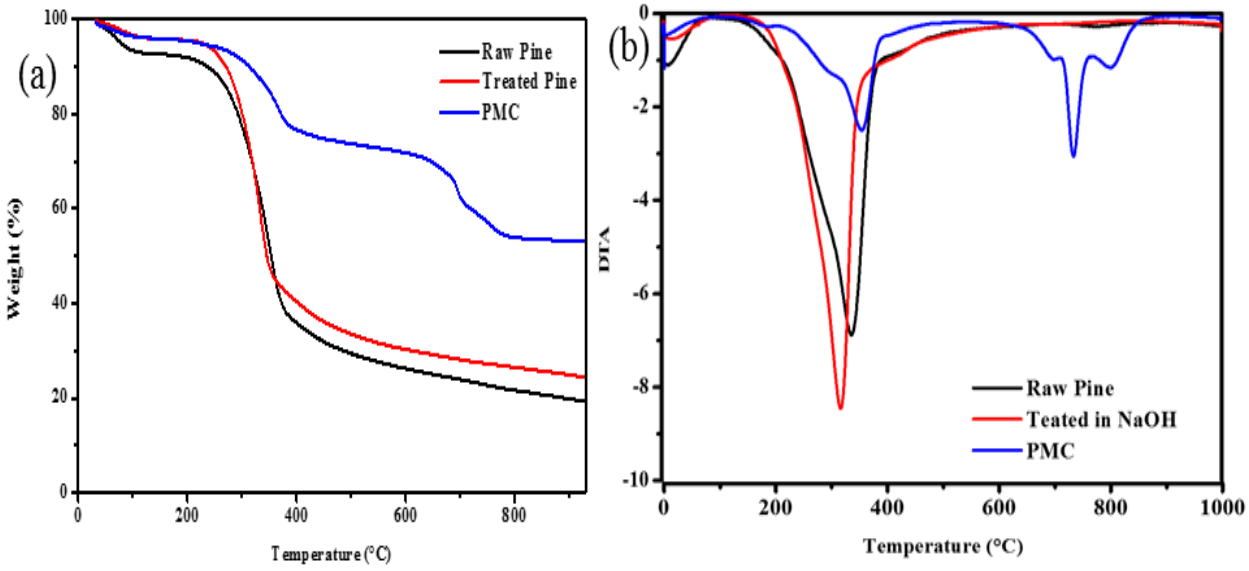

Figure 4.4 (a) TGA curve of raw, treated, and modified pine-magnetite composite, (b) DTA curve of raw, treated pine and modified pine-magnetite composite

4.3.5. Surface properties

Table 4.1 is an indication of the effect of modification on surface area of the materials. The pure pine-magnetite nanoparticles showed a surface area of 113.60 $m^2.g^{-1}$ pore volume of 0.6321 $cm^3.g^{-1}$ and pore size of 25.86 nm the NaOH treated pine had surface area of 2.25 $m^2.g$, pore volume of 0.0177 $cm^3.g^{-1}$ and pore size of 10.17 nm. Pine-magnetite composite exhibited surface area of 54.80 $m^2.g^{-1}$, pore volume of 0.1522 $cm^3.g^{-1}$ and pore size of 23.10 nm.

The higher the surface area may be due to the pinecone structure, attributed to smaller size of the PMC bio-composite. Such high surface area will be important for the improvement of mass diffusion and adsorptive capacity. These results confirm that extraction of the pinecone organic component occurred.

Table 4.1 BET surface area and pore characteristics for synthesized materials.

Properties	Pure Magnetite nanoparticles	NaOH treated Pine	Pine-magnetite Composite (PMC)
Surface area ($m^2.g^{-1}$)	113.60	2.25	54.80
Pore volume ($cm^3.g^{-1}$)	0.6321	0.0177	0.1522
Ave. pore size (nm)	25.86	10.17	23.10

4.3.6. pH at point zero charge (pH_{pzc})

To further investigate the effects of modifications on the suitability of the synthesized materials for adsorption, the isoelectric point or point of zero charge (pH_{PZC}) was determined. The solution pH is an important parameter for dye adsorption because it does not only change the surface charge of the adsorbent but also it affects the molecule structure of the dye. As methylene blue is a cationic dye, it can easily form positively charged species over a wide pH range. At the isoelectric point, the net surface charge is 0 therefore, the material is neither negatively nor positively charged and is effectively neutral. Below the isoelectric point, the surface possesses a positive charge and attracts negatively charged ions through electrostatic attraction. Above the point of zero charge, the surface has a net negative charge hence attracting positively charged ions. The point of intersection of the resulting curve at which $\Delta pH = 0$ gave 8.56 as the pH_{pzc} for the pine-magnetite composite.

4.3.7. Vibrating sample magnetometer (VSM)

Figure 4.5 shows the saturation magnetization of PMC. Magnetic separation enjoys the advantages of effectiveness and rapidness compared to the traditional solid-liquid separation method. Magnetic behavior of the nanoparticles was characterized at 25 °C using a Quantum Design MPMS-7, measuring the applied field dependence of magnetization between −15 and 15 kOe. Where the biomass reacted with magnetite. Low coercivity confirmed that nanoparticles are superparamagnetic. The reduction in saturation magnetization may be due to the interaction of organics from the pinecone with iron oxide and the reduced primary size of the magnetite material.

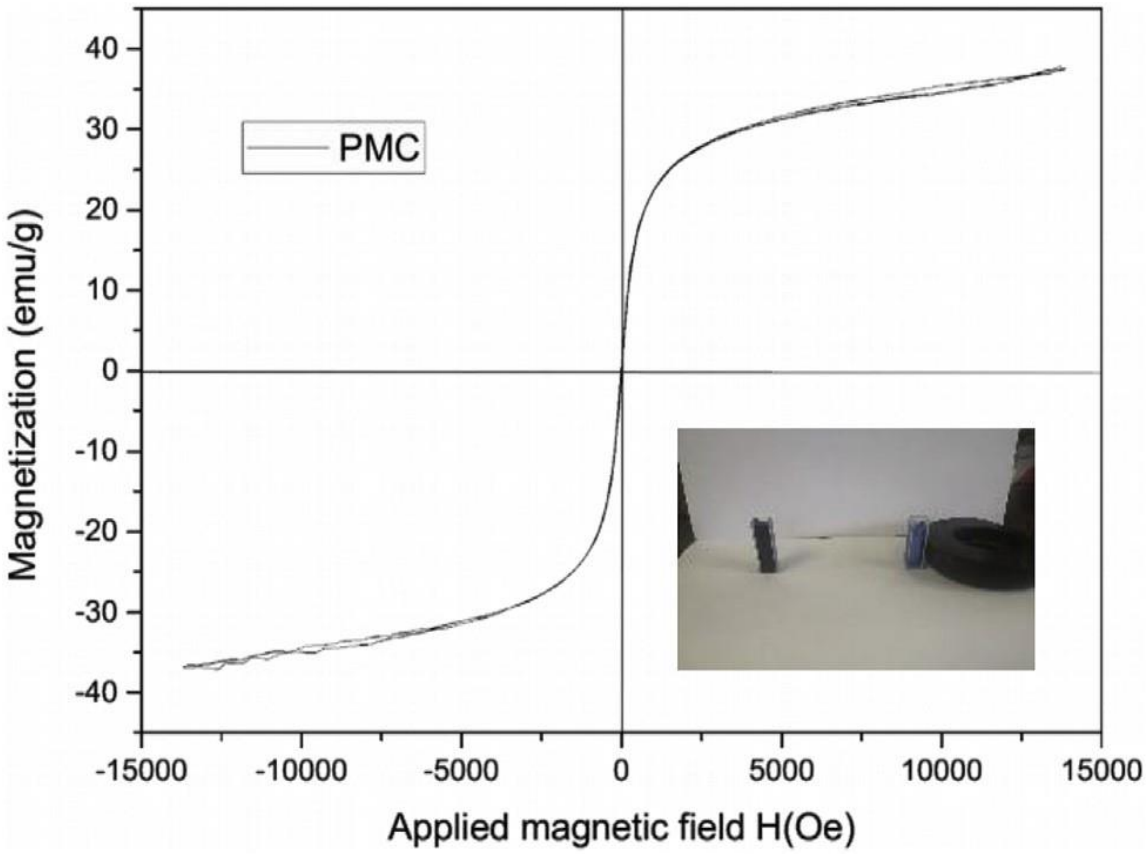

Figure 4.5 Saturation magnetization of PMC

4.4. Optimization of the reaction conditions

4.4.1. Effect of NH_4OH volume and pinecone powder mass

Figure 4.7(a) shows investigation of the influence of volume NH_4OH which was varied from 5, 20, 30, 35 and 40 cm^{-3} (***Figure 4.7***). The pH of the reaction solution is important in the production of nano particles by a co-precipitation method [24]. The formation of nano-Fe_3O_4 in the co-precipitation reaction of Fe^{3+}/Fe^{2+} involves phase transformation of iron oxyhydroxides rather than a direct reaction between Fe^{3+} and Fe^{2+} in aqueous solution [25]. In addition to the required amount of NH_4OH to the mixture there is formation between two contact interfaces between the iron solution and NH_4OH solution at the initial stage for a short period. This phase represents a low pH Fe^{3+}-rich phase, which reacts with NH_4OH and increase the solution pH and convert the less stable Fe^{3+} into akaganeite (β-FeOOH) and further transformation of akaganeite to goethite (α-FeOOH) as described in equations (1) and (2). In the high-NH_4OH region, Fe^{2+} is converted to ferrous hydroxide as described in equation (3). These two nucleation processes are initiated in solution to produce nano particles of Fe_3O_4 in

equation (4). According to Lian et al. (2004) the mechanism of formation of nano-Fe_3O_4 from the mixture of Fe^{3+} and Fe^{2+} is as follows:

$$Fe^{3+}+3OH^{-}\rightarrow Fe(OH)_3 \quad (1)$$

$$Fe(OH)_3\rightarrow FeOOH+H_2O \quad (2)$$

$$Fe^{2+}+2OH^{-}\rightarrow Fe(OH)_2 \quad (3)$$

$$Fe(OH)_2+2FeOOH\rightarrow Fe_3O_4+2H_2O \quad (4)$$

Under these reaction conditions, akaganeite growth is suppressed while goethite formation is strengthened, therefore goethite and ferrous hydroxide are the major intermediates controlling the phase transition and particle size [25]**.** Sun et al. (2014), suggested that nano-Fe_3O_4 nucleation increases below solution pH 11, while above pH 11 the growth of nano-Fe_3O_4 nucleus prevails producing particles of larger sizes [26]. We observed a gradual increase from 5 to 35 cm^{-3} and a decrease afterwards. The 35 cm^{-3} was taken as the optimum volume for NH_4OH. The influence of the pine mass is shown in ***Figure 4.7***(b). The effect of pinecone mass on the reaction of Pine-Fe_3O_4 magnetite was performed by adding different masses (1.0–3.5g) of pinecone in 80 cm^3 of double distilled water containing iron salts and 35 cm^3 NH_4OH at 80°C. The initial decrease in particle size may be due to increase stabilization of the Fe_3O_4 nucleus by the cellulose and lignin fraction of the pinecone as mass is increased from 1.0 g to 1.5 g [27]. Increase in pine mass at constant amounts of iron salts and volume of NH_4OH above 1.5 g gave rise to aggregation of the large pinecone particles and eventually increases in final particle size.

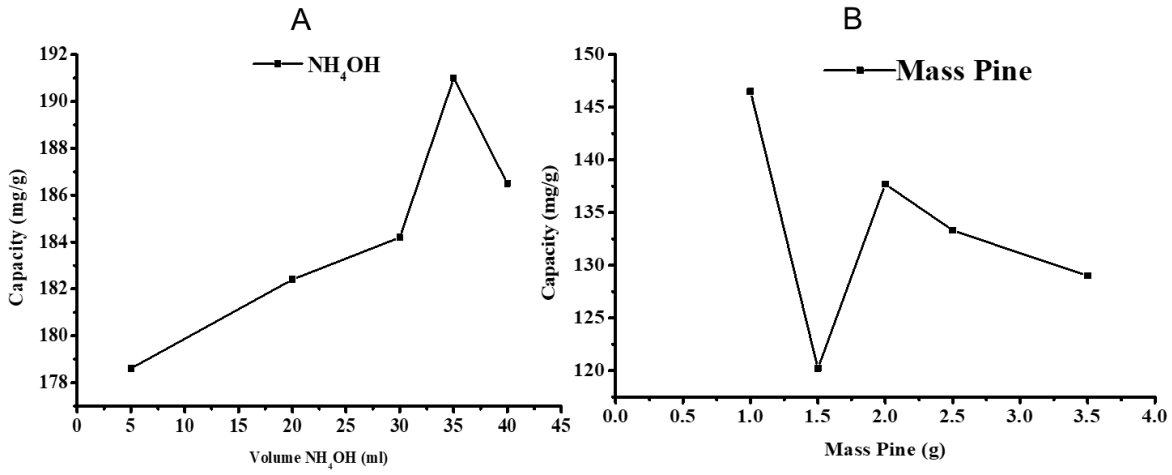

Figure 4.6 a) Influence of NH_4OH volume on adsorption of methylene blue; (b) influence of pine mass dose on adsorption of methylene blue

4.4.2. Effect of reaction temperature and contact time

The influence of the reaction temperature and contact time is shown in ***Figure 4.7*** (c) and (d). The effect of reaction temperature on the formation of nano-Fe_3O_4-pinecone composite was studied in a reaction mixture containing 1.5 g of pine in a solution of iron salts with 35 cm^3 of NH_4OH at temperatures ranging between 40 and 100 °C. Increasing temperature increases the rate of interaction between the functional groups on the pinecone and the nano-Fe_3O_4 nucleus, which stabilizes the nano-Fe_3O_4 particles keeping their sizes small [27]**.** When temperature was increased above 60°C, the growth of nanoFe_3O_4 nucleus (aggregation) was encouraged [26]**.** The effect of reaction temperature on the formation of nano-Fe_3O_4 pinecone composite was studied in a reaction mixture containing 1.0 g of pine in a solution of iron salts with 35 cm^3 of NH_4OH, at 80°C. ***Figure 4.7*** (d) showed that a longer time of mixing gives a higher displacement of methylene blue contact time ranging from 15 min to 60 min was also studied from determination of absorbance. After the required volume of NH_4OH and 1.0 g of pinecone was added to the solution of iron salts at 80°C, different time intervals were allowed for the precipitation to occur. As contact time increased from 15 to 60 min, we observed that short contact time of the reaction means few amounts of nano-Fe_3O_4 nucleation occurred. Therefore, the fewer the nano-Fe_3O_4 coverage, the larger the particle size of the bionanocomposite. At 45 min optimum contact time of methylene blue was observed.

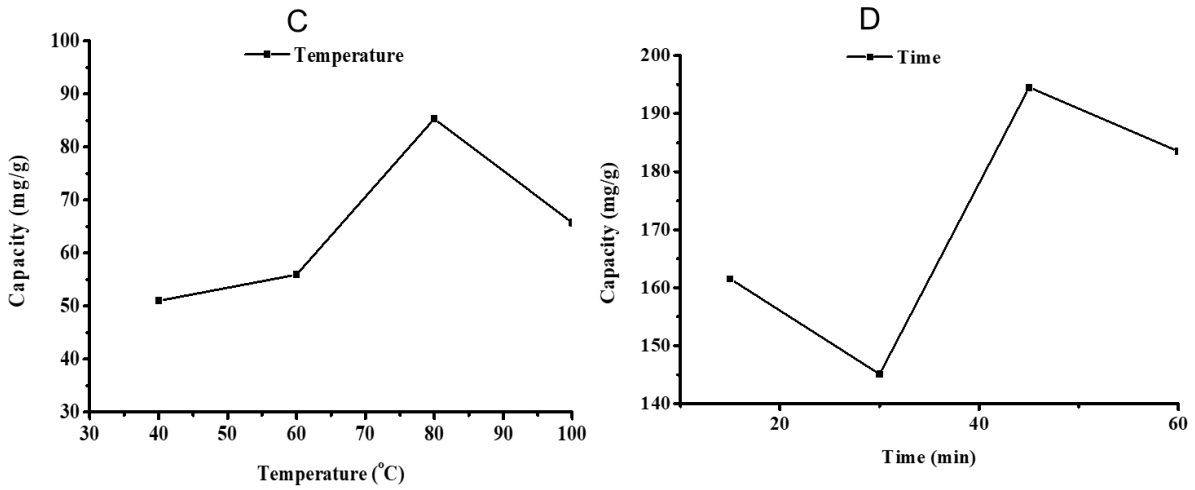

Figure 4.7 Influence of temperature on the adsorption of methylene blue (d) Influence of time on the adsorption of methylene blue

4.4.3. Effect of the initial concentration

Figure 4.8 shows the influence of the initial concentration on the adsorption of methylene blue. There was a rapid increase in adsorption capacity from157 to 168 $mg.g^{-1}$in the concentration range100 to 200 ppm and then a sharp decrease afterwards. We reason that when the adsorbent loading increases past 200 ppm, the interparticle forces between the nanoparticles increases such that there is an overall attraction between them, a phenomenon which results in agglomeration of the adsorbent.

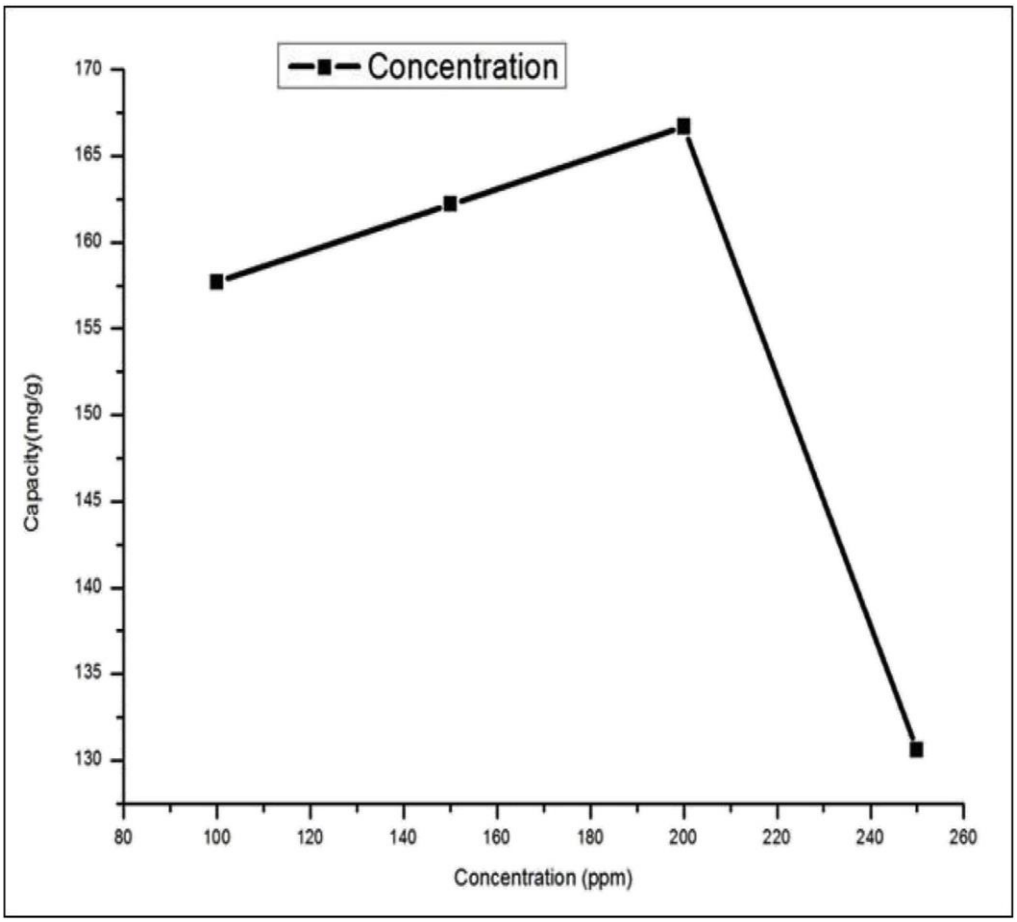

Figure 4.8 Influence of temperature on the adsorption of methylene blue

4.4.4. X-ray fluorescence (XRF) analysis

Figure 4.10 (a and b) show XRF results on NH_4OH volume and mass dose on the pine-magnetite composite. The percentage of iron oxide determined for NH_4OH volume of 35 cm^{-3} was found to be the highest at 76.5% and mass dose of 1 g at 78.2%. ***Figure 4.10*** (a and b) show the effect of temperature and contact time confirmed by XRF analysis. Temperature was found to be highest with 75.4% at 80°C and contact time highest with 78.3% at 45 min. XRF

confirmed the optimum values of volume NH_4OH, mass of pinecone powder, reaction temperature and contact time due to the highest iron oxide percentage present on the pine-magnetite composite.

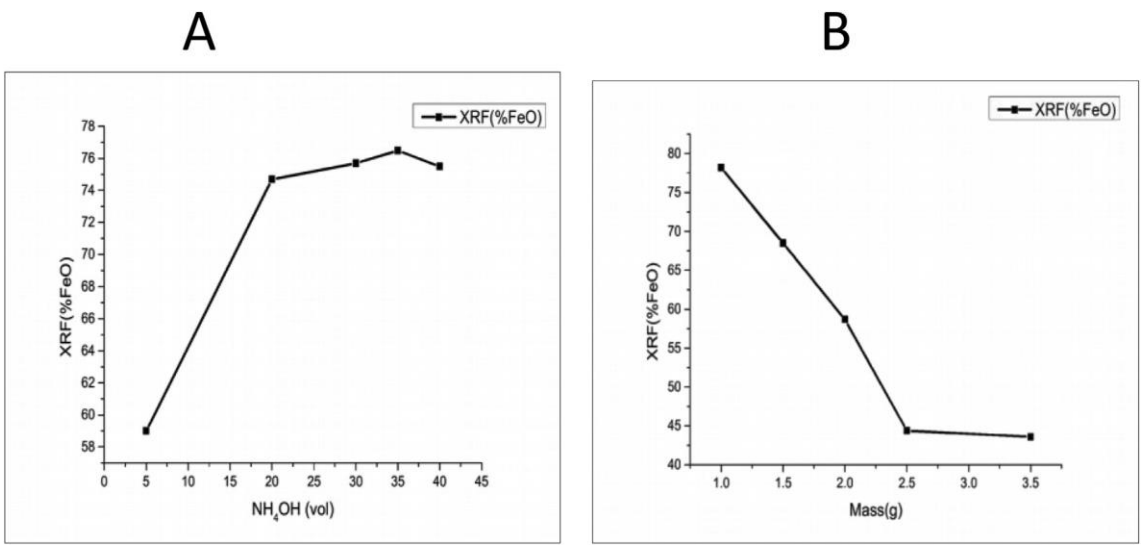

Figure 4.9 (a) XRF on NH_4OH volume and (b) XRF on mass dose of pine-magnetite composite.

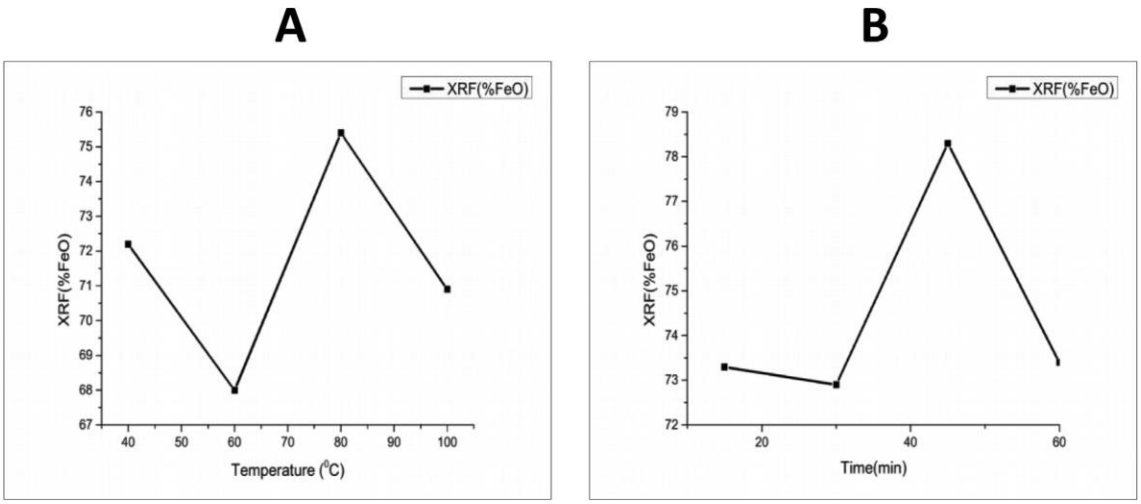

Figure 4.10 (a) XRF on reaction temperature and (b) XRF on contact time of pine-magnetite composite.

4.4.5. Adsorption studies for PMC

The magnitude of electrostatic charges imparted by the ionization of metal ions and the functional groups on the adsorbent surface are primarily controlled by pH of the medium.

Figure 4.11 shows the effect of pH on the adsorption of methylene blue. The increase in pH showed the increase in percentage removal. This is because at pH above 7 there is an abundance of ^{-}OH ions in the solution which are repelled by the lone pairs of electrons on magnetite. MB, on the other hand, being cationic and remaining as an ion in the solution will have an electrostatic attraction from the magnetite. At pH 12 we observed that there is a high percentage removal for methylene blue compared to any other pH value. ***Figure 4.11*** shows the effect of adsorbent dose on the percentage removal and amount of dye adsorbed. It is apparent that by increasing the dose of the pine-magnetite composite, the number of adsorption sites available for adsorbent-solute interaction is increased, thereby resulting in the increased percentage dye removal from solution.

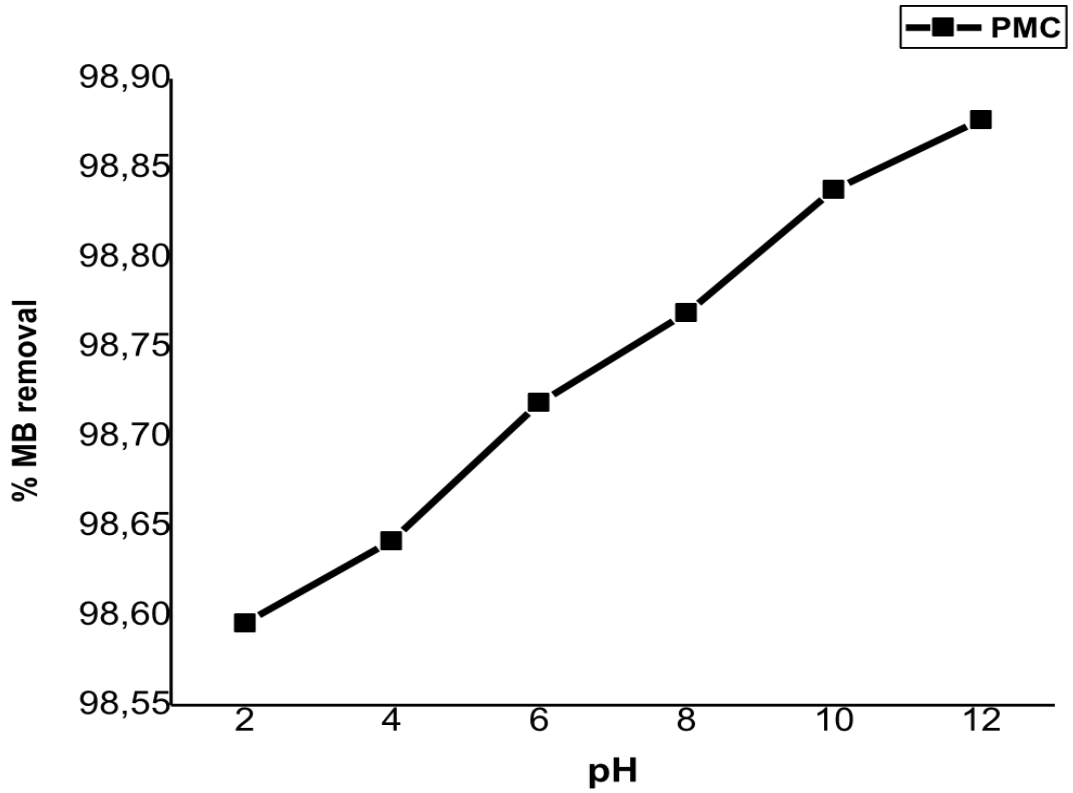

Figure 4.11 Effect of solution pH on the adsorption of methylene blue.

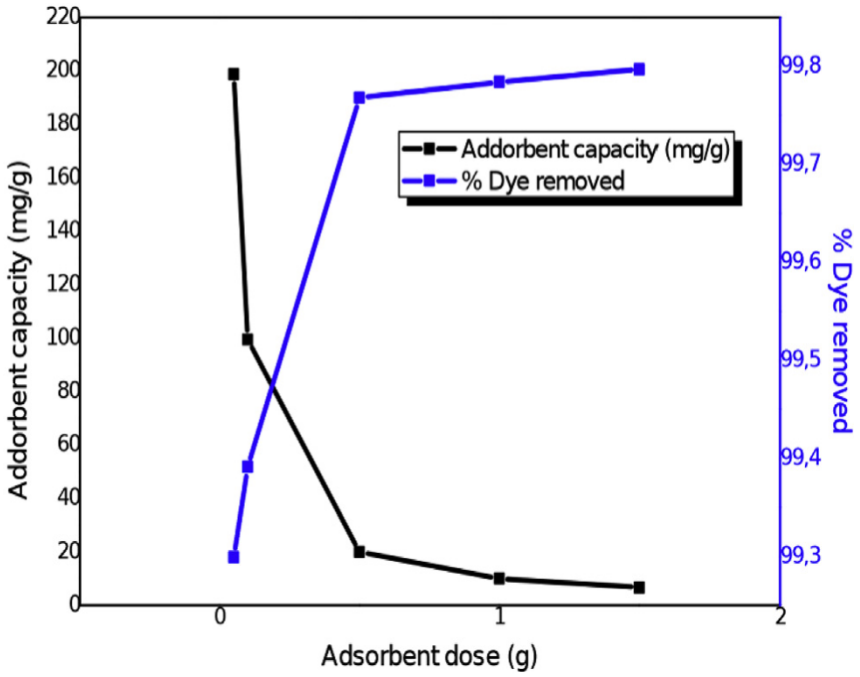

Figure 4.12 Effect of adsorbent dose on the percentage removal amount of dye adsorbed.

4.4.6. Adsorption kinetics

The plots show the amount of methylene blue adsorbed from solution per mass of adsorbent for each PMC dose against the effective time of contact (***Figure 4.13***). As per observation for all adsorbent doses, a large fraction of the total amount of MB was removed from the solution within the first few minutes. This can be explained from the fact that at this stage adsorbent molecules are being adsorbed onto the surface where there are no other such molecules and consequently the sorbate-sorbate interactions are negligible [28,29]. The rapid initial phase is followed by a slower uptake which might be due to saturation of adsorption sites. The adsorption data fitted the pseudo-second order with regression coefficient of 1 and the q_e values coincided with the expected q_e values ($q_{e_{exp}}$) (***Table 4.2***). All this proves the adsorption obeys the pseudo-second order model meaning the controlling rate step is chemisorption [30,31]**.**

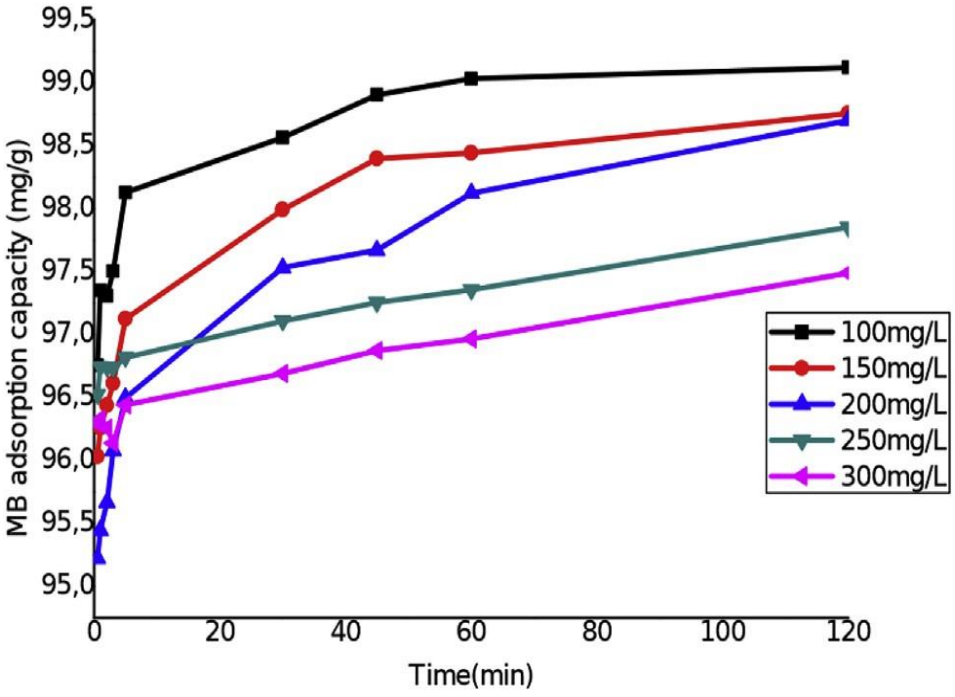

Figure 4.13 Effect of adsorption kinetics on PMC.

Table 4.2 Kinetic parameters and correlation coefficients for MB adsorption at different concentrations onto PMC (299K, pH 12)

Conc.	First order kinetic model				Second order kinetic model			
	k_1 (min^{-1})	$q_e exp$ ($mg.g^{-1}$)	$q_e mod$ ($mg.g^{-1}$)	R^2	k_2 ($g.mg^{-1}.min^{-1}$)	H ($mg.g^{-1}\ min^{-1}$)	$q_e mod$ ($mg.g^{-1}$)	R^2
100	0.0492	9.9118	5.27722	0.9689	0.0057	0.55988	9.9108	1
150	0.0362	14.8755	3.87637	0.9243	0.0048	1.06293	14.881	1
200	0.0273	19.8701	3.27036	0.9625	0.0036	1.42287	19.8807	1
250	0.0147	24.7851	8.52242	0.973	0.0013	0.79649	24.7525	1
300	0.0147	29.7488	8.11164	0.9633	0.001	0.88577	29.7619	1

4.4.7. Adsorption isotherms

Isotherm studies can describe the qualitative information of the adsorbate interaction with adsorbent at constant temperature [32]. The isotherm provides the relationship between the concentration of dye in solution and the amount of dye adsorbed on the solid phase when both phases are in equilibrium. The equilibrium data were analyzed by fitting Langmuir, Freundlich an Temkin isotherm models. The Langmuir isotherm model presume a monolayer adsorption onto the surface containing finite number of adsorption sites of uniform energies of adsorption with no transmigration of adsorbate in the surface plane [35].

The Langmuir isotherm model is represented by the following equation:

$$\frac{C_e}{q_e} = \frac{1}{q_m.k_L} + \frac{C_e}{q_m} \qquad \textbf{Equation 4.2}$$

where q_e is the amount of dye adsorbed at the equilibrium time ($mg.g^{-1}$), C_e is the equilibrium dye concentration ($dm^3.mg^{-1}$), q_m is the maximum adsorption capacity ($mg.g^{-1}$) and K_L is the Langmuir adsorption equilibrium constant ($dm^3.mg^{-1}$). Freundlich linear expression was represented by:

$$\boldsymbol{logq_e = logk_F + \frac{1}{C_e}} \qquad \textbf{Equation 4.3}$$

Where $\boldsymbol{k_F}$ is the equilibrium adsorption coefficient ($dm^3.mg^{-1}$) and $\frac{\mathbf{1}}{\boldsymbol{C_e}}$ is an empirical constant. Temkin isotherm model describes the chemisorption between the adsorbate and adsorbent Temkin model is expressed by:

$$\boldsymbol{q_e = \frac{RT}{b_T.lnK} + \frac{RT}{b_T.C_e}} \qquad \textbf{Equation 4.4}$$

where K is Temkin isotherm equilibrium binding constant ($L.mg^{-1}$) related to the maximum binding energy, b_T is Temkin isotherm constant ($J.mol^{-1}$) related to the heat of adsorption, R is the universal gas constant ($8.314 J.mol^{-1}K^{-1}$) and T is the absolute temperature.

The isotherms calculated from the experimental data and the parameters obtained from the linear regression by all the three models is summarized in ***Table 4.3***. According to the observation, R^2 values for the Langmuir are higher than those of the Freundlich isotherm model, which suggests the Langmuir isotherm is suitable for defining the adsorption equilibrium of MB onto PMC. This implies the adsorption process occurs in a homogeneous surface giving homogeneous distribution of active sites on the PMC. The value of K_L shows a decrease with increase in temperature, which implies that low temperature favored the adsorption process. The adsorption is evidently favorable as Freundlich constant n is 2.47, 2.23 and 2.02 for PMC. Higher K_F indicate higher adsorption capacity meaning temperature 299 K gives better adsorption. Temkin constants K, b_T together with R^2 values are also summarized in ***Table 4.3***. The heat of adsorption of all the molecules in the layer showed decrease linearly

with coverage due to adsorbate/adsorbent interactions. K, decreased as the experimental temperature increased from 299 to 309 K, which implies that the adsorption process is exothermic and favoured at higher temperatures [33]

Table 4.3 Isotherm parameters for the adsorption of MB onto PMC

Isotherms	**Parameters**	**Temperature**		
		299	**304**	**309**
Langmuir	q_m (mg.g^{-1})	60.6	64.5	68.5
	K_L (dm^3·mg^{-1})	0.11	0.10	0.09
	R^2	0.9944	0.9872	0.9650
Freundlich	K_F (dm^3·mg^{-1})	11.7	10.7	9.8
	N	2.47	2.23	2.03
	R^2	0.8892	0.8760	0.8378
Temkin	b_T (J.mol^{-1})	35.21	39.77	46.12
	K (L.mg^{-1})	2.17	1.21	1.10
	R^2	0.9582	0.9484	0.9108

4.4.8. Desorption and recycling efficiency

The main aim of desorption studies is the reusability of adsorbents in the multiple adsorption or desorption cycles and beneficial for their practical and economical applications. Desorption studies were performed with 0.01 M, 0.05 M and 0.1 M HCl. PMC (1 g) saturated with 100 mg.dm^{-3} of methylene blue was placed in different desorption solutions and constantly stirred in a water bath at 200 rpm for 2 h. The adsorbent solutions were centrifuged and analyzed using UV-VIS spectrophotometer. ***Figure 4.14*** demonstrates the effect of eluent concentrations on MB dye desorption efficiency. It was observed that desorption efficiency increased with increase in the eluent concentration even though the shift is small in percentage. The maximum desorption percentage was found at 0.1 M HCl (99.3%) whereby 001 M HCl showed the minimum desorption efficiency (98.96%). Increase in HCl concentration results in increase in H^+ ions concentration which lead to the increase in dye desorption efficiency.

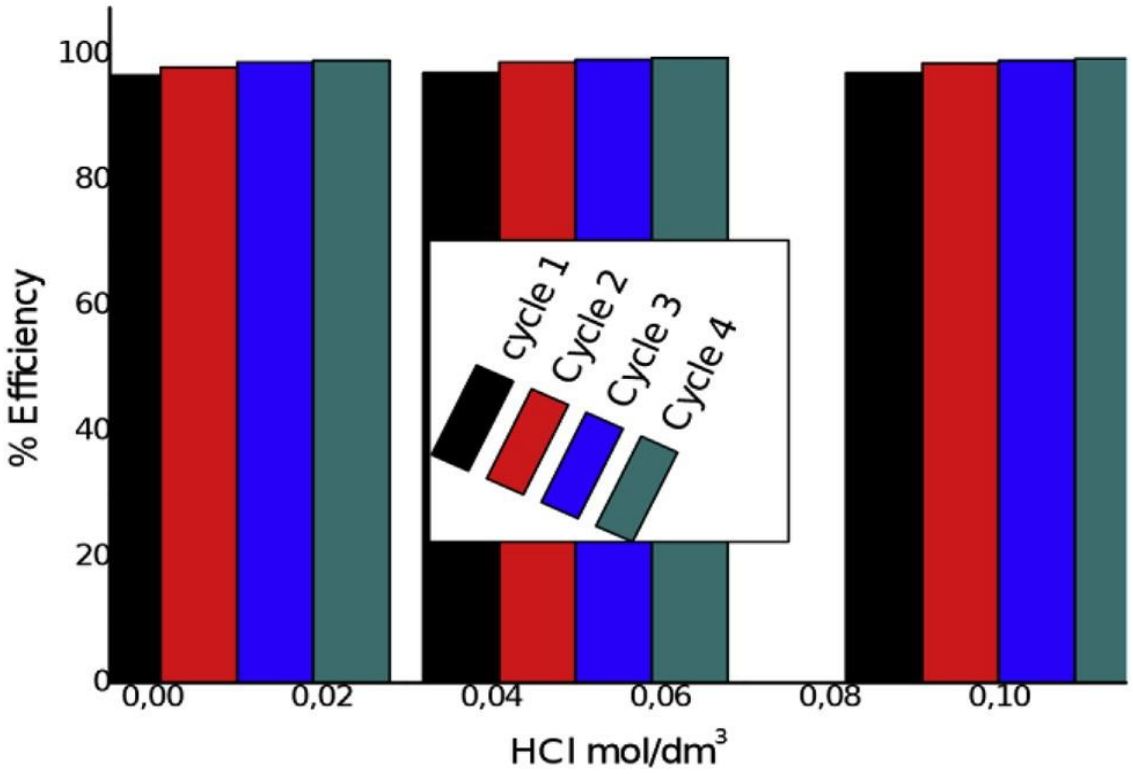

Figure 4.14. Recycling efficiency of PMC on MB removal.

4.5. Conclusions

Observations from the present study showed that pine-magnetite composite was successfully synthesized using co-precipitation method as it indicated potentially good magnetic material that can have good magnetic quality. The results also showed that the optimization of the Pine-magnetite composite was dependent on the chosen parameters of interest. Optimization conditions were the composite showed to be optimum at NH_4OH = 35 cm^3, Temperature = 80 °C, Time = 45 min, Mass Pine = 1,0 g and concentration dosage = 200 ppm. XRF analysis confirmed the optimization conditions by showing the highest % of FeO present on the parameters selected. XRD analysis confirmed the spherical structure of Fe_3O_4 and the binding of Fe_3O_4 onto pinecone. FTIR confirmed the functional groups on the NaOH treated pinecone and the Pine-magnetite composite as literature states. Removal of dye was found to have a capacity of 168 $mg.g^{-1}$ using pine-magnetite composite. The results showed that the adsorbent shows a promising adsorption capacity for removal of methylene blue dye. PMC also exhibit excellent magnetic separation after adsorption process due to the large surface area and magnetic property. The adsorption kinetics studies showed the adsorption processes increase with increase in time. The pine-magnetite composite showed improvement in adsorption

capacity and reusability which further demonstrates that it can be used as the promising adsorbent in the practical treatment of wastewater contaminated with dyes.

4.6. References

[1] B.S. Choudri, Y. Charabi, M. Baawain, M. Ahmed, Textiles, Water Environ. Res. 89 (2017) 1424–1440. doi:10.2175/106143017X15023776270502.

[2] S. Kulkarni, D. Blackwell, C. Blackard, C. Stackhouse, W. Alexander, Textile dyes and dyeing equipment: classification, properties, and environmental aspects, United States Environ. Prot. Agency. (1985) 1–5.

[3] E. Bazrafshan, F.K. Mostafapour, A.R. Hosseini, A. Raksh Khorshid, A.H. Mahvi, Decolorisation of Reactive Red 120 dye by using single-walled carbon nanotubes in aqueous solutions, J. Chem. 2013 (2013). doi:10.1155/2013/938374.

[4] M. Joshi, R. Bansal, R. Purwar, Colour removal from textile effluents, Indian J. Fibre Text. Res. 29 (2004) 239–259. doi:10.1016/0043-1354(91)90006-C.

[5] Y. El Mouzdahir, A. Elmchaouri, R. Mahboub, A. Gil, S.A. Korili, Equilibrium modeling for the adsorption of methylene blue from aqueous solutions on activated clay minerals, Desalination. 250 (2010) 335–338. doi:10.1016/j.desal.2009.09.052.

[6] General introduction to the chemistry of dyes, IARC Monogr. Eval. Carcinog. Risks to Humans. 99 (2010) 55–67.

[7] N. Mathur, P. Bhatnagar, P. Nagar, M.K. Bijarnia, Mutagenicity assessment of effluents from textile/dye industries of Sanganer, Jaipur (India): A case study, Ecotoxicol. Environ. Saf. 61 (2005) 105–113. doi:10.1016/j.ecoenv.2004.08.003.

[8] I. Ali, M. Asim, T.A. Khan, Low cost adsorbents for the removal of organic pollutants from wastewater, J. Environ. Manage. 113 (2012) 170–183. doi:10.1016/j.jenvman.2012.08.028.

[9] V.K. Gupta, Suhas, Application of low-cost adsorbents for dye removal - A review, J. Environ. Manage. 90 (2009) 2313–2342. doi:10.1016/j.jenvman.2008.11.017.

[10] A. Bhatnagar, E. Kumar, M. Sillanpää, Fluoride removal from water by adsorption-A review, Chem. Eng. J. 171 (2011) 811–840. doi:10.1016/j.cej.2011.05.028.

[11] H.P. Srivastava, G. Arthanareeswaran, N. Anantharaman, V.M. Starov, Performance of modified poly(vinylidene fluoride) membrane for textile wastewater ultrafiltration, Desalination. 282 (2011) 87–94. doi:10.1016/j.desal.2011.05.054.

[12] E.O. Oyelude, F. Appiah-Takyi, Removal of methylene blue from aqueous solution using alkali-modified malted sorghum mash, Turkish J. Eng. Environ. Sci. 36 (2012) 161–169. doi:10.3906/muh-1108-6.

[13] P. Liu, L. Zhang, Adsorption of dyes from aqueous solutions or suspensions with clay nano-adsorbents, Sep. Purif. Technol. 58 (2007) 32–39. doi:10.1016/j.seppur.2007.07.007.

[14] J.M. Chern, C.Y. Wu, Desorption of dye from activated carbon beds: Effects of temperature, pH, and alcohol, Water Res. 35 (2001) 4159–4165. doi:10.1016/S0043-1354(01)00127-0.

[15] M. Sarioglu, Removal of methylene blue by using biosolid, Glob. NEST JournalGlobal NEST Int. J. 8 (2018) 113–120. doi:10.30955/gnj.000351.

[16] A.E. Ofomaja, S.L. Ngema, E.B. Naidoo, The grafting of acrylic acid onto biosorbents: Effect of plant components and initiator concentration, Carbohydr. Polym. 90 (2012) 201–209. doi:10.1016/j.carbpol.2012.05.024.

[17] V. Ţucureanu, A. Matei, A.M. Avram, FTIR Spectroscopy forcarbon family study, Crit. Rev. Anal. Chem. 46 (2016) 502–520. doi:10.1080/10408347.2016.1157013.

[18] J. Chen, Y.G. Wang, Z.Q. Li, C. Wang, J.F. Li, Y.J. Gu, Synthesis and characterization of magnetic nanocomposites with Fe 3O4 core, J. Phys. Conf. Ser. 152 (2009). doi:10.1088/1742-6596/152/1/012041.

[19] Z. Xu, C. Shen, Y. Tian, X. Shi, H.J. Gao, Organic phase synthesis of monodisperse iron oxide nanocrystals using iron chloride as precursor, Nanoscale. 2 (2010) 1027–1032. doi:10.1039/b9nr00400a.

[20] S.S. Idris, N.A. Rahman, K. Ismail, A.B. Alias, Z.A. Rashid, M.J. Aris, Investigation on thermochemical behaviour of low rank Malaysian coal, oil palm biomass and their blends during pyrolysis via thermogravimetric analysis (TGA), Bioresour. Technol. 101 (2010) 4584–4592. doi:10.1016/j.biortech.2010.01.059.

[21] K. Raveendran, A. Ganesh, K.C. Khilar, Pyrolysis characteristics of biomass and biomass components, Fuel. 75 (1996) 987–998. doi:10.1016/0016-2361(96)00030-0.

[22] O.S.G.P. Soares, R.P. Rocha, A.G. Gonçalves, J.L. Figueiredo, J.J.M. Órfão, M.F.R. Pereira, Easy method to prepare N-doped carbon nanotubes by ball milling, Carbon N. Y. 91 (2015) 114–121. doi:10.1016/j.carbon.2015.04.050.

[23] Y.C. Chang, D.H. Chen, Preparation and adsorption properties of monodisperse chitosan-bound Fe_3O_4 magnetic nanoparticles for removal of Cu(II) ions, J. Colloid Interface Sci. 283 (2005) 446–451. doi:10.1016/j.jcis.2004.09.010.

[24] G. Gnanaprakash, S. Mahadevan, T. Jayakumar, P. Kalyanasundaram, J. Philip, B. Raj, Effect of initial pH and temperature of iron salt solutions on formation of magnetite nanoparticles, Mater. Chem. Phys. 103 (2007) 168–175. doi:10.1016/j.matchemphys.2007.02.011.

[25] T. Ahn, J.H. Kim, H.M. Yang, J.W. Lee, J.D. Kim, Formation pathways of magnetite nanoparticles by coprecipitation method, J. Phys. Chem. C. 116 (2012) 6069–6076. doi:10.1021/jp211843g.

[26] X. Sun, L. Yang, Q. Li, J. Zhao, X. Li, X. Wang, H. Liu, Amino-functionalized magnetic cellulose nanocomposite as adsorbent for removal of Cr(VI): Synthesis and adsorption studies, Chem. Eng. J. 241 (2014) 175–183. doi:10.1016/j.cej.2013.12.051.

[27] K. Tao, H. Dou, K. Sun, Interfacial coprecipitation to prepare magnetite nanoparticles: Concentration and temperature dependence, Colloids Surfaces A Physicochem. Eng. Asp. 320 (2008) 115–122. doi:10.1016/j.colsurfa.2008.01.051.

[28] K.G. Varshney, A.A. Khan, U. Gupta, S.M. Maheshwari, Kinetics of adsorption of phosphamidon on antimony (V) phosphate cation exchanger: Evaluation of the order of reaction and some physical parameters, Colloids Surfaces A Physicochem. Eng. Asp. 113 (1996) 19–23. doi:10.1016/0927-7757(96)03546-7.

[29] Y.S. Ho, G. McKay, Sorption of basic dye from aqueous solution by pomelo, Chem. Eng. J. 70 (1998) 115–124.

[30] D. Robati, Pseudo-second-order kinetic equations for modeling adsorption systems for removal of lead ions using multi-walled carbon nanotube, J. Nanostructure Chem. 3 (2013) 55. doi:10.1186/2193-8865-3-55.

[31] S.A. Akolo, A.S. Kovo, Comparative Study of Adsorption of Copper Ion onto Locally Developed and Commercial Chitosan, J. Encapsulation Adsorpt. Sci. 05 (2015) 21–37. doi:10.4236/jeas.2015.51003.

[32] K. Li, X. Wang, Adsorptive removal of Pb(II) by activated carbon prepared from Spartina alterniflora: Equilibrium, kinetics and thermodynamics, Bioresour. Technol. 100 (2009) 2810–2815. doi:10.1016/j.biortech.2008.12.032.

[33] A.M. Aljeboree, A.N. Alshirifi, A.F. Alkaim, Kinetics and equilibrium study for the adsorption of textile dyes on coconut shell activated carbon, Arab. J. Chem. 10 (2017) S3381–S3393. doi:10.1016/j.arabjc.2014.01.020.

CHAPTER 5

CHARACTERIZATION OF GRAFTED ACRYLAMIDE ONTO PINE-MAGNETITE COMPOSITE FOR THE REMOVAL OF METHYLENE BLUE FROM WASTEWATER[2]

5.1. Introduction

The rapid development of the textile industry has resulted to a large proportion of industrial wastewater pollution. Methylene blue (MB) dye is a most widely used dye by industries like textile, paper, rubber, plastics, leather, cosmetics, food industries and pharmaceuticals. The textile industry is classified into three main categories, namely; cellulose fibers (cotton, rayon, linen, ramie, hemp and lyocell), protein fibers (wool, angora, mohair, cashmere and silk) and synthetic fibers (polyester, nylon, spandex, acetate, acrylic, ingeo and polypropylene) [1]. The type of dyes and chemicals used in the textile industry are found to differ depending on the fabrics manufactured. Reactive dyes (remazol, procion MX and cibacron F), direct dyes (Congo red, direct yellow 50 and direct brown 116), naphthol dyes (fast yellow GC, fast scarlet R and fast blue B) and indigo dyes (indigo white, tyrian purple and indigo carmine) are some of the dyes used to dye cellulose fibers [2]. The textile industry is known to be the main creator of wastewater effluents because it consumes more water for its wet processes. Therefore, globally it is estimated that all wastewater discharge is highly populated. According to the world bank estimation, textile dyeing and finishing treatment given to a fabric generates at least 17 - 20% of world's industrial wastewater [3], [4].

Dyes often discharged in water effluents contain residues that are highly visible and undesirable even at low concentrations [5]. In addition, they are toxic due to their harmful effects on the human beings. Therefore, it is of vital importance that they are removed from water [6]. Wastewater containing dyes needs to be treated before being discharged into water bodies [7]. Various techniques including chemical oxidation, coagulation, flocculation, membrane processes and biological treatment have shown effectiveness in the removal of methylene blue from wastewater [8]. The limitation most of these techniques possess is the incomplete dye

[2] Chapter published as a peer reviewed book Chapter: Book Chapter citation: KNG Mtshatsheni, EB Naidoo and AE Ofomaja (2020): Characterization of grafted acrylamide onto pine-magnetite composite for the removal of methylene blue from wastewater, Waste in textile and leather sectors, INTECHOPEN, ISBN: 987-1-78985-244-1

removal, poor detection, requirement of expensive equipment and monitoring systems [7]. The performance of adsorption techniques which have been mostly applied due to their effectiveness since they remove the entire dye molecule, leaving no fragments in the effluent [9].

Extensive research in recent years has focused on utilizing waste materials from agricultural products (such as pinecones and others) since they are eco-friendly, cost-effective and renewable [10]. Pinecones are naturally occurring agricultural wastes widely found in a plantation in Vanderbijlpark, Gauteng, South Africa. They are of commercial importance and value which is extensively used in different industries [11]. One pinecone consists of 46.5% hemicellulose, 37.4% lignin, 18.8% cellulose and 15,4% extractives [12]. Pinecone powder has been studied extensively in the removal of heavy metal pollutants such as lead, cesium, copper nickel and arsenic from water systems. Activated carbon has been the most employed adsorbent for the removal of dyes due to its outstanding adsorption properties. However, it has limitations by being expensive and it cannot be used in large applications of wastewater treatment. The use of biomass and other microbial cultures in the removal of methylene blue has been extensively studied in recent years. Among others, carbonized organic materials, fly ashes, peat moss, recycled alum sludge, fishery residues and microorganisms such as fungus and algae [13].

The present study reports the development and characterization of grafted pine-magnetite composite using grafted acrylamide (GACA) for the removal of methylene blue in wastewater. Grafting is a process of chemically or physically manipulating the surface properties of plant materials such as type and number of functional groups, surface area and porosity by extraction of plant chemical components to improve its adsorptive ability. Grafting of synthetic monomers onto pure biological materials has been successfully performed e.g., grafting of acrylonitrile onto starch [14] and methyl acrylonitrile onto cotton [15].

5.2. Materials and methods

5.2.1. Materials

Pinecones are naturally occurring agricultural wastes found in a plantation in Vanderbiljpark, Gauteng, South Africa. All the chemicals and reagents used throughout this study were of analytical grade reagents and used without any further purification. Acrylic amide, ceric

ammonium nitrate (CAN), nitric acid (HNO_3), sodium hydroxide (NaOH), ammonium hydroxide (NH_4OH), ferric sulphate ($FeSO_4$) and methylene blue was supplied by Merck, South Africa. Deionized was used for the preparation of all solutions. The stock solution for methylene blue (1000 $mg.L^{-1}$) was prepared by dissolving the required quantity of dyes in a 1000 ml of deionized water and the stock solution was further diluted for batch experiments.

5.2.2. Methods

5.2.2.1. *Synthesis of pine-magnetite composites*

A mixture of $FeSO_4.7H_2O$ (2.1 g) and of $Fe(SO_4)_3.XH_2O$ (3.1 g) were dissolved under inert atmosphere in 100 cm^3 of double-distilled water with vigorous stirring. Thereafter, 20 cm^3 of 28% ammonium hydroxide and the appropriate amount of pine powder was added. The reaction was left to run for 45 min at 80 °C under constant stirring. The resulting particles, consisting of magnetite attached to the cellulose (hereafter referred to as bio-composite) were washed several times with deionized water and ethanol and dried in a vacuum oven at 60°C overnight. To determine the optimum conditions to achieve the desired products of the bio-composites, we experimented with the following variables: volume of NH_4OH 5, 10, 20, 30, and 40 cm^3; weight of pine powder 1.0, 1.5, 2.0, 2.5, 3.0 and 3.5 g; temperatures 40, 60, 80 and 100 °C and reaction times 15, 30, 45 and 60 min

5.2.2.2. *Synthesis of grafted pine-magnetite composite*

PMC(1 g), 20 cm^3 of 1.5 M acrylic amide and 135 cm^3 of deionized water were transferred into a three-neck round bottom flask at a temperature of 42 °C. The reaction was bubbled under nitrogen gas for 30 min to remove the dissolved oxygen under stirring. CAN (10 cm^3) of 0.5 M, dissolved in 0.3 M HNO_3 was slowly added to the reaction to initiate graft co-polymerization and stirring was continued for 2 h. Reaction mass was neutralized by 50% NaOH and precipitated in methanol and thereafter washed with methanol/water (90:10) several times, so that the unreacted PMC and ceric salt were removed. The final residue was dried in a vacuum oven at 40 °C.

5.3. Characterization

Qualitative and fundamental identification of the functional chemical groups of grafted pine-magnetite composite (GPMC) were carried out with a FTIR (Perkin- Elmer) in the range 450 - 4000 cm^{-1}. An X'Pert PRO X-ray diffractometer (PAN analytical, PW3040/60 XRD; CuKα anode; λ = 0.154 nm) was used for particle size measurements. The size of the synthesized particles was observed using transmission electron microscope (TEM, FEI TECNAI G^2 SPIRIT) at an accelerating voltage of 150 kV. TGA (Perkin-Elmer (USA) Simultaneous Thermal Analyzer 6000 instrument) was used for determining the weight loss as a function of temperature. Changes in morphology were studied using scanning electron microscopy (SEM), HRSEM Instrument Specs Model: Jeol JSM 7800F field emission scanning electron microscope run at Operational voltage: 5kV Elemental composition was determined using a Thermofischer UltraDry EDS Detector.

5.4. Results and discussions

5.4.1. FTIR spectroscopy results

The FTIR spectrum shown in ***Figure 5.1*** (a) represents the pine-Fe_3O_4 magnetite (PMC). The FTIR spectrum showed some changes in band intensities, indicating the functional groups on the surface that had been modified. A compressed –OH peak at 3350 cm^{-1} with an increase in intensity was observed. This might have been due to the presence of extracted lignin in pinecone. Clearly, the COO- peak was converted to esters at 1622 cm^{-1}, C–H aliphatic peaks were observed at 1416 cm^{-1} which represent the increase in the internal surface of the pinecone and a new peak was found at 567 cm^{-1} which was assigned to the vibration of Fe–O band of Fe_3O_4.

The FTIR spectrum of GACA (***Figure 5.1*** (b)) shows a slightly broad band observed at 3389 cm^{-1} ascribed to the existence of –OH and –NH groups. The compressed peak at 1654 cm^{-1} corresponds to a carbonyl functional group of acrylamide, whereas the one at 1030 cm^{-1} reflects on the vibrations of N-CH_2 groups. The last peak at 546 cm^{-1} reflects the –C–O–C– functional groups. These functional groups might have participated in the interactions with MB which involved the mechanism of surface complex, hydrogen bonding, and electrostatic attractions.

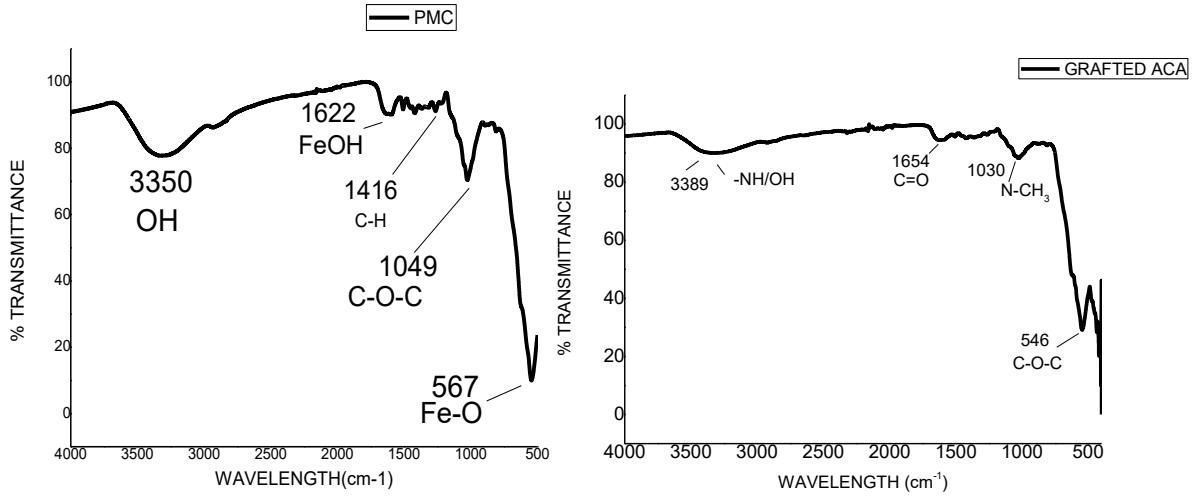

Figure 5.1 (a) FTIR spectrum for PMC and (b) GACA

5.4.2. XRD analyses

The XRD spectrum of grafted pine-magnetite composite with acrylamide is shown in ***Figure 5.2(a)***. The prominent peaks at 2θ values of 30.5°, 38.7°, 43.9.0°, 59.8° and 63.7° corresponding to (220), (311), (400), (422), (511), respectively, attributes to the cellulose peaks due to the presence of iron oxide magnetite composite and crystal planes of grafted pine magnetic composite respectively [16]. The composite has shown a cubic crystal structure. The composite has shown a cubic crystal structure It is observed that diffraction intensity of the broad peak at 43.9° was weakened indicating that the crystallinity of the PMC decreased after grafting. This phenomenon might be due to the strong interaction of covalent bonds between the PMC and the acrylamide.

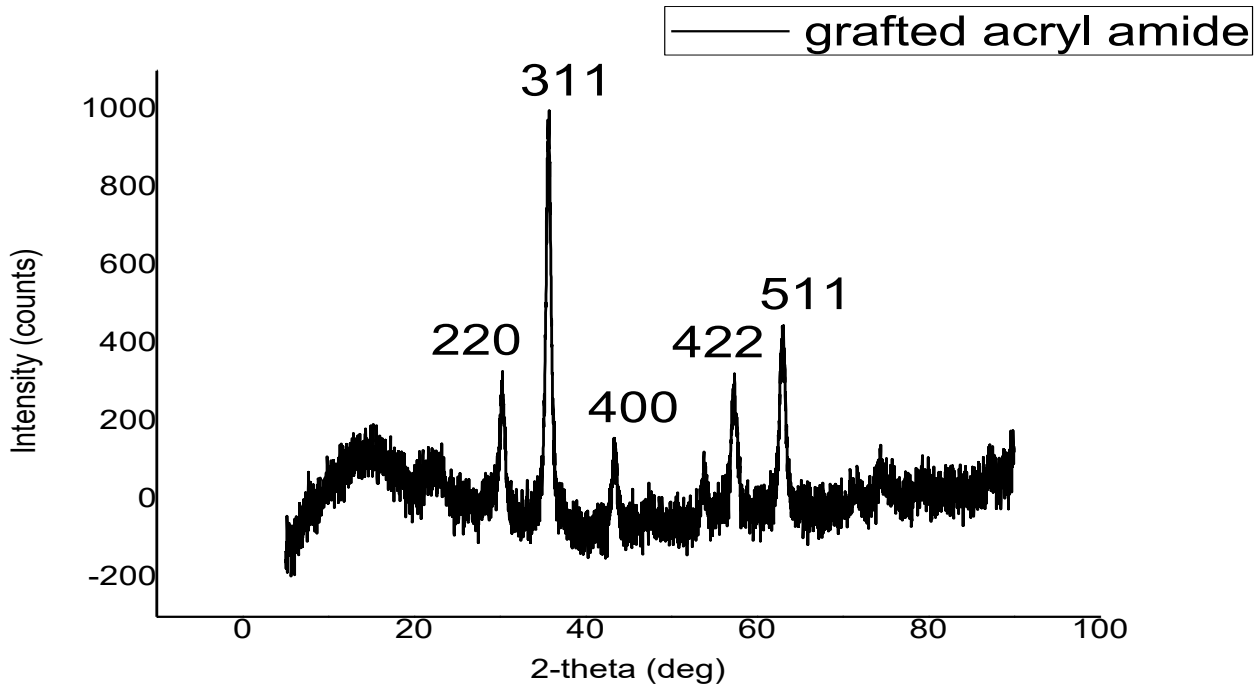

Figure 5.2 XRD spectrum for GACA

5.4.3. TGA analyses

The TGA and DTG curve shown in ***Figure 5.3*** demonstrates the thermal stability of grafted pine-magnetite composite. The incorporation of the Fe_3O_4 magnetite composite showed the changes in the thermal properties of the cellulose. The initial thermal decomposition of GACA occurred at 100 – 240°C temperature range which corresponds to loss of water molecules and volatile compounds. The second stage thermal decomposition in the temperature range 380 – 640°C may be due to the breakdown of the polymer matrix and cross-links between different polymeric chains. The last stage of decomposition at a temperature of 700°C corresponds to the lignin degradation [17]. Grafting with acrylamide presented a better thermal stability due to the different types of covalent bonds in the grafting of copolymer backbone [14]. Differential thermal analysis (DTA) showed endothermic peaks associated with degradation of various materials. The degradation behavior exhibited two stage decomposition effects. Observation at different temperatures (380 – 620°C) was attributed to the cellulose decomposition at low temperature and grafted acrylamide composite at higher temperatures. This confirmed the stabilizing effect of the incorporation of Fe_3O_4 composite onto acrylamide.

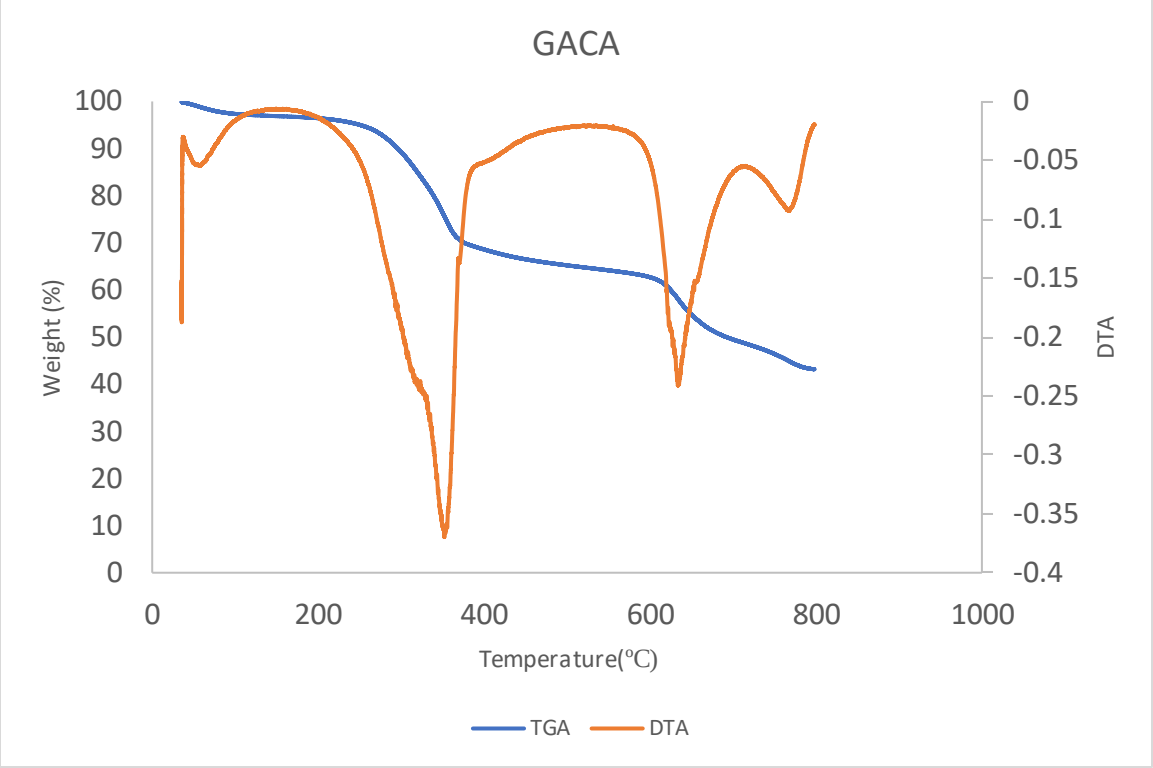

Figure 5.3 TGA and DTA curves for GACA

5.4.4 TEM studies

The TEM image in ***Figure 5.4*** shows the appearance of the typical images of grafted pine magnetic composite with acrylamide and the nanoparticle size distribution of GACA. The spherical nanoparticles are attributed to the shape and the incorporation of the magnetic nanoparticles in the polymer matrix. The size distribution of the GACA shows mean particle size to be 11.4 ± 3.16 nm.

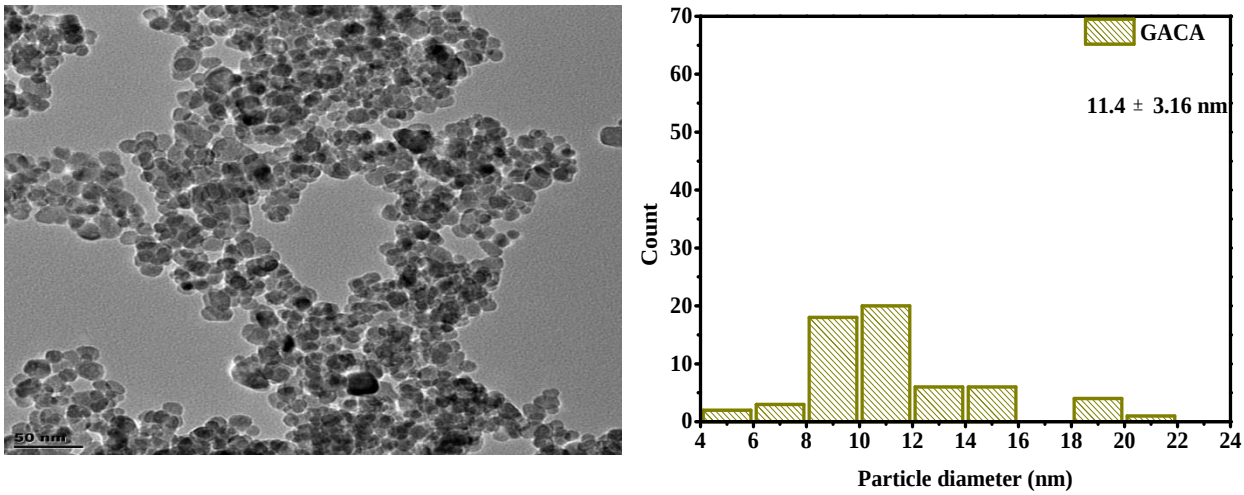

Figure 5.4 TEM image and size distribution of grafted pine-magnetite composite with acrylamide (GACA)

5.4.4. SEM studies

SEM images of grafted pine-magnetite composite with acrylamide is shown in ***Figure 5.5***. The observation showed changes in morphology of the GACA because of the graft copolymerization process and incorporation iron oxide magnetite. Supporting information showed the granular smooth surface. Roughness of the surface increased after modification; better matrix coherence was achieved after incorporation of the iron oxide magnetite nanoparticles. All the observations confirmed that grafting pine-magnetite composite with acrylamide allows better compatibility. The presence of the Fe peak in the EDX of the nanocomposite showed successful incorporation of iron oxide composite in the polymer matrix ***Figure 5.6***.

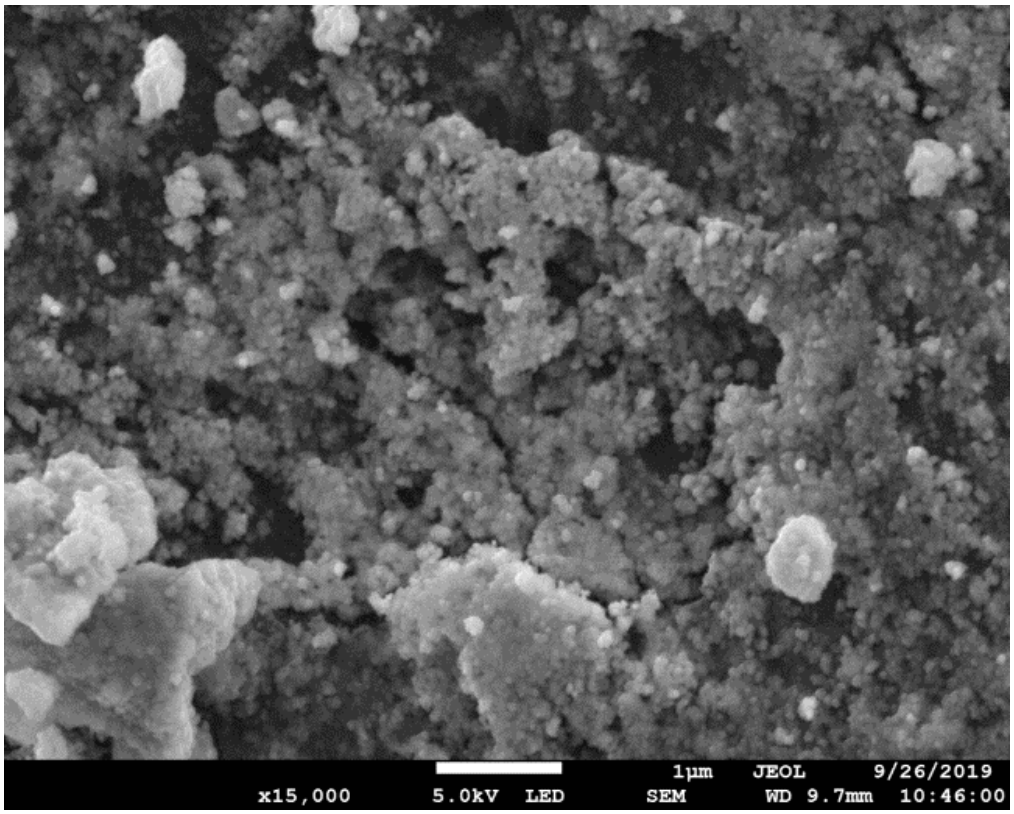

Figure 5.5 SEM image of the GACA

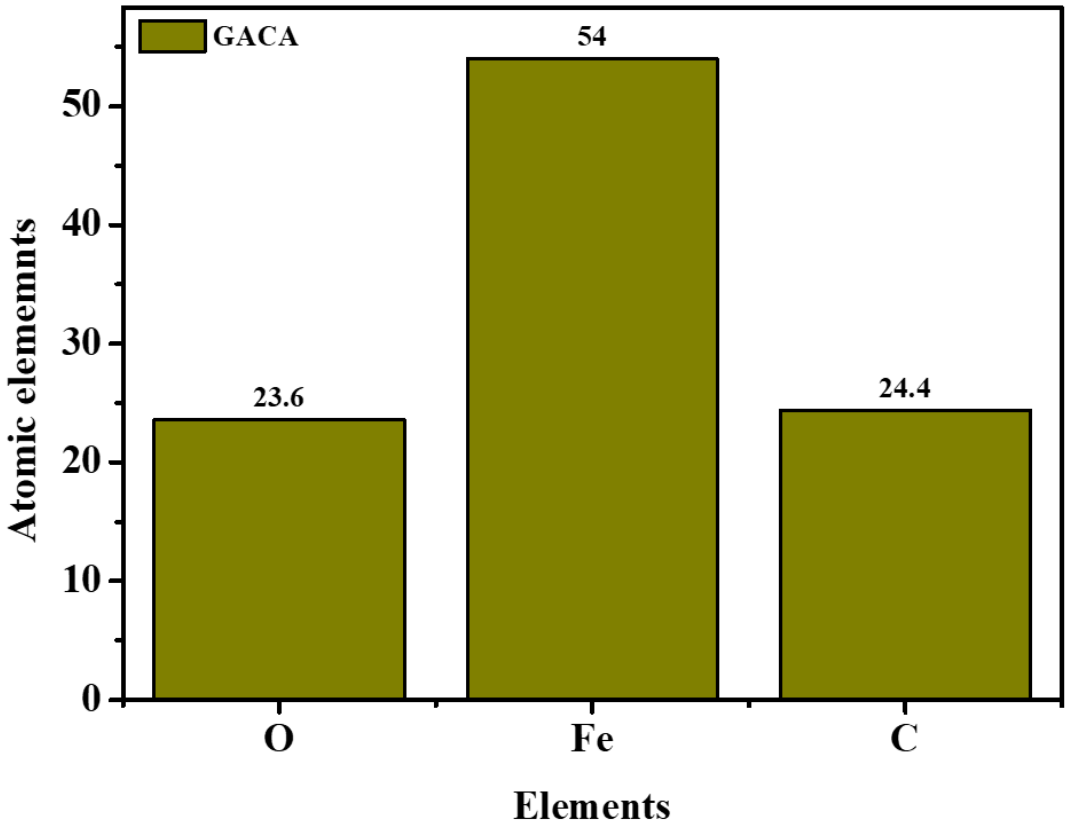

Figure 5.6 Elemental analysis from SEM-EDX

5.4.5. BET (Surface area) analyses

A surface property of an adsorbent describes the effect of modification on the surface area of the adsorbent. (***Table 5.1*** BET surface area and pore characteristics for synthesized materials shows comparison of the effect of modification on the surface area of the materials. The pure pine-magnetite nanoparticles showed a surface area of 113.60 $m^2.g^{-1}$, pore volume of 0.6321 $cm^3.g^{-1}$ and pore size of 25.86 nm. On the other hand, the NaOH treated pine had a surface area of 2.25 $m^2.g^{-1}$, pore volume of 0.0177 $cm^3.g^{-1}$ and pore size of 10.17 nm. Pine-magnetite composite exhibited surface area of 54.80 $m^2.g^{-1}$, pore volume of 0.1522 $cm^3.g^{-1}$ and pore size of 23.10 nm. Grafted acrylamide reflected the surface area of 57, 77 $m^2.g^{-1}$, pore volume of 0.1591 $cm^3.g^{-1}$ and pore size of 17.33 nm. The higher surface area was due to the pinecone structure which was found to be important for the improvement of mass diffusion and adsorptive capacity. An increase in surface area, pore volume and pore size confirmed that GACA can adsorb MB more efficiently than the PMC. The distinct pore structure size enables fast transportation of particles.

Table 5.1 BET surface area and pore characteristics for synthesized materials

Properties	**Pure magnetite composite**	**NaOH treated pine**	**Pine-magnetite composite (PMC)**	**Grafted acrylamide**
Surface area (m^2.g)	113.60	2.25	54.80	57.77
Pore Volume (cm_3.g)	0.6321	0.0177	0.1522	0.1591
Ave. pore size (nm)	25.86	10.17	23.10	17.33

5.4.6. Point Zero Charge (pHpzc)

To further investigate the effects of modifications on the suitability of the synthesized materials for adsorption, the isoelectric point or point of zero charge (pH_{PZC}) was determined. The solution pH is an important parameter for dye adsorption because it does not only change the surface charge of the adsorbent but also it affects the molecular structure of the dye. As MB is a cationic dye, it can easily form positively charged species over a wide pH range. The solid addition method was used to determine the pH_{pzc} of the pinecone composite. To a series of 100 cm^3 volumetric flasks, 45 cm^3 of 0.01 $mol.dm^{-3}$ KNO_3 solution were transferred. The pH_i values of the solutions were roughly adjusted between pH 2 to 12 by the addition of either 0.1 $mol.dm^{-3}$ HCl or NaOH on a pH meter with constant stirring. The total volume of the solution in each flask was made up to 50 cm^3 by the addition of KNO_3 solution of the same strength. The pH_i of the solutions was accurately noted, and 0.1 g of pinecone composite were added to each volumetric flask, which was then immediately closed. The suspensions were allowed to equilibrate for 48 h on a shaker operating at 200 rpm. The pH_f values of the supernatant were accurately noted and the difference between the initial and final pH values ($\Delta pH = pH_f - pH_i$) were plotted against the pH_i. The solution pH is an important parameter for dye adsorption because it does not only change the surface charge of an adsorbent, but it also reflects the molecular structure of the dye.

Changes in the point of zero charge values within the sample can be attributed by the difference in types and amounts of surface functional groups present on the surface of the adsorbent. pH_{pzc} is observed when modification on the suitability of the synthesized materials is determined. It is known to be the pH at which the amount of positive charges on a biosorbent surface equals the amount of the negative charge i.e. the pH at which the biosorbent surface has net electrical

neutrality [18], [19]. Methylene blue is a cationic dye and can easily form positively charged species over a wide pH range. The pH_{pzc} of pine-magnetite composite was found to be 8.56 and grafted pine-magnetite with acrylamide was found to be 6.2. The decrease in the pH_{pzc} is attributed to the modification of the surface area.

5.5. Adsorption studies

5.5.1. Effect of solution pH

The adsorption experiments were carried out using batch equilibration techniques. Various Methylene Blue (MB) solutions with different pH range, initial concentrations and mass dosage were prepared by diluting1000 $mg.dm^{-3}$. Equilibrium experiments, to determine the adsorption capacity of pine-magnetite composite were conducted using 250 cm^3 bottles. 0.1 g of PMC and 100 cm^3 of the MB solution were added and shaken for 2h at 26 °C. Thereafter, absorbance was determined using UV-VIS spectrophotometer at the wavelength corresponding to the maximum absorbance (λ_{max} = 665 nm) as determined from the plot. This wavelength was used for measuring the absorbance of residual concentration of MB. pH of the solution was adjusted using 0.1 M HCl and 0.1 M NaOH.

Figure 5.7 showed the effect of pH on the adsorption of MB. It is observed that the bionanocomposite adsorbs efficiently across a wide range of pH and thus demonstrating its versatility and suitability for real wastewater systems. A slight variation occurs in that an increase in pH showed an increase in percentage removal from 99% at pH 1 to around 99.9% at pH 12. We attribute this to the adsorption due to the plant material and the additional adsorption due to the surface groups from the functionalization with acrylamide. This indicated that the lower adsorption of MB at acidic pH was due to the presence of excess H^+ ions. The influence of low pH to MB adsorption was that H^+ ions could occupy the binding sites; this was not favorable for the adsorption of MB. Furthermore, MB possessed positive surface charges and could be repulsed by H^+ ions to prevent MB adsorption onto grafted pine magnetic composite.

With increasing pH, the number of hydrogen ions in solution was reduced and the competitive effect, repulsive interaction weakened, lead to an increase in the removal rate. The MB removal rate became stable when the pH reached 12, where the higher percentage removal for MB was observed in comparison to other pH values.

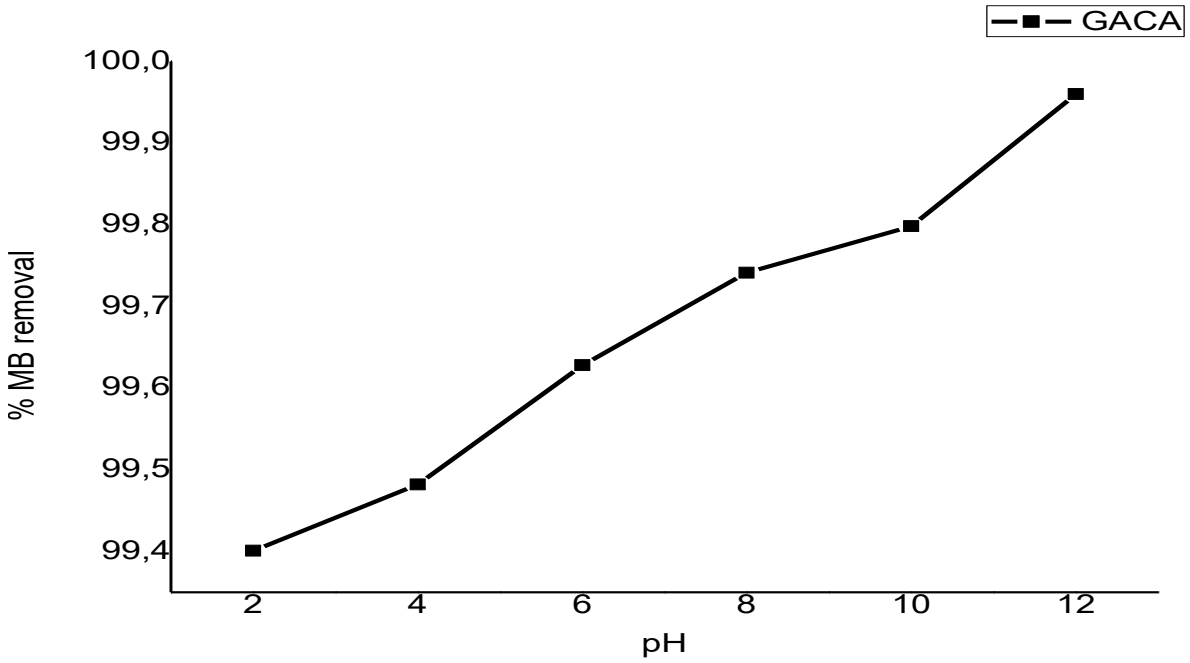

Figure 5.7 Effect of pH on the adsorption of MB

5.5.2. Effect of adsorbent dose

Figure 5.8 shows the effect of adsorbent dose on the percentage removal and amount of dye that was adsorbed. This effect was necessary to observe how the novel adsorbent used impacted on the adsorption stoichiometry. It also gave an idea of the propensity of dye molecules to be adsorbed with the smallest amount of adsorbent. When the mass of the adsorbent was 0.5 g, the percentage adsorption removal increased rapidly, which contributed to the increased surface area of the adsorbent which in turn increased the number of binding sites [20]. The adsorption capacity decreased past 0.5 g of adsorbent dosage and we attribute that to increased interactions between the adsorbent nanoparticles and hence increased agglomeration. At mass 0.5 g the highest percentage removal of 99.8% was achieved.

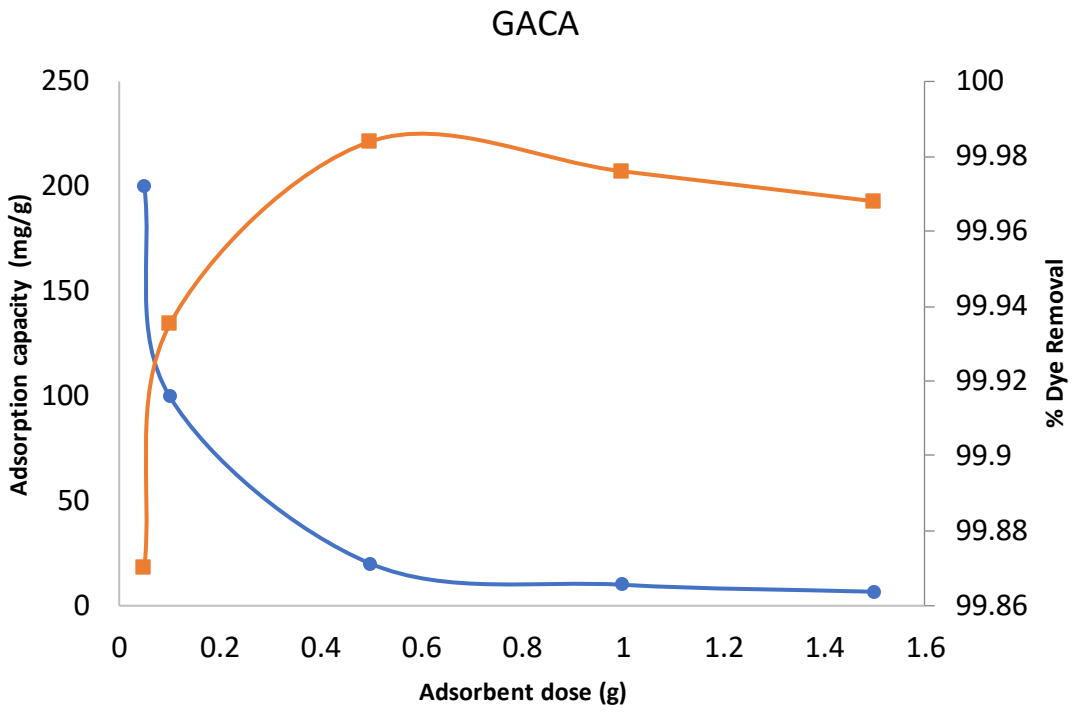

Figure 5.8 Effect of adsorbent dose on the adsorption of MB

5.5.3. Effect of contact time

The effect of contact time on the grafted pine-magnetite composite with acrylamide for the adsorption of methylene blue is shown in ***Figure 5.9***. The adsorption experiment was done at 100 mg.L^{-1} concentration. The adsorption rate of the grafted composite on the removal of MB is faster from the beginning which might be influenced by the grafted composite with higher specific gravity which makes them better in dispersity and more efficient contact with MB. The adsorption capacity of the grafted composite is higher due to its the high surface area.

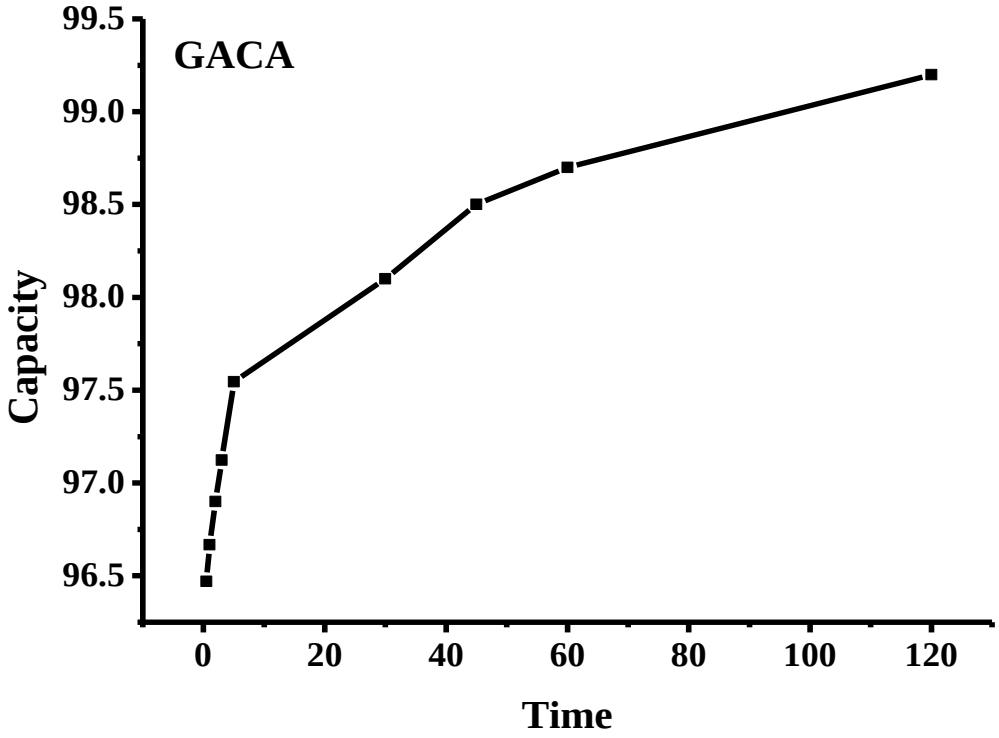

Figure 5.9 Effect of contact time at 100 mg.L^{-1} on the MB adsorption of the GACA

5.6. Adsorption isotherms

The adsorption isotherm explains the relationship between an adsorbate in the liquid phase and the adsorbate adsorbed on the surface of the adsorbent at equilibrium at constant temperature [21]. To successfully obtain the adsorptive behavior of any substance from the liquid to the solid phase, it is important to have a satisfactory description of the equilibrium state between two phases composing the adsorption system. Langmuir and Freundlich isotherms are the well-known isotherms which have been used to describe the equilibrium of adsorption systems. Typically, the Langmuir model describes the monolayer sorption on a surface containing a limited number of sites and predicting a homogeneous distribution of sorption energies [22]. Freundlich describe the heterogeneity distribution. The results of the MB concentration dependence study were subjected to analyses by using Langmuir and Freundlich isotherm models.

The theoretical Langmuir isotherm is represented by the following equation:

$$\frac{C_e}{q_e} = \frac{1}{q_m} + \frac{C_e}{q_m} \qquad \textbf{Equation 5.1}$$

Where q_e is the amount of dye adsorbed at the equilibrium time (mg.g^{-1}), C_e is the equilibrium dye concentration (dm^3 mg^{-1}), q_m is the maximum adsorption capacity (mg.g^{-1}) and K_L is the Langmuir adsorption equilibrium constant (dm^3.mg^{-1}). Freundlich linear expression was represented by:

$$\boldsymbol{Log\ q_e = log\ K_f + \frac{1}{n\ log C_e}} \qquad \textbf{Equation 5.2}$$

Where K_F is the equilibrium adsorption coefficient (dm^3.mg^{-1}) and $\frac{1}{n}$ is an empirical constant. The parameters of the isotherm models are calculated from the experimental data and the values of correlation coefficient (R^2) are demonstrated in ***Table 5.2*** below. The results show R^2 values for the Langmuir are higher than those of Freundlich isotherm model. This imply that the equilibrium adsorption data comply with the Langmuir isotherm, suggesting that the adsorption process occurs in a homogeneous surface. Also, it can be stated that the results demonstrate no interaction and transmigration of dyes in the plane of the neighboring surface [23]. Higher K_f value for GACA indicates a higher adsorption capacity for methylene blue and a value of n>1 indicates favourable adsorption conditions [24], [25].

Table 5.2 Isotherm parameters for methylene blue dye adsorption on GACA

Langmuir isotherm model				**Freundlich isotherm model**		
Temperature (K)	Q_m (mg.m^{-1})	K_L(dm^3.mg^{-1})	R^2	K_f(mg.g^{-1})(dm^3.mg^{-1})	N	R^2
299	57.47	0.2107	0.9957	17.7174	2.862	0.9819
304	82.64	0.0588	0.9745	7.66655	1.725	0.9635
309	78.74	0.0968	0.9825	10.7226	1.873	0.9691
314	68.03	0.1786	0.9851	15.01067	2.293	0.9097
319	67.11	0.2569	0.9925	18.02603	2.455	0.8879

5.7. Desorption and Regeneration

The main goal of desorption studies is the competitiveness of adsorbents reusability in the multiple adsorption or desorption cycles and their beneficial potential in practical and economical applications. Desorption studies were performed with 0.01 M, 0.05 M and 0.1 M

HCl. Typically, 1 g of PMC saturated with 100 mg.L^{-1} of MB was placed in different desorption solutions and constantly stirred in a water bath at 200 rpm for 2 h. The adsorbent solutions were centrifuged and analyzed using UV-VIS spectrophotometer. ***Figure 5.10*** demonstrates the effect of eluent concentrations on MB dye desorption efficiency. It was observed that desorption efficiency increased with increase in the eluent concentration even though the shift is small in percentage. The maximum desorption percentage was found at 0.1 M HCl (99.8%) whereby 0.01 M HCl showed the minimum desorption efficiency (98.8%). An increase in HCl concentration resulted in an increase in H^+ ions concentration which led to a subsequent increase in dye desorption efficiency.

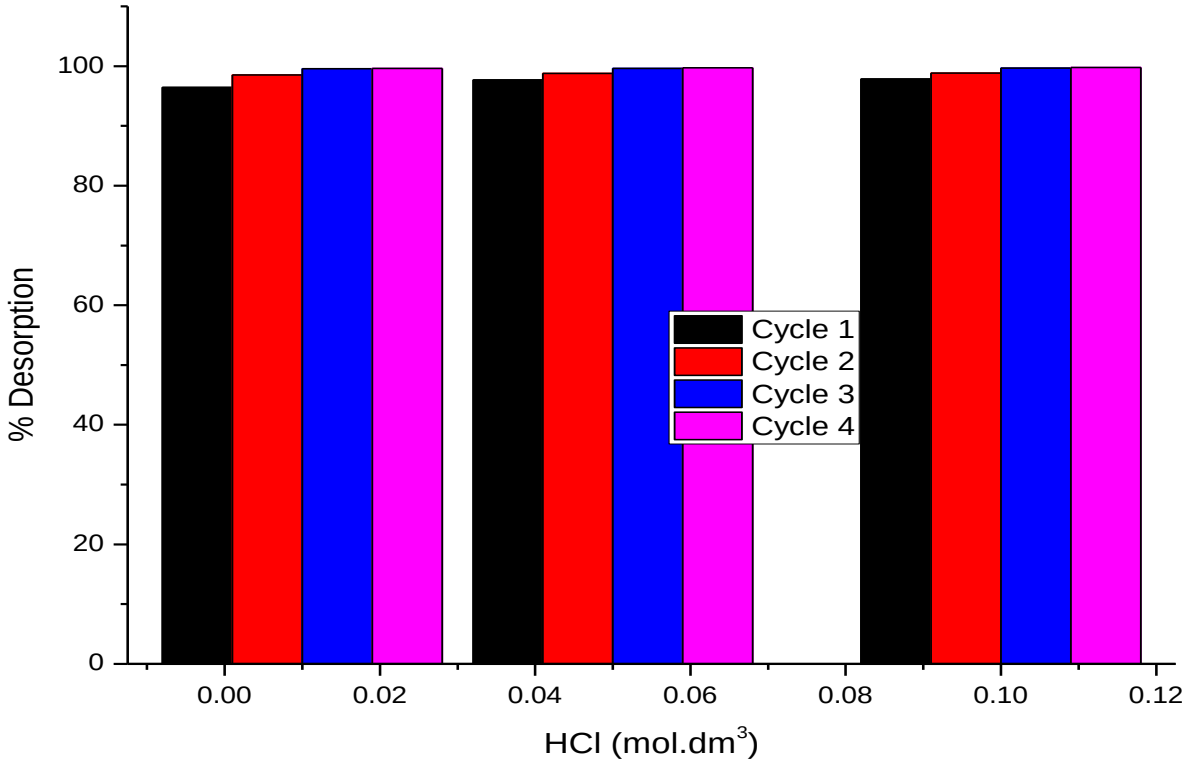

Figure 5.10 Desorption characteristics of MB adsorbed

Regeneration shows the competitiveness of the adsorbent where it expresses the good reusability and recycling abilities. ***Figure 5.11*** demonstrates the possibility of regeneration and reusability of the grafted pine-magnetite composite with acrylamide. Adsorption-desorption reaction cycles were repeated 4 times using 0.1 M HCl as the desorbing agent. Observation showed that there was a gradual reduction from 29.8% to 14.03% after cycle 4. The results

explain that the higher adsorption capacity proves the adsorbent to be a good adsorbent for the removal of MB.

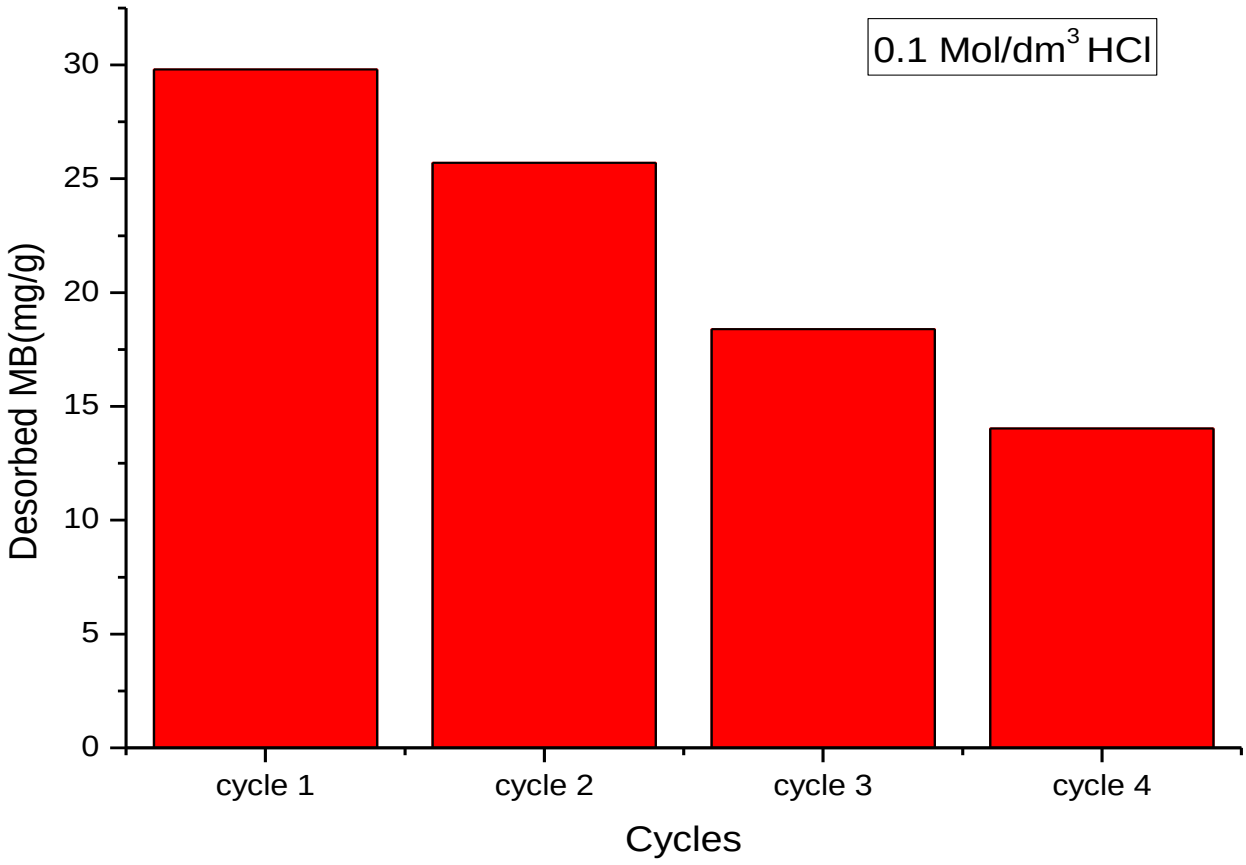

Figure 5.11 Regeneration characteristics of MB adsorbed

5.8. Conclusions

The study showed that acrylamide was successfully grafted onto pine-magnetite composites. FTIR, BET, SEM, TEM and XRD characterization provided sufficient evidence to demonstrate the incorporation and distribution of the iron oxide nanoparticles within the polymer matrix. GACA nanocomposites were shown to be effective in the adsorption of methylene blue at a pH of 12. The role of adsorbent dose and contact time demonstrated excellent results in the adsorption of methylene blue due to the increased surface area and high rate of the adsorption were achieved. The adsorption data was adequately interpreted by Langmuir and Freundlich isotherm models respectively. It was found that Langmuir isotherm model gave the best equilibrium fit.

5.9. References

[1] A.G. R Ananthashankar, Production, Characterization and Treatment of Textile Effluents: A Critical Review, J. Chem. Eng. Process Technol. 05 (2013). https://doi.org/10.4172/2157-7048.1000182.

[2] C. O'Neill, F.R. Hawkes, D.L. Hawkes, N.D. Lourenço, H.M. Pinheiro, W. Delée, Colour in textile effluents - Sources, measurement, discharge consents and simulation: A review, J. Chem. Technol. Biotechnol. 74 (1999) 1009–1018. https://doi.org/10.1002/(SICI)1097-4660(199911)74:11<1009::AID-JCTB153>3.0.CO;2-N.

[3] C.R. Holkar, A.J. Jadhav, D. V. Pinjari, N.M. Mahamuni, A.B. Pandit, A critical review on textile wastewater treatments: Possible approaches, J. Environ. Manage. 182 (2016) 351–366. https://doi.org/10.1016/j.jenvman.2016.07.090.

[4] D.A. Yaseen, M. Scholz, Textile dye wastewater characteristics and constituents of synthetic effluents: a critical review, Springer Berlin Heidelberg, 2019. https://doi.org/10.1007/s13762-018-2130-z.

[5] F.M. Amaral, M.T. Kato, L. Florêncio, S. Gavazza, Color, organic matter and sulfate removal from textile effluents by anaerobic and aerobic processes, Bioresour. Technol. 163 (2014) 364–369. https://doi.org/10.1016/j.biortech.2014.04.026.

[6] A. Kausar, M. Iqbal, A. Javed, K. Aftab, Z. i. H. Nazli, H.N. Bhatti, S. Nouren, Dyes adsorption using clay and modified clay: A review, J. Mol. Liq. 256 (2018) 395–407. https://doi.org/10.1016/j.molliq.2018.02.034.

[7] G. Oguntimein, J. Hunter, D.H. Kang, Biosorption of Azure Dye with Sunflower Seed Hull : Estimation of Equilibrium , Thermodynamic and Kinetic Parameters, Int. J. Eng. Res. Dev. 10 (2014) 26–41.

[8] S. Debnath, N. Ballav, A. Maity, K. Pillay, Competitive adsorption of ternary dye mixture using pine cone powder modified with β-cyclodextrin, J. Mol. Liq. 225 (2017) 679–688. https://doi.org/10.1016/j.molliq.2016.10.109.

[9] S. Dawood, T.K. Sen, Review on Dye Removal from Its Aqueous Solution into Alternative Cost Ef-fective and Non-Conventional Adsorbents Citation: Tushar K Sen, et al. (2014) Review on Dye Removal from Its Aqueous Solution into Alternative Cost Effective and Non-Conventional Ads, J Chem Proc Eng. 1 (2014) 104.

[10] M. Alshabanat, G. Alsenani, R. Almufarij, Removal of crystal violet dye from aqueous solutions onto date palm fiber by adsorption technique, J. Chem. 2013 (2013). https://doi.org/10.1155/2013/210239.

[11] M.A. Martín-Lara, G. Blázquez, M. Calero, A.I. Almendros, A. Ronda, Binary biosorption of copper and lead onto pine cone shell in batch reactors and in fixed bed columns, Int. J. Miner. Process. 148 (2016) 72–82. https://doi.org/10.1016/j.minpro.2016.01.017.

[12] A.E. Ofomaja, Intraparticle diffusion process for lead(II) biosorption onto mansonia wood sawdust, Bioresour. Technol. 101 (2010) 5868–5876. https://doi.org/10.1016/j.biortech.2010.03.033.

[13] A. Tshikovhi, S.B. Mishra, A.K. Mishra, Nanocellulose-based composites for the removal of contaminants from wastewater, Int. J. Biol. Macromol. 152 (2020) 616–632. https://doi.org/10.1016/j.ijbiomac.2020.02.221.

[14] S. Thakur, O. Arotiba, Synthesis, characterization and adsorption studies of an acrylic acid-grafted sodium alginate-based TiO_2 hydrogel nanocomposite, Adsorpt. Sci. Technol. 36 (2018) 458–477. https://doi.org/10.1177/0263617417700636.

[15] H.T. Lokhande, V.D. Gotmare, Utilization of textile loomwaste as a highly absorbent polymer through graft co-polymerization, Bioresour. Technol. 68 (1999) 283–286. https://doi.org/10.1016/S0960-8524(98)00148-5.

[16] A. Pholosi, E.B. Naidoo, A.E. Ofomaja, Enhanced Arsenic (III) adsorption from aqueous solution by magnetic pine cone biomass, Mater. Chem. Phys. 222 (2019) 20–30. https://doi.org/10.1016/j.matchemphys.2018.09.067.

[17] A.E. Ofomaja, S.L. Ngema, E.B. Naidoo, The grafting of acrylic acid onto biosorbents: Effect of plant components and initiator concentration, Carbohydr. Polym. 90 (2012) 201–209. https://doi.org/10.1016/j.carbpol.2012.05.024.

[18] A.E. Ofomaja, E.B. Naidoo, S.J. Modise, Removal of copper(II) from aqueous solution by pine and base modified pine cone powder as biosorbent, J. Hazard. Mater. 168 (2009) 909–917. https://doi.org/10.1016/j.jhazmat.2009.02.106.

[19] M. Kumari, C.U. Pittman, D. Mohan, Heavy metals [chromium (VI) and lead (II)] removal from water using mesoporous magnetite (Fe_3O_4) nanospheres, J. Colloid Interface Sci. 442 (2015) 120–132. https://doi.org/10.1016/j.jcis.2014.09.012.

[20] A.J.K. Kupeta, E.B. Naidoo, A.E. Ofomaja, Kinetics and equilibrium study of 2-nitrophenol adsorption onto polyurethane cross-linked pine cone biomass, J. Clean. Prod. 179 (2018) 191–209. https://doi.org/10.1016/j.jclepro.2018.01.034.

[21] K. Yokwana, A.T. Kuvarega, S.D. Mhlanga, E.N. Nxumalo, Mechanistic aspects for the removal of Congo red dye from aqueous media through adsorption over N-doped graphene oxide nanoadsorbents prepared from graphite flakes and powders, Phys. Chem. Earth. 107 (2018) 58–70. https://doi.org/10.1016/j.pce.2018.08.001.

[22] G.N. Hlongwane, P.T. Sekoai, M. Meyyappan, K. Moothi, Simultaneous removal of pollutants from water using nanoparticles: A shift from single pollutant control to multiple pollutant control, Sci. Total Environ. 656 (2019) 808–833. https://doi.org/10.1016/j.scitotenv.2018.11.257.

[23] K.Y. Foo, B.H. Hameed, Insights into the modeling of adsorption isotherm systems, Chem. Eng. J. 156 (2010) 2–10. https://doi.org/10.1016/j.cej.2009.09.013.

[24] B.H. Hameed, D.K. Mahmoud, A.L. Ahmad, Equilibrium modeling and kinetic studies on the adsorption of basic dye by a low-cost adsorbent: Coconut (*Cocos nucifera*) bunch waste, J. Hazard. Mater. 158 (2008) 65–72. https://doi.org/10.1016/j.jhazmat.2008.01.034.

[25] B.H. Hameed, A.A. Ahmad, Batch adsorption of methylene blue from aqueous solution by garlic peel, an agricultural waste biomass, J. Hazard. Mater. 164 (2009) 870–875. https://doi.org/10.1016/j.jhazmat.2008.08.084.

CHAPTER 6

SURFACE STRUCTURE-PROPERTY RELATIONSHIP OF ACRYLIC ACID-GRAFTED PINE-MAGNETITE BIONANOCOMPOSITES AND ITS EFFECT ON THE ADSORPTION OF MB FROM WATER[3]

6.1. Introduction

The ever-increasing pollution of surface waters by textile waste necessitates the exploration of sustainable means of wastewater remediation. The key tenets of sustainability in water treatment are (i) the fabrication of environmentally benign yet efficient nanomaterials and (ii) the use of materials that are synthesized through natural biosynthetic processes, preferably with minor or no modification [1,2]. The mechanical and chemical stabilization of nanomaterials prior to their application in wastewater treatment is key to rendering these nanomaterials environmentally benign in that it helps protect the material from reacting with environmental components and thus getting degraded. These stabilized materials can further be mechanically stabilized by anchoring onto a bulk support to minimize their leaching into the environment [3,4]. Stabilization is achieved through several methods including the capping of the nanomaterials with chemical capping agents [5].

While the technique of capping nanoparticles with polymer or their monomers is commonly used in biomedical applications, it is gaining momentum in water treatment technologies such as adsorption and photocatalysis. For example, polyvinyl pyrrolidone (PVP)-capped magnetite has been demonstrated to be effective in the adsorptive removal of undesirable micropollutants [6]. These capping agents themselves should interact with the pollutant to minimise the loss of activity of the capped nanomaterial in removing the pollutant. For instance, ZnS nanoparticles have been capped with polyvinyl alcohol and starch and the resultant composites were shown to have an improved removal of Cr(VI) ions from water owing to the polymer having an interaction with the ions and thus acting as extended sites for the adsorption of the ions [7]. In another work a new copolymer, poly(1,4,8,11-cyclo- tetradecane [2,2-bipyridine]-5,5-dicarboxamine) (PNH) was found to promote the adsorption of tetracycline and enhance charge separation in Fe_2O_3 nanoparticles [6]. The polymer chains on these polymer-capped nanomaterials increase the amount of functional groups such that these capped nanoparticles

[3] Submitted for peer review to the Journal of Nanoscience and Nanotechnology

have a lower propensity of leaching out of bulkier nano artefacts such as polymeric membranes [1,8]. This makes capped nanomaterials best suited for process optimization through the combination of two technologies into one artefact.

Poly acrylic acid has been found suited for the capping of adsorptive nanomaterials because of its high hydrophilicity, negative zeta potential a propensity for the charge-based selective adsorption of pollutants (both organic and inorganic) [9]. In addition, acrylic acid, is an ecofriendly molecule that is typically used to impute chemical stability to nanoparticles [10]. For example, polyacrylic acid has been grafted onto the surface of a PES membrane so as to bind onto TiO_2–nitrogen-doped carbon quantum dots composite [11]. It was demonstrated that the polyacrylic acid not only enhanced the adhesion of the composite but also played a role in promoting the adsorption of the pollutant onto the membrane; a step that is essential for the photocatalytic degradation of the pollutant. While substantial progress has been made in the fabrication and assembly of new synthetic technologies, the use of renewable resources is key to increasing the economic feasibility of these technologies [12].

The use of renewable resources in synthesis processes relating to wastewater remediation has had a positive impact on agriculture, environment, and economy in that, otherwise useless, but environmentally benign agricultural waste is put into good use without increasing the carbon footprint in the environment [13,14]. To this end, plant material-based synthesis of nanomaterials has remained a key means to improving the environmental-friendliness of nanotechnology-based water treatment technologies. Pinecones are one of the commonly used nanomaterials and are a rich resource of crystalline cellulose, lignin, and their amorphous forms-the hemicelluloses. These biopolymers consist of fibers that are enriched with surface –OH and –COOH groups [15]. These surface groups make celluloses and, in our, pinecone powder good candidates as supports for nanoparticles. In addition, the high concentration of these groups on the surfaces of the polymers nanofibers and nanoparticles exert their influence on the surface charge of bionanocomposites of pinecones and other cellulose-rich resources [16]. These characteristics, can further be influenced by etching organic polymer and monomer molecules onto the surface of the bionanocomposites [17]. NaOH-activated pinecone powder was used for the adsorptive removal of malachite green (MG) from wastewater. This modified pinecone powder had a higher adsorption capacity for MG (111.1 $mg.g^{-1}$) compared to unmodified pinecone powder (30 – 60 $mg.g^{-1}$) [18,19].

Previous studies on the applicability of pinecone composite in wastewater remediation have primarily focused on the adsorption of heavy metals [18]. Little amount of work has been carried out to investigate their efficacy in the removal of synthetic dyes and to understand the mechanism involved. Magnetite is renowned for being amphoteric and hence reduced adsorption capacity [20]. Coupling magnetite with an inherently negatively charged biopolymers and a strongly hydrophilic polymer such as acrylic is anticipated to have a significant effect on the structural and surface properties that make the bionanocomposites better stabilized without loss of adsorptive activity. Our previous work investigated the parameters for the synthesis of high performance pinecone-magnetite composite (PMC) and compared the performance to the adsorption performance for alkali treated pinecone powder [21]. The results demonstrated that the best performing PMC composite was synthesized using a mass ration of 2:1 $FeSO_4.7H_2O$ and $Fe_2(SO_4)_3$. XH_2O, 35 mL of 28% NaOH, 1.5 g pinecone powder at a temperature of 80 °C and 45 min aging time for the PMC composites with the smallest, well dispersed, and firmly attached magnetite and pine composites.

The present study makes use of these optimized parameters to synthesize PMC and further graft PMC with acrylic acid as a monomer to form unique acrylic acid-grafted pinecone-magnetite grafted bionanocomposites (herein referred to as GAA). The surface and morphological properties and their influence on the mechanistic aspects of methylene blue (MB) adsorptive removal from wastewater are investigated. Focus is placed on understanding the structure-property relationship of acrylic acid-grafted pine-magnetite bionanocomposites and its effect on the adsorption of MB. In addition, reusability studies are carried out to investigate the economic feasibility of modified pinecone composites in wastewater treatment. The bionanocomposites were synthesized and characterized to evaluate their adsorption efficiency on MB. The effects of the reaction variables such as contact time, initial dye concentration, temperature, pH and adsorbent dosage on the dye adsorption were systematically investigated and the changes in surface charge and efficiency of adsorption were monitored. This work, consequently, evaluates in detail, the reusability of these natural adsorbents, the mechanistic models responsible for the adsorption process and the role of structure and property on the adsorption process.

6.2. Materials and methods

6.2.1. Chemicals and reagents and equipment

Pinecones were collected from a local plantation in South Africa, washed several times in deionized water and dried before crushing them into a powder using a blender. The resultant powder was in successive repetition using a domestic flour sieve in to obtain a fine powder. Acrylic acid (AA) (99.0%), ceric ammonium nitrate (CAN) (ACS reagent 98.5%), nitric acid (HNO_3) (ACS reagent 70.0%), sodium hydroxide (NaOH) (ACS reagent 97.0%), ammonium hydroxide (28%), iron (II) sulfate hydrate ($FeSO_4.7H_2O$) (99.9%), iron (III) sulfate hydrate ($Fe_2(SO_4)_3.XH_2O$) (97.0%), potassium nitrate (KNO_3) (ACS reagent 99.0%), hydrochloric acid (HCl) (ACS reagent 37.0% and (MB) (95%) were supplied by Merck, South Africa. All the reagents used were of analytical grade and were used without any further pre-treatment.

6.2.2. Synthesis of grafted pinecone-magnetite bionanocomposites

6.2.2.1. *Synthesis of pinecone-magnetite composites (PMC)*

First, the pinecone powder was washed in NaOH and dried using an established procedure for treating pinecone as had been used in our previous work [21]. The preparation procedure for anchoring the magnetite onto the pinecone powder is an in-situ coprecipitation procedure that was adapted from previous work in our group in which $FeSO_4.7H_2O$ and $Fe_2(SO_4)_3.XH_2O$ at mass ration 2:3 were dissolved in 100 mL of distilled water with vigorous stirring under a nitrogen atmosphere [21,22]. Upon completion of dissolution of the salts, approximately 50 g of NaOH-treated pinecone powder was simultaneously added with 28% NH_4OH (20 mL) with continued stirring. The precipitate formed was aged under stirring at 80 °C for 45 min and then filtered using vacuum filtration to obtain a brown powder (hereafter referred to as pinecone-magnetite (PMC) bionanocomposites) After washing several times with deionized water and ethanol and drying in a vacuum oven at 60 °C overnight the resultant powder was kept in a desiccator for further use.

6.2.2.2. *Synthesis of acrylic acid-grafted pinecone-magnetite composite (GAA)*

PMC (1 g) (prepared from co-precipitation method), 20 mL of 1.5 M acrylic acid and 135 mL of deionized water were transferred into a three-neck round bottom flask at 42 °C. Nitrogen gas was then bubbled in the reaction mixture for 30 min to remove dissolved oxygen under

stirring. This was followed by the slow addition of 10 mL of 0.5 M CAN, dissolved in 0.3 M HNO_3 to initiate graft co-polymerization and stirring was continued for a further 2 h under inert conditions. The reaction was neutralised by adding 50% NaOH followed by precipitation in methanol. Thereafter, the resulting product washed with methanol/water (90:10) several times to remove unreacted PMC and ceric salt. The final residue was dried in a vacuum oven at 40 °C and stored for further analyses.

6.3. Characterization and performance evaluation of pine-magnetite (PMC) and grafted pine-magnetite composites (GAA)

6.3.1. Morphology and surface characteristics

Qualitative and fundamental identification of the functional chemical groups of grafted pinecone-magnetite composite samples for FTIR spectroscopy were identified by FTIR (Perkin- Elmer) in the range 450 - 4000 cm^{-1} using diamond attenuated total reflectance (ATR). The surface elemental composition of the bionanocomposites was determined through X-ray photoelectron spectroscopic (XPS) analysis on a Thermo ESCAlab 250Xi model. A monochromatic X-ray beam with a spot size of 900 μm, generated from an Al Kα (1486.7eV) shell was blazed onto a pelletized sample that was held in a pressurized chamber at 10^{-8} mBar. A Rikagu Smartlab diffractometer operated at 45kV and 200 mA XRD; CuKα anode; $\lambda = 0.154$ nm) was used for particle size measurement. The relative intensities were recorded in the range of 10- 90 (2θ) at a scanning rate of 50 min^{-1}. The morphology and average size of the synthesized particles were observed using transmission electron microscope (TEM, FEI TECNAI G^2 SPIRIT) at an accelerating voltage of 150 kV. TGA experiments were conducted in the temperature range 30 - 900 ^oC at a ramp rate 10 $^oC.min^{-1}$ under N_2 atmosphere. Scanning electron microscopy (SEM) was used to observe the microstructure and surface morphology of PMC and GAA. SEM images were generated from a Jeol JSM 7800F field emission microscope equipped with an LED detector. Samples were carbon coated using a Quorum QT 150 sputter coater before HRSEM analysis and Thermofischer UltraDry EDS Detector was used for elemental analysis. The specific surface area of the PMC and GAA adsorbents were measured by a Micromeritics TriStar II 3020 BET analyzer (n). The BET surface area and pore size distribution were determined using computer controlled N_2 gas adsorption analyzer. Degassing was carried out for 1 h at 90 °C and increased to 120 °C for 2 h. A mass of 0.2 g of the PMC and GAA material was used for analysis.

6.3.1.1. *pH at point zero charge (pH_{pzc}) of the pinecone bionanocomposites*

The pH at point zero charge (pH_{pzc}) of the pinecone composite was determined by the solid addition method [23]. To a series of 100 mL volumetric flasks, 45 mL of 0.01 M KNO_3 solution were transferred. The initial pH (pH_i) values of the solutions were roughly adjusted between pH 2 to 12 by the addition of either 0.1 M HCl or NaOH on a pH meter with constant stirring. The total volume of the solution in each flask was made up to 50 mL by the addition of KNO_3 solution of the same strength. The pH_i of the solutions was accurately noted, and 0.1 g of the pinecone composite was added to each volumetric flask, which was then immediately closed. The suspensions were allowed to equilibrate for 48 h on a shaker operating at 200 rpm. The final pH (pH_f) values of the supernatant were accurately noted and the difference between the initial and final pH values ($\Delta pH = pH_f - pH_i$) were plotted against the pH_i.

6.3.1.2. *Adsorption studies*

Adsorption measurements were determined by batch experiments of known amount of the adsorbent with 50 mL of aqueous (MB) solutions of known concentration in a series of 250 mL conical flasks. The mixture was shaken at a constant temperature using Thermoline Scientific Orbital Shaker Incubator at 120 rpm at 30 °C temperature for 180 min. At predetermined time, the bottles were withdrawn from the shaker, and the residual dye concentration in the reaction mixture was analyzed by centrifuging the reaction mixture and then measuring the absorbance of the supernatant at the wavelength corresponding to the maximum absorbance (λ_{max} = 665 nm) of the sample. The dye concentration in the reaction mixture was calculated from the calibration curve. Adsorption experiments were conducted by varying initial solution pH, contact time, adsorbent dose, initial (MB) dye concentration, temperature, and salt concentration under the aspect of adsorption kinetics, adsorption isotherm and thermodynamic studies.

6.4. Results and discussion

6.4.1. Chemical composition analysis of the acid-grafted pine-magnetite bionanocomposites

6.4.1.1. *Analysis of bionanocomposites by surface functional groups composition*

The FTIR spectra shows a broad peak at 3313.5 cm^{-1} corresponding to the stretching vibrations of –OH that is common to NaOH treated pinecone powder, PMC and GAA (***Figure 6.1***). Other peaks common to all the materials (i) the peak at 2895.5, 1600.3, 1269.9 and 1020.6 cm^{-1} which are due to the aliphatic C–H group, C=O stretching, aromatic –OH and –C–O–C stretching [24]. This indicative of the presence of the cellulose from the pinecone powder [25]. Additionally, peaks due to the asymmetric and symmetric stretching vibration of ionic carboxylic groups ($–COO^-$ and –COOH) were observed at 1639 cm^{-1} 1265 cm^{-1} respectively [26]. The intensities of these peaks are highest for NaOH treated pinecone and the least for GAA and therefore indicative of the presence and functionalization of cellulose from the pinecone powder. Most notable is the decrease of the intensities for these peaks with the incorporation of magnetite to form PMC and a further decrease after the grafting of PMC with acrylic acid. This indicates that a number of these functional groups are used for the formation of bonds between the NaOH treated pinecone powder and the Fe_2O_3 and a further use of the remaining functional groups for bonding with the acrylic acid after grafting. The presence of Fe_3O_4 in PMC and GAA is confirmed by the occurrence of the peak at 569 cm^{-1} which is characteristic of the vibration of Fe–O bond [21].

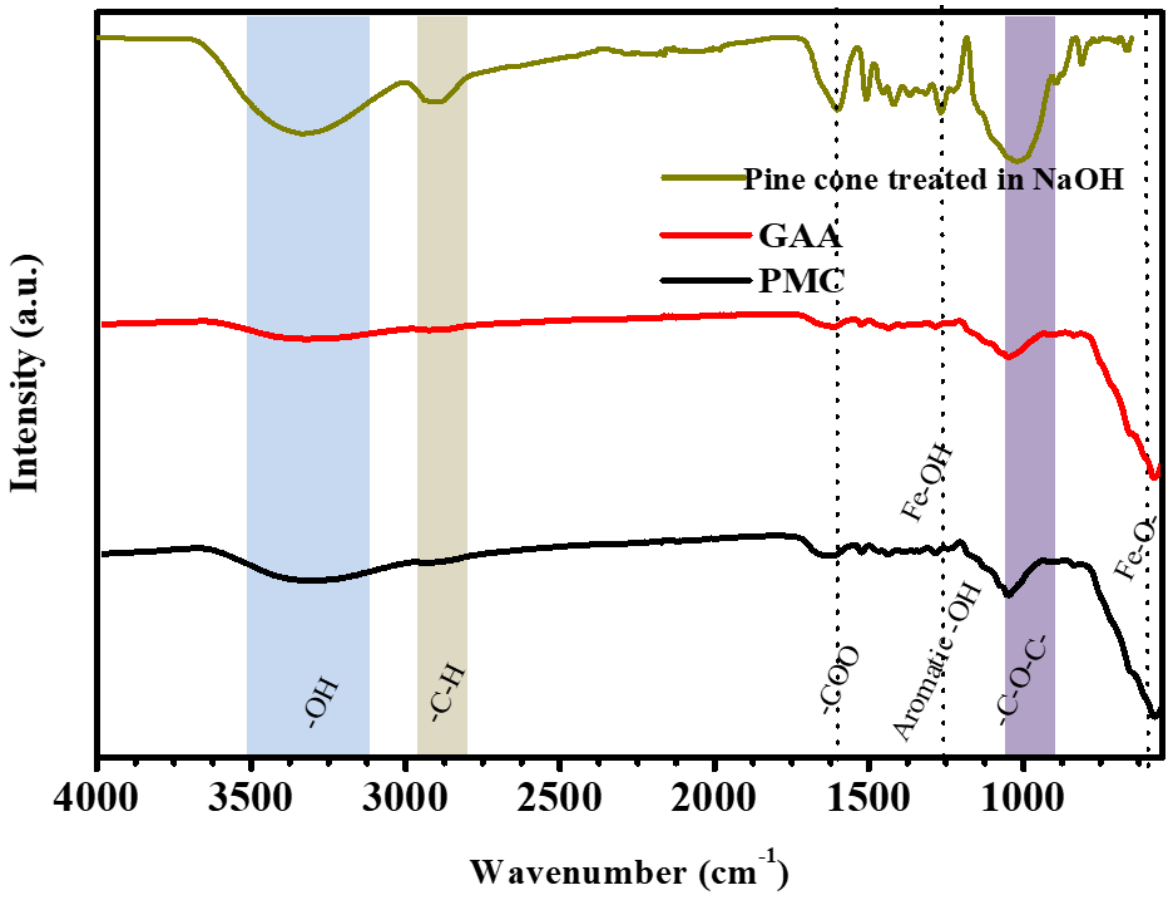

Figure 6.1 FTIR spectra of treated pinecone, pinecone-magnetite composite (PMC) and acrylic acid modified pinecone composites

6.4.1.2. *Elemental composition, oxidation state and bonding configuration analysis of the PMC bionanocomposites*

Energy dispersive X-ray analysis

EDX analysis of the PMC bionanocomposites, indicates the presence of C (16.85%), O (21.85%) and Fe(61.85%) (***Figure 6.2***). The GAA bionanocomposites, on the other hand, shows an increase in the atomic C (50.00%) and atomic O (35.8%) and a significant decrease in Fe (14.6%). Moreover, the presence of Fe % in the EDX of the nanocomposites showed successful incorporation and uniform distribution of the iron oxide in the PMC polymer matrix and therefore successful grafting of acrylic acid. In addition, the increase in the at.% of C and O in GAA are due the incorporation of polyacrylic acid, which predominantly consists of carbon and oxygen. For the same reason, while the amount of Fe_2O_3 is expected to remain the same after the grafting of polyacrylic acid, the at.% decreases after the significant increase in the carbon and oxygen.

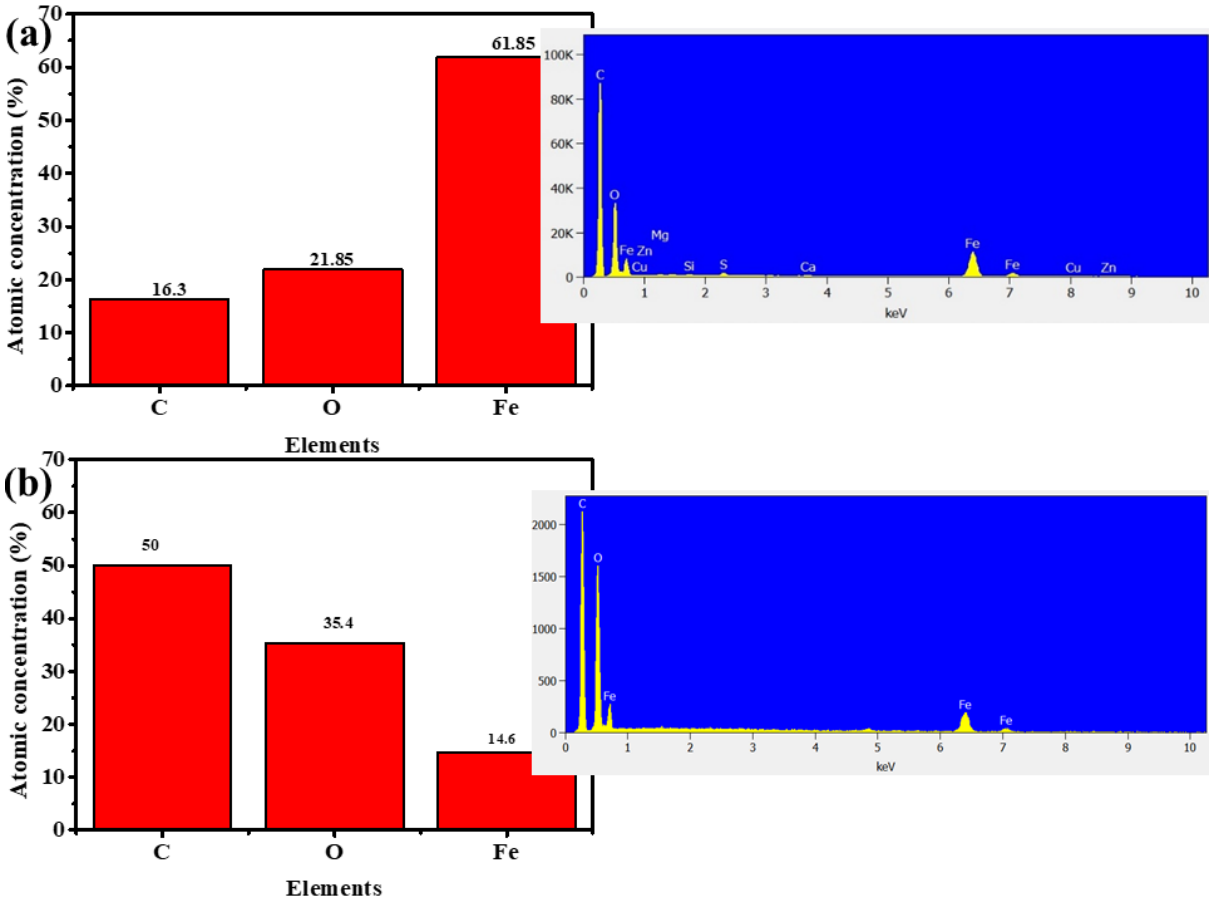

Figure 6.2: Atomic concentrations and elemental analysis for (a) PMC and (b) GAA bionanocomposites

X-ray photoelectron spectroscopy analysis

PMC and GAA bionanocomposites are characterized by the occurrence of C, N and O (***Figure 6.3*** (a), ***Table 6.1***). There is a striking difference between the bionanocomposites in the % composition of the N atom (and related functional groups) and the O atoms as indicated by the XPS spectra (***Figure 6.3*** (b) and (c)). The at.% associated with the N-based groups accounts for 2.6% in PMC while it is 0.3% in GAA (***Table 6.1***). The N1s spectra for PMC has peak at 398.5 eV is attributed to N substituted into a six membered carbon ring while that at 400.05 eV is indexed to the binding energy for –N–H in the bonding configuration $–CONH_2$ [27–29]. The existence of the $–CONH_2$ is corroborated by the O1s peak appearing at 531 eV [27]. These results suggest a reaction between the cellulose in the pinecone powder and the NH_4OH. Upon incorporation the capping of PMC with acrylic acid, the overall N content decreases, the peak at 400.5 eV disappears while another N1s peak appears at 399.6 eV. Since XPS is a surface probing technique, the disappearance of the peaks suggest that the N becomes

the centers through which the acrylic acid monomers coordinate onto PMC. Additionally, the peak at 399.6 eV is attributed to the six membered ring N coordinating to the acrylic acid molecule through the alcohol group.

The C1s spectra in both bionanocomposites accounts for the highest at.% composition and is deconvoluted to the C1s (C–C) *sp2* and C1s (C–C) *sp3* bonding configurations at 284.2 eV (***Figure 6.3*** (d) and (e)). The C1s peak which is attributed to the (C=O) bonding configuration also occurs at the same binding energy for both nanocomposites. A complimentary O1s peak at 533.1 and 533.0 (in PMC and GAA respectively) confirms the occurrence of the C=O functional group (***Figure 6.3*** (f) and (g)). There also appears a C1s C–O bonding configuration at 285.5 eV and a complimentary O1s C–O bonding configuration at 531.7and 531.6 eV (in PMC and GAA respectively). The C1s C–C, C–O bonding configurations are attributed to the skeletal carbon in the cellulose monomer units and the glucose rings making in lignin that make up the pinecones. The C1s C–O bonding configuration is attributed to the C–O–H bond in carbon number 6, the monomer bridging ether and the ether bond between C1 and C5 in the glucose monomers that make the cellulose and lignin. The bionanocomposites has an additional C1s peak at 288.9 eV which is attributed to the bonding configuration (O–C=O). This functional group is attributed –R–COO groups formed from the hydrolytic breaking down of the ether linkage between the lignin and cellulose monomer units during the treatment of the pinecones with NaOH. The presence of Fe_2O_3 was detected in larger amounts in PMC bionanocomposites than in GAA as indicated by the Fe $2p_{3/2}$ and Fe $2p_{1/2}$ peaks at 710.5 and 724.5 eV (***Figure 6.3*** (h) and (i)). Further confirmation of the presence of larger amounts of magnetite in PMC was indicated by the occurrence of the O1s 530.0 eV which are due to Fe^{3+} and O^{2-}. Typically, the Fe $2p_{3/2}$ peak appears at 710.8 [30] and so the shift in the case of the PMC and GAA bionanocomposites suggest that there is a strong interaction between the magnetite and pinecone nanoparticles. The low intensity of Fe $2p_{3/2}$ and Fe $2p_{1/2}$ peaks in GAA is consistent with the EDS analysis and is thought to be due to the small amounts of Fe precursor used which could result in Fe_2O_3 not being at the surface during sample preparation. It is also worth noting that the O1s peaks are shifted towards lower binding energy while the C1s (C=O) is shifted toward a higher binding energy in the GAA bionanocomposites. These features are attributed to the grafting of acrylic acid onto both the Fe_2O_3 and pinecone nanoparticles. The grafting of acrylic acid and subsequent polymerization into polyacrylic acid could also result in shielding of the already small amounts of Fe_2O_3 from being detected by

XPS. The PMC bionanocomposites also have a higher at.% of N compared to GAA. In addition, the N in PMC is deconvoluted to indicate the presence of organic, azide and cyanide N. The N in GAA is unassigned to these groups hence suggesting that these groups play a role in the bonding of polyacrylic acid onto the bionanocomposites. It is hypothesized that these N groups are acted on and possibly removed by the treatment with ceric ammonium nitrate during the grafting.

Table 6.1 XPS peak designation for the PMC and GAA bionanocomposites

	PMC			**GAA**		
Name	**Peak binding energy (eV)**	**FWHM eV**	**Atomic %**	**Peak binding energy (eV)**	**FWHM (eV)**	**Atomic %**
C1s (C-C) sp^2	284.2	1	56.5	284.2	1	39.4
C1s (C-C) sp^3	284.8	1	17.3	284.7	1	31
C1s (C-O)	285.8	1.5	12.4	285.8	1.4	12.9
C1s (C=O)	287.5	1.5	1.6	288	1.4	2.2
C1s (O-C=O)	288.9	1.5	1.1	-	-	-
Fe2p^3 (Fe_2O_3)	710.5	3.2	0.6	-	-	-
N1s (Cyanides; azides)	398.1	1.8	1.6	399.6*	1.1*	0.3*
N1s (Organic N)	400.5	1.8	1	-	-	-
O1s (C-O)	531.7	1.6	3.1	531.6	1.8	5.5
O1s (C=O)	533.1	1.8	2.2	533	1.8	5.6
O1s (Metal oxide)	530	1.5	2	-	-	-
Si2p (Organic Si)	101.7	1.3	0.4	-	-	-

*N- assigned to organic, cyanides or azides

Most importantly, XPS is generally in agreement with FTIR spectra of the bionanocomposites in that the PMC bionanocomposites have a higher intensity of surface groups, groups that are essential for the successful grafting of the acrylic acid. After the grafting, the polyacrylic acid polymer play the role of pollutant adsorption especially for the positively charged ions. In

addition, polyacrylic acid is renowned for bonding strongly with iron oxides because of its tendency to have a negative charge, and thus stabilizing the magnetite in the case of the GAA bionanocomposites [31]. Since methylene blue is a cationic dye and the XPS spectra suggests an inherent negative surface charge, GAA is better equipped for adsorption of MB, all cationic dyes and metallic ions.

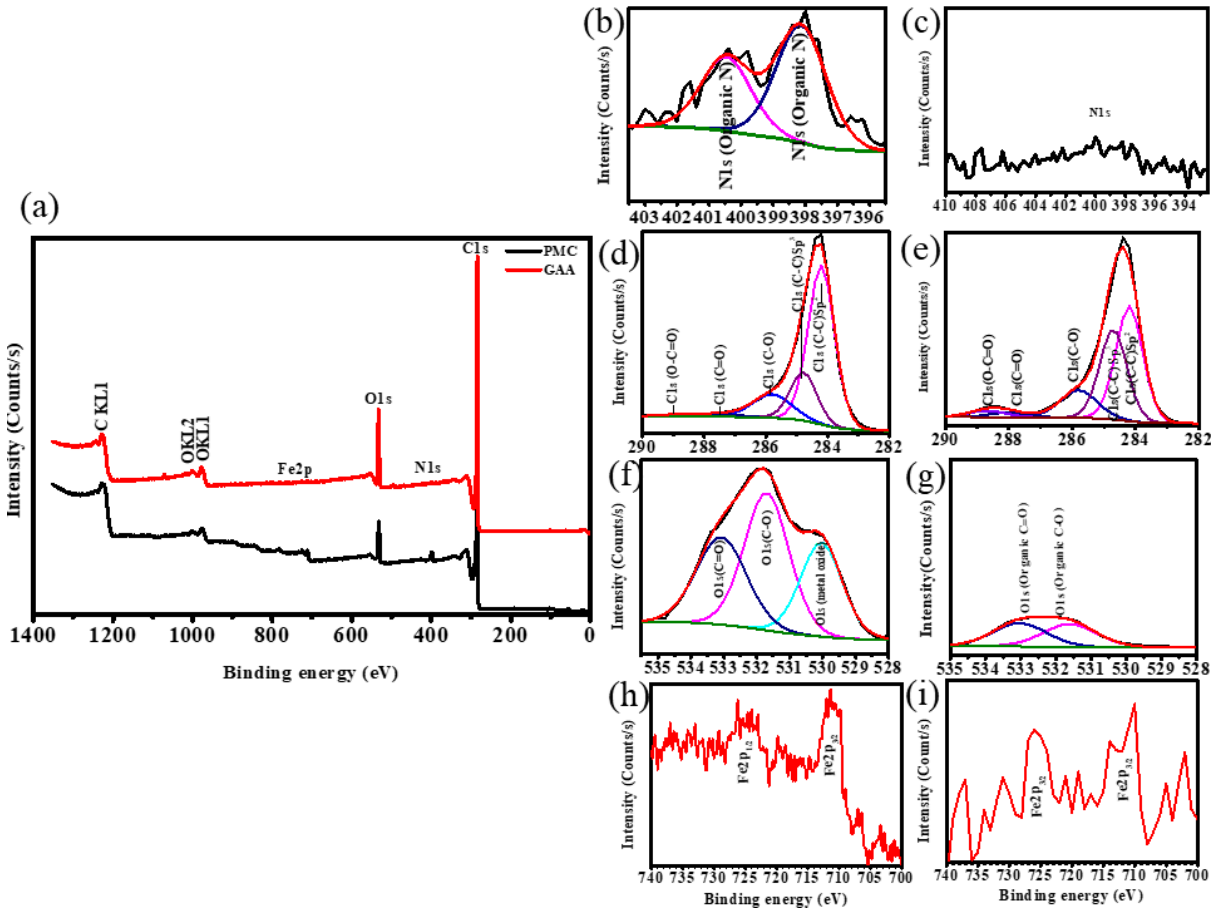

Figure 6.3 A comparison XPS results for PMC and GAA bionanocomposites (a) broad spectrum, (b) N1s, (d) C1s, (f) O1s, (h) Fe*2p* for GAA bionanocomposites and (c) N1s, (e) C1s, (g) O1s, (i) Fe*2p* for PMC bionanocomposites

6.4.2. Particle morphology, crystallinity, and internal microstructure analysis

6.4.2.1. *X-ray diffraction (XRD) studies*

X-ray diffraction analysis was used for structural determination and estimation of crystallite size of the bionanocomposites as shown in **Figure *6.4***. Prominent peaks were observed at 2θ values of 30.2°, 35.6°, 43.3°, 53.8°, 57.3°, 62.9° and 74.5° corresponding to the (220), (311),

(300), (422), (511) and (440) cubic, spinel magnetite phase crystalline planes respectively [32,33]. Additional, low intensity peaks at 11.0°, 15.4° and 22.7° were observed, of which the last peak is indexed to the (002) crystalline facet of cellulose [34,35]. It is worth noting that the cellulose peaks in GAA are more intense than in GAA. Similar observations have been made [17]. The increased crystallinity of cellulose after grafting the surface with acrylic acid could be due to The GAA bionanocomposites show a more intense (002) cellulose peak than in the PMC bionanocomposites. Additionally, the peaks attributed to magnetite have a higher intensity for the GAA bionanocomposites than the PMC bionanocomposites. This suggests higher crystallinity for magnetite in GAA than in PMC the additional crystallinity of magnetite and lignin/cellulose is attributed to the polyacrylic acid forming bonds with PMC through the surface groups of both the pinecone and the magnetite [17]. Surface groups on crystalline nanoparticles synthesized at low temperatures are associated with low crystallinity in that the bond strength of the atoms in the crystal is weakened by having these surface atoms bond with other atomic groups. Crystalline size was calculated using Scherer equation (Equation 6.1)[36].

- $D_c = \frac{k\lambda}{\beta Cos\theta}$ **Equation 6.1**

D_c is the crystalline size as determined from the length of the longest crystal facet; which is the 311 faced, k is the crystal shape factor; which is 0.89 for magnetite, λ is the x-ray wavelength, which is 0.154060 nm, β is the full width at half maximum height for the 311 peak and θ is the angle. Crystalline size for GAA is 13.14 nm and 11.6 nm for PMC of which the values are significantly close to the particle size as determined from TEM.

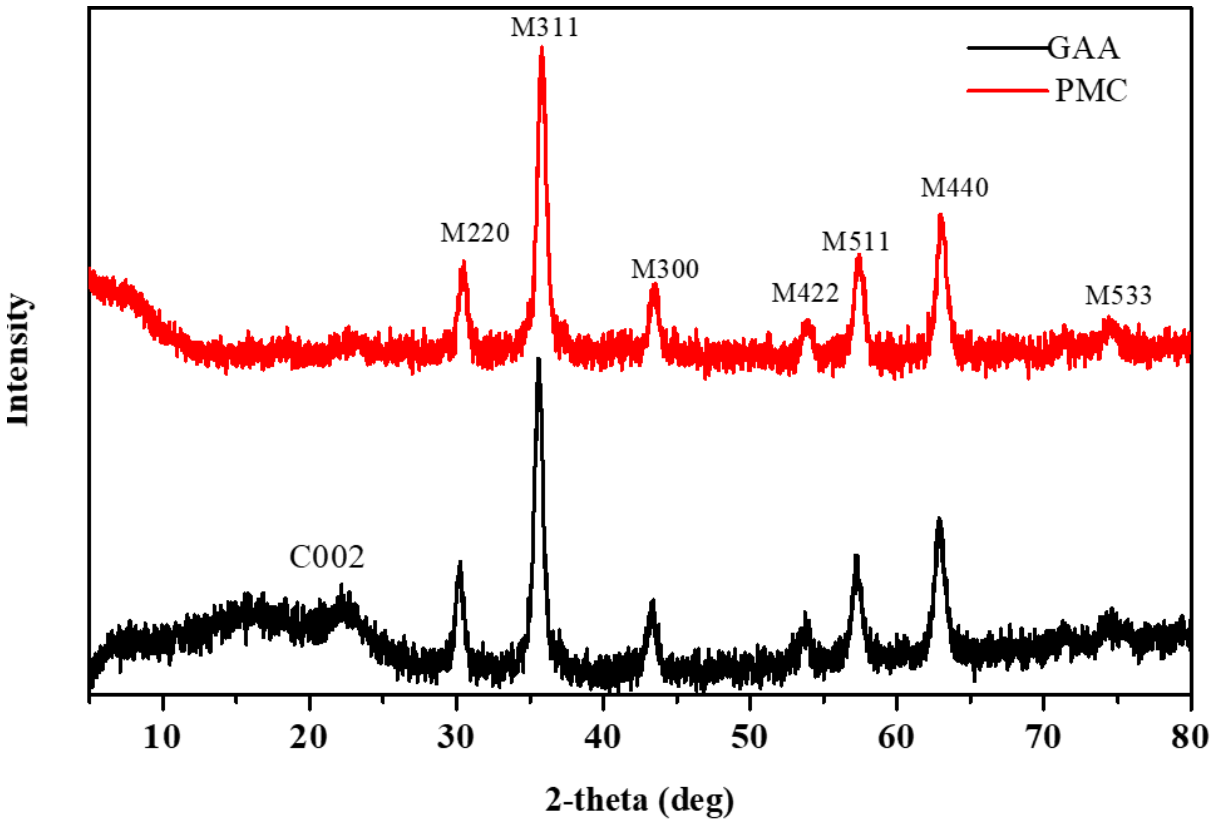

Figure 6.4: XRD spectra comparison for PMC and GAA

6.4.2.2. *Structural morphology*

Scanning electron microscopy was effectively used to study the microstructure and surface properties of these unique adsorbents. The HRSEM images show globular structures that are aggregated onto an uneven surface (***Figure 6.5***(a) and (b)). This configuration suggests a microporous structure with a rough surface area. Porosity and surface roughness suggest good surface area for adsorption of pollutants [37]. The internal pores were generated, and roughness of surface was increased after the incorporation of PMC with grafted acrylic acid (***Figure 6.5*** (b)). Additional variation in the morphology was observed in the PMC bionanocomposites having a higher mean aggregate size and a narrower size variation (46.5 $\pm$8.50 nm) than GAA (45.8$\pm$11.8 nm).

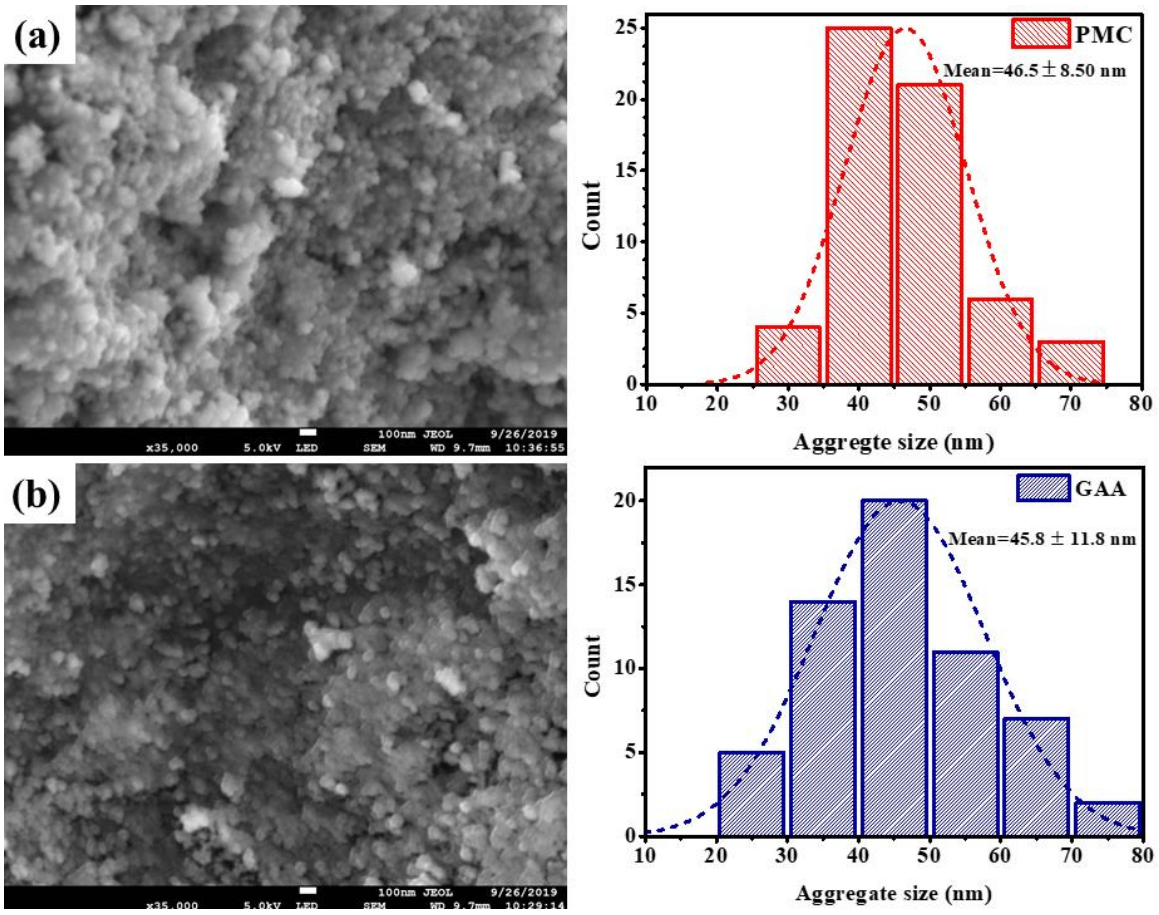

Figure 6.5: SEM images and aggregate sizes of (a) PMC and (b) PMC grafted with acrylic acid

TEM images in (***Figure 6.6*** (a) and (b)) shows the appearance of the synthesized pine magnetic composite and grafted with acrylic acid. The micrographs show spherical uniform morphology for the two bionanocomposites. The mean particle size for the PMC bionanocomposites is 14.0±3.20 nm while that for GAA is 13.00±1.90 nm. In addition, the particle size range for PMC is 6 – 24 nm, making it wider than that of GAA which is 8 – 16 nm. Modal particle size range for PMC is in the range 14 – 16 nm and accounts for 23% of the nanoparticle count while that of GAA is in the range 12 – 14 nm and accounts for 67% of the total particle count. The results suggest that GAA has a smaller particle size and has a narrow particle size distribution than PMC. A similar pattern is observed with respect to the nanoparticle aggregates as shown in HRSEM (Section 3.4). Small particle size and a narrow particle size range is associated with a larger surface area and hence higher adsorption capacity [38].

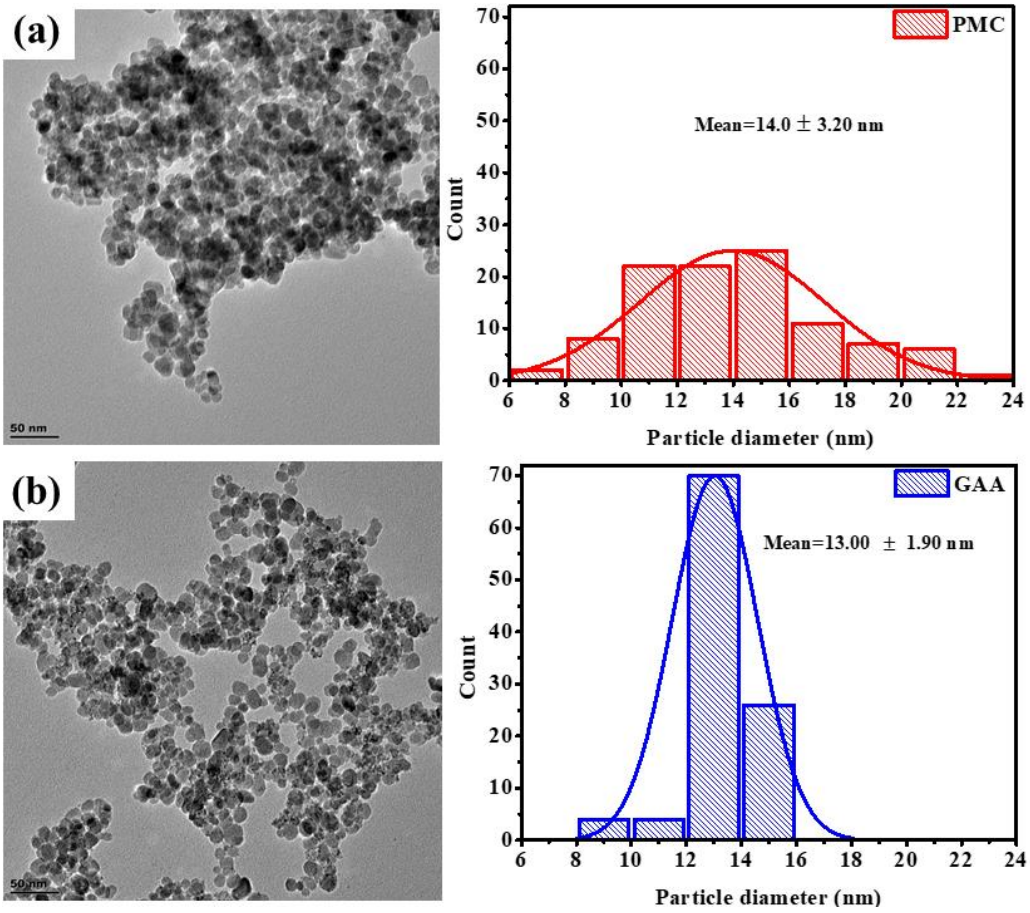

Figure 6.6 (a) TEM image and (b) and size distribution of PMC and GAA

6.4.3. Thermogravimetric analysis (TGA) investigations

Figure 6.7 (a) and (b) shows the changes in the thermal properties between GAA grafted acrylic acid after the incorporation of pinecone-magnetite composite PMC in the polymer matrix. It was observed that the initial decomposition of PMC occurred in the temperature range 50 – 210 °C while the final decomposition took place in the temperature range 210 – 800 °C. However, the thermal decomposition pattern of GAA has three decomposition stages. The first stage of decomposition occurred in the temperature range 50 – 250 °C giving weight loss that may be due to the loss of water molecules and volatile components. The second stage of decomposition occurred in the temperature range of 260 – 330 °C and the weight loss observed may be due the breakdown of the polymer matrix and grafting between different polymeric chains [39]. The final decomposition temperatures were observed at 530 and 610 °C, respectively, for PMC and GAA. The decomposition after the incorporation of the pinecone-magnetite composite occurred at higher temperatures with comparatively lower percentage loss. It was also observed that the thermal stability of the grafted composite

increased after incorporation of the PMC in the polymer matrix. DTA confirmed the maximum decomposition as it showed peaks due to degradation of various materials. Therefore, TGA and DTA studies clearly showed that the thermal stability of pinecone-magnetite composite increased when grafted with acrylic acid [40]. This is due to the higher amounts of acrylic acid used during the grafting process [41].

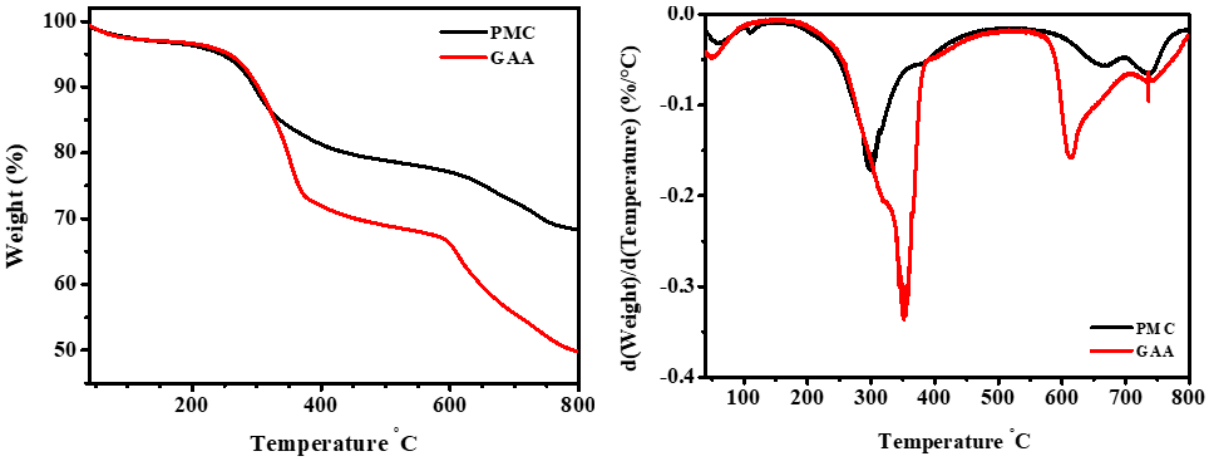

Figure 6.7 (a) TGA and (b) DTA curves of PMC and PMC grafted with acrylic acid

6.4.4. Surface area, pore volume and surface charge

The N_2 adsorption isotherms for the BET bionanocomposites are of the type II IUPAC category and the hysteresis loop of the type H3 [42] (***Figure 6.8***). This suggests that the bionanocomposites surface consists of micropores and the substrate consists of non-rigid plate like particles. There also exists a kink on the desorption arm of the GAA bionanocomposites and therefore suggesting a change in the desorption energy, a phenomenon that indicates the desorption of a multilayer adsorbate. It is further demonstrated that at there is a low curvature of the isotherms at the region from the onset of the flattening of the curve. This indicates that the onset of multilayer adsorption begins before the completion of monolayer adsorption [43]. BET surface area, pore volume and pore diameter of PMC was found to be 58.4 $m^2.g^{-1}$, 0.237 $cm^3.g^{-1}$ and 16.00 nm, respectively. These BET value decreased to 53.9 $m^2.g^{-1}$, the pore volume to 0.225 $cm^3.g^{-1}$ while the average pore size increased to 16.7 nm after the grafting of polyacrylic acid to form GAA. The surface analysis estimates the particle size to be 11.1 nm for GAA and 10.1 nm for PMC which is opposed to the particle size as determined by the TEM in (Section 3.3). It is worth noting that the BET surface area, and pore volume for the PMC in the current work is higher than the best performing PCM synthesized in the optimization

studies of our previous work [21]. These parameters were 54.80 $m^2.g^{-1}$ and 0.152 $cm^3.g^{-1}$ respectively. Furthermore, the BET surface area of the current study was lower than that of pure magnetite and still higher than that of NaOH-treated pinecone powder (***Table 6.2***). The smaller surface area in GAA is contrary to what would be expected given that GAA has small particle sizes and narrow particle size distribution as shown by the TEM micrograph analysis. HRSEM particle aggregate analysis shows GAA to have a smaller aggregate size compared to PMC. We attribute this small surface area to possible aggregation of the GAA bionanocomposite nanoparticles due to the polyacrylic acid coating of GAA nanoparticles making the particles to remain stuck together. Typically, a consideration of the surface area properties independent of the surface change and the properties of the solute warrant for a higher adsorptive surface area in an adsorbent [38,44].

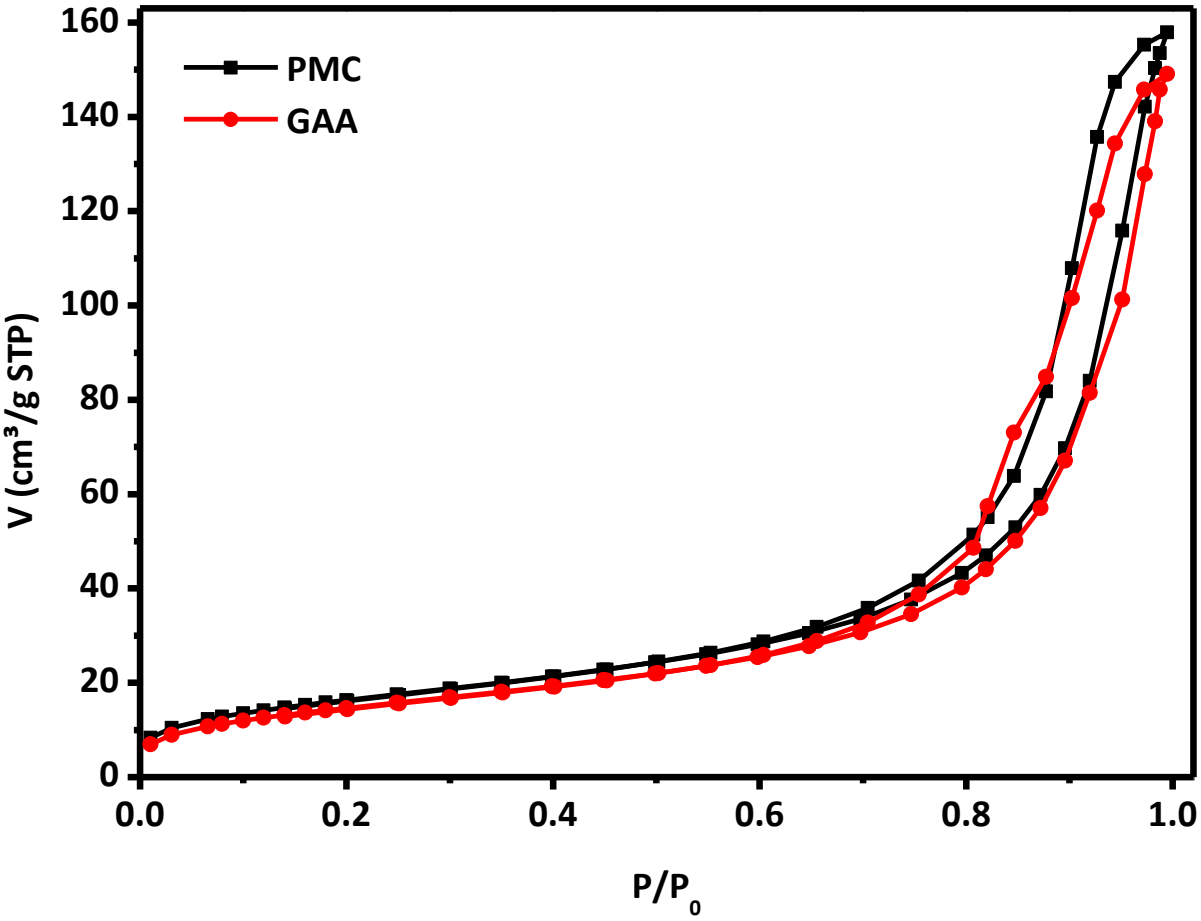

Figure 6.8 BET adsorption and desorption isotherms for the adsorptive bionanocomposites

Table 6.2 BET surface area and pore characteristics for PMC and GAA fabricated in this work compared to the surface properties for pure magnetite nanoparticles and NaOH-treated pine as synthesized in our previous work.

Properties	**Pure magnetite nanoparticles ***	**NaOH treated pine***	**Pinecone-magnetite composite (PMC)**	**Grafted acrylic acid (GAA)**
Surface area ($m^2.g^{-1}$)	113.60	2.25	58.4	53.9
Pore Volume ($cm^3.g^{-1}$)	0.632	0.0177	0.237	0.225
Ave. pore diameter (nm)	25.86	10.17	16.00	16.7
Surface charge (pH_{pzc})	-	-	8.56	6.80

*Parameters collected from our previous work for comparison [21].

The pH_f values of the supernatant were accurately recorded and the difference between the initial and final pH values (change in pH (ΔpH) = final pH – initial pH ($pH_f - pH_i$) were plotted against the pH_i. pH_{pzc} is observed when modification on the suitability of the synthesized materials is determined. It is known to be the pH at which the amount of positive charge on biosorbent surface equal to the amount of the negative charge, which means pH at which biosorbent surface has net electrical neutrality [23,44]. The pH_{pzc} of pinecone-magnetite composite (PMC) was found to be 8.56 and grafted pinecone-magnetite with acrylic acid (GAA) was found to be 6.8. The results are consistent with the occurrence of polyacrylic acid on the surface of GAA. Polyacrylic acid is known for having a net negative charge and hence the lower pH_{pzc} [31,45]. The decrease is attributed by the modification of the surface area by the $–COO^-$ functional groups from the acid. The net effect is that the GAA should have a higher dispersion at pH 12 due to the equilibrium shifting towards more negatively charged bionanoparticles.

6.4.5. Adsorptive removal of the MB dye

6.4.5.1. *Effect of pH on the adsorption of methylene blue*

The effect of pH on the PMC and GAA was studied in pH range 2 - 12. The pH has been found to exert profound effects on the removal of (MB) by these bionanomaterials (***Figure 6.9***). This is because it impacts on the adsorption sites of the adsorbent and the ionization process of the dye. Low adsorption capacity in the acidic medium might be due to the fact in acidic medium H^+ ions competed with the (MB) dye for the adsorption sites which inhibited the adsorption of

the dye and the process decreased the amount of the dye adsorbed. In the basic medium, the adsorbent became negatively charged and enhanced the adsorption of (MB) through electrostatic forces of attraction [46,47]**.** As demonstrated in ***Figure 6.9***, the pH of 12 was found to be the maximum high percentage removal for (MB). This is in keeping with the idea of the GAA bionanocomposites having more negative surface charge that PMC at pH=12.

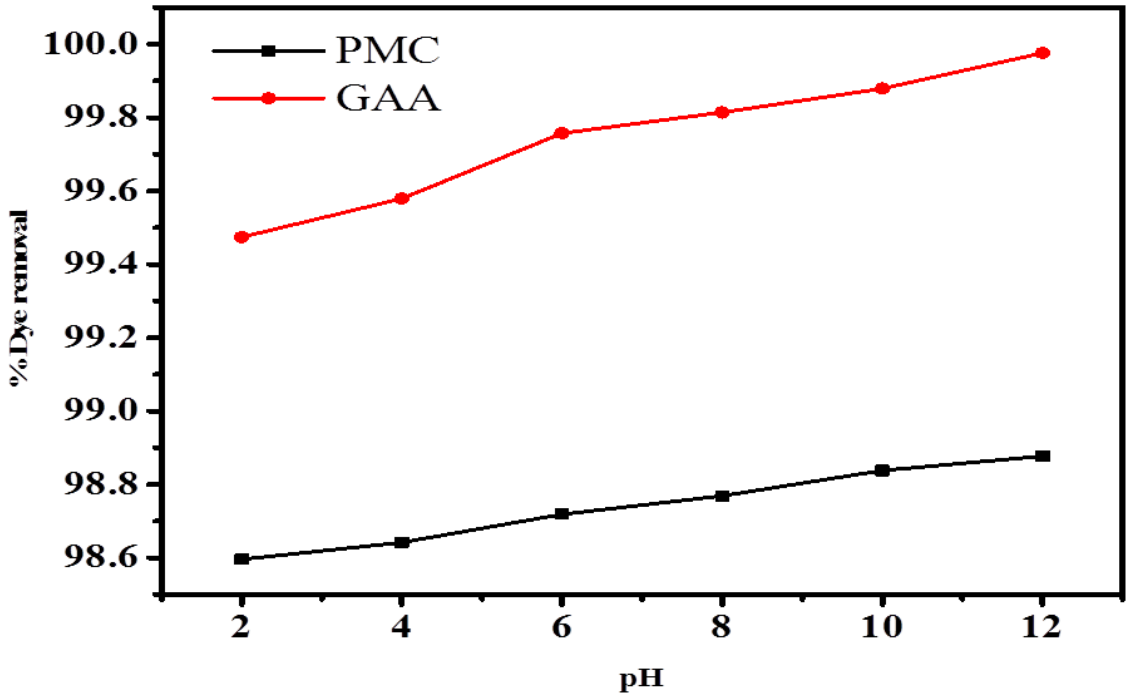

Figure 6.9 Effect of solution pH on MB adsorption of the PMC and GAA

6.4.5.2. *Effect of adsorbent dose on the adsorption of methylene blue*

A good adsorbent is known to have the ability to remove relatively high number of dyes at lower doses. ***Figure 6.10*** (a) and (b) show the effect of adsorbent dose on the percentage adsorption GAA bionanocomposites and is compared to that of PMC from our previous work [21]. The adsorbent was studied at different doses ranging from 0.1 g to 1.5 g in a neutral solution. From the results, an increase in adsorbent dose from 0.1 to 1.5 g resulted in a decrease in adsorption capacity from 120 to 15.5 $mg.g^{-1}$ for GAA, of which is a lower decrease compared to that of uncapped PMC as synthesized in our previous work. However, MB removal percentage removal sharply increased with an increase in adsorbent dosage from 99.3 to 99.9 % for GAA. It was observed that initially, the percentage adsorption of MB increases with increase in adsorbent dose. Constant adsorption was observed with further increase in the

amount of the adsorbent. Increase in adsorption of MB percentage is presumably due to the increase in the number of adsorption sites with an increase in the adsorbent dose [48]. Lastly, the optimum adsorbent dosage is 0.5 g for GAA whereas PMC had an optimum dosage at 1.4 g with the same removal efficiency. As such, capping PMC with acrylic acid enables lowers the adsorption dosage for the same removal efficiency.

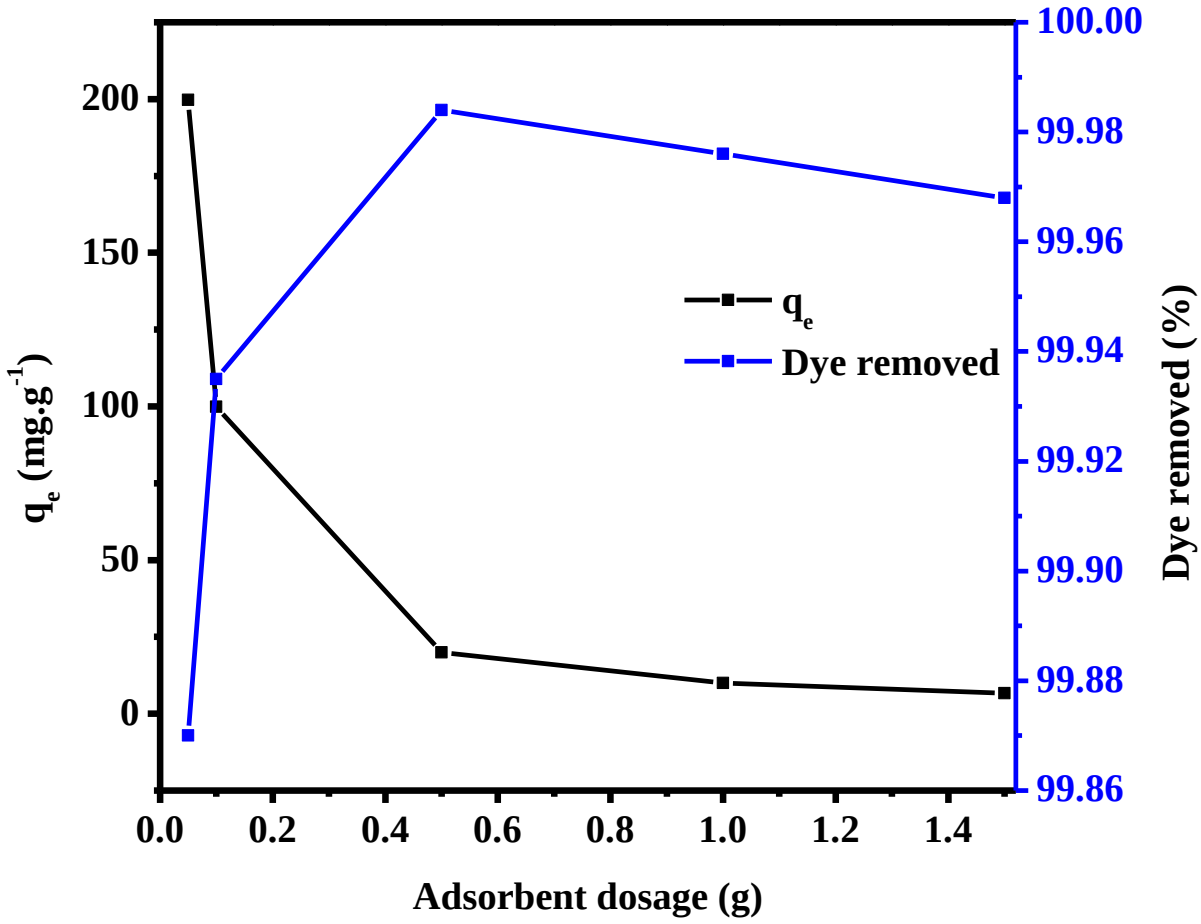

Figure 6.10 Effect of adsorbent dose on the (MB) adsorption for GAA

6.4.5.3. *Effect of contact time on the adsorption of (MB)*

The effect of contact time on the PMC and GAA for the adsorption of (MB) is shown in (***Figure 6.11***). The adsorption rate of the PMC and GAA bionanocomposites on the removal of (MB) was rapid in the beginning, proceeded at a slower rate and finally attained equilibrium at approximately 120 min which is influenced by the availability of the larger surface area of the adsorbent in the beginning. GAA had a slightly higher adsorption efficiency (98.7%)-an increase of 1% compared to that of PMC. When the surface adsorption sites became exhausted,

the uptake rate is then controlled by the rate at which the adsorbate is transported from the exterior to the interior sites of the adsorbent [49]. The adsorption, therefore, occurred due to attractive Van der Waals forces, electrostatic attractions, and fast diffusion onto the external surface of the adsorbent. In addition, the occurrence of polyacrylic acid on GAA as suggested by the XPS and FTIR spectroscopy results points to the possibility of GAA having a net negative charge and hence a higher affinity of the positively charged MB ion [45]. Additionally, the BET surface area properties suggest that the average pore diameter (which is higher in GAA) plays a more significant role in the adsorption of MB than the average surface area and the pore volume which are lower in GAA than in PMC ***Table 6.2***. In this scenario, the inherent negative charge of the polyacrylic acid enhances the adsorption of positively charged MB molecules to the point of enabling these molecules to permeate into the pores that are wider in GAA. Previous research has demonstrated that there molecular properties and the surface charge of an adsorbing substrate can give a different result than what would be predicted by N_2 BET adsorption [50,51]. Most importantly, the GAA maintains its adsorption efficiency even after coating with acrylic acid. This suggests that plant-based bionanoadsorbents can be made more environmentally friendly and compatible with bulk polymer structures without loss of adsorptive activity.

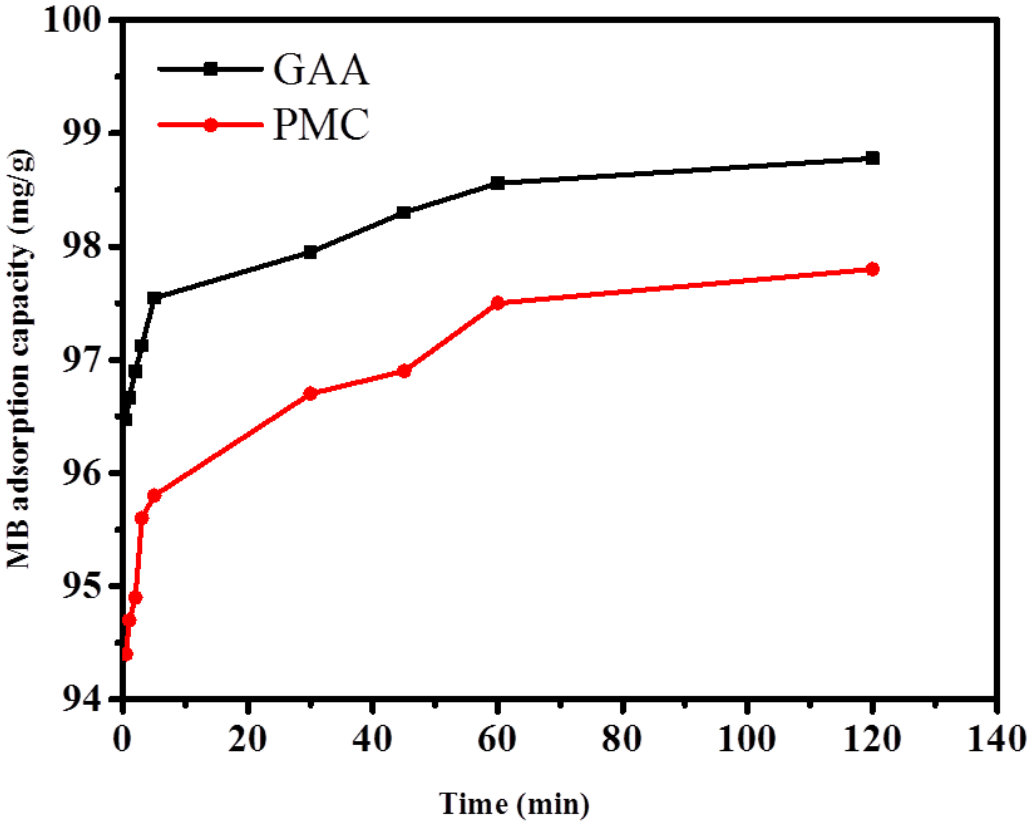

Figure 6.11 Effect of contact time at 100 mg.dm^3 on the (MB) adsorption of the PMC and GAA

6.4.6. Adsorption kinetics

Kinetic studies are of utmost importance to the adsorption process because they depict the uptake rate of adsorbate and control the residual time of the whole adsorption process [52]. To further understand the characteristics of the adsorption process, the kinetics study of adsorption of MB onto PMC and GAA was explored on the pseudo-first order and pseudo second order models. These models were applied to fit experimental data obtained from the batch experiments. The linear forms of the pseudo-first order and pseudo-second order are represented by the following equation

$$Ln(q_e - q_t) = Lnq_e - k_{1t} \qquad \text{Equation 6.2}$$

$$\frac{t}{q_t} = \frac{1}{k_2 . q_e^2} + \frac{t}{q_e} \qquad \text{Equation 6.3}$$

where K_1 (min^{-1}) and K_2 ($g.mg^{-1}.min^{-1}$) are the rate constants of the pseudo-first order, pseudo-second order, respectively. The parameters q_e and q_t ($mg.g^{-1}$) are the amount of MB adsorbed at equilibrium and at time t (min). The values of the K_1 and q_{mod} were calculated from the slopes ($-K_1$) and the intercepts ($\ln q_e$) of the plots of $\ln (q_e - q_t)$ vs. t, respectively, and are reported in ***Table 6.3*** and ***Table 6.4***. The values of regression correlation coefficients (R^2) for pseudo- first order is not close to unity and a large difference in the values of q_{mod} and q_{exp} for the adsorbent concluded that the pseudo-first-order model is not suitable to describe the kinetic profile of the adsorption. The adsorption data fitted the pseudo-second order with regression coefficient of 1 and the q_e values coincided with the expected q_e values ($q_e$exp). All this suggests that the adsorption obeys the pseudo-second order model meaning the controlling rate step is chemisorption.

Table 6.3 Kinetic parameters and correlation coefficients for MB adsorption at different concentrations onto PMC (299K, pH 12)

Conc.	First order kinetic model				Second order kinetic model			
	k_1 (min^{-1})	$q_e$exp ($mg.g^{-1}$)	$q_e$mod ($mg.g^{-1}$)	R^2	k_2 ($g.mg^{-1}.min^{-1}$)	H ($mg.g^{-1}\ min^{-1}$)	$q_e$mod ($mg.g^{-1}$)	R^2
100	0.0492	9.9118	5.27722	0.9689	0.0057	0.55988	9.9108	1
150	0.0362	14.8755	3.87637	0.9243	0.0048	1.06293	14.881	1
200	0.0273	19.8701	3.27036	0.9625	0.0036	1.42287	19.8807	1
250	0.0147	24.7851	8.52242	0.973	0.0013	0.79649	24.7525	1
300	0.0147	29.7488	8.11164	0.9633	0.001	0.88577	29.7619	1

Table 6.4 Kinetic parameters and correlation coefficients for MB adsorption at different concentrations onto GAA (299K, pH 12)

Conc.	First order kinetic model				Second order kinetic model			
	k_1 (min^{-1})	$q_e$exp ($mg.g^{-1}$)	$q_e$mod ($mg.g^{-1}$)	R^2	k_2 ($g.mg^{-1}.min^{-1}$)	H ($mg.g^{-1}\ min^{-1}$)	$q_e$mod ($mg.g^{-1}$)	R^2
100	0.0348	9.90412	3.9626	0.8517	0.0119	1.16655	9.90099	1
150	0.0257	14.8888	4.36667	0.8489	0.0058	1.28437	14.881	1
200	0.0318	19.8668	4.37935	0.884	0.0028	1.10668	19.8807	1
250	0.0224	24.9004	3.85318	0.9089	0.0024	1.48511	24.8756	1
300	0.0459	29.9123	4.64411	0.9298	0.0007	0.62749	29.9401	1

6.4.6.1. *Intra-particle diffusion*

The intra-particle diffusion model was also employed to identify the steps involved during adsorption process. The possibility of intra particle diffusion of MB onto the PMC and GAA were investigated using the intra-particle diffusion model

The possibility of intra-particle diffusion of MB onto the prepared activated carbon was

$$q_t = t^{0.5} + C \qquad \text{Equation 6.4}$$

Where qt is the amount of dye adsorbed ($mg.g^{-1}$) at time t; C is the boundary layer thickness and Kp is the intra-particle diffusion rate constant ($mg.g^{-1}\ min^{-0.5}$). The plots of the amount adsorbed, qt versus $t^{0.5}$ at different initial concentration are shown in ***Figure 6.12*** and ***Figure 6.13*** respectively. The intra-particle diffusion constants at different initial concentration are shown in ***Table 6.5***. As shown in ***Figure 6.12*** and ***Figure 6.13***, plots represent multi-linearity, meaning that two or more steps take place. The initial region represents the diffusion adsorption stage, attributing to the diffusion of MB dye through the solution to the external surface of the adsorbent meaning the external diffusion. The second region shows a gradual adsorption stage, thus corresponds to the intra –particle diffusion of the dye molecules through the pores of the adsorbent (intra-particle diffusion). The observed multilinearity plots suggests that the intra-particle diffusion is not a rate the rate limiting step [53]. The values for K_p and C were calculated from the slope and intercept plots of q_t versus $t^{0.5}$ and the results are summarized in ***Table 6.5***. K_p increase with increase in concentration, and this is an attribution to the external mass transfer of MB to the adsorbent surface. The increase in the intercept (C) of the intra particle diffusion reflects the boundary layer effect. This implies a significant contribution of the surface adsorption in the rate limiting step [54], thus meaning the limiting step contributed in the surface adsorption.

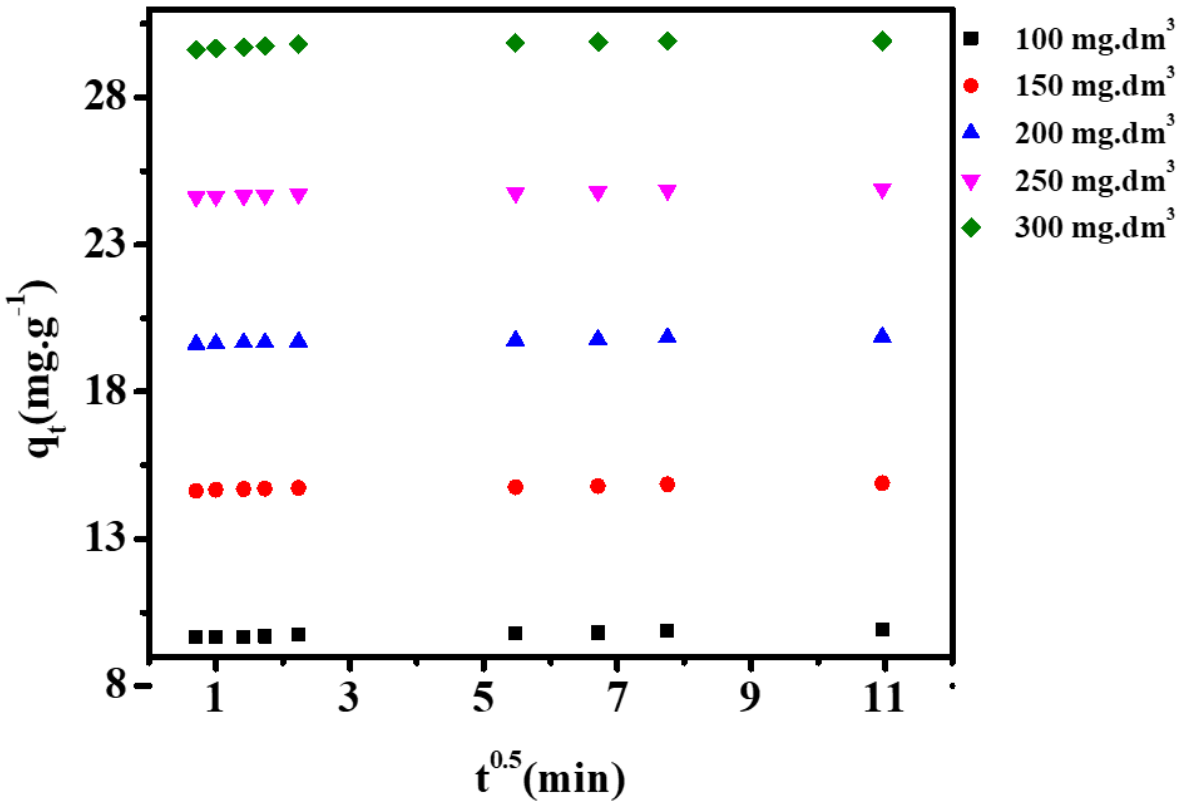

Figure 6.12 Intra-particle diffusion plots for the adsorption of MB onto GAA

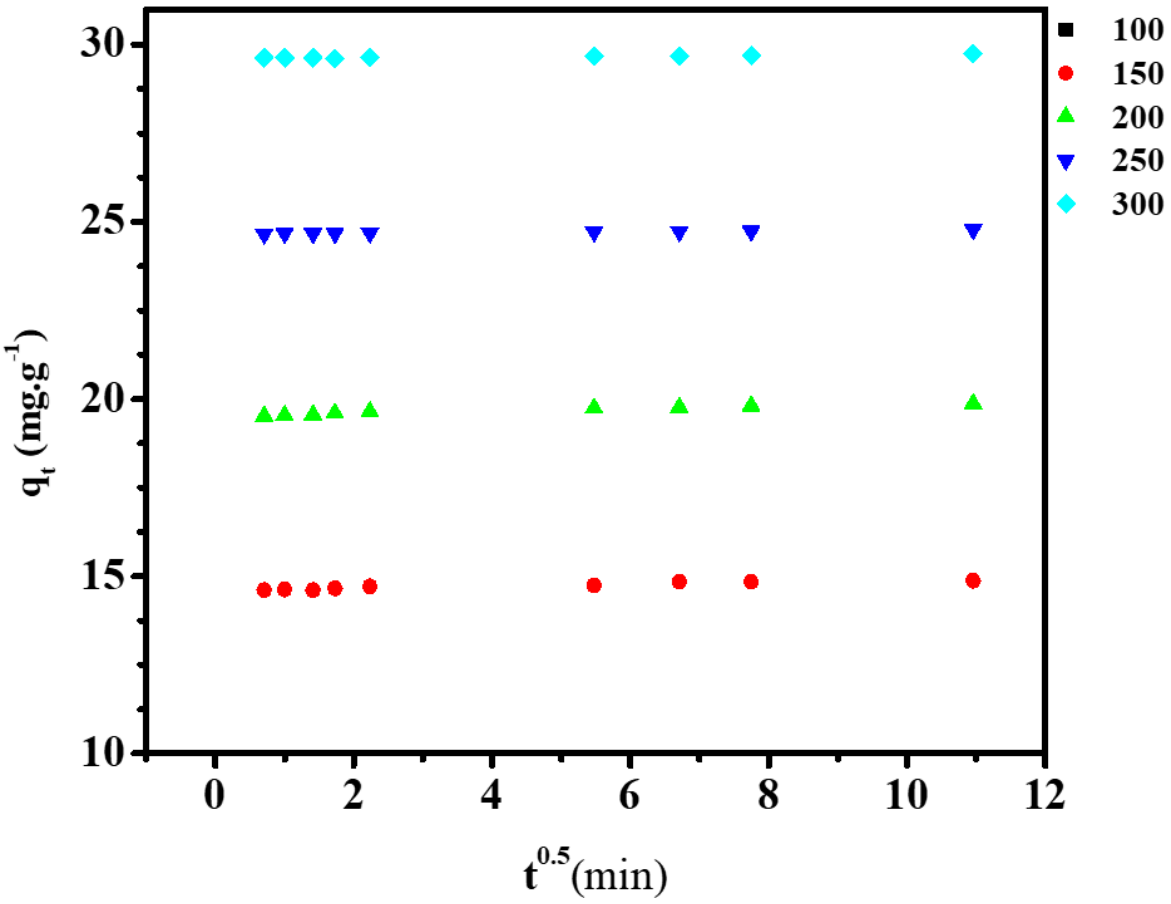

Figure 6.13 Intra-particle diffusion plots for the adsorption of MB onto PMC

Table 6.5 Intra-particle diffusion model parameters for the adsorption of MB onto GAA and PMC

Concentration	**GAA**			**PMC**		
	K_p (mg.g^{-1}min$^{0.5}$)	**C (mg.g^{-1})**	**R^2**	**K_p (mg.g^{-1}min$^{0.5}$)**	**C (mg.g^{-1})**	R^2
100	0.026	9.6455	0.925	0.022	9.7152	0.8514
150	0.0228	14.646	0.9367	0.028	14.603	0.9087
200	0.0234	19.631	0.9484	0.034	19.534	0.9495
250	0.0262	24.619	0.9607	0.011	24.654	0.9759
300	0.0263	29.678	0.9834	0.012	29.611	0.9828

6.4.7. Adsorption isotherms

Isotherm studies can describe the qualitative information of the adsorbate interaction with adsorbent at constant temperature [55]. The isotherm provides the relationship between the concentration of dye in solution and the amount of dye adsorbed on the solid phase when both phases are in equilibrium. The equilibrium data were analyzed by fitting Langmuir, Freundlich an Temkin isotherm models. The Langmuir isotherm model presume a monolayer adsorption onto the surface containing finite number of adsorption sites of uniform energies of adsorption with no transmigration of adsorbate in the surface plane [35].

The Langmuir isotherm model is represented by the following equation:

- $\frac{C_e}{q_e} = \frac{1}{q_m.k_L} + \frac{C_e}{q_m}$ Equation 6.5

where q_e is the amount of dye adsorbed at the equilibrium time ($mg.g^{-1}$), C_e is the equilibrium dye concentration ($dm^3.mg^{-1}$), q_m is the maximum adsorption capacity ($mg.g^{-1}$) and K_L is the Langmuir adsorption equilibrium constant ($dm^3.mg^{-1}$). Freundlich linear expression was represented by

- $logq_e = logk_F + \frac{1}{C_e}$ Equation 6.6

Where K_F is the equilibrium adsorption coefficient ($dm^3.mg^{-1}$) and 1/n is an empirical constant. Temkin isotherm model describes the chemisorption between the adsorbate and adsorbent Temkin model is expressed by:

- $q_e = \frac{RT}{b_T.lnK} + \frac{RT}{b_T.C_e}$ Equation 6.7

where K is Temkin isotherm equilibrium binding constant ($L.mg^{-1}$) related to the maximum binding energy, b_T is Temkin isotherm constant ($J.mol^{-1}$) related to the heat of adsorption, R is the universal gas constant ($8.314J.mol^{-1}K^{-1}$) and T is the absolute temperature.

The isotherms calculated from the experimental data and the parameters obtained from the linear regression by all the three models is summarized in ***Table 6.6*** and ***Table 6.7***. According to the observation, R^2 values for the Langmuir are higher than those of the Freundlich isotherm model, which suggests the Langmuir isotherm is suitable for defining the adsorption equilibrium of MB onto GAA and PMC. This implies the adsorption process occurs in a

homogeneous surface giving homogeneous distribution of active sites on the GAA. The value of K_L shows a decrease with increase in temperature, which implies that low temperature favored the adsorption process. The adsorption is evidently favorable as Freundlich constant n is 2.27, 2.08 and 1.74 respectively for GAA and 2.47, 2.23 and 2.02 for PMC, they are all higher than 1. Higher K_F indicate higher adsorption capacity meaning temperature 299 K gives better adsorption. Temkin constants K, b_T together with R^2 values are also summarized in ***Table 6.6*** and ***Table 6.7***. The heat of adsorption of all the molecules in the layer showed decrease linearly with coverage due to adsorbate/adsorbent interactions. K, decreased as the experimental temperature increased from 299 to 309 K, which implies that the adsorption process is exothermic and favored at higher temperatures [56]

Table 6.6 Isotherm parameters for the adsorption of MB onto GAA

Isotherms	**Parameters**	**Temperature**		
		299	**304**	**309**
Langmuir	q_m (mg.g^{-1})	63.3	67.1	81.3
	K_L (dm^3.mg^{-1})	0.09	0.08	0.05
	R^2	0.9980	0.9950	0.9901
Freundlich	K_F (dm^3.mg^{-1})	10.1	9.2	7.4
	N	2.27	2.08	1.74
	R^2	0.9588	0.9514	0.9728
Temkin	b_T (J.mol^{-1})	36.24	40.71	49.6
	K (L.mg^{-1})	1.26	1.13	1.06
	R^2	0.9892	0.9836	0.9900

Table 6.7 Isotherm parameters for the adsorption of MB onto PMC

Isotherms	**Parameters**	**Temperature**		
		299	**304**	**309**
Langmuir	q_m (mg.g^{-1})	60.6	64.5	68.5
	K_L (dm^3.mg^{-1})	0.11	0.10	0.09
	R^2	0.9944	0.9872	0.9650
Freundlich	K_F (dm^3.mg^{-1})	11.7	10.7	9.8
	N	2.47	2.23	2.03
	R^2	0.8892	0.8760	0.8378
Temkin	b_T (J.mol^{-1})	35.21	39.77	46.12
	K (L.mg^{-1})	2.17	1.21	1.10
	R^2	0.9582	0.9484	0.9108

6.4.8. Reusability of the biomass nanoadsorbents

Adsorbents obtained from biomass are generally economic because they require minimum processing and therefore, they reduce production costs by using a cheap raw material and eliminating energy costs associated with any thermal treatment [57]. ***Figure 6.14*** shows the feasibility of regeneration and reusability of the pinecone-magnetite composite grafted with acrylic acid. Adsorption-desorption reaction cycles were repeated four times using 0.01, 0.05 and 0.1 M HCl as the desorbing agents. Approximately 1 g of GAA powder was dispersed in 200 mL of 100 $mg.L^{-1}$ of an MB solution. Results showed a decrease from 42 to 12 $mg.g^{-1}$ for 0.1 M HCl, 23 to 11 for 0.05 M and 19 to 9 $mg.g^{-1}$ for 0.01 M after cycle 4. The results still demonstrate that the use of 0.1M HCl as a desorbing agent is the most feasible. In addition, in spite of the loss of adsorption capacity is comparable to that of other plant-derived biochar [58] and previous works in which pinecone-magnetite was used as an adsorbent [59].

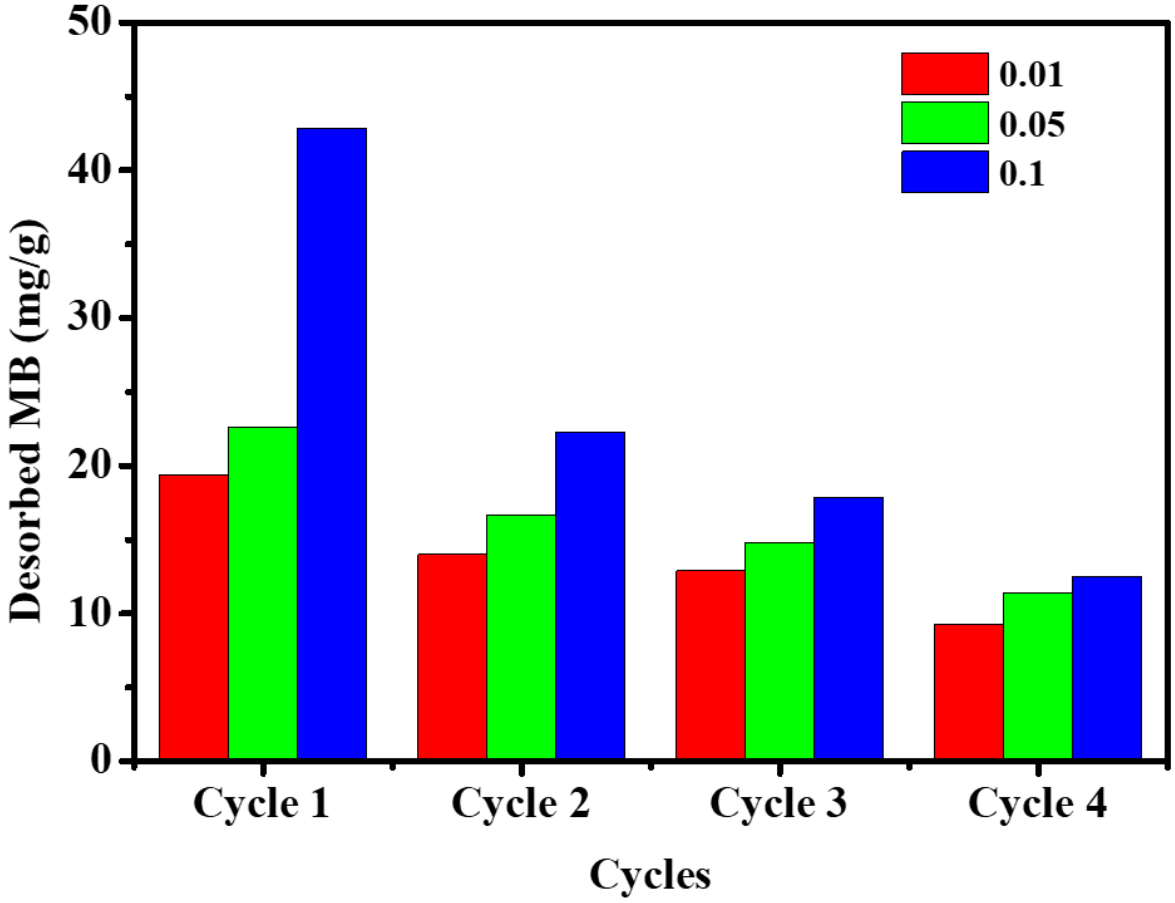

Figure 6.14 Regeneration characteristics of MB adsorbed

6.4.9. Mechanisms of adsorption

The removal of (MB) by adsorption on GAA was found to be rapid at the initial period of contact time and then become slow and stagnate with increase in contact time. It is known that for a solid/liquid adsorption process, the solute transfer is usually characterized by either external mass transfer and/or intra-particle diffusion [34]. The mechanism of (MB) removal from aqueous phase by adsorption is therefore assumed to consist of four steps: (i) migration of the dye molecules from the bulk solution to the surface of the sorbent, (ii) diffusion through the boundary layer to the surface of the sorbent, (iii) adsorption at sites and (iv) intra-particle diffusion into the interior of the adsorbent [54,60]. The overall rate of adsorption is controlled by the slowest step, which would be either film diffusion or pore diffusion [39]. However, the controlling step might be distributed between intra-particle and external transport mechanisms and external diffusion will be involved in the adsorption process.

The adsorption of (MB) onto pinecone particles may be controlled due to film diffusion at earlier stages, and as the adsorbent particles are loaded with dye ions (as shown is Section 3.9) the sorption process may be controlled due to intra-particle diffusion. In addition to this, the adsorption capacity of the adsorbent was determined by the structure and functional behavior of the adsorbate molecule, surface characteristics of the adsorbent and mass transport process. The FTIR spectra of NaOH treated pine, PMC and GAA adsorbent showed interaction sites between the biosorbents and dye molecule. If we compared the FTIR spectrum of GAA, the characteristic peaks shifted slightly (***Figure 6.1***). The -OH shifted from 3350 to 3315 cm^{-1} this was an attribution of modification of the adsorbent (PMC to GAA) [44]. The C=O stretching vibration shifted from 1600 to 1265cm^{-1} for MB and the asymmetric and symmetric stretching vibration of C-O-C shifted from 1049 to 1020 cm^{-1}. Insertion of the Fe-OH and Fe-O was illustrated successfully at 1622 and 569 cm^{-1} respectively. C-H stretching vibration shifted from 2856 to 1416 cm^{-1}. All these features demonstrate the specific electrostatic and hydrogen bonding interactions between the functional groups of the MB and the bionanosorbents. The adsorption capacity of different adsorbents towards methylene blue dye has been compared to pinecone-magnetite composite reported in the literature presented in ***Table 6.8***.

Table 6.8 Comparison of adsorption capacities of various adsorbents for removal of MB dye

Composite	nanomaterial	Adsorbate material (adsorption capacity, q_m ($mg.g^{-1}$)	Mechanism	Reference
Pinecone biomass (*Pinus radiate*)	_	MB (109.89)	Intra particle diffusion	[61]
M-MWCNTs	Fe_3O_4	MB (48.06)	π-π stacking interaction	[62]
Fig tree	Fe_3O_4	MB (61.72)	_	[63]
Magnetite-palm shell-waste activated carbon	Fe_3O_4	MB (163.3)	π-π electron donor acceptor interaction	[64]
Banana peel	Fe_3O_4	MB (862)	_	[65]

It is hereby demonstrated that the formation of polyacrylic acid on the surface of the PMC bionanocomposites does not reduce the adsorption efficiency of GAA. These characteristics are due to the reduction of the point of zero charge and by providing a multi-layered particle in which each layer actively adsorbs. This multi-layered adsorption is further promoted by the fact that each of the materials in the binanocomposites are rich in surface groups, mainly oxidative groups. The additional effect of polyacrylic acid coating is reduction in particle size of the magnetite nanoparticles, which translates to a large adsorptive surface area for GAA bionanocomposites.

6.5. Conclusion

The grafting of acrylic acid onto pinecone-magnetite bionanocomposites has been successfully carried out and resulted into the encapsulation of the PMC bionanocomposites with polyacrylic acid. This reduces reduce the particle size of magnetite and the size of the GAA aggregates as predicted by TEM and SEM respectively. Furthermore, this encapsulation results in the reduction of the point of zero charge and increased crystallinity of the magnetite. These features, together with the improved crystallinity of magnetite in the GAA bionanocomposites, improve the adsorptive capacity towards cationic species such as the MB organic ion in spite of the smaller surface area and pore diameter and of the GAA bionanocomposites. These results suggest that the larger pore diameter in GAA, molecular properties of MB and the solution

properties play a significant role in the adsorption capacity for the bionanocomposites more than the available surface area. The parameters influencing adsorption such as solution pH, contact time and adsorbent dose showed significant influence on the graft polymerization process. The adsorption kinetics and isotherm studies showed that the adsorption process obey pseudo second order kinetics and Langmuir isotherm. GAA and MB interaction mechanism was confirmed by intra particle diffusion. The adsorbent also showed improvement in the adsorption capacity and reusability promising to be used for removal of dyes in an industrial scale. This is owing to the polyacrylic acid on GAA and its interaction with water to produce a net negative surface charge. The adsorption is a factor of the net surface charge of the bionanocomposites at pH 12. With GAA having a lower pH_{pzc} that PMC, the net charge of the bionanoparticles has shifted more towards negative than in PMC.

6.6. References

[1] P.G. Jessop, S. Trakhtenberg, J. Warner, The twelve principles of green chemistry, ACS Symp. Ser. 1000 (2009) 401–436. https://doi.org/10.1021/bk-2009-1000.ch012.

[2] R. Jose Varghese, N. Zikalala, E.H.M. Sakho, O.S. Oluwafemi, Green synthesis protocol on metal oxide nanoparticles using plant extracts, in: S. Thomas, A.T. Sani, P. Velayudhan (Eds.), Colloid. Met. Oxide Nanoparticles-Synthesis, Charact. Appl., 3rd ed., Amsterdam, 2020: pp. 67–82. https://doi.org/10.1016/b978-0-12-813357-6.00006-1.

[3] S. Iqbal, C. Zahoor, S. Musaddiq, M. Hussain, R. Begum, A. Irfan, M. Azam, Z.H. Farooqi, Silver nanoparticles stabilized in polymer hydrogels for catalytic degradation of azo dyes, Ecotoxicol. Environ. Saf. 202 (2020) 110924. https://doi.org/10.1016/j.ecoenv.2020.110924.

[4] M.K. Corbierre, N.S. Cameron, M. Sutton, S.G.J. Mochrie, L.B. Lurio, A. Rühm, R.B. Lennox, Polymer-stabilized gold nanoparticles and their incorporation into polymer matrices, J. Am. Chem. Soc. 123 (2001) 10411–10412. https://doi.org/10.1021/ja0166287.

[5] S. Davari, M. Omidkhah, S. Salari, Role of polydopamine in the enhancement of binding stability of TiO_2 nanoparticles on polyethersulfone ultrafiltration membrane, Colloids Surfaces A Physicochem. Eng. Asp. 622 (2021). https://doi.org/10.1016/j.colsurfa.2021.126694.

[6] T. Zhang, J. Liu, F. Zhou, S. Zhou, J. Wu, D. Chen, Q. Xu, J. Lu, Polymer-Coated Fe2O3 Nanoparticles for Photocatalytic Degradation of Organic Materials and Antibiotics in Water, ACS Appl. Nano Mater. 3 (2020) 9200–9208. https://doi.org/10.1021/acsanm.0c01829.

[7] T. Xaba, Green synthesis of ZnS nanoparticles and fabrication of ZnS – chitosan nanocomposites for the removal of Cr(VI) ion from wastewater, Green Process. Synth. 10 (2021) 374–383. https://doi.org/https://doi.org/10.1515/gps-2021-0026.

[8] L.M. Gilbertson, J.B. Zimmerman, D.L. Plata, J.E. Hutchison, P.T. Anastas, Designing nanomaterials to maximize performance and minimize undesirable implications guided by the Principles of Green Chemistry, Chem. Soc. Rev. 44 (2015) 5758–5777.

https://doi.org/10.1039/c4cs00445k.

[9] L. Nie, P. Chang, C. Ji, F. Zhang, Q. Zhou, M. Sun, Poly (acrylic acid) capped iron oxide nanoparticles via ligand exchange with antibacterial properties for biofilm applications, Colloids Surfaces B Biointerfaces. 197 (2021) 111385. https://doi.org/10.1016/j.colsurfb.2020.111385.

[10] R. Bywalez, H. Karacuban, H. Nienhaus, C. Schulz, H. Wiggers, Stabilization of mid-sized silicon nanoparticles by functionalization with acrylic acid, Nanoscale Res. Lett. 7 (2012) 1–7. https://doi.org/10.1186/1556-276X-7-76.

[11] Z.W. Heng, W.C. Chong, Y.L. Pang, C.H. Koo, Self-assembling of NCQDs-TiO_2 nanocomposite on poly(acrylic acid)-grafted polyethersulfone membrane for photocatalytic removal and membrane filtration, Mater. Today Proc. 2020 (2021). https://doi.org/10.1016/j.matpr.2021.02.021.

[12] B.S. Choudri, Y. Charabi, M. Baawain, M. Ahmed, Textiles, Water Environ. Res. 89 (2017) 1424–1440. https://doi.org/10.2175/106143017X15023776270502.

[13] Y. Dai, Q. Sun, W. Wang, L. Lu, M. Liu, J. Li, S. Yang, Y. Sun, K. Zhang, J. Xu, W. Zheng, Z. Hu, Y. Yang, Y. Gao, Y. Chen, X. Zhang, F. Gao, Y. Zhang, Utilizations of agricultural waste as adsorbent for the removal of contaminants: A review, Chemosphere. 211 (2018) 235–253. https://doi.org/10.1016/j.chemosphere.2018.06.179.

[14] B. Makgabutlane, L.N. Nthunya, M.S. Maubane-Nkadimeng, S.D. Mhlanga, Green synthesis of carbon nanotubes to address the water-energy-food nexus: A critical review, J. Environ. Chem. Eng. (2020) 104736. https://doi.org/10.1016/j.jece.2020.104736.

[15] M.A. Martín-Lara, G. Blázquez, M. Calero, A.I. Almendros, A. Ronda, Binary biosorption of copper and lead onto pine cone shell in batch reactors and in fixed bed columns, Int. J. Miner. Process. 148 (2016) 72–82. https://doi.org/10.1016/j.minpro.2016.01.017.

[16] N. Ayrilmis, U. Buyuksari, T. Dundar, Waste Pine Cones as a Source of Reinforcing Fillers for Thermoplastic Composites, J. Appl. Polym. Sci. 117 (2010) 2324–2330. https://doi.org/10.1002/app.

[17] S. Wohlhauser, G. Delepierre, M. Labet, G. Morandi, W. Thielemans, C. Weder, J.O. Zoppe, Grafting Polymers from Cellulose Nanocrystals: Synthesis, Properties, and Applications, Macromolecules. 51 (2018) 6157–6189. https://doi.org/10.1021/acs.macromol.8b00733.

[18] E. Kavci, Malachite green adsorption onto modified pine cone: Isotherms, kinetics and thermodynamics mechanism, Chem. Eng. Commun. 0 (2020) 1–10. https://doi.org/10.1080/00986445.2020.1715961.

[19] N.M. Mahmoodi, B. Hayati, M. Arami, C. Lan, Adsorption of textile dyes on Pine Cone from colored wastewater: Kinetic, equilibrium and thermodynamic studies, Desalination. 268 (2011) 117–125. https://doi.org/10.1016/j.desal.2010.10.007.

[20] E. Illés, E. Tombácz, The role of variable surface charge and surface complexation in the adsorption of humic acid on magnetite, Colloids Surfaces A Physicochem. Eng. Asp. 230 (2003) 99–109. https://doi.org/10.1016/j.colsurfa.2003.09.017.

[21] K.N.G. Mtshatsheni, A.E. Ofomaja, E.B. Naidoo, Synthesis and optimization of reaction variables in the preparation of pine-magnetite composite for removal of methylene blue dye, South African J. Chem. Eng. 29 (2019) 33–41. https://doi.org/10.1016/j.sajce.2019.05.002.

[22] A. Pholosi, E.B. Naidoo, A.E. Ofomaja, Intraparticle diffusion of Cr(VI) through biomass and magnetite coated biomass: A comparative kinetic and diffusion study, South African J. Chem. Eng. 32 (2020) 39–55. https://doi.org/10.1016/j.sajce.2020.01.005.

[23] E. McCafferty, Relationship between the isoelectric point (pHpzc) and the potential of zero charge (Epzc) for passive metals, Electrochim. Acta. 55 (2010) 1630–1637. https://doi.org/10.1016/j.electacta.2009.10.040.

[24] A.L. Vega-Negron, L. Alamo-Nole, O. Perales-Perez, A.M. Gonzalez-Mederos, C. Jusino-Olivencia, F.R. Roman-Velazquez, Simultaneous adsorption of cationic and anionic dyes by chitosan/cellulose beads for wastewaters treatment, Int. J. Environ. Res. 12 (2018) 59–65. https://doi.org/10.1007/s41742-018-0066-2.

[25] V. Ţucureanu, A. Matei, A.M. Avram, FTIR Spectroscopy for carbon family study, Crit. Rev. Anal. Chem. 46 (2016) 502–520. https://doi.org/10.1080/10408347.2016.1157013.

[26] S. Lefrant, M. Baibarac, I. Baltog, Raman and FTIR spectroscopy as valuable tools for the characterization of polymer and carbon nanotube based composites, J. Mater. Chem. 19 (2009) 5690–5704. https://doi.org/10.1039/b821136a.

[27] C.N. Flynn, C.P. Byrne, B.J. Meenan, Surface modification of cellulose via atmospheric pressure plasma processing in air and ammonia-nitrogen gas, Surf. Coatings Technol. 233 (2013) 108–118. https://doi.org/10.1016/j.surfcoat.2013.04.007.

[28] M. Šetka, R. Calavia, L. Vojkůvka, E. Llobet, J. Drbohlavová, S. Vallejos, Raman and XPS studies of ammonia sensitive polypyrrole nanorods and nanoparticles, Sci. Rep. 9 (2019) 1–10. https://doi.org/10.1038/s41598-019-44900-1.

[29] D.Y. Osadchii, A.I. Olivos-Suarez, A. V. Bavykina, J. Gascon, Revisiting Nitrogen Species in Covalent Triazine Frameworks, Langmuir. 33 (2017) 14278–14285. https://doi.org/10.1021/acs.langmuir.7b02929.

[30] H. Liu, G. Wei, Z. Xu, P. Liu, Y. Li, Quantitative analysis of Fe and Co in Co-substituted magnetite using XPS: The application of non-linear least squares fitting (NLLSF), Appl. Surf. Sci. 389 (2016) 438–446. https://doi.org/10.1016/j.apsusc.2016.07.146.

[31] J.E. Gebhardt, D.W. Fuerstenau, Adsorption of polyacrylic acid at oxide/water interfaces, Colloids and Surfaces. 7 (1983) 221–231. https://doi.org/10.1016/0166-6622(83)80048-1.

[32] Z.W. Ouyang, E.C. Chen, T.M. Wu, Thermal stability and magnetic properties of polyvinylidene fluoride/magnetite nanocomposites, Materials (Basel). 8 (2015) 4553–4564. https://doi.org/10.3390/ma8074553.

[33] H. Baseri, S. Tizro, Treatment of nickel ions from contaminated water by magnetite based nanocomposite adsorbents: Effects of thermodynamic and kinetic parameters and modeling with Langmuir and Freundlich isotherms, Process Saf. Environ. Prot. 109 (2017) 465–477. https://doi.org/10.1016/j.psep.2017.04.022.

[34] N. Mabaso, E.B. Naidoo, A. Ofomaja, Synthesis, structural and morphological studies of Pine Cone powder by fenton oxidation and grafting with acrylic acid using ammonium ceric nitrate as initiator, Nat Prod Ind J. 14 (2018) 116.

[35] G. Guo, S. Li, L. Wang, S. Ren, G. Fang, Separation and characterization of lignin from bio-ethanol production residue, Bioresour. Technol. 135 (2013) 738–741. https://doi.org/10.1016/j.biortech.2012.10.041.

[36] R.L. Penn, J.F. Banfield, Morphology development and crystal growth in nanocrystalline aggregates under hydrothermal conditions: Insights from titania, Geochim. Cosmochim. Acta. 63 (1999) 1549–1557. https://doi.org/10.1016/S0016-7037(99)00037-X.

[37] S.M. Miranda, G.E. Romanos, V. Likodimos, R.R.N. Marques, E.P. Favvas, F.K. Katsaros, K.L. Stefanopoulos, V.J.P. Vilar, J.L. Faria, P. Falaras, A.M.T. Silva, Pore structure, interface properties and photocatalytic efficiency of hydration/dehydration derived TiO_2/CNT composites, Appl. Catal. B Environ. 147 (2014) 65–81. https://doi.org/10.1016/j.apcatb.2013.08.013.

[38] M. Kumari, C.U. Pittman, D. Mohan, Heavy metals [chromium (VI) and lead (II)] removal from water using mesoporous magnetite (Fe_3O_4) nanospheres, J. Colloid Interface Sci. 442 (2015) 120–132. https://doi.org/10.1016/j.jcis.2014.09.012.

[39] A. Pourjavadi, P. Eftekhar Jahromi, F. Seidi, H. Salimi, Synthesis and swelling behavior of acrylatedstarch-g-poly (acrylic acid) and acrylatedstarch-g-poly (acrylamide) hydrogels, Carbohydr. Polym. 79 (2010) 933–940. https://doi.org/10.1016/j.carbpol.2009.10.021.

[40] S. Thakur, O. Arotiba, Synthesis, characterization and adsorption studies of an acrylic acid-grafted sodium alginate-based TiO_2 hydrogel nanocomposite, Adsorpt. Sci. Technol. 36 (2018) 458–477. https://doi.org/10.1177/0263617417700636.

[41] A.E. Ofomaja, E.B. Naidoo, S.J. Modise, Removal of copper(II) from aqueous solution by pine and base modified pine cone powder as biosorbent, J. Hazard. Mater. 168 (2009) 909–917. https://doi.org/10.1016/j.jhazmat.2009.02.106.

[42] M. Thommes, K. Kaneko, A. V. Neimark, J.P. Olivier, F. Rodriguez-Reinoso, J. Rouquerol, K.S.W. Sing, Physisorption of gases, with special reference to the evaluation of surface area and pore size distribution (IUPAC Technical Report), Pure Appl. Chem. 87 (2015) 1051–1069. https://doi.org/10.1515/pac-2014-1117.

[43] K.A. Cychosz, M. Thommes, Progress in the Physisorption Characterization of Nanoporous Gas Storage Materials, Engineering. 4 (2018) 559–566. https://doi.org/10.1016/j.eng.2018.06.001.

[44] A.E. Ofomaja, S.L. Ngema, E.B. Naidoo, The grafting of acrylic acid onto biosorbents: Effect of plant components and initiator concentration, Carbohydr. Polym. 90 (2012) 201–209. https://doi.org/10.1016/j.carbpol.2012.05.024.

[45] A.K. Sarkar, A. Pal, S. Ghorai, N.R. Mandre, S. Pal, Efficient removal of malachite green dye using biodegradable graft copolymer derived from amylopectin and poly(acrylic acid), Carbohydr. Polym. 111 (2014) 108–115. https://doi.org/10.1016/j.carbpol.2014.04.042.

[46] M. Doğan, M. Alkan, Y. Onganer, Adsorption of methylene blue from aqueous solution onto perlite, Environ. Earth Sci. 120 (1999) 229–248. https://doi.org/https://doi.org/10.1023/A:1005297724304.

[47] T.A. Khan, S. Dahiya, I. Ali, Use of kaolinite as adsorbent: Equilibrium, dynamics and thermodynamic studies on the adsorption of Rhodamine B from aqueous solution, Appl. Clay Sci. 69 (2012) 58–66. https://doi.org/10.1016/j.clay.2012.09.001.

[48] M. Bhaumik, T.Y. Leswifi, A. Maity, V. V. Srinivasu, M.S. Onyango, Removal of fluoride from aqueous solution by polypyrrole/F3O4 magnetic nanocomposite, J. Hazard. Mater. 186 (2011) 150–159. https://doi.org/10.1016/j.jhazmat.2010.10.098.

[49] V.K. Gupta, Suhas, Application of low-cost adsorbents for dye removal - A review, J. Environ. Manage. 90 (2009) 2313–2342. https://doi.org/10.1016/j.jenvman.2008.11.017.

[50] A. Grosman, C. Ortega, Capillary condensation in porous materials. Hysteresis and interaction mechanism without pore blocking/percolation process, Langmuir. 24 (2008) 3977–3986. https://doi.org/10.1021/la703978v.

[51] W.J. Braida, J.J. Pignatello, Y. Lu, P.I. Ravikovitch, A. V. Neimark, B. Xing, Sorption hysteresis of benzene in charcoal particles, Environ. Sci. Technol. 37 (2003) 409–417. https://doi.org/10.1021/es020660z.

[52] E. Demirbas, M. Kobya, E. Senturk, T. Ozkan, Adsorption kinetics for the removal of chromium (VI) from aqueous solutions on the activated carbons prepared from agricultural wastes, Water SA. 30 (2004) 533–539. https://doi.org/10.4314/wsa.v30i4.5106.

[53] L. Ai, C. Zhang, L. Meng, Adsorption of methyl orange from aqueous solution on hydrothermal synthesized Mg-Al layered double hydroxide, J. Chem. Eng. Data. 56 (2011) 4217–4225. https://doi.org/10.1021/je200743u.

[54] V. Vadivelan, K. Vasanth Kumar, Equilibrium, kinetics, mechanism, and process design for the sorption of methylene blue onto rice husk, J. Colloid Interface Sci. 286 (2005) 90–100. https://doi.org/10.1016/j.jcis.2005.01.007.

[55] K. Li, X. Wang, Adsorptive removal of Pb(II) by activated carbon prepared from Spartina alterniflora: Equilibrium, kinetics and thermodynamics, Bioresour. Technol. 100 (2009) 2810–2815. https://doi.org/10.1016/j.biortech.2008.12.032.

[56] A.M. Aljeboree, A.N. Alshirifi, A.F. Alkaim, Kinetics and equilibrium study for the adsorption of textile dyes on coconut shell activated carbon, Arab. J. Chem. 10 (2017) S3381–S3393. https://doi.org/10.1016/j.arabjc.2014.01.020.

[57] V.K. Gupta, A. Mittal, R. Jain, M. Mathur, S. Sikarwar, Adsorption of Safranin-T from wastewater using waste materials- activated carbon and activated rice husks, J. Colloid Interface Sci. 303 (2006) 80–86. https://doi.org/10.1016/j.jcis.2006.07.036.

[58] B.I. Olu-Owolabi, P.N. Diagboya, F.M. Mtunzi, R.A. Düring, Utilizing eco-friendly kaolinite-biochar composite adsorbent for removal of ivermectin in aqueous media, J. Environ. Manage. 279 (2021) 111619. https://doi.org/10.1016/j.jenvman.2020.111619.

[59] A. Pholosi, E.B. Naidoo, A.E. Ofomaja, Enhanced Arsenic (III) adsorption from aqueous solution by magnetic pine cone biomass, Mater. Chem. Phys. 222 (2019) 20–30. https://doi.org/10.1016/j.matchemphys.2018.09.067.

[60] V. Vimonses, S. Lei, B. Jin, C.W.K. Chow, C. Saint, Kinetic study and equilibrium isotherm analysis of Congo Red adsorption by clay materials, Chem. Eng. J. 148 (2009) 354–364. https://doi.org/10.1016/j.cej.2008.09.009.

[61] T.K. Sen, S. Afroze, H.M. Ang, Equilibrium, kinetics and mechanism of removal of methylene blue from aqueous solution by adsorption onto pine cone biomass of Pinus radiata, Water. Air. Soil Pollut. 218 (2011) 499–515. https://doi.org/10.1007/s11270-010-0663-y.

[62] L. Ai, C. Zhang, F. Liao, Y. Wang, M. Li, L. Meng, J. Jiang, Removal of methylene blue from aqueous solution with magnetite loaded multi-wall carbon nanotube: Kinetic, isotherm and mechanism analysis, J. Hazard. Mater. 198 (2011) 282–290. https://doi.org/10.1016/j.jhazmat.2011.10.041.

[63] N. Alizadeh, S. Shariati, N. Besharati, Adsorption of Crystal Violet and Methylene Blue on Azolla and Fig Leaves Modified with Magnetite Iron Oxide Nanoparticles, Int. J. Environ. Res. 11 (2017) 197–206. https://doi.org/10.1007/s41742-017-0019-1.

[64] K.T. Wong, N.C. Eu, S. Ibrahim, H. Kim, Y. Yoon, M. Jang, Recyclable magnetite-loaded palm shell-waste based activated carbon for the effective removal of methylene blue from aqueous solution, J. Clean. Prod. 115 (2016) 337–342. https://doi.org/10.1016/j.jclepro.2015.12.063.

[65] P. Zhang, D. O'Connor, Y. Wang, L. Jiang, T. Xia, L. Wang, D.C.W. Tsang, Y.S. Ok, D. Hou, A green biochar/iron oxide composite for methylene blue removal, J. Hazard. Mater. 384 (2020) 121286. https://doi.org/10.1016/j.jhazmat.2019.121286.

CHAPTER 7

PINECONE-BASED ADSORPTIVE BIONANOCOMPOSITES AS MODIFIERS FOR MONODOPED AND CO-DOPED AMORPHOUS TiO_2: TOWARDS GREENER PHOTOCATALYST SYNTHESIS AND DEGRADATION PROCESSES[4]

7.1. Introduction

The scourge of water shortage is continuously revealing the need for newer and more efficient water treatment technologies to be unearthed. This is because the conventional wastewater treatment methods have been shown to fail to remove a wide range of pollutant molecules, particularly those from the dye industries [1]. Recent research has also revealed the benefits of synergizing different water treatment methods for maximum removal of pollutants [2]. Photocatalysis and adsorption are among the most technically feasible techniques to combine for several because the adsorbent material enhances contact between the pollutant and the photocatalytic composite [3]. The combination of the photocatalyst and the adsorbent material typically has the advantage of lowering the process costs as opposed to a hybrid system [4]. In addition, the combination of a photocatalyst and an adsorbent reduces secondary pollution by the concentrated waste coming from the adsorptive stage. Most importantly, the combined photocatalyst and adsorbent eliminates the need for washing the adsorbent and thus cutting on both the environmental footprint and the running costs of the treatment process. Additionally, the cost of the process can be reduced through a selection of readily available and cheap precursors for the catalyst in photocatalysis and other oxidative treatment methods. Waste plant material offer a good source of readily available, naturally available and hence low-cost biopolymers for the tailoring of nanophotocatalysts and their composites [5].

Composites formed between various plant-based biopolymers and semiconductor nanocatalysts have been applied for various purposes including, material strength enhancement, adsorption and photocatalysis [6]. The lignin, cellulose and hemicellulose are the major constituents of plant materials and the viable biopolymers to use for the modification of photocatalytic semiconductors [7]. Lignin has been used as a template in the synthesis of titania nanoparticles with calcination at 300℃ resulting in reduced particle size (8.5 nm), increased surface area and hence high photocatalytic degradation by the mesoporous TiO_2 [8].

[4] Chapter has been submitted to Journal of Environmental Chemical Engineering for peer review

Porous cellulose nanofiber mats have also been coated with CdS and applied for the H2 generation under visible light [9].

Titania deposited onto wood has been shown to improve the mechanical and thermal properties of wood [10]. In-situ deposition of the titania through ultrasonication assisted solgel deposition and subsequent curing of the wood-titania composite in air at 103 ℃ for 20h. Typically the use of plant materials and plant biopolymers in the modification of semiconductors has proceeded through i) precipitation of the semiconductor in a suspension of the plant material powder, ii) aging the mixture, drying, washing and iii) calcination of the composite [7], [11]. Calcination of the bionanocomposites in an oxidising atmosphere typically burns off the plant material, leaving the semiconductor nanoparticles with small amounts of carbon intercalated into the nanoparticles. In this way, the plant material acts as a template. Calcination of the amorphous bionanocomposite in an inert atmosphere, however, results in formation of car bon nanosheets with the semiconductor nanoparticles anchored onto the surfaces of these nanosheets. In all the scenarios, the plant material has demonstrated a profound effect in reducing the particle size of the semiconductor nanoparticles [12], [13].

Plant biopolymer based photocatalysts have been fabricated in several ways including supporting ZnO on carbon that has been derived from plant lignin [12], [13]. The ZiO-lignin-derived carbon composites were shown to have lower energy band gap, low charge recombination and high BET surface area. These characteristics were suffice to impute the composite with improved photocatalytic degradation of organic dyes [14]. A similar procedure was adopted for anchoring Cerium oxide nanoparticles onto the lignin-derived carbon resulting in a composite with improved optical properties and photocatalytic activity for desulfurization of water [15]. Most importantly, these results demonstrated that the mechanism by which lignin keeps the particle size of the semiconductors low is hinged on the surface properties of lignin. The crystallinity of TiO_2 is influenced by several factors such as, i) drying and calcination temperature, ii) presence of impurities. Typically, the presence of impurities reduces the crystallinity.

Amorphous materials are typically characterized by inhomogeneity in the particle size distribution [16]. Studies on the similarities between the amorphous and crystalline polymorphs of nanomaterials show that both materials typically have similar crystallite building unit except that in amorphous materials, these units are not packed in any order [16]. With respect to optical properties, amorphous semiconductor nanomaterials are characterized by the Urbach energy as

shown by the Urbach tail at the absorption edge on their absorption spectrum [17]. This additional energy has been shown to extend the absorption of the semiconductor nanomaterials into the visible spectrum [17], [18].The preparation of amorphous semiconductors offer an economic advantage of scaling up their production in that, unlike the crystalline materials, the amorphous materials are prepared at low temperatures and if any heating, for shorter times [19]. Amorphous nanomaterials are also renowned for small particle size and hence adsorptive surface area. In addition, the low calcination temperatures and durations leave a lot of the surface groups and organic moieties in the semiconductor matrix. The surface groups are known to impute selectivity in terms of the materials in that if the surface is rich in negatively charged groups, the material will tend to adsorb positively charged ions. The organic residue that remains in the nanopowders prepared at low temperatures enable the doping of semiconductor material with such elements as carbon, sulfur, and nitrogen. In addition, the intercalated organic residue themselves play a role in influencing the optical properties of the semiconductor materials. Amorphous TiO_2 has shown photocatalytic activity comparable to that of crystalline TiO_2 and ease of recyclability [19]. As such amorphous TiO_2 offers a niche in the exploration of cost effective and efficient methods of water decontamination. The use of plant material to impute these amorphous characteristics further expands of the economic feasibility of the use of amorphous TiO_2.

The main aim of this work is to investigate the extent to which plant-based biopolymers influence physicochemical and optical properties of TiO_2. TiO_2 is modified by synthesizing it through in-situ precipitation of TiO_2 from a precursor in the presence of alkali treated pinecone powder. Another composite is fabricated by depositing of amorphous TiO_2 onto polyacrylic acid-coated magnetite-pinecone composite. Similar composites of amorphous TiO_2 are prepared using a similar method except that a nitrogen dopant is added to the precursor solution.

7.2. Materials and methods

7.2.1. Materials

Previously synthesized pinecone-magnetite (PMC) and acrylic acid-grafted pinecone magnetite (GAA) bionanocomposites. Acetyl acetone (99%), 1-Butanol (99.4%), 1-Propanol (99.7%) and Ethanol (96%), Titanium (IV) butoxide (97%) were supplied by Merck, South Africa. All the reagents used were of analytical grade and were used without any further pre-treatment.

7.2.2. Preparation of bionanocomposites

Approximately 5.0 mg of the bionanocomposite powders (PMC/GAA) (calculated to be equivalent to 9 wt.% of the mass of Ti in the amount of titanium precursor) was sonicated in 50 mL ethanol (EtOH) at 40 for 30 min. A TiO_2 precursor was prepared by dissolving 10 mL of titanium butoxide (TiOBut) in a 100 mL, butanol: propanol (80:20 v/v) and adding 2 mL acetylacetone. A hydrolysing solution was made by mixing EtOH and deionized water at 1:1 (v/v). The hydrolysing solution and the precursor solution were simultaneously added dropwise into the suspension of the bionanocomposite with continued sonication and stirring using a mechanical stirrer. The preparation of the bionanocompostes with N doped TiO_2 was carried out using a similar procedure except that the hydrolysing solution also functioned as the dopant carrier in that ethylene diamine was added such that the v/v ratio was 1:1:1. At completion of mixing the reagents, the resultant sol was stirred for 5 h on a heater/ stirrer plate. Afterwards the heating mantle was switched on and set at 70 ℃ to evaporate the solvents. After complete evaporation of the solvents (about 24 h), the remaining powder was crushed using a mortar and pestle and stored for further use.

7.2.3. Characterization

The surface functional groups were determined through Fourier transform spectroscopic (FTIR) with scans of each sample carried out in in the range 450 - 4000 cm^{-1} using diamond attenuated total reflectance (ATR) using a Frontier Perkin-Elmer spectrophotometer. The surface elemental composition of the was determined using the X-ray photoelectron spectroscopic (XPS) technique in a Thermo ESCAlab 250Xi model. A monochromatic X-ray beam with a spot size of 900 μm, generated from an Al Kα (1486.7eV) shell was blazed onto a pelletized sample that was held in a pressurized chamber at 10^{-8} mBar. The morphology of the powders at bulk scale were determined using a MIRA3 TESCAN high resolution microscope and images were collected at 5.0kV. The morphology of the photocatalytic bionanocomposites determined using transmission electron microscope (TEM, FEI TECNAI G^2 SPIRIT) at an accelerating voltage of 150 kV. The absorbance spectra of the photocatalytic bionanocomposites powders were determined using a Perkin Elmer UV-Vis spectrophotometer.

7.2.4. Photocatalytic degradation studies.

The photocatalytic performance of the bionanocomposites was studied using a photocatalytic reactor designed by Lelesil Innovative Systems (Thane, Maharashtra India). An additional water cooled, double walled borosilicate glass immersion well is inserted into the reaction chamber and a lamp inserted into the well. Cold water from an external water tank is circulated in the double walled well to cool the lamp during operation. In this case, 10 mg of each photocatalytic bionanocomposite was dispersed in a solution consisting of pre-mixed equal volumes (100 mL) 25 ppm RR 120 and RhB dyes at equal concentration (25 ppm). The resultant suspension was sonicated in the dark for 1 h to achieve adsorption-desorption equilibrium. During this time, aliquots (6 mL) were collected at 15 min intervals, starting with the dye cocktail before introducing the photocatalysts. Afterwards, the dye cocktail-catalyst suspension was place in the reaction chamber for the photocatalytic reactor, the reactor covered with the immersion well and a UV-lamp (450 watts) inserted into the immersion well. Aliquots were collected at 30 min intervals for 180 min using a plastic syringe fitted with a PVDF membrane filter module for removing the catalyst powder from the filtrate. Each aliquot was run in a UV-vis spectrophotometer for absorbance in the range 200 – 800 nm. The removal kinetics were determined from the absorbance spectra of the aliquots collected at the various times.

7.3. Results and discussion

7.3.1. Morphological and crystallographic analysis of bionanocomposites

7.3.1.1. *High resolution scanning electron microscopy*

Generally, both the TiO_2 and $NTiO_2$ aggregates are spherical in shape. The main difference is in that the $NTiO_2$ aggregates are extremely agglomerated and only get dispersed by incorporation of bionanocomposites (***Figure 7.1*** and ***Figure 7.2***). PMC disperses $NTiO_2$ nanocomposites the most than GAA. PMC–TiO_2 and GAA–TiO_2 have two types of structures with a stark difference in the size. The larger (226–557 nm) structures are attributed to the pine powder from the PMC while the smaller structures (46 – 155nm) are attributed to TiO_2. PMC Larger globular structures in PMC–TiO_2 and GAA–TiO_2 identified as the bionanocomposites structures. These structures are coated with $NTiO_2$ in PMC–TiO_2 and GAA–$NTiO_2$ hence suggesting $NTiO_2$ binds with ease onto the pine structures. A strong bond and many bonding sites between TiO_2/$NTiO_2$ and the bionanocomposites are essential for the promotion of

electron transfer between the bionanocomposite and TiO_2/NTiO_2. In essence, the presence of nitrogen in TiO_2 promotes the bonding of TiO_2 onto the bionanocomposite.

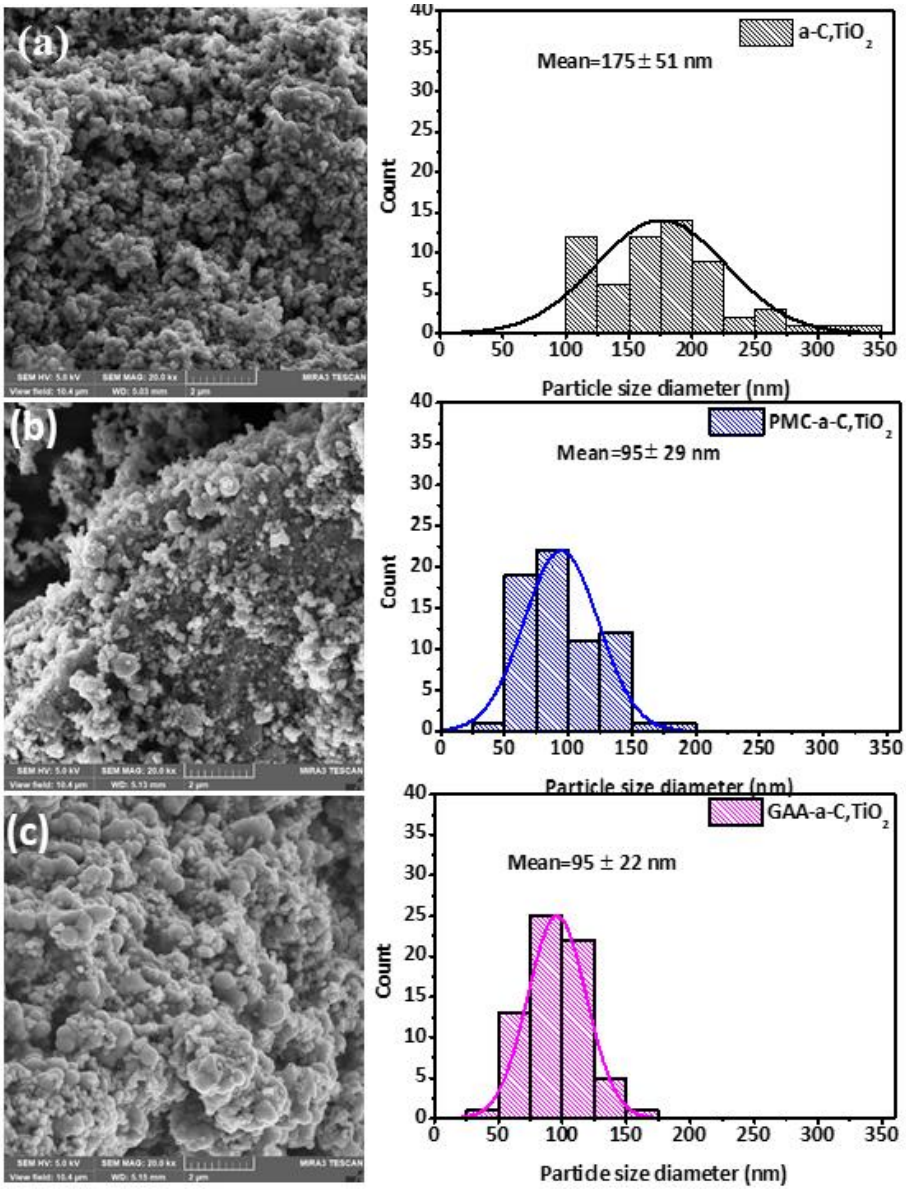

Figure 7.1 Scanning electron microscopy micrographs for (a) a-C,TiO_2, the photocatalytic bionanocomposites (b) PMC–a-C,TiO_2 and (c) GAA–a-C,TiO_2.

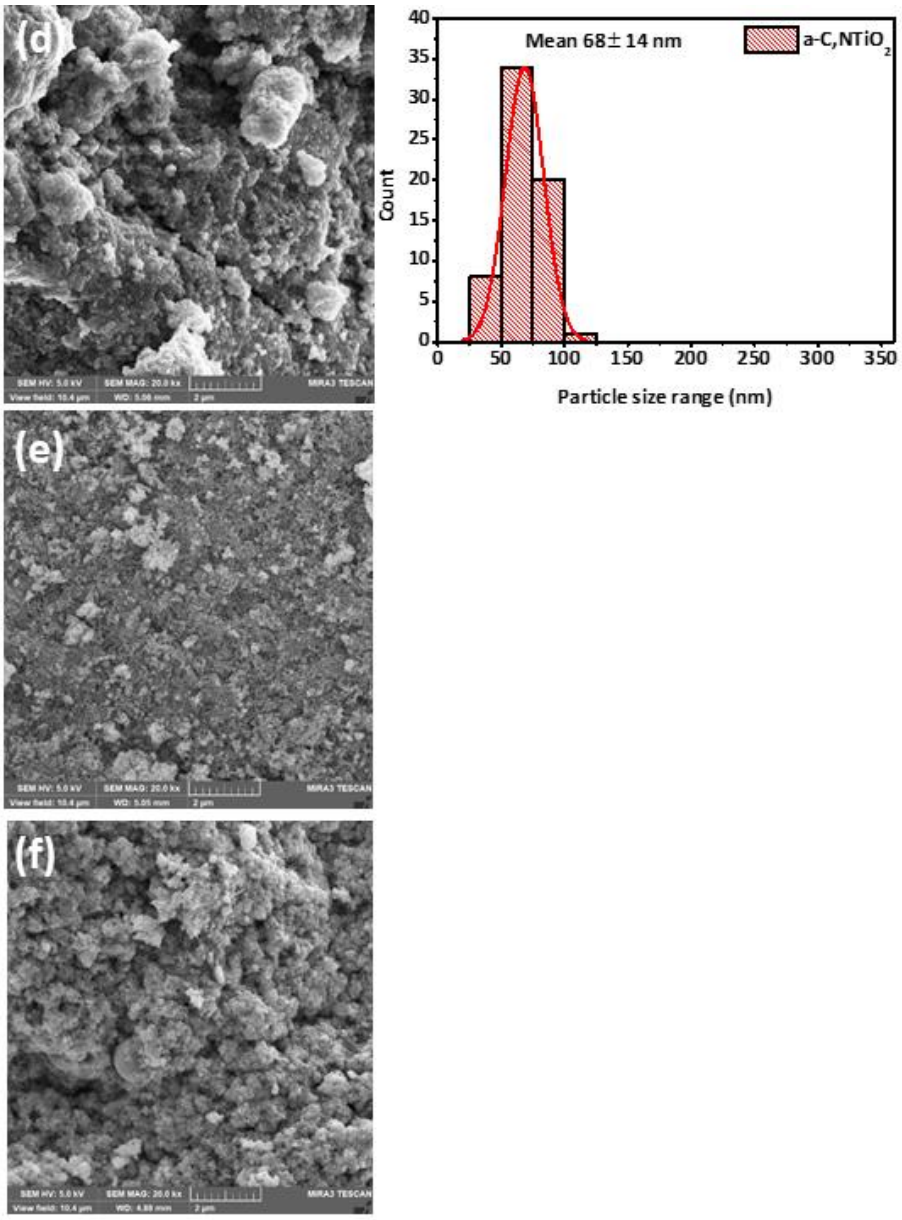

Figure 7.2 Scanning electron microscopy micrographs for (d) a-C,NTiO_2 and the photocatalytic bionanocomposites (e) PMC–a-C,TiO_2, (f) GAA–a-C,NTiO_2.

7.3.1.2. *Transmission electron microscopy and X-ray diffraction spectroscopic analysis of photocatalytic bionanocomposites*

The TEM micrographs show that the photocatalytic bionanocomposites consist of aggregated mass of nanoparticles almost forming a porous matrix (***Figure 7.3***). The average particle size is estimated to be at 4 nm. Porous materials are renowned for providing a good surface area for the adsorption of organic pollutants. a-C,TiO_2 of a similar structure has been shown effectively degrade Rhodamine B and 4-chlorophenol under UV light [20].

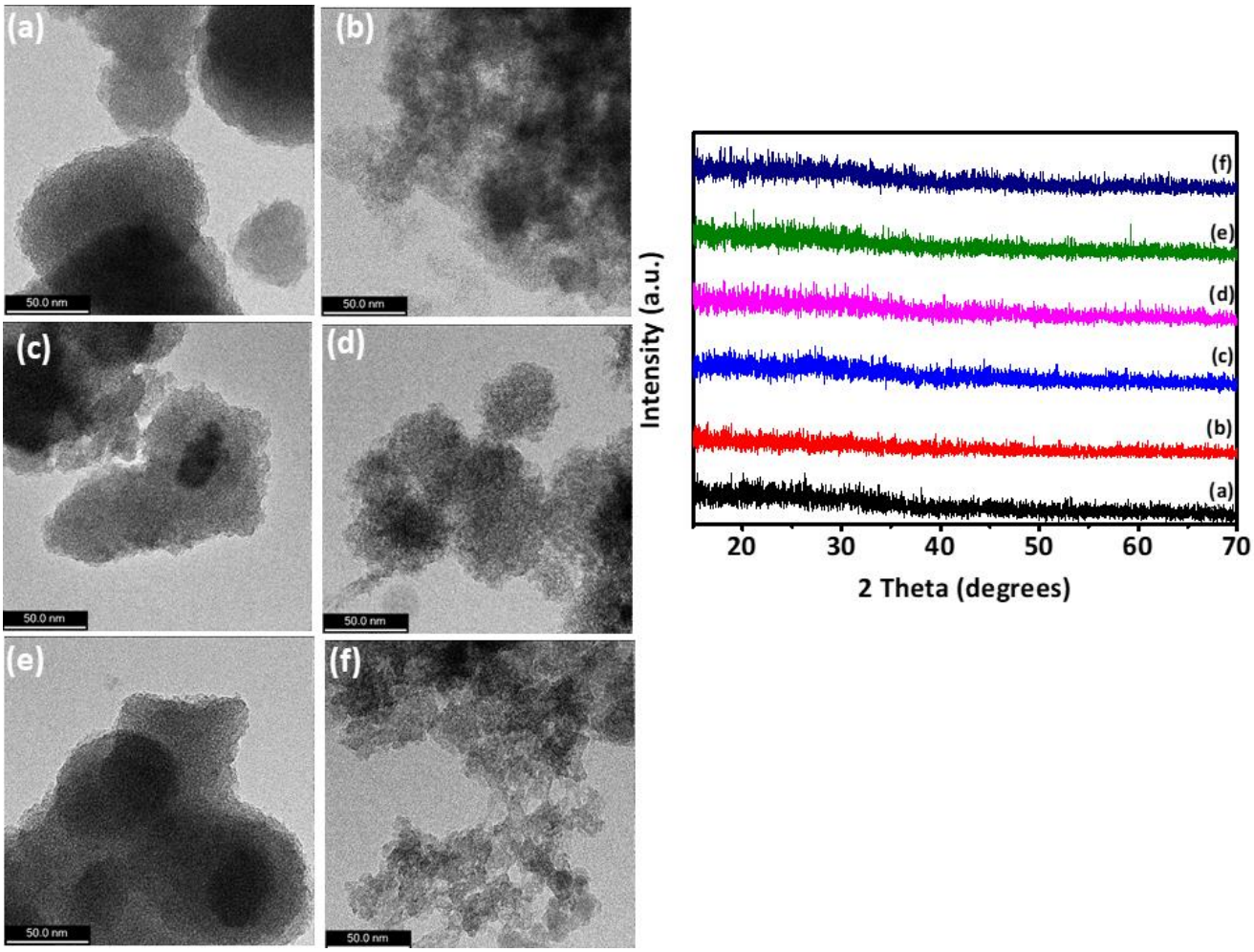

Figure 7.3 TEM micrographs and XRD spectra for (a) a-C,TiO_2, (b) a-C,$NTiO_2$ and the bionanocomposites (c) PMC–aC,TiO_2, (d) PMC–a-C,$NTiO_2$, (e) GAA–a-C,TiO_2 and (f) GAA–a-C,$NTiO_2$

N-doped TiO_2 and the bionanocomposites PMC–a-C,$NTiO_2$ and GAA–a-C,$NTiO_2$ are better dispersed compared to their counterparts taking the form of mesoporous materials. Similar structures have been observed in the synthesis of titania using lignin as a template [8].

7.3.2. Elemental and surface composition analysis of bionanocomposites

7.3.2.1. *Fourier transform infrared spectroscopy analysis*

All the photocatalytic bionanocomposites have a broad peak in the range 3665 – 2600 indexed to – OH alcohol stretching (***Figure 7.4***). This would arise from the stretching of the –OH groups of the cellulose and cellulose derivatives in the plant material [21]. A corresponding strong peak at 1640 cm^{-1} indexed to surface adsorbed –OH groups demonstrates that all the bionanocomposites are rich in surface groups. a-C,$NTiO_2$, PMC–a-C,TiO2 and

GAA–a-C,NTiO$_2$ have a notable shoulder of the –OH peak at around 3400 cm^{-1} which is attributed to the –N–H stretching of surface attached amine groups on the photocatalytic bionanocomposites. A corresponding shoulder at ~ 3000 cm^{-1} occurs on PMC–a-C,NTiO$_2$ and GAA–a-C,NTiO$_2$ and the peak is attributed to an amine salt, which in the case of the bionanocomposites suggest the occurrence of the NH^+ bonded to an organic molecule. In the case of this material, this suggests the incorporation N into the bionanocomposites as NH^+.

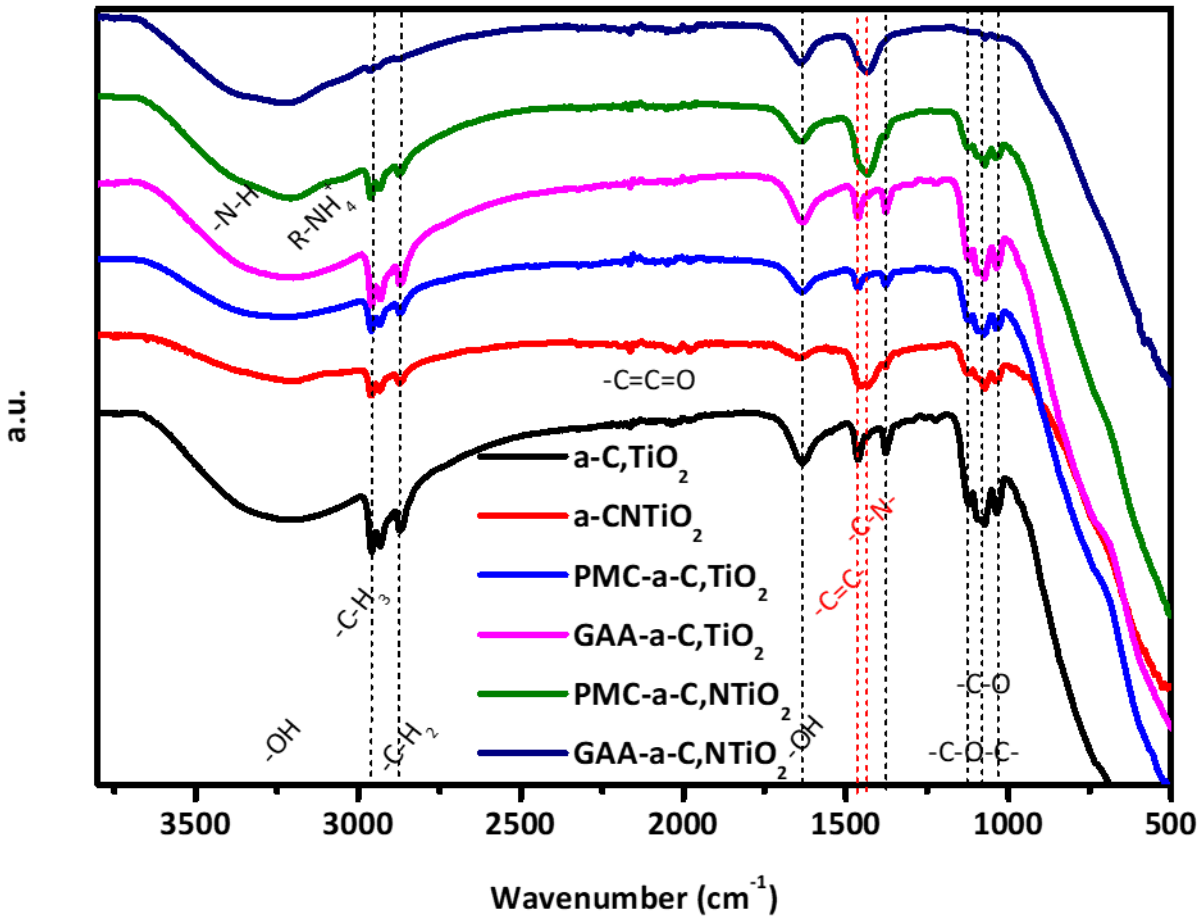

Figure 7.4 FTIR analysis of bionanocomposites

Sharp peaks occurring at 2960, 2934 and 2874 cm^{-1} which are due to –C–H$_2$, R–CHO and –C–CH$_3$ stretching [22]. in the case of the materials, these would be peaks arising from the stretching of the –C–H groups attached onto the carbon skeleton of the cellulose chains of the plant material. These peaks are stronger even in TiO$_2$ although there was no plant material incorporated. This would, therefore, suggest that the solvents and preparation chemicals leave a lot of the carbon residue and hence the carbon residue playing a role in tailoring the properties of the TiO$_2$ and NTiO$_2$. Ther are weak peak in the range 2190 – 1900 cm^{-1} occur in all bionanocomposites and these are indexed to C=C=O [21]. A strong broad peak centered at

1430 occurs in the photocatalytic bionanocomposites PMC–a-C,NTiO_2, GAA–a-C,NTiO_2 and a-C,NTiO_2. The peak is due to –C–N bond [23]. This confirms the incorporation of nitrogen into these nanohybrids and suggests that the nitrogen occurs in organic form, bonded either to the plant carbon matrix. A sharp peak at 1462 in a-C,TiO_2, PMC–a-C,TiO_2, GAA–a-C,TiO_2, also occurs as a shoulder peak in GAA–a-C,NTiO_2 due to the stretching movements of the –C=C– bond. Peak in 1400 – 1348 cm^{-1} occurs on all bionanocomposites and is indexed to – OH bending, which is indicative of the presence of synthesis chemicals residue in all the photocatalytic nanohybrids [21]. There are peaks in the range 1177 – 987 indexed to the –C–O and –C–O–C– stretching movements in various chemical groups such as the alcohol, ester and ether functional groups [21], [24].

Amorphous TiO_2 has strong affinity for the chemical moieties from the process chemicals as shown by the strong peaks of carbon-based groups in FTIR and the high wt.% in EDS. The carbon mostly occurs as carbon based surface groups such as the carboxylic acid group [25]. The implication of this on the material performance is that the occurrence of carbon as organic groups may not have a significant effect on the electronic properties of TiO_2 and hence no significant promotion of the photocatalytic activity of the TiO_2. A comparison of the FTIR spectra of TiO_2 and NTiO_2 also shows a decrease in the peak intensity of the –CH_2, –CH_3 and –CHO groups with incorporation of nitrogen. The intensity of these peaks only increases with the incorporation of GAA into TiO_2 and PMC into NTiO_2.

7.3.2.2. *EDS analysis*

Photocatalytic bionanocomposites confirmed to consist of O, Ti, C, and trace amounts of sulfur (***Figure 7.5***). High carbon content for TiO_2 than the bionanocomposites. Carbon in TiO_2 would come from the process reagents. This would suggest a high affinity for the solvents for the TiO_2 crystals.

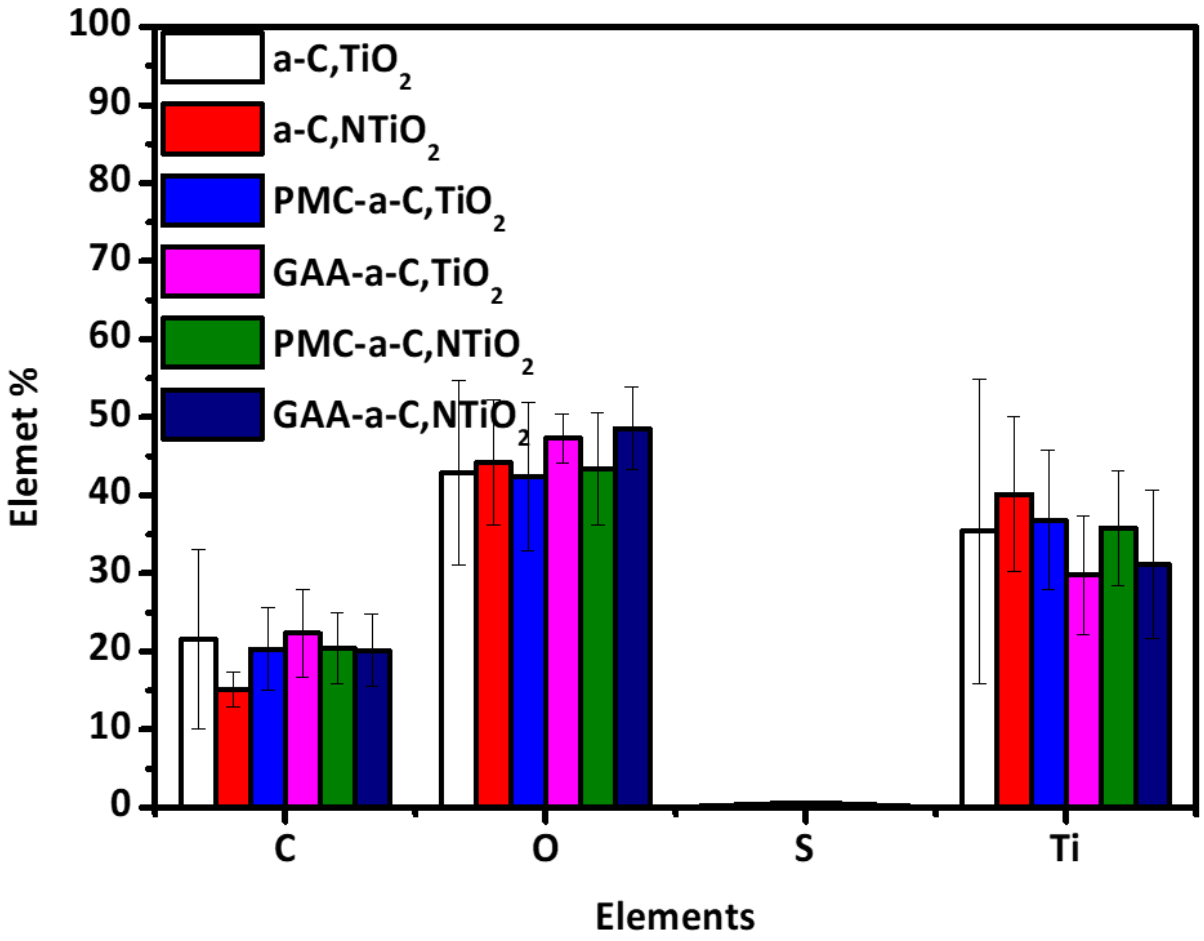

Figure 7.5 EDS analysis of the photocatalytic bionanocomposites

7.3.3. X-ray photoelectron spectroscopy analysis

All elements (C, Ti, O) were confirmed present in all the photocatalytic bionancomposites, hence corroborating the EDS analysis in preceding sections (***Figure 7.6(a)*** and ***Table 7.1***). The occurrence of N in the $NTiO_2$ based bionanocomposites (GAA–a-C,$NTiO_2$ and PMC–a-C,TiO_2) confirmed and hence doping of TiO_2 successful. GAA–a-C, $NTiO_2$ has a higher N, content than PMC–a-C,TiO_2 and a higher O and Ti content than all the nanohybrids. C1s peaks also higher in the PMC based composites (PMC–a-C, TiO_2 and PMC–a-C, $NTiO_2$ than the GAA counterparts. C1s and Ti2p peaks shifted to higher binding energy for GAA–a-C, $NTiO_2$ and PMC–a-C,$NTiO_2$. This greater shift compared to the other nanohybrids suggests the presence of C–N and Ti–N bonds. The GAA based nanocomposites (GAA–a-C,TiO_2 and GAA–a-C,$NTiO_2$) have organic fluorine, suggesting that the fluorine comes with the GAA. ***Table 7.2*** An analysis of the bonding configurations for the photocatalytic bionanocomposites shows the bonding configurations for each of the photocatalytic bionanocomposites. The O1s (C–O) bonding configuration is due to carbon skeleton chain, which would be the plant material

and the polymer material. The O1s peak at 533 eV for PMC-TiO_2 and GAA–aTiO_2 is for adsorbed oxygen in the form of –OH and –COOH groups [26]. This peak is slightly shifted to a higher binding energy of 533.2 for the N-doped photocatalytic bionanocomposites (***Figure 7.6 (d)***). Typically, a shift to a higher wave number indicates a bond with a more electronegative element and in the case of these nanocomposites, F is the only element with a higher electronegativity than O. Peaks corresponding to the Fe_2O_3 were not detected for all the nanohybrids. This is due to small amounts of Fe_2O_3 in the primary adsorptive bionanocompoisites as indicated in the previous Chapter.

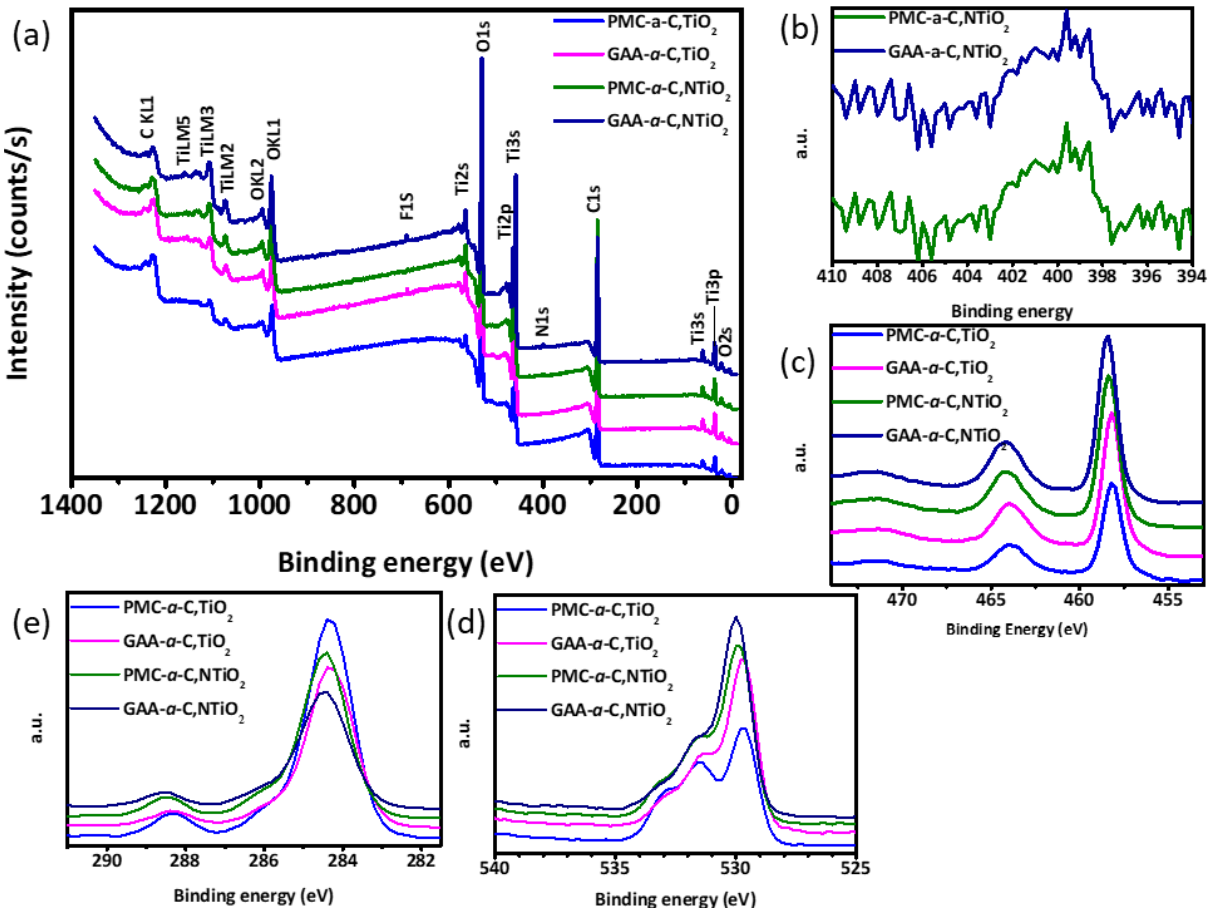

Figure 7.6 XPS summary of results showing (a) the broad scan, (b) N1s for PMC-$NTiO_2$ and GAA-$NTiO_2$, (c) Ti2p, (d) O1s and (e) the C1S spectra for the photocatalytic bionanocomposites

N1s peak is at 400.7 for PMC–a-C,$NTiO_2$ and at 399.5 for GAA–a-C,$NTiO_2$. This is the binding energy region in which nitrogen bonded to carbon hence suggesting that in both nanocomposites, the N exists in –N–C bonding configuration [27]. The N1s peaks have a high FWHM with the peak bases spanning from around 398 eV and tailing towards the higher BE

(***Table 7.2***). The tailing towards the higher binding energies suggests presence of the N–O and the O–N–O bonding configurations. The lack of peaks in the lower binding energies in the range 398 – 395.5 suggests that the N does not bond directly to Ti centers since the binding energy for the Ti–N bonding configuration typically occurs in this region.

Table 7.1 Elemental composition of the bionanocomposites.

Photocatalytic bionanocomposite	**Peak Binding energy (eV)**				**FWHM (eV)**				**At.%**			
	C1s	O1s	Ti2p	N1s	C1s	O1s	Ti2p	N1s	C1s	O1s	Ti2p	N1s
PMC-TiO_2	284.3	530.7	458	-	3	4.6	2.6	-	69.3	24.9	6	-
GAA-TiO_2	284.2	530.2	458	-	3	2.6	2.8	-	58.4	31.2	9.9	-
PMC-NTiO_2	284.8	530	458.3	400.4	3.1	2.5	2.8	3.6	58.5	31.7	9.4	0.4
GAA-NTiO_2	284.7	530.7	458.3	400.1	3.1	3.5	2.8	3.2	48.7	36.9	12.9	0.7

Table 7.2 An analysis of the bonding configurations for the photocatalytic bionanocomposites

Bonding configuration	**PMC-TiO_2**			**GAA-TiO_2**			**PMC-NTiO_2**			**GAA-NTiO_2**		
	Peak BE	FWHM (eV)	Atomic %	Peak BE	FWHM (eV)	Atomic %	Peak BE	FWHM (eV)	Atomic %	Peak BE	FWHM eV	Atomic %
C1s (C-C)	284.4	1.4	58.4	284.4	1.4	50	284.5	1.3	46.8	284.5	1.4	39.8
C1s (C-O)	286.1	1.3	4.8	286.1	1.4	3.4	286.1	1.3	5.3	286.1	1.4	4.9
C1s (O-C=O)	288.3	1.3	5.2	288.4	1.4	3.9	288.5	1.3	4.6	288.6	1.4	4.1
F1s (Organic F)	-	-	-	688.1	0.6	0.3	-	-	-	689.8	0.6	0.5
N1s (Organic N)	-	-	-	-	-	-	400.7	1.9	0.4	399.5	3.2	0.6
O1s (C-O)	531.5	1.7	10	531.3	1.8	11.4	531.5	1.9	12.4	531.6	1.7	11
O1s (C=O)	533	1.3	4	533	1.3	2.4	533.2	1.2	2.3	533.2	1.4	2.3
O1s (Metal Oxide)	529.7	1.3	11.2	529.7	1.3	18.1	529.9	1.3	17.8	530	1.3	23.7
Ti2p3 (TiO_2)	458.2	1.2	6.4	458.2	1.2	10.5	458.3	1.2	10.4	458.4	1.2	13

7.3.4. Brunauer-Emmett-Teller surface area analysis of the photocatalytic bionanocomposites

Isotherms for all the photocatalytic bionanocomposites are characterized by a low concave curvature of the isotherms at completion of multilayer adsorption than the convex curvature of the same isotherms at high P/P_0. The bionanocomposites with N-dopant have a more pronounced concave curvature of the isotherms in the region A than the bionanocomposites without N-doping. Secondly, all the bionanocomposites exhibit the type II isotherm and therefore suggesting both mono and multilayer adsorption on a microporous surface. Additionally, the N-doped bionanocomposites have closed type H3 hysteresis loops as per the IUPAC system [28], [29].

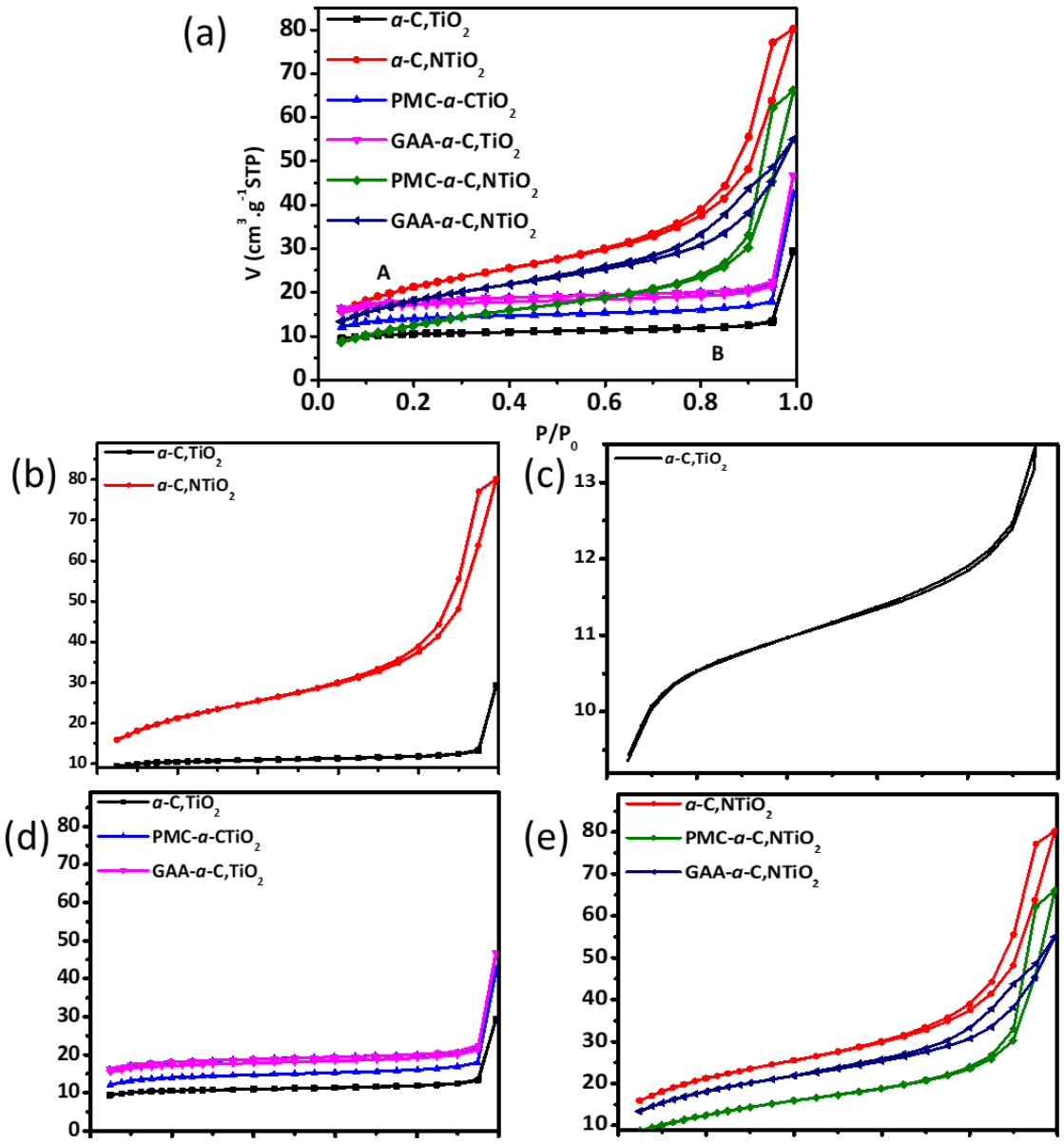

Figure 7.7 Brunauer-Emmet-Teller isotherms for photocatalytic bionanocomposites (a) combined isotherms (b) isotherms for doped photocatalysts without bionanocomposites, (c) isotherms for a-C,TiO_2 (vertical axis panned out), (d) photocatalysts without N-doping and (e) photocatalysts with N-doping.

Most importantly, the bionanocomposites without the N-dopant (a-C,TiO_2, PMC–a-C,TiO_2 and GAA–aC,-TiO_2) exhibit This indicates that these composites are microporous and likely consist of 2-D nanoplate materials. As such the adsorption on these materials is multilayer and the less concave curvature at the onset of the linear portion of the curve suggests a simultaneous occurrence of multilayer and monolayer adsorption. Incorporation of N into a-C,TiO_2 increases the BET surface area (by up to 130%), pore volume (3.04 – 8.55 ($\times 10^{-1} cm^3 . g^{-1}$) and pore diameter (5.77 – 6.87 nm). A similar pattern is observed with the incorporation of N into

PMC– a-CTiO_2 and GAA– a-C,TiO_2. An exception is observed for the decrease in pore diameter from 0.28 nm to 0.27 nm with incorporation of N into GAA–aC,TiO_2.

Most notable is the occurrence of open hysteresis loops for the photocatalysts a-C,TiO_2-loops that become wider with the incorporation of PMC and GAA. Open loops are rare but have been observed for the adsorption of benzene onto biochar [30] and recently in BET surface area analysis of wood pyrochar using N_2 as a probe gas [31], [32]. Such loops have been associated with physical entrapment of the probe molecules in the porous matrix of the material, possible deformation of the pores due to the entrapment. This phenomenon is likely linked to pores that have a constricted opening but wide lumen or pores that are interconnected [33]. As such, materials with these loops are seen as good materials for gas storage [30]. In the case of the use of these materials for adsorption, such a behavior would be useful for the removal of the pollutant.

Most notable also is the disappearance of the open loops with the incorporation of nitrogen as a dopant. Since N-doping was carried out through a one-pot in situ doping process, it is suggested that the N-dopant (ethylene diamine) interacts more with the organic material (cellulose, hemicellulose) resulting in the modification of the surface and a chemical modification – a phenomenon corroborated by the occurrence of N in its organic form as depicted by the XPS spectra (***Figure 7.6***, ***Table 7.1, Table 7.2***).

The incorporation of the adsorptive bionanocomposites into a-C,TiO_2 also results in an increase in the BET surface area and the pore volume. The average pore diameter is, however, reduced. This suggests that the bionanocomposites impute the photocatalytic bionanocomposites with deep but narrow pores that ultimately offer a large surface area for adsorption. Such a surface area is favorable for the adsorption molecules that have a smaller diameter but not for large molecules.

In the case of the incorporation of GAA and PMC into a-C,NTiO_2, however, there is generally a drastic decrease of the surface area by up to 43%, pore volume up to 49% and average pore diameter by an even higher magnitude. Additionally, the results demonstrate that the N-doped photocatalysts modified with the adsorptive bionanocomposites have a higher surface area and pore volume but narrow pores. This is to suggest that the synergistic effect of N, doping and bionancomposite modification produces a surface area with narrow but deep pores, a scenario that is suited for the adsorption of molecules whose diameter is ~1 nm or less.

The nanocomposites a-C,TiO_2 and PMC–a-C,TiO_2 do not show a hysteresis loops and their adsorption isotherms best fit the type II adsorption isotherm except that the point of inflection of the has relatively lower curvature than the curves for the N-doped photocatalysts. This suggests a more simultaneous multilayer adsorption

GAA – a-C,TiO_2 adsorption best fits the type H4 hysteresis loop and the low curvature at the onset of the linear part of the curve indicates that the adsorption isotherm best fits the Type I (a) isotherm [28]. As such the photocatalytic bionanocomposite is microporous with the pores being narrow and therefore limiting the adsorptive surface area.

Table 7.3 Brunauer-Emmett-Teller surface area, pore volume and pore radius for photocatalytic bionanocomposites

Composite	**Surface area ($m^2.g^{-1}$)**	**Pore volume ($\times 10^{-1} cm^3.g^{-1}$)**	**Average pore diameter (nm)**
a-C,TiO_2	211.2	3.04	5.77
a-C,NTiO_2	498.3	8.55	6.87
PMC–a-C,TiO_2	282.0	4.33	0.307
GAA– a-C,TiO_2	343.9	4.82	0.280
PMC–a-C,NTiO_2	302.7	6.78	8.96
GAA–a-C,NTiO_2	471.3	6.36	0.27

7.3.5. Optical properties of photocatalytic bionanocomposites

The energy band gap (E_g) was determined from the reflectance spectra of the nanohybrids using the equation:

$$[F(R)hv]^n = k(hv - E_g)$$

Where $F(R)$ is the reflectance coeficiant and an equivalent of the absorption coeficient α, hv is the photon energy, k is the characteristic constant for the material, E_g is the energy band gap and ^{n} is the order of the electronic transitions between the band staes within the semiconductor. a-C,TiO_2 was treated as a direct semiconductor and hence ^{n} was taken to be $^1/_2$

Therefore a plot of $[F(R)hv]^{1/2}$ vs hv gives the Tauc plots for each of the photocatalytic bionanocomposites. The E_g is the photon energy at which an extrapolation of the Tauc plots intervept the x-axis (***Figure 7.8 (b)***).

The absorbance spectra for the nanohybrids consist of two main regions: the first one corresponding to the band edge typical of a-TiO_2 and the second bein the region where the plant material and the magnetite absorb (***Figure 7.8(a)***). It is observed that there is photosensitization of the photocatalytic bionanocomposites by the carbon doping and the plant material, resulting in the broad absorption band in the region 380 – 680 nm. All the photocatalysts show this band in varying degrees, with GAA– a-C, TiO_2 showing the strongest intensity of this band. The increased absorbance due to this band is expected to enhance the photocatalytic activity of the bionanocomposites.

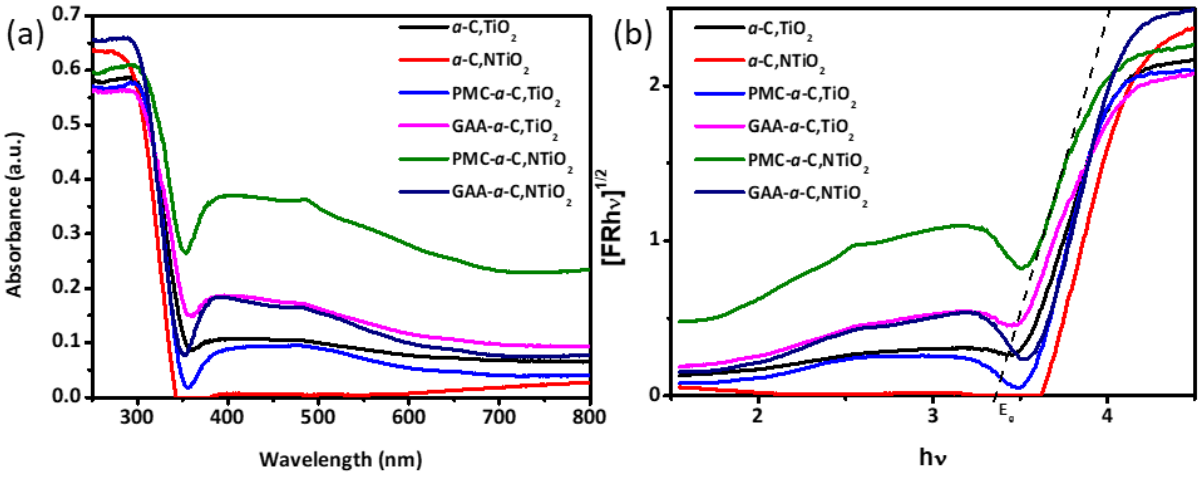

Figure 7.8 (a) UV-vis spectra and (b) Tauc plots for the photocatalytic bionanocomposites

With respect to the band edge and E_g, the photocatalytic bionanocomposites are arranged in order of decreasing energy band gap a-C,$NTiO_2$; PMC–a-C,TiO_2; GAA–a-C,$NTiO_2$; a-C,TiO_2; GAA–a-C,TiO_2 and PMC–a-C,$NTiO_2$ whose band gaps are 3.62, 3.57, 3.55, 3.46, 3.40 and 3.33 eV respectively. The results suggest that doping of amorphous TiO_2 with N does increases the energy band gap (E_g). The reduction in the energy band gap below that of TiO_2 is only observed for GAA–TiO_2 and PMC–a-C,TiO_2. We attribute the increase in the energy band gap to the extremely small size of the TiO_2 and $NTiO_2$ nanoparticles; more so the even further decreased particle size with addition of ethylene diamine as an N-dopant. The generally high E_g for the bionanocomposites is most likely due to their amorphous nature of which the incorporation of N and the bionanocomposites further reduces the crystallinity. The quantum confinement effects on the optical properties become more pronounced as the particle size

decreases [34]. It has been previously demonstrated that lower post-calcination temperatures generally result in higher energy band gaps and hence poor visible light absorption [35]. Similar observations were made with nano amorphous Co_3O_4 co-catalyst increasing the photocurrent density of WO_3, accompanied by a high hydrogen evolution of the Co_3O_4–WO_3 composite [36]. It also seems that the presence of elemental and surface molecular carbon on the a-C, TiO_2 and a-C, $NTiO_2$ affects the energy band gap. This is shown by the a-C, TiO_2 (with high residual carbon content from the precursors) has a lower energy band gap than a-C, $NTiO_2$ and GAA–a-C,$NTiO_2$.

7.3.6. Photocatalytic degradation of a dye cocktail

Absorbance spectra for the 25 ppm dyes RhB, RR 120 and the basic dye cocktail was determined using the UV-Vis spectrophotometer. The results indicate that RhB has a broader absorption peak; a peak that upon mixing RhB with RR 120 the peak takes the shape of that RR120. As such the main peak at $lambda_{max}$=554 nm. As such this peak was used as the reference peak for the calculation of the concentration of the dye cocktail. In addition, the absorbance for the dye cocktail was treated as representative of 25 ppm of the dye cocktail. ***Figure 7.9*** (b) shows the absorbance curves for the dye cocktail made of a mixture of RhB and RR120 at 10, 16, 20 and 25 ppm and ***Figure 7.9(c)*** shows the calibration curve.

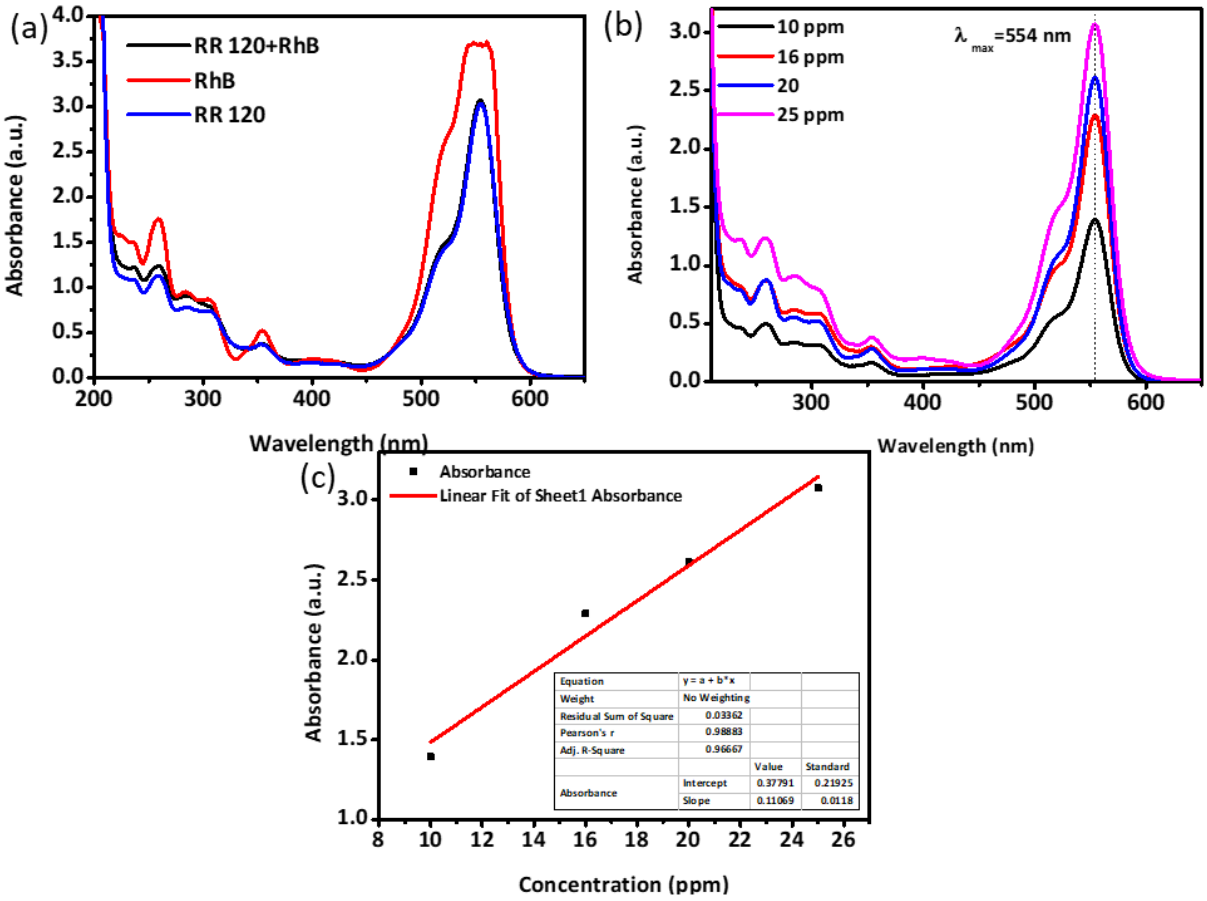

Figure 7.9 Dye degradation calibration data: (a) absorbance spectra for the dyes and dye cocktail, (b) absorbance curves for dye at specified concentration and, (c) calibration curve for calculating the concentration.

Dye removal by adsorption was evaluated at $t = 0$ which is after 60 min of sonicating the catalyst, dye suspension in the dark and the results are shown in ***Figure 7.10***. Generally, the removal of the dye molecules by adsorption is extremely low (less than 10%). The best performing bionanocomposite in terms of the dye removal by adsorption is PMC–a-C,TiO_2 with 9.90% removal and the least performing is PMC–a-C,NTiO_2 with 1.96% removal. The bionanocomposite PMC–a-C,TiO_2, has the highest ada-C,TiO_2 shows highest adsorption in first 15 min with 8.20% adsorbed then subsequent desorption. A closer look in the patterns followed by the bionanocomposites in the removal of the dye shows that the photcatalysts achieve adsorption-desorption equilibrium at different times. a-C,TiO_2 has the highest dye removal by adsorption, with up to 8.8% dye removed in the first 15 min. However, at $t = 0$ a-C, TiO_2 has low dye removal by adsorption. Worth noting is the fact that the bionanocomposite GAA – a-C,TiO_2 is the least adsorbing yet second highest in terms of dye removal hence demonstrating its catalytic efficiency. This observed low adsorption by the nanocomposites

demonstrate that the subsequent dye removal will proceed mostly through photocatalytic degradation, as opposed to previously observed cases where the dye is removed mainly by adsorbing onto the catalyst.

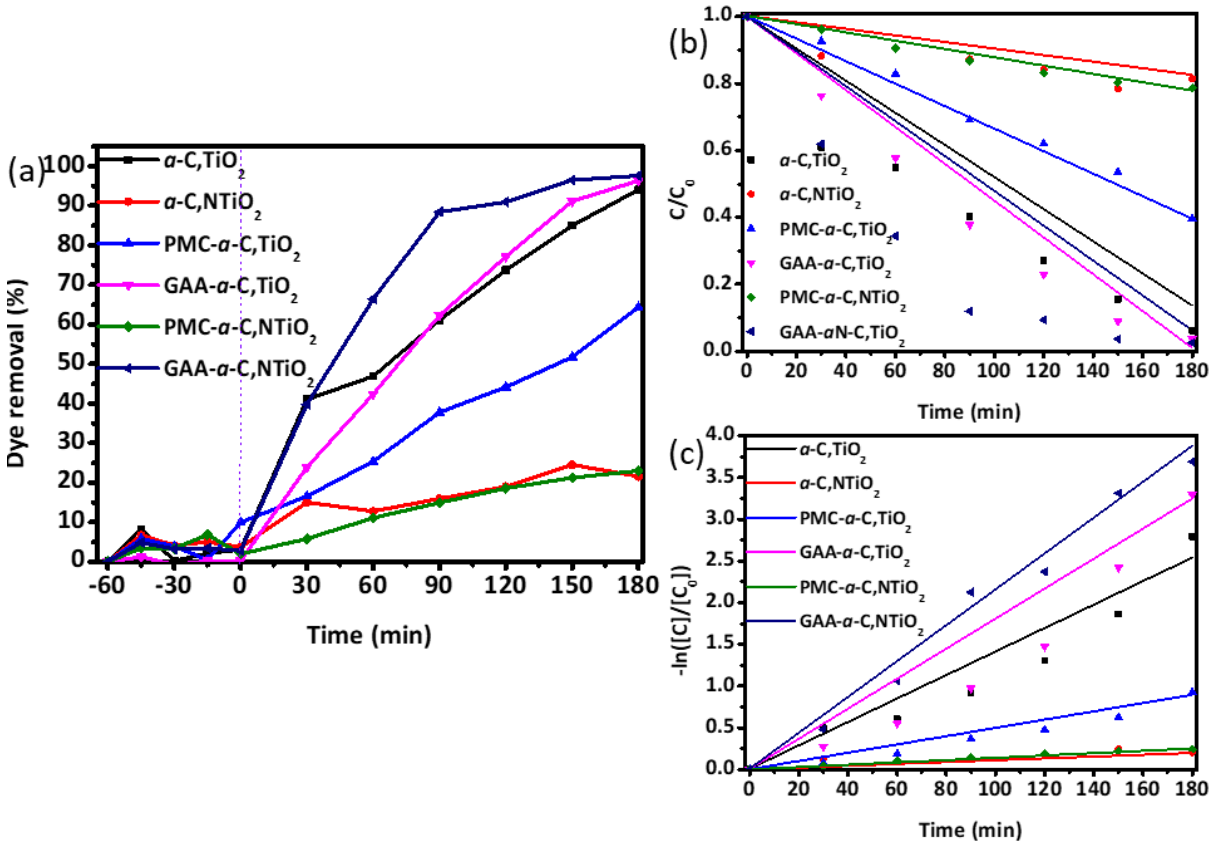

Figure 7.10 Dyes removal efficiency and kinetics: (a) % dye removal, (b) zero-order kinetics rate curves and (c) first-order kinetics rate curves

Table 7.4 A summary of the dye removal efficiency and kinetics for the photocatalytic bionanocomposites

Composite	Dye removal at t=0 (%)	Dye removal t=180 min (%)	$k_{0\ app}$ ($\times 10^{-3}$)	R^2	k_{1app} ($\times 10^{-3}$)	R^2	Kinetics order description	Energy band gap (eV)
a-C,TiO_2	3.09	94.1	4.76	0.939	14.0	0.934	0	3.46
a-C,$NTiO_2$	3.7	21.6	0.97	0.805	1.1	0.815	1st	3.62
PMC–a-C,TiO_2	9.90	64.3	3.30	0.993	4.96	0.966	0	3.57
GAA–a-C,TiO_2	0.228	96.3	5.46	0.974	18.0	0.938	0	3.40
PMC–a-C,$NTiO_2$	1.96	23.0	1.23	0.980	1.39	0.990	1st	3.33
GAA–a-C,$NTiO_2$	2.79	97.6	5.17	0.830	21.5	0.990	1st	3.55

With respect to the overall dye removal, the GAA-based photocatalytic bionanocomposites have the best performance with GAA–a-C,$NTiO_2$ being the first and GAA–a-C,TiO_2 being the second best performing (***Table 7.3***). Most notably, the PMC based bionanocomposites and a-C,$NTiO_2$ have extremely low dye removal than a-C,TiO_2. The influence of grafted acrylic acid in enhancing the photocatalytic activity of both C-doped TiO_2 and C, N co-doped TiO_2 is revealed. We attribute this to the hydrophilic nature of polyacrylic acid aiding the attachment of the TiO_2 onto the adsorptive bionanocomposite.

In studying the kinetics for the removal of the dye molecules, the data was fitted for zero-order, first order and second order kinetic. It was shown that none of the photocatalytic bionanocomposites followed the second order in the removal of the dye. Secondly, the N-doped photocatalysts a-$NTiO_2$, PMC–a-$NTiO_2$ and GAA–a-TiO_2 followed the pseudo first order kinetics as determined by the correlation coefficients (***Table 7.4***). The Incorporation of the N as a dopant imputes catalyst with 1st order degradation kinetics since a-$NTiO_2$, PMC–a-$NTiO_2$ and GAA–a-TiO_2 all fit pseudo first order kinetics for the removal of the dye. This implies that the is initiated by multilayer adsorption of the dye molecules onto the surface of the catalyst. As such, the adsorption is the rate-determining step. The pattern in the photocatalytic efficiencies of the photocatalytic bionancomposites can be linked to their morphology as shown

bt the TEM micrographs. GAA–a-C,NTiO_2 and PMC–a-C,NTiO_2 were shown to have a better dispersion by the TEM microhtaphs and small nanoparticle aggregates by the HRSEM and hence likely to have the advantage of a high surface area. It

a-TiO_2, PMC–a-TiO_2 and GAA– a-TiO_2 all follow the pseudo zero order kinetics for the removal of the dyes implying that the degradation is independent of the concentration. While it is common that heterogenous photocatalysis follows pseudo first order, there have been cases where the degradation follows pseudo first order at the onset of the degradation and as the concentration decreases the reaction rate follows the pseudo first order [37]. The pseudo zero order kinetics could imply that the degradation mainly proceeds through the release of the reactive oxidative species (typically OH or COOH). These radicals then permeate the dye solution and on interacting with the dye molecules, degrade the molecules. In retrospect, this work has demonstrated that in-situ modification of amorphous TiO_2 with plant based adsorptive photocatalytic bionanocomposites significantly affects the physicochemical properties and the chemical properties and that these effects are seen in the photocatalytic performance of the bionanocomposites. In addition, the modification with the plant-based bionanocomposites enables multiple elements doping of the TiO_2 as shown in ***Table 7.5***. It has hereby been demonstrated that such modified amorphous TiO_2 has photocatalytic performance that is comparable to previous accounts of amorphous TiO_2 and that the performance is closely matched to that of crystalline TiO_2

Table 7.5 A comparison of the current work with previous work on the photodegradation using photocatalytic bionanocomposites.

Photocatalytic material composition	**Target pollutant and degradation conditions**	**Results**	**Ref**
	Amorphous TiO_2		
a-TiO_2	2-propanol degradation under UV light	-2-propanol under UV-light -2-propanol conversion lowest for a-TiO_2	[38]
C-doped a-TiO_2	500 ppm c-doped a-TiO_2 in 5 ppm RhB solution	Rhodamine B and 4-chlorophenol with	[20]

	500 ppm c-doped a-TiO_2 in 5 ppm Chlorophenol	k_1app=4.6×10^{-2} for 4-Chlorophenol removal	
C-doped TiO_2 microspheres	1000 ppm catalyst in 10 ppm RhB under solar simulation	RhB decolorization under simulated solar light. $k_{1app} = 5.1 \times 10^{-2}$ for a-TiO_2 and 3.7 for P25	[39]
	Photocatalytic TiO_2 bionanocomposites		
TiO_2–microfibrilated cellulose–polyamide amine epichlorohydrin (PAE)	Methyl orange (MO) (5 ppm) under UV light	95% removal of MO in 150 min	[40]
TiO_2–carbon fiber – cellulose fibers (Na_2SiO_3, $Al_2(SO_4)_3$ and PAE as binders	MO (20 ppm) under UV light	~99% MO removal after 7 h and recyclability of the composite due to strengthening effect of PAE	[41]
TiO_2/Ag – cellulose fibers	MO and methylene blue (MB) 20 ppm under UV light	~ 95% removal of MO in 4 hours and second run	[42]
Spherical a-TiO_2	Rhodamine B		
	Current work		
a-C,TiO_2 a-C,NTiO_2 PMC–a-C,TiO_2 GAA–a-C-TiO_2 PMC–a-C,NTiO_2 GAA–a-C,NTiO_2	10 ppm of catalysts dispersed in a mixture of RhB and RR 120 each 25 ppm before mixing. Degradation carried under UV light	97% dye decolorization in 180 min for the best performing photocatalytic bionanocomposite GAA–a-C,NTiO_2	Current work

7.4. Conclusions

Pinecone powder based bionanocomposite adsorbents were successfully employed as modifiers and additives to form amorphous TiO_2 and amorphous $NTiO_2$ composites. The bionanocomposites promoted the amorphosity of the ultimate photocatalytic bionanocomposites and enabled carbon doping of all the photocatalysts. Additional doping of the photocatalytic bionanocomposites with N resulted in the reduction in particle size and the sizes of the particle aggregates. Co-doping TiO_2 with N and C resulted in decreased photocatalytic efficiency of the nanohybrid. Similarly, the incorporation of pine-magnetite bionanocomposite into C, TiO_2 did not improve the photocatalytic efficiency past that of a-C,TiO_2. Significant improvement in photocatalytic efficiency was realized when acrylic acid grafted pine-magnetite composite was used for the modification of a-C,TiO_2 resulting in GAA –a-C,TiO_2 bionanocomposites removing 97% of the dye molecules. Additional doping of this bionanocomposite with N further improved the photocatalytic performance of the resultant GAA –a-C,TiO_2 bionanocomposites. This work has therefore, successfully demonstrated that pinecone based magnetite composites can be successfully applied in the tailoring of a-TiO_2 for improved photocatalytic efficiency without calcining the resultant bionancomposites at high temperatures. In addition, monodoped and co-doped amorphous TiO_2 has been demonstrated to be an effective catalyst for the degradation of organic pollutants.

7.5. References

[1] P. Rajasulochana, V. Preethy, Comparison on efficiency of various techniques in treatment of waste and sewage water – A comprehensive review, Resour. Technol. 2 (2016) 175–184. https://doi.org/10.1016/j.reffit.2016.09.004.

[2] W. Liu, J. Ni, X. Yin, Synergy of photocatalysis and adsorption for simultaneous removal of Cr(VI) and Cr(III) with TiO_2 and titanate nanotubes, Water Res. 53 (2014) 12–25. https://doi.org/10.1016/j.watres.2013.12.043.

[3] S. Natarajan, H.C. Bajaj, R.J. Tayade, Recent advances based on the synergetic effect of adsorption for removal of dyes from waste water using photocatalytic process, J. Environ. Sci. (China). 65 (2018) 201–222. https://doi.org/10.1016/j.jes.2017.03.011.

[4] T. Fazal, A. Razzaq, F. Javed, A. Hafeez, N. Rashid, U.S. Amjad, M.S. Ur Rehman, A. Faisal, F. Rehman, Integrating adsorption and photocatalysis: A cost effective strategy for textile wastewater treatment using hybrid biochar-TiO_2 composite, J. Hazard. Mater. 390 (2020) 121623. https://doi.org/10.1016/j.jhazmat.2019.121623.

[5] S. Mohan, O.S. Oluwafemi, N. Kalarikkal, S. Thomas, S.P. Songca, Biopolymers – Application in Nanoscience and Nanotechnology, in: Recent Adv. Biopolym., 2016: pp. 47–72. https://doi.org/http://dx.doi.org/10.5772/62225.

[6] J.C. Colmenares, R.S. Varma, P. Lisowski, Sustainable hybrid photocatalysts: Titania immobilized on carbon materials derived from renewable and biodegradable resources, Green Chem. 18 (2016) 5736–5750. https://doi.org/10.1039/c6gc02477g.

[7] B. Joseph, S. Krishnan, V.K. Sagarika, A. Tharayil, N. Kalarikkal, S. Thomas, Bionanocomposites as industrial materials, current and future perspectives: a review, Emergent Mater. 3 (2020) 711–725. https://doi.org/10.1007/s42247-020-00133-x.

[8] X. Chen, D.H. Kuo, D. Lu, Y. Hou, Y.R. Kuo, Synthesis and photocatalytic activity of mesoporous TiO_2 nanoparticle using biological renewable resource of un-modified lignin as a template, Microporous Mesoporous Mater. 223 (2016) 145–151. https://doi.org/10.1016/j.micromeso.2015.11.005.

[9] D. Ke, S. Liu, K. Dai, J. Zhou, L. Zhang, T. Peng, CdS/regenerated cellulose nanocomposite films for highly efficient photocatalytic H2 production under visible light irradiation, J. Phys. Chem. C. 113 (2009) 16021–16026. https://doi.org/10.1021/jp903378q.

[10] B. Wang, M. Feng, H. Zhan, Improvement of wood properties by impregnation with TiO_2 via ultrasonic-assisted sol-gel process, RSC Adv. 4 (2014) 56355–56360. https://doi.org/10.1039/c4ra04852k.

[11] P. Lisowski, J.C. Colmenares, O. Mašek, W. Lisowski, D. Lisovytskiy, A. Kamińska, D. Łomot, Dual Functionality of TiO_2/Biochar Hybrid Materials: Photocatalytic Phenol Degradation in the Liquid Phase and Selective Oxidation of Methanol in the Gas Phase, ACS Sustain. Chem. Eng. 5 (2017) 6274–6287. https://doi.org/10.1021/acssuschemeng.7b01251.

[12] H. Wang, X. Qiu, W. Liu, D. Yang, Facile preparation of well-combined lignin-based carbon/ZnO hybrid composite with excellent photocatalytic activity, Appl. Surf. Sci. 426 (2017) 206–216. https://doi.org/10.1016/j.apsusc.2017.07.112.

[13] A. Khan, V. Nair, J.C. Colmenares, R. Gl, Lignin-Based Composite Materials for Photocatalysis, in: M. Olivucci, W.-Y. Wong (Eds.), Top. Curr. Chem. Collect. Chem., 1st ed., 2018: pp. 1–31. https://doi.org/10.1007/978-3-030-00590-0.

[14] H. Wang, X. Qiu, R. Zhong, F. Fu, Y. Qian, D. Yang, One-pot in-situ preparation of a lignin-based carbon/ZnO nanocomposite with excellent photocatalytic performance, Mater. Chem. Phys. 199 (2017) 193–202. https://doi.org/10.1016/j.matchemphys.2017.07.009.

[15] N. Wang, H. Fan, S. Ai, Lignin templated synthesis of porous carbon-CeO2composites and their application for the photocatalytic desulphuration, Chem. Eng. J. 260 (2015) 785–790. https://doi.org/10.1016/j.cej.2014.09.051.

[16] J. Mavračić, F.C. Mocanu, V.L. Deringer, G. Csányi, S.R. Elliott, Similarity between Amorphous and Crystalline Phases: The Case of TiO_2, J. Phys. Chem. Lett. 9 (2018) 2985–2990. https://doi.org/10.1021/acs.jpclett.8b01067.

[17] B. Choudhury, B. Borah, A. Choudhury, Extending photocatalytic activity of TiO_2 nanoparticles to visible region of illumination by doping of cerium, Photochem. Photobiol. 88 (2012) 257–264. https://doi.org/10.1111/j.1751-1097.2011.01064.x.

[18] V. Nadtochenko, N. Denisov, A. Gorenberg, Y. Kozlov, P. Chubukov, J.A. Rengifo, C. Pulgarin, J. Kiwi, Correlations for photocatalytic activity and spectral features of the absorption band edge of TiO_2 modified by thiourea, Appl. Catal. B Environ. 91 (2009) 460–469. https://doi.org/10.1016/j.apcatb.2009.06.015.

[19] B. Prasai, B. Cai, M.K. Underwood, J.P. Lewis, D.A. Drabold, Properties of amorphous and crystalline titanium dioxide from first principles, J. Mater. Sci. 47 (2012) 7515–7521. https://doi.org/10.1007/s10853-012-6439-6.

[20] P. Shao, J. Tian, Z. Zhao, W. Shi, S. Gao, F. Cui, Amorphous TiO_2 doped with carbon for visible light photodegradation of rhodamine B and 4-chlorophenol, Appl. Surf. Sci. 324 (2015) 35–43. https://doi.org/10.1016/j.apsusc.2014.10.108.

[21] Sigma-Aldrich, IR Spectrum Table & Chart, Sigma Aldrich. (2019) 1–6. https://www.sigmaaldrich.com/technical-documents/articles/biology/ir-spectrum-table.html (accessed May 15, 2021).

[22] D.S. Ahmed, A.L. Abed, G.K. Salman, Fabrication of carbon nanotube/titanium dioxide nanocomposite photocatalyst using sol-gel method, Iraqi J. Appl. Phys. 12 (2016) 2309–1673.

[23] F. Xiao, B. Wang, X. Hu, S. Nair, Y. Chen, Thin film nanocomposite membrane containing zeolitic imidazolate framework-8 via interfacial polymerization for highly permeable nanofiltration, J. Taiwan Inst. Chem. Eng. 83 (2018) 159–167. https://doi.org/10.1016/j.jtice.2017.11.033.

[24] M. Touihri, F. Guesmi, C. Hannachi, B. Hamrouni, L. Sellaoui, M. Badawi, J. Poch, N. Fiol, Single and simultaneous adsorption of Cr(VI) and Cu (II) on a novel Fe_3O_4/pine cones gel beads nanocomposite: Experiments, characterization and isotherms modeling, Chem. Eng. J. 416 (2021). https://doi.org/10.1016/j.cej.2021.129101.

[25] S. Sun, P. Song, J. Cui, S. Liang, Amorphous TiO_2 nanostructures: Synthesis, fundamental properties and photocatalytic applications, Catal. Sci. Technol. 9 (2019) 4198–4215. https://doi.org/10.1039/c9cy01020c.

[26] E. Martínez-Ferrero, Y. Sakatani, C. Boissière, D. Grosso, A. Fuertes, J. Fraxedas, C. Sanchez, Nanostructured titanium oxynitride porous thin films as efficient visible-active photocatalysts, Adv. Funct. Mater. 17 (2007) 3348–3354. https://doi.org/10.1002/adfm.200700396.

[27] H.N. Fernandez-Escamilla, J. Guerrero-Sanchez, E. Contreras, J.M. Ruiz-Marizcal, G. Alonso-Nunez, O.E. Contreras, R.M. Felix-Navarro, J.M. Romo-Herrera, N. Takeuchi, Understanding the Selectivity of the Oxygen Reduction Reaction at the Atomistic Level on Nitrogen-Doped Graphitic Carbon Materials, Adv. Energy Mater. 11 (2021) 1–12. https://doi.org/10.1002/aenm.202002459.

[28] M. Thommes, K. Kaneko, A. V. Neimark, J.P. Olivier, F. Rodriguez-Reinoso, J. Rouquerol, K.S.W. Sing, Physisorption of gases, with special reference to the evaluation of surface area and pore size distribution (IUPAC Technical Report), Pure Appl. Chem. 87 (2015) 1051–1069. https://doi.org/10.1515/pac-2014-1117.

[29] K.A. Cychosz, M. Thommes, Progress in the Physisorption Characterization of Nanoporous Gas Storage Materials, Engineering. 4 (2018) 559–566. https://doi.org/10.1016/j.eng.2018.06.001.

[30] W.J. Braida, J.J. Pignatello, Y. Lu, P.I. Ravikovitch, A. V. Neimark, B. Xing, Sorption hysteresis of benzene in charcoal particles, Environ. Sci. Technol. 37 (2003) 409–417. https://doi.org/10.1021/es020660z.

[31] P. Maziarka, P. Sommersacher, X. Wang, N. Kienzl, S. Retschitzegger, W. Prins, N. Hedin, F. Ronsse, Tailoring of the pore structures of wood pyrolysis chars for potential use in energy storage applications, Appl. Energy. 286 (2021) 116431. https://doi.org/10.1016/j.apenergy.2020.116431.

[32] P. Maziarka, P. Sommersacher, X. Wang, N. Kienzl, W. Prins, N. Hedin, F. Ronsse, Supplementary data Potential of pyrochars for energy storage applications: Changes in specific surface area with pyrolysis temperature and leaching pretreatment of beech wood Temperature Surface, Appl. Energy. 286 (2021) 1–5.

[33] A. Grosman, C. Ortega, Capillary condensation in porous materials. Hysteresis and interaction mechanism without pore blocking/percolation process, Langmuir. 24 (2008) 3977–3986. https://doi.org/10.1021/la703978v.

[34] T. Edvinsson, Optical quantum confinement and photocatalytic properties in dimensional nanostructures, R. Soc. Open Sci. 5 (2018) 180387. https://doi.org/10.1098/rsos.180387.

[35] M. Lal, P. Sharma, C. Ram, Calcination Temperature Effect on Titanium Oxide (TiO_2) Nanoparticles Synthesis, Optik (Stuttg). (2021) 104847. https://doi.org/10.1016/j.ijleo.2021.166934.

[36] C.S. Chua, D. Ansovini, C.J.J. Lee, Y.T. Teng, L.T. Ong, D. Chi, T.S. Andy Hor, R. Raja, Y.F. Lim, The effect of crystallinity on photocatalytic performance of Co3O4 water-splitting cocatalysts, Phys. Chem. Chem. Phys. 18 (2016) 5172–5178. https://doi.org/10.1039/c5cp07589k.

[37] K. Babic, V. Tomašic, V. Gilja, J. Le Cunff, V. Gomzi, A. Pintar, G. Žerjav, S. Kurajica, M. Duplancic, I.E. Zelic, T.V. Pavicic, I. Grcic, Photocatalytic degradation of imidacloprid in the flat-plate photoreactor under UVA and simulated solar irradiance conditions - The influence of operating conditions, kinetics and degradation pathway, J. Environ. Chem. Eng. 9 (2021) 1–14. https://doi.org/10.1016/j.jece.2021.105611.

[38] B. Ohtani, Y. Ogawa, S.I. Nishimoto, Photocatalytic activity of amorphous-anatase mixture of titanium(IV) oxide particles suspended in aqueous solutions, J. Phys. Chem. B. 101 (1997) 3746–3752. https://doi.org/10.1021/jp962702+.

[39] Y. Wang, H. Yang, W. Zou, Preparation of amorphous sphere-like TiO_2 with excellent photocatalytic performance, Mater. Lett. 254 (2019) 54–57. https://doi.org/10.1016/j.matlet.2019.06.108.

[40] U.M. Garusinghe, V.S. Raghuwanshi, W. Batchelor, G. Garnier, Water Resistant Cellulose-Titanium Dioxide Composites for Photocatalysis, Sci. Rep. 8 (2018) 1–13. https://doi.org/10.1038/s41598-018-20569-w.

[41] J. Zhang, W. Liu, P. Wang, K. Qian, Photocatalytic behavior of cellulose-based paper with TiO_2 loaded on carbon fibers, J. Environ. Chem. Eng. 1 (2013) 175–182. https://doi.org/10.1016/j.jece.2013.04.022.

[42] J. Wang, W. Liu, H. Li, H. Wang, Z. Wang, W. Zhou, H. Liu, Preparation of cellulose fiber-TiO_2 nanobelt-silver nanoparticle hierarchically structured hybrid paper and its photocatalytic and antibacterial properties, Chem. Eng. J. 228 (2013) 272–280. https://doi.org/10.1016/j.cej.2013.04.098.

CHAPTER 8

CONCLUSIONS AND RECOMMENDATIONS

8.1. Conclusions

The main purpose of this study was to produce novel, effective and cheap bio-nanocomposite adsorbents and subsequently photocatalysts from pinecone (the plant material) for the removal of dyes from aqueous solutions. This thesis revealed that pinecone-based bionanocomposites are not only suitable for adsorptive removal of dyes but also as potential modifiers for existing semiconductor photocatalysts to form photocatalytic bionanocomposites. It was shown that plant-based photocatalytic bionanocomposites have the potential to significantly lower the cost of manufacturing photocatalysts.

The first part of the thesis showed the successful production of magnetic pine-magnetite bionanocomposite (PMC) using an enhanced co-precipitation method. The observations also showed that the optimization of the pine-magnetite composite was dependent on the chosen parameters XRF analysis confirmed the optimization conditions by showing the highest % of FeO present on the parameters selected. XRD analysis confirmed the spherical structure of Fe_3O_4 and the binding of Fe_3O_4 onto pinecone while FTIR confirmed the functional groups on the NaOH treated pinecone and the PMC. Removal of dye was found to have a capacity of 195 $mg.g^{-1}$ using pine-magnetite composite compared to treated pinecone which gave 90 $mg.g^{-1}$ highest capacity. The adsorbent shows a promising adsorption capacity for the removal of methylene blue dye. PMC also exhibit excellent magnetic separation after adsorption process due to the large surface area and magnetic property.

The adsorption kinetics studies showed the adsorption processes increase with increase in time. The adsorption data was adequately interpreted by Langmuir and Freundlich isotherm models respectively. R^2 values for the Langmuir showed to be higher than those of the Freundlich isotherm model, which suggests the Langmuir isotherm gave suitable reason for defining the adsorption equilibrium of MB onto PMC. This implies that the adsorption process occurs in a homogeneous surface thus giving homogeneous distribution of active sites on the PMC. The value of K_L showed a decrease with increase in temperature, which implies that low temperatures favored the adsorption process. The adsorption is evidently favorable as

Freundlich constant n is 2.47, 2.23 and 2.02 for PMC. Therefore, it can be concluded that Langmuir isotherm model gave the best equilibrium fit. Temkin constants K, b_T together with R^2 values also concluded that the heat of adsorption of all the molecules in the layer showed decrease linearly with coverage due to adsorbate/adsorbent interactions. K, decreased as the experimental temperature increased from 299 to 309 K, which implies that the adsorption process is exothermic and favored at higher temperatures. The PMC showed improvement in adsorption capacity and reusability which further demonstrates that it is a promising adsorbent in the wastewater treatment at a larger scale.

The second part of the study described the incorporation of grafting with acrylic acid or acrylamide monomers prepared composite via a free radical initiated grafting. The study of grafting with acrylamide showed that it was successfully incorporated onto pine-magnetite composite. FTIR, BET, SEM, TEM and XRD characterization gave sufficient evidence to demonstrate the incorporation and distribution of the iron oxide nanoparticles within the polymer matrix. GACA nanocomposites were shown to be effective in the adsorption of methylene blue at a pH of 12. The adsorbent dose and contact time demonstrated excellent results in the adsorption of methylene blue due to the increased surface area and high rate of the adsorption. At mass dosage of 0.5 g, the highest percentage removal of 99.8% was obtained. When it comes to contact time, the adsorption rate of the grafted composite on the removal of MB showed to be faster at the beginning which might have been influenced by the grafted composite with higher specific gravity and that made them better in dispersity and more efficient contact with MB. The kinetics studies showed that GACA behaved similarly to PMC in the adsorption of MB.

The grafting of acrylic acid onto pine-magnetite bionanocomposites was also successfully carried out in this work. The results obtained demonstrated that there was a reduction on the particle size of magnetite and reduction on the point zero charge due to grafting. These features, together with the improved crystallinity of magnetite, improved the adsorptive capacity towards cationic species such as the MB organic ion. The parameters influencing adsorption such as solution pH, contact time and adsorbent dose showed significant influence on the graft polymerization process. The results also showed that grafting PMC with acrylic acid leads to reduced crystalline and particle sizes of the iron oxide resulting in higher surface area for GAA bionanocomposites, thus leading to excellent adsorption performance. The polyacrylic acid

formed from the condensation reaction of acrylic acid resulted to surface coating of the grafted acrylic acid bionanocomposites. GAA and MB interaction mechanism was confirmed by intra particle diffusion. The adsorbent also showed improvement in the adsorption capacity and reusability promising to be used for removal of dyes in an industrial scale. This is owing to the polyacrylic acid on GAA and its interaction with water to produce a net negative surface charge. The adsorption is a factor of the net surface charge of the bionanocomposites at pH 12. With GAA having a lower pH_{pzc} than PMC, the net charge of the bio-nanoparticles has shifted more towards negative than in PMC.

The last part of the study demonstrated that pinecone-based bionanocomposites make a good starting material for the fabrication of TiO_2-based photocatalytic bionanocomposites. Firstly, the synthesis method employed allowed for the formation of amorphous titania and, because of the low drying temperatures (200 °C), the photocatalytic bionanocomposites retain large amounts of carbon. In this way, carbon-doped amorphous titania was synthesized. Additional doping of the amorphous titania with N, was achieved. Subsequently, pine-magnetite composites and grafted acrylic acid composites were used to form modified forms of the a-C,TiO_2 and a-C,NTiO_2. FTIR and EDS demonstrated that all the photocatalysts were rich in carbon to the point of suggesting that most of the carbon doping was due to the carbon residue from the process chemicals. The influence of incorporating GAA and PMC as modifiers for a-CTiO_2 and a-C,NTiO_2 was seen in that the N-doped photocatalysts all had small aggregates of the titania and the nanoparticles were relatively well dispersed. However, with respect to speeding up the photocatalytic efficiency, only the composites of GAA had a better photocatalytic activity than the baseline photocatalyst (a-C,TiO_2). This is suggested to be due to the polyacrylic acid facilitating the bonding of the a-C,TiO_2 and a-C,NTiO_2 onto the adsorptive bio-nanocomposite during the formation of the a-C,TiO_2 nanoparticles. Ultimately, the synergy of co-doping a-TiO_2 with C and N and further modifying with GAA was shown to be the most efficient in terms of improving the photocatalytic efficiency of GAA–a-C,NTiO_2 bionanocomposites.

This work has demonstrated that adsorptive and photocatalytic bionanocomposites can be prepared from plant material and synthesis processes that use lesser energy. As such a step in improving the economic feasibility of the adsorption and photocatalysis processes has been achieved.

8.2. Recommendations

Based on the aims, objectives, scope, and limitations of this study the following recommendations can be made:

i. The adsorption capacity of the following bionanocomposites, PMC, PMC_GAA, PMC-GACA, PMCTiO– a-C,TiO_2 , PMC–a-C,$NTiO_2$, GAA–a-C,TiO_2 and GAA–a-C,$NTiO_2$ be explored in other binary mixtures of pollutants and crude wastewater.

ii. Additional kinetic models and isotherms of these bionanocomposites should be studied for better understanding in the removal of undesirable pollutants such as micropollutants.

iii. Studies on the role of plant biopolymers as templates for crystalline, carbon doped amorphous TiO_2 and crystalline TiO_2 should be carried out. In this sense, understanding the effect of doping a-C,TiO_2 with a metallic ions and co-doping with non-metallic ions will be determined.

iv. Other effective means by which the visible light absorption of a-C,TiO_2 can be improved should be explored.

v. Reusability studies for amorphous titania that has been modified using plant-based biopolymers should be carried out.

vi. The cost of synthesizing these bionanomaterials, their toxicity and environmental sustainability should be explored.